Gas Separation Using
Nanoporous Single-Layer Graphene Membranes

by

Zhe Yuan
B.S., Chemical Engineering, Tsinghua University (2015)

Submitted to the Department of Chemical Engineering
in partial fulfillment of the requirements for the degree of

DOCTOR OF PHILOSOPHY IN CHEMICAL ENGINEERING

at the

MASSACHUSETTS INSTITUTE OF TECHNOLOGY

September 2021

Author ……
Department of Chemical Engineering
June 16, 2021

Certified
by ……
Daniel Blankschtein
Herman P. Meissner (1929) Professor of Chemical Engineering
Thesis Advisor

Certified
by ……
Michael S. Strano
Carbon P. Dubbs Professor in Chemical Engineering
Thesis Advisor

Accepted
by ……
Patrick S. Doyle
Robert T. Haslam (1911) Professor of Chemical Engineering
Chairman, Committee for Graduate Students

Gas Separation Using
Nanoporous Single-Layer Graphene Membranes

by

Zhe Yuan

Submitted to the Department of Chemical Engineering on June 16, 2021
in partial Fulfillment of the Requirements for the Degree of
Doctor of Philosophy in Chemical Engineering

Abstract

Nanoporous single-layer graphene is regarded as a highly promising membrane material for gas separation due to its atomic thickness. When single-layer graphene contains a high density of gas sieving nanoscale pores, it can exhibit both a high gas permeance and a high selectivity, which is beneficial for reducing the cost of gas separation processes. However, significant challenges remain for matching theoretical predictions with experimental measurements and for the real application of graphene membranes for gas separations. To tackle these challenges, in this thesis, I carry out both theoretical and experimental investigations to understand and to improve the gas separation properties of nanoporous single-layer graphene membranes.

On the theoretical side, first, using molecular dynamics simulations, I investigate the mechanism of activated gas permeation through sub-nanometer graphene pores when energy barriers exist for pore crossing. I develop an analytical framework based on transition state theory to predict the gas permeance through a given graphene nanopore. Second, I extend the analytical framework mentioned above from sub-nanometer pores to larger pores. I formulate the transport kinetics associated with the direct impingement from the bulk and with the surface diffusion from the adsorption layer on graphene, and then combine them to predict the overall gas permeation rate using a reaction network model. Last, I apply the theory developed above to predict the total gas permeance through a pore ensemble with a realistic pore size distribution, which is generated by Kinetic Monte Carlo simulations. I show that the total gas permeance through a pore ensemble is dominated by a small fraction of large nanopores having low energy barriers of pore crossing.

On the experimental side, I demonstrate temperature-dependent gas mixture separation using single-layer graphene membranes. The membranes contain intrinsic nanopores formed during the chemical vapor deposition synthesis of graphene. I investigate the formation mechanism of the intrinsic graphene nanopores, and systematically control the density of the intrinsic graphene nanopores while maintaining appropriate pore sizes for gas sieving. I identify that nanoscale molecular fouling of the graphene surface where graphene pores are partially blocked by hydrocarbon contaminants under experimental conditions, affects both gas permeance and selectivity.

Thesis Supervisor: Daniel Blankschtein
Title: Herman P. Meissner (1929) Professor of Chemical Engineering
Thesis Supervisor: Michael S. Strano
Title: Carbon P. Dubbs Professor in Chemical Engineering

Acknowledgements

It has been a long and tortuous journey since I started my PhD career in 2015. Here, I would like to take this opportunity to thank the many people who have supported me, helped me, and accompanied me along the way. Without them, this thesis would not have been completed.

First and foremost, I would like to thank my thesis advisors, Professor Daniel Blankschtein and Professor Michael Strano for their generous support the entire time. They are perfect role models in my research career. I am constantly inspired by their work ethics, integrity, and enthusiasm in science. They are the type of scientist that I hope to become. Professor Blankschtein is always calm and patient. His encouragement during the dark days when nothing seemed to work out was the safeguard for me. Despite tremendous back pain, he continues to perform high-quality teaching and research. His perseverance taught me the right attitude to face the difficulties in life. He is a very hardworking and meticulous theorist. I really thank him for spending great effort correcting my grammatical errors and digesting my experimental research updates. Professor Strano's passion for science is a constant driving force during my PhD. Despite always having a very busy schedule, he never stops thinking about new ideas. I am constantly amazed by his scientific intuition, his vision about scientific advances, and his ability to simplify complicated problems. I enjoyed serving as a teaching assistant for his graduate course "10:585: Engineering Nanotechnology", and I learned a lot from the breadth of his scientific knowledge.

I want to thank Professor William Green and Professor Gregory Rutledge for being a part of my Thesis Committee. They offered important feedback to my research and helped me improve my thesis. I am grateful to Professor Allen Myerson and Professor Jing Kong for their constructive input to this thesis. I am also grateful to my undergraduate advisor Professor Qiang Zhang for his continued endorsement.

I would like to thank my colleagues here at MIT for their tutoring, support, assistance, and company. It has been great pleasure working with Vishnu Sresht, Hari Katepalli, Diviya Sinha, Ananth Govind Rajan, Rahul Prasanna Misra, Annalisa Cardellini, and Satish Kumar Iyemperumal from the Blankschtein Group, and Kumar Varoon Agrawal, Guangwei He, Pingwei Liu, Jesse Benck, Amir Kaplan, Matthias Kuehne, Sylvia Xin Li, Yuwen Zeng, Volodymyr Koman, Ananth Govind Rajan, Lee Drahushuk, Samuel Faucher, Ge Zhang, Jingfan Yang, and Song Wang from the Strano Group. I also would like to thank my classmates here at MIT, Weike Sun, Zhenshu Wang, and Hongbo Zhao.

Finally, I want to thank my parents, Maode Yuan and Minfen He, for their love and unconditional support. Confucius said, "whilst thy father and mother are living, do not wander afar." I did not follow this ancient maxim, but my parents always believe in me. I also want to thank my significant other, Yan Xiong, for her love and company, despite the long distance.

Articles Resulting from this Thesis

Parts of this thesis were published, or will be published, as follows:

Chapter 1
Yuan, Z.; He, G.; Strano, M. S.; Blankschtein, D. Gas Separations using Nanoporous Atomically Thin Membranes: Recent Theoretical, Simulation, and Experimental Advances. In preparation.

Chapter 2
Yuan, Z.; Govind Rajan, A.; Misra, R. P.; Drahushuk, L. W.; Agrawal, K. V.; Strano, M. S.; Blankschtein, D. Mechanism and Prediction of Gas Permeation through Sub-Nanometer Graphene Pores: Comparison of Theory and Simulation. *ACS Nano* **2017**, 11 (8), 7974–7987.

Chapter 3
Yuan, Z.; Benck, J. D.; Eatmon, Y.; Blankschtein, D.; Strano, M. S. Stable, Temperature-Dependent Gas Mixture Permeation and Separation through Suspended Nanoporous Single-Layer Graphene Membranes. *Nano Lett.* **2018**, 18 (8), 5057–5069.

Chapter 4
Yuan, Z.; Misra, R. P.; Govind Rajan, A.; Strano, M. S.; Blankschtein, D. Analytical Prediction of Gas Permeation through Graphene Nanopores of Varying Sizes: Understanding Transitions across Multiple Transport Regimes. *ACS Nano* **2019**, 13 (10), 11809–11824.

Chapter 5
Yuan, Z.; Govind Rajan, A.; He, G.; Misra, R. P.; Strano, M. S.; Blankschtein, D. Predicting Gas Separation through Graphene Nanopore Ensembles with Realistic Pore Size Distributions. *ACS Nano* **2021**, 10.1021/acsnano.0c09420.

Chapter 6
Yuan, Z.; He, G.; Faucher, S.; Kuehne, M.; Li, X.; Blankschtein, D.; Strano, M. S. Direct Chemical Vapor Deposition Synthesis of Porous Single-Layer Graphene Membranes with High Gas Permeances and Selectivities. Under review in *Advanced Materials*.

Table of Contents

List of Figures

List of Tables

1 Introduction

1.1 Single-Layer Graphene Membranes for Gas Separation

Separation processes account for nearly half of the energy consumption in the industrial sector and 10–15% of the world's total energy consumption.[1–3] The enormous production scale of chemical commodities is an important reason for the high energy consumption. The dominance of thermal-based separation processes, including distillation and evaporation is another reason.[4] These thermal-based separations rely on phase changes and are highly energy intensive, accounting for more than 80% of the energy consumed by chemical separations.[4] Membrane separations, on the other hand, are much more energy efficient and environmentally friendly because they do not require extensive heating or cooling.[1] However, much improvement is required for the membranes to be competitive application-wise.[5,6]

The separation of gaseous mixtures is essential in the chemical industry, including hydrogen separation in ammonia or petrochemical plants, nitrogen separation from air, CO_2 separation in natural gas processing,[7] and H_2S separation from sour gas.[8] Similar to separation processes in general, thermal-based gas separation methods, such as cryogenic distillation, amine adsorption, and vapor condensation, consume a high amount of energy, which can be significantly reduced using gas separation membrane units.[5,8] A membrane that can separate gases allows certain components in a mixture to permeate at higher rates than others. The economic competitiveness of a gas separation membrane highly depends on its gas permeance K and its selectivity S. The permeance K_i of gas species i (in SI units of mol m^{-2} s^{-1} Pa^{-1}) is defined as $K_i = F_i/\Delta p_i$, where F_i (in SI unit of mol m^{-2} s^{-1}) is the flux of gas i through the membrane, and Δp_i is the partial pressure difference (the driving force) of gas i between the feed side and the permeate side. For relatively thick conventional membranes, whose cross-membrane transport resistance is dominated by the bulk interior, the permeance K_i is inversely proportional to the membrane thickness d. Correspondingly, the permeability P_i of gas i (in SI units of mol m^{-1} s^{-1} Pa^{-1}) is defined as $P_i = K_i d = F_i d/\Delta p_i$, which is an intrinsic property of a material. The selectivity S_{ij} between gases i and j is defined as $S_{ij} = K_i/K_j = P_i/P_j$.

Polymers have been the most widely used materials for gas separation membranes for decades because of their relatively low cost and low manufacturing difficulty.[8,9] However, membrane separations using state-of-the-art polymeric membranes have not gotten competitive enough economically compared to the thermal-based separation methods.[7] One of the limitations of the polymeric membranes is the trade-off between permeability and selectivity, originally investigated by Robeson.[10,11] The best combination of permeability and selectivity for a binary gas pair is referred to as the polymer upper bound. This trade-off originates from the interplay between the free volume spacing in the polymer matrices and the size of the gas molecules.[12] Smaller polymeric spacing increases the selectivity but sacrifices the permeability due to the lower gas diffusivity inside the polymer, and vice versa. Note that this permeability-selectivity trade-off exist for all materials, but the upper bound for polymers can be surpassed by many other materials with more rigid pore structures, such as zeolites,[13,14] metal organic frameworks (MOFs),[15,16] silica,[17] carbon-based materials,[18–20] mixed matrix composites,[21,22] and even polymers which are thermally rearranged.[9] However, membranes made of the materials mentioned above need to be sufficiently thick to prevent collapsing due to their low mechanical strength or weak structural integrity. Furthermore, the permeability-selectivity trade-off constrains the permeability of a material in order to guarantee a reasonable selectivity. These two factors combined lead to low permeances through those conventional membrane materials ($K_i = P_i/d$).

Recent experimental and modeling advances in graphene technologies offers great opportunities for potential breakthroughs in the membrane separation field.[23,24] As mentioned above, gas permeance through a membrane is inversely correlated to its thickness.[25] Therefore, porous single-layer graphene shows high promise as the next-generation gas separation membrane.[24,26,27] The decent mechanical strength[28] and chemical stability[29,30] of graphene also enable it to serve as an effective membrane. Note that defect-free graphene is almost impermeable to gases, except H_2 with an extremely low permeance.[31–33] Therefore, pores need to be created in graphene for gas permeation by removing a certain number of carbon atoms. In order to discriminate between different gas molecules whose kinetic diameters are typically 0.2–0.6 nm, the diameter of these pores should be on the nanometer scale. Compared to pore matrices inside polymeric membranes, nanopores in single-layer graphene have negligible pore lengths. As a result, gas transport through the graphene nanopores experiences minimal

internal resistance, and is instead dominated by the transport resistances at the pore entrance and at the pore exit. This important feature makes the solution-diffusion model not readily applicable to gas transport through nanoporous graphene membranes.[34]

In recent years, progress has been made in both theoretical and experimental aspects regarding nanoporous graphene membranes for gas separation. However, much work is still needed for matching theory with experimental measurements and for the large-scale application of graphene membranes for gas separations. The theoretical and experimental challenges will be discussed in Sections 1.2 and 1.3, respectively.

1.2 Theoretical Challenges

From a theoretical viewpoint, the ability to predict the correlation between gas permeance and pore structure will be useful to interpret experimental permeation data, and to identify desired pore structures for targeted gas separation pairs. In other words, the central aim is to predict the gas permeance K through an ensemble of graphene pores given their structures, and then to confirm the predictions with experimental measurements. However, the mechanism of gas transport through a two-dimensional (2D) pore is fundamentally different from that through a polymeric membrane (a solution-diffusion mechanism, where gas permeability equals the product of gas solubility and diffusivity in the polymer).[34] The permeation of gas molecules through a 2D graphene pore follows different mechanisms, depending on the relation between the pore diameter D_p, the gas mean free path λ, and the kinetic diameter D_m of the gas molecule. Nanopores in single-layer graphene are nearly circular,[35] and therefore, their dimensions can be represented by their pore diameters D_p for simplicity. The kinetic diameter of a gas molecule is its size in the context of molecular collision, which is typically 0.2–0.6 nm.[36] The gas mean free path λ is the average distance travelled by a gas molecule between successive collisions, and is ~100 nm at ambient pressure and room temperature.[37] Four gas permeation mechanisms are illustrated in Figure 1-1, corresponding to different pore diameter ranges.

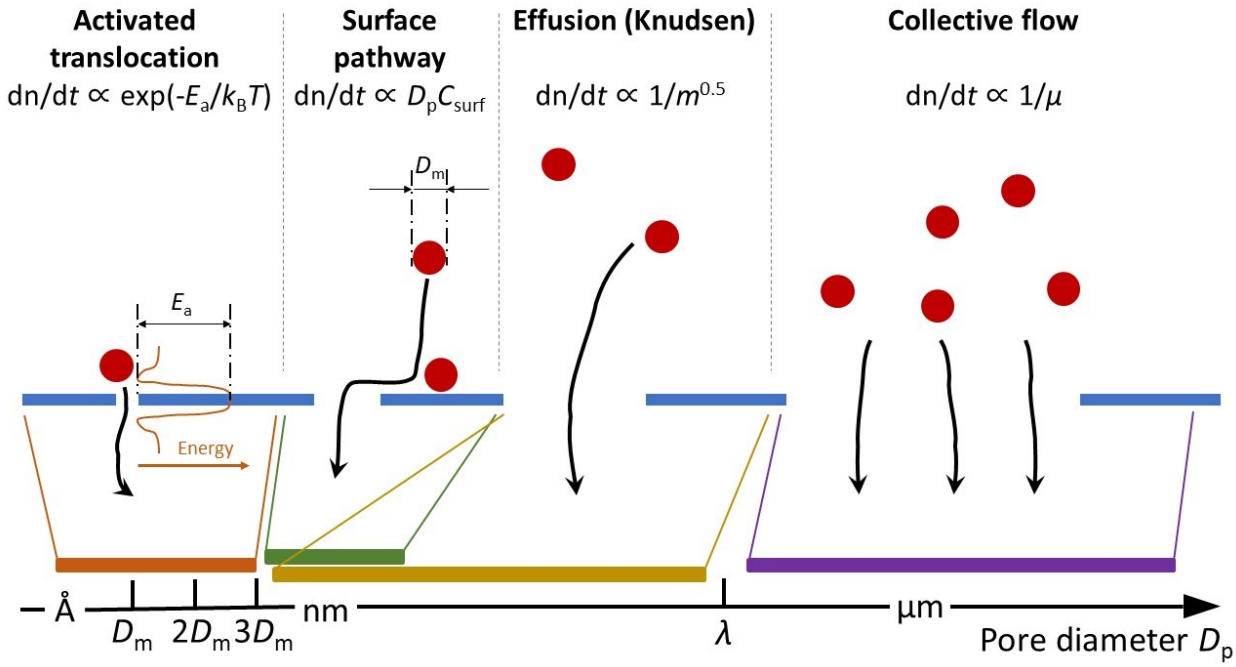

Figure 1-1. Schematic of gas transport mechanisms through nanopores in single-layer graphene with different pore diameters. D_m, gas kinetic diameter; D_p. pore diameter; dn/dt, molar gas permeation rate; m gas molecular weight; E_a, energy barrier associated with pore crossing; k_B, the Boltzmann constant; T, absolute temperature; C_{surf}, areal density of adsorbed gas molecules; μ, viscosity.

(1) Collective flow. When the pore diameter D_p is larger than the gas mean free path λ (or equivalently, when the Knudsen number Kn = $\lambda/D_p < 1$), the gas can be treated as a continuum because a gas molecule can collide with other ones while crossing the pore. In this D_p range ($D_p > \lambda$), gas transport through the pore is dominated by collective gas flow, which can be predicted by the Navier-Stokes equations. An analytical solution to the Navier-Stokes equations exists when the membrane is modelled as an infinitesimally thin plate (which is a good approximation for single-layer graphene), and is known as the modified Sampson's formula.[38–40] Because different gas components are well mixed and can exchange momenta when crossing the pore, the selectivity approaches 1, making gas mixture separation infeasible in this range.

(2) Effusion. When $D_p < \lambda \sim 100$ nm (Kn > 1), the cross-pore transport of a gas molecule is mostly not affected by other gas molecules and the continuum approximation breaks down. Specifically, gas transport is governed by effusion when $D_p >> D_m$ (gas kinetic diameter). Effusion, by definition, is the process where gas molecules escape through a pore without any interference from the other gas molecules (guaranteed by $D_p < \lambda$) or from the pore edge (guaranteed by $D_p >> D_m$).[41] Therefore, the rate

of effusion is equal to the rate of impingement of the gas molecules onto the pore area from the bulk, and can be predicted by the kinetic theory of gases as follows:[42]

$$\frac{\mathrm{d}n}{\mathrm{d}t} = \frac{\Delta p A_\mathrm{p}}{\sqrt{2\pi m k_\mathrm{B} T}} = \frac{\Delta p}{\sqrt{2\pi m k_\mathrm{B} T}} \cdot \frac{\pi D_\mathrm{p}^2}{4} \tag{1-1}$$

where dn/dt is the molar gas permeation rate through the pore (mol s^{-1}), A_p is the pore area, m is the gas molecular weight, k_B is the Boltzmann constant, and T is the absolute temperature in degrees Kelvin. It is useful define the permeance per pore Π, or equivalently, the permeation coefficient (both appear in the literature), which is equal to the molar gas flow rate dn/dt normalized by the pressure difference Δp, that is:

$$\Pi = \frac{1}{\Delta p} \cdot \frac{\mathrm{d}n}{\mathrm{d}t} \tag{1-2}$$

Note that the difference between Π (in mol s^{-1} Pa^{-1}) and permeance K (in mol m^{-2} s^{-1} Pa^{-1}) is that Π is not normalized by the total membrane area, and therefore, is typically used to describe gas transport through individual pores in both theory and simulation studies. In contrast, permeance K is more often used in experimental studies. The two terms are connected by the areal pore density ρ: $K = \rho\Pi$. For gas permeation governed by effusion, the permeance per pore Π_effusion can be expressed as follows:

$$\Pi_\mathrm{effusion} = \frac{A_\mathrm{p}}{\sqrt{2\pi m k_\mathrm{B} T}} = \frac{1}{\sqrt{2\pi m k_\mathrm{B} T}} \cdot \frac{\pi D_\mathrm{p}^2}{4} \tag{1-3}$$

Correspondingly, the selectivity S_{12} between gas species 1 and 2 is given by:

$$S_{12,\mathrm{effusion}} = \sqrt{\frac{m_2}{m_1}} \tag{1-4}$$

which is known as Graham's law of effusion, or the Knudsen selectivity.[11]

Equation (1-4) is accurate in the limit when $D_\mathrm{p} >> D_\mathrm{m}$, because the probability of gas permeation being affected by the pore edge is infinitesimally small. However, as D_p decreases and approaches D_m, the steric effect imposed by the pore edge becomes more pronounced and should be considered – not all the impingement attempts of gases become successful permeation events. In the range when $\lambda > D_\mathrm{p} > 3D_\mathrm{m}$, the pore is sufficiently large such that no energy barrier exists for gas permeation. In other words, an impingement attempt of a gas molecule will succeed if it avoids hitting the pore edge and getting

bounced off. In this D_p range, gas permeation is still governed by effusion, but with a correction due to the steric effect. However, this steric effect has not been quantitatively modelled or confirmed by atomic scale simulations.

(3) Surface pathway. Graphene is very different from other conventional membrane materials because it has negligible thickness. For conventional thick membranes, the transport resistance is dominated by the interior paths inside the membrane, and gas adsorption on the membrane surface is not important. However, for graphene, due to the small transport resistance "inside" the pore, surface diffusion along the adsorption layer can play an important role in determining the overall gas flux. Gases such as CO_2, CH_4, and SF_6 are adsorptive on graphene,[43–45] and the adsorption layer provides another pathway to the pore besides direct impingement from the bulk (as described in the effusion mechanism).[46,47] Sun and Bai modeled the surface pathway as a parallel transport resistance,[48] but a quantitative and validated description of this regime is lacking in the literature. The pore diameter range associated with this regime is not yet clear.

(4) Activated translocation. When the pore diameter D_p further decreases below $2D_m$~$3D_m$, the repulsive interactions from the pore rim atoms become significant, leading to an energy barrier (or activation energy) E_a associated with pore translocation. In this activated regime, the translocation step associated with crossing the pore can be assumed to be the rate-limiting step, and the gas permeance K is related to the energy barrier E_a in the form of the Arrhenius equation $K = A\exp(-E_a/k_BT)$, where A is the prefactor. The energy barrier is highly sensitive to the atomic structure of both the gas molecule and the graphene pore. Therefore, the activated regime is of particular interest because ultrahigh gas selectivity could be achieved based on strong molecular sieving. However, it is also the least understood regime in terms of detailed theoretical description.

Ab initio calculations have been carried out to determine the energy barrier E_a,[25,49–64] but they are computationally expensive and restricted to small-scale systems. Large-scale molecular Dynamics (MD) simulations[46–48,65–90] or combined MD and *ab initio* simulations[91–108] have also been carried out, but the lack of analytical equations limits the efficiency of predicting activated gas permeation through graphene nanopores. Figure 1-2a summarizes the simulation results of gas permeation through graphene

nanopores resulting from the studies referenced above. The gases considered in Figure 1-2a include H_2, He, H_2O, CO_2, N_2, O_2, CH_4, H_2S, Ar, SF_6, ethane, and ethene. Motivated by Equation (1-4), the gas permeances per pore plotted on the y axis in Figure 1-2a are multiplied by $m^{1/2}$ to offset the effect of gas molecular weight. Meanwhile, the pore diameter D_p on the x axis is normalized by the gas kinetic diameter D_m to offset the difference in kinetic diameters of the various gases. As shown in Figure 1-2a, the $m^{1/2}$-corrected gas permeance per pore generally increases as D_p/D_m increases, with a transition at $D_p/D_m \sim 1$. The high energy barrier of pore translocation when $D_p/D_m < 1$ leads to an exponentially reduced gas permeation. In contrast, the permeance increase when $D_p/D_m > 1$ is much milder. The transition approximately matches the experimental results of gas permeation through individual graphene nanopores.[109,110] Despite the general trend, Figure 1-2a still shows a considerable discrepancy between the simulation studies.

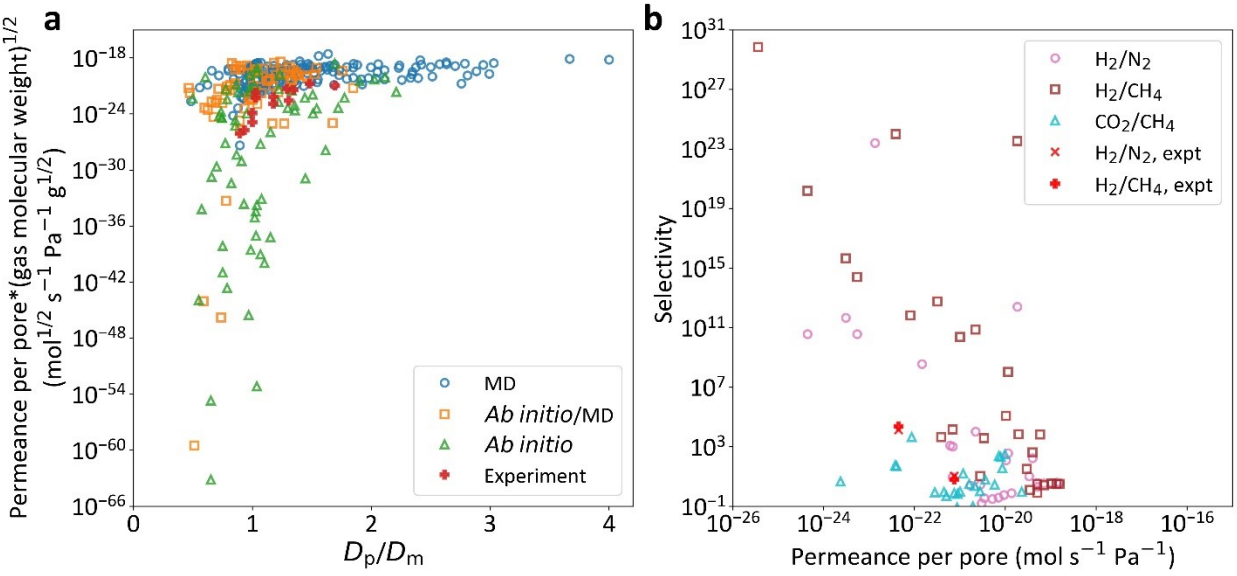

Figure 1-2. (a) Compilation of simulation and experimental data of gas permeance per pore (normalized by gas molecular weight) as a function of pore diameter (normalized by gas kinetic diameter). The simulation methods include MD,[46–48,65–90] *ab initio* calculations,[25,49–64] and a combination of both,[91–108] and the experimental results are from ref. [109] and ref. [110]. (b) Compilation of simulation and experimental data of H_2/N_2, H_2/CH_4, and CO_2/CH_4 selectivities as functions of permeance per pore (permeance per pore of H_2 for the H_2/N_2 pair, of H_2 for the H_2/N_2 pair, and of CO_2 for the CO_2/CH_4 pair). Data sources are the same as in (a).

Figure 1-2b summarizes the selectivity-permeance trade-offs of H_2/N_2, H_2/CH_4, and CO_2/CH_4 separations, using the same compilation of dataset as in Figure 1-2a. Compared to Figure 1-2a, the datapoints in Figure 1-2b are even less organized. Generally, H_2/CH_4 exhibits the highest selectivity

because it has the largest kinetic diameter difference (0.289 nm vs. 0.38 nm), followed by H_2/N_2 (0.289 nm vs. 0.364 nm), and then CO_2/CH_4 (0.33 nm vs. 0.38 nm).[36] The large discrepancies observed in Figure 1-2 suggest the need for a reliable theoretical model that unifies the simulation results.

1.3 Experimental Challenges

The final goal of developing nanoporous graphene membranes is to utilize them for industrial separation processes. Because graphene membranes can potentially exhibit much higher gas permeances than conventional polymeric membranes, the membrane area, and subsequently, the size of the permeation module, can be substantially reduced while maintaining the same gas outflow. However, major challenges remain in order to fabricate single-layer graphene membranes that qualify for real gas mixture separation applications, regarding advanced graphene perforation methods and scaling up the membrane area.

The first major challenge is to develop a reliable, scalable, and controllable method of creating graphene nanopores. The almost complete impermeability of graphene implies that they need to be perforated in order to obtain practically meaningful gas permeances. The perforation process, or the pore creation process, is undoubtedly the key step that determines the gas separation performance of a graphene membrane. In order to simultaneously yield high gas permeance and high selectivity, the areal pore density in graphene should be high, and the pore sizes should fall into the activated regime (typically < 1 nm) for effective molecular sieving. Because of their high scalability, currently, the most frequently used perforation strategies include ion beam bombardment, oxidative etching, and intrinsic defect formation during chemical vapor deposition (CVD). Below, these perforation methods are discussed one-by-one.

(1) Ion bombardment. The rationale behind this method is quite straightforward – high energy ions hit graphene and remove carbon atoms by collision. Celebi *et al.* used Ga-based and He-based focus ion beam (FIB) to perforate double-layer graphene and demonstrated the gas separation capability of graphene membranes for the first time.[111] The pore diameters in this study ranged from 7.6 nm to 1 μm, covering the transition from the effusion-dominated regime to the collective flow regime. Later, Ga^+ ion beam was used to perforate double-layer graphene[112] and triple-layer graphene[113] and yielded

approximately Knudsen selectivities. Recently, ion bombardment is more often used for pore nucleation. Liu *et al*. used He^+ ion bombardment to perforate double-layer graphene.[114] Boutilier *et al*. used Ga^+ ion bombardment to trigger pore nucleation in single-layer graphene and then expanded the pores by oxygen plasma.[115] Similarly, Schlichting and Poulikakos nucleated pores in double-layer graphene by Ga^+ ion bombardment and then expanded the pores by O_2 gas at 300 °C.[116] In general, the gas selectivities of the ion bombarded graphene membranes could exceed the Knudsen selectivities, but rarely exceeded 10 (blue circles in Figure 1-3).

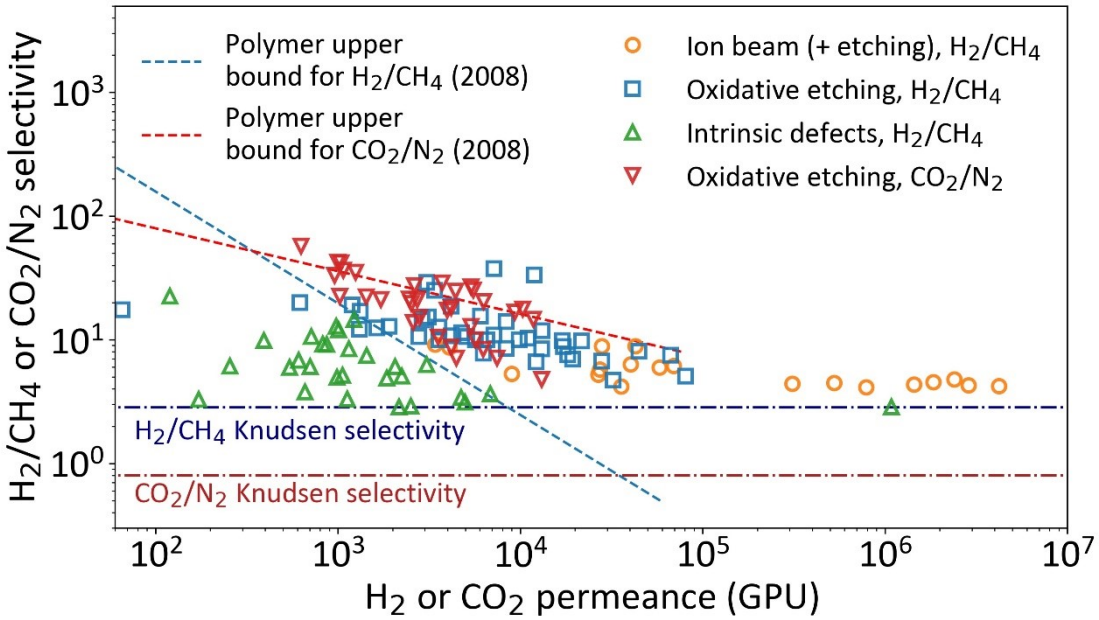

Figure 1-3. Compilation of experimentally measured H_2/CH_4 and CO_2/N_2 separation performances by graphene membranes in a selectivity-permeance Robeson plot. The experimental results are categorized by perforation methods, including ion beam bombardment (some followed by additional chemical etching),[111–117] oxidative etching,[118–125] and intrinsic defect formation during chemical vapor deposition (CVD).[118,120,121,125–130] The Robeson upper bounds for polymers are plotted assuming 1 μm thickness.[11]

(2) Oxidative etching. This has recently become a frequently used method to perforate graphene because of its low requirement for equipment and high scalability. So far, the etchants utilized to generate nanoporous graphene membranes for gas separation include ozone (O_3), oxygen plasma, and O_2 at a high temperature. Koenig *et al.* used ultraviolet light to generate O_3 from air, which then generated a handful of sub-nanometer pores in double-layer graphene exhibiting H_2/CH_4 selectivity > 10^4.[109] In spite of the low areal pore density, this study showed the high promise of the oxidative etching method. O'Hern *et al.* used $KMnO_4$ in an acid solution to expand single-layer graphene nanopores

nucleated by ion bombardment, and then used the resulting single-layer graphene membranes for ion separation and nanofiltration.[131,132] Surwade *et al.* used oxygen plasma to etch single-layer graphene and obtained high salt rejection rates and impressive water permeabilities through the nanoporous single-layer graphene membranes.[133] These studies inspired researchers to apply the oxidative etching methods to fabricating graphene membranes for gas separation. Huang *et al.* exposed CVD-grown single-layer graphene to O_3 at various temperatures ranging from 25 to 100 °C and improved the H_2/CH_4 selectivity to 17 while maintaining a H_2 permeance of 1.3×10^3 GPU.[120] He *et al.* used oxygen plasma to generate nanopores in single-layer graphene with an areal density of $\sim10^{16}$ m^{-2} and obtained a CO_2/N_2 selectivity of 12 and a H_2/CH_4 selectivity of 16.[118,121] Since then, O_3 and oxygen plasma treatment have been frequently reported to nucleate and expand pores in graphene.[119,123,125] Zhao *et al.* proposed a two-step procedure: single-layer graphene was first exposed to oxygen plasma to create a high density of pore nuclei, and was then treated by O_3 for controllable pore expansion, which further improved the H_2/CH_4 selectivity to 29.[122] Huang *et al.* used a short burst of O_3 for pore nucleation in single-layer graphene and then expanded the pores by O_2 at 200 °C, resulting in CO_2/N_2 selectivities of 24 and CO_2 permeances $\sim10^4$ GPU.[124] As shown by the blue and orange squares in Figure 1-3, graphene membranes perforated by oxidative etching methods generally performed better than those perforated by ion bombardment. The oxidatively etched graphene membranes not only exhibited selectivities which are higher than the Knudsen selectivities, but also surpassed the 2008 Robeson upper bound of polymeric membranes for H_2/CH_4 separation (assuming 1 μm thickness).[11] The CO_2/N_2 upper bound of polymers has rarely been surpassed because polymeric membranes can be tuned to preferentially absorb CO_2 due to its stronger electrostatic interactions than those of N_2.

The two strategies discussed above (ion bombardment and oxidative etching) are top-down approaches. In other words, pores were created by removing carbon atoms from "high-quality graphene" synthesized by chemical vapor deposition (CVD) or mechanical exfoliation. These etching-based methods have a major disadvantage: both pore nucleation and pore growth are enhanced as the energy input for etching increases. As a result, one needs to increase the energy input for etching to attain a higher pore density in graphene, but this also causes the pores to grow larger and become less selective. This undesirable outcome decreases the overall gas separation performance of graphene membranes.

(3) Intrinsic defect formation during chemical vapor deposition. Apart from the top-down pore creation methods, a promising alternative method is to control the formation of intrinsic defects in graphene during its CVD synthesis. Defects in CVD-synthesized graphene consist of mainly two types: nanometer-scale intrinsic defects and micrometer-scale large tears. The latter is not favorable for gas separation purposes because such tears lead to non-selective collective gas flow. Boutilier *et al.* studied the gas separation properties of graphene with large tears and showed that the gas selectivity could be improved by stacking multiple graphene layers and by carefully engineering the gas transport resistance through the support that carried the graphene membrane.[126] Unfortunately, the existence of large tears in the graphene membranes limits the gas selectivity below the Knudsen selectivity. Later, the development of mechanical enhancement methods prevented the large tears from forming and allowed the gas separation properties of the nanometer-scale intrinsic defects to be measured. Huang *et al.* showed that the intrinsic defects in CVD-grown SLG could yield a H_2/CH_4 selectivity of 22.[120] Khan *et al.* synthesized SLG by CVD using benzene as the precursor, and the benzene-derived SLG exhibited a H_2/CH_4 selectivity of 8 and a H_2 permeance of 1152 GPU at 150 °C.[128] Other researchers have also measured close to or slightly higher than the Knudsen selectivities through intrinsic defects in SLG.[125,129,130] These results show that the intrinsic defects in graphene have the potential to be highly gas sieving. However, the formation mechanism of the intrinsic defects was the least understood among the three perforation methods, and it led to low controllability and mediocre gas separation performances (blue triangles in Figure 1-3).

The second major challenge is to scale up the area of the graphene membranes. Although single-layer graphene is mechanically strong on a microscopic scale due to the strong C–C bonds, it is macroscopically fragile and is easily ruptured, especially when it comes in contact with liquids with high surface tensions during transfer or when it is suspended over a hole in a supporting substrate.[134–136] In fact, the probability of membrane failure significantly increases when a membrane is suspended over a larger hole.[136] Therefore, a reasonable strategy to scale up the membrane area is increasing the number of holes in the substrate. However, a single membrane crack on one hole can cause the entire membrane array to lose gas selectivity. For example, the overall survival rate of a graphene membrane on a 100-hole array is only 37% even if its survival rate on each hole is 99% ($0.99^{100} = 0.37$).

The third major challenge is to narrow the pore size distribution in the graphene membranes. Ideally, all the pores are of the same size and are highly gas selective. In this case, the pore size distribution is a degenerate distribution for discrete pore sizes, or is a delta function for continuous pore sizes. However, pores in graphene membranes created by the top-down etching-based methods typically have a wide pore size distribution which shows a long right tail (right-skewed).[118,124,131,132] The long right tail of the pore size distribution is unfavorable for a high gas separation performance. In spite of their low fraction among all the pores, the large pores in the right tail can dominate the overall gas permeance and are less gas selective. In order for the entire graphene membrane to preserve high gas selectivity, the right tail needs to be kept short. However, that would cause the majority of the pores to become too small to contribute any gas permeance, leading to a trade-off between permeance and selectivity. A wider pore size distribution lowers the upper limit of the permeance-selectivity trade-off. This effect of the pore size distribution applies not only for graphene membranes, but also for polymeric membranes. Polymers with soft chains and flexible pore structures have wider pore size distributions, and therefore, have been outperformed by semi-rigid polymers (*e.g.*, polymers of intrinsic microporosity and thermally rearranged polymers) and rigid molecular sieves (*e.g.*, carbon molecular sieves, zeolites, and metal-organic frameworks).[9] Unfortunately, the strategy of narrowing the pore size distribution in the case of polymers has not been directly transferrable to graphene membranes because, currently, most graphene pores are created by etching methods. In contrast, pores in polymers are formed in the interspace between the polymer chains through a bottom-up assembly process.

1.4 Thesis Objectives and Overview

With the theoretical challenges (Section 1.2) and the experimental challenges (Section 1.3) in mind, the overarching goal of my thesis is (1) developing a comprehensive theoretical framework to predict the gas permeance through a nanoporous graphene membrane, and (2) fabricating nanoporous single-layer graphene membranes with high gas permeances and high selectivities. In order to achieve these goals, the following thesis objectives were accomplished and will be presented in each chapter of this thesis.

In Chapter 2, I investigate the gas permeation mechanism through graphene nanopores in the activated regime. The key goal in this objective is to propose an efficient method to predict the prefactor

A and the energy barrier E_a, and then to predict the gas permeance per pore Π through any nanopore structure in the activated regime. To accomplish this objective, the applicability of the Arrhenius equation needs to be confirmed by carrying out molecular dynamics (MD) simulations at various temperatures. Equipped with this method, gas permeances through a large library of pore structures can then be predicted with high throughput.

In Chapter 3, I investigate the gas permeation mechanism through graphene nanopores across multiple regimes. Although the activated regime is the most interesting, other gas permeation regimes should also be investigated. This is because the activated regime requires sub-nanometer pore diameters, which imposes a strong constraint in actual experiments.[131] Therefore, it is useful to model the gas permeation mechanism in a unified manner, such that the transition between the activated regime and the effusion regime can be described analytically. Furthermore, the resulting unified model should also incorporate the surface pathway. In this manner, the significance of the surface pathway can be examined.

In Chapter 4, I predict the gas separation performances of graphene nanopore ensembles having realistic pore size distributions. Chapter 2 and Chapter 3 report predictions of the gas permeance through a graphene pore with any given diameter D_p. However, in order to match the theoretical predictions to experimental data, the pore size distribution in actual graphene membranes should be considered. When created in a graphene lattice by an etching method (the predominant way to create nanopores), the nanopores are distributed in terms of their sizes and shapes, instead of being identical.[115,131,137] Therefore, this research objective involves (i) simulating the pore size and shape distributions of nanopores generated by etching, (ii) predicting the gas permeance through each nanopore, (iii) adding up the permeances, and (iv) comparing the predicted total gas permeances and selectivities with those measured experimentally.

In Chapter 5, I demonstrate stable, temperature-dependent gas mixture separation through single-layer graphene membranes. To directly measure the gas mixture separation performance of graphene membranes, a homemade gas permeation module connected to a real-time mass spectrometer was built. In this way, gas permeances of multiple components from a mixture can be measured by sweeping the permeated gases to the mass spectrometer. Furthermore, the permeation measurements were carried out

at different temperatures, in order to investigate if the gas permeation is activated. Single-layer graphene was synthesized by CVD, and intrinsic defects in CVD graphene were evaluated for their gas mixture separation performances.

In Chapter 6, I attain both high gas permeance and selectivity using single-layer graphene with intrinsic defects. According to the theoretical study by Wang *et al*., the formation of the intrinsic defects during CVD is triggered by the random insertion of catalytic metal atoms into the front-most graphene edge during growth,[138] which is decoupled from oxidative etching. The CVD synthesis conditions for graphene is tuned to increase the density of these intrinsic nanopores. This can be done without significantly increasing the sizes of the nanopores themselves, which is important because it allows graphene membranes to present higher gas permeances while maintaining high selectivities. Furthermore, I scale up the area of the graphene membranes by 10000 times by mechanical enhancement using a highly gas permeable support layer.

In Chapter 7, I conclude my thesis by summarizing all the key findings in Chapters 2–6, and discussing my insights and potential future research directions.

2 Mechanism of Gas Permeation through Graphene Nanopores in the Activated Regime

2.1 Introduction

Permselective membrane technology is gaining attention in the field of gas separation.[8,139] The rise in energy cost makes conventional technologies (*e.g.*, cryogenic distillation of air, condensation of organic vapors, and amine absorption of sour gases) unfavorable, because they involve energy-intensive phase changes.[8] Membrane separation consumes less energy, requires no addition solvents, and utilizes smaller separation units.[140] Various types of materials have been used as separation membranes, including polymers,[11,12,141] zeolites,[13,142] metal organic frameworks (MOFs),[16,143] and carbon-based materials.[20,144]

Rapid advances in graphene technology provides opportunities for breakthroughs in permselective membranes.[145] The permeance (the permeante flux normalized by the pressure difference between the feed and the permeate sides) of a membrane is inversely proportional to the membrane thickness.[25] Therefore, the one-atomic-layer thickness of graphene makes it a promising platform for developing gas separation membranes. In addition, the outstanding mechanical strength of graphene allows it to withstand large tensile forces.[28,146]

A perfectly crystalline graphene sheet is almost impermeable, even to small gas molecules such as helium.[31] In order to attain a high gas permselectivity, pores with sub-nanometer diameters should be created on the graphene basal plane. This is because the pore size should be comparable to the size of gas molecules in order to sieve them. Experimentally, ion bombardment followed by oxidative etching[131] and electron beam exposure[147] were used to perforate single-layer graphene and create sub-nanometer-sized pores. Ultraviolet-induced oxidative etching was also used to introduce a small number of angstrom-sized graphene pores, and the detected pressure-normalized permeation rates of H_2 and CO_2 ranged from 10^{-23} to 10^{-21} mol s^{-1} Pa^{-1}.[109,110,148]

Computational tools can be used to gain a deeper understanding of gas separation using porous graphene membranes. Among these, electronic structure density functional theory (DFT) was used to calculate the energy barrier for gas molecule translocation across a graphene pore.[25,49,55,57] Large separation factors for various gas pairs were predicted due to large differences in the translocation energy barriers corresponding to different gases. Unfortunately, due to its high computational cost and small simulation size requirement, DFT cannot directly predict gas permeance by simulating a large number of gas molecules. Accordingly, large-scale molecular dynamics (MD) simulations were carried out in order to estimate the gas permeance in a more direct manner, including investigating the mechanism of molecular permeation.[46,47,66,68,79,95] It is noteworthy that the adsorption of gas molecules on graphene was found to play a significant role in gas permeation through graphene pores, particularly in the case of large and adsorptive gases, including N_2,[47] CO_2,[74] and CH_4.[46]

Although the studies listed above provide mechanistic understanding of gas permeation through graphene nanopores, there remain at least three critical challenges: (1) More accurate and efficient permeance estimations. The existence of an energy barrier for permeation typically leads to a small exponential term and a small permeance, particularly for smaller pores where the energy barriers are large. Therefore, the permeation of gas molecules through porous graphene becomes a rare event of a highly stochastic nature.[77,79] As a result, long simulation times and multiple trials are required to fully capture the permeation behavior, which results in low efficiency and accuracy in permeance estimations. (2) A need for quantitative equations to calculate permeances. Although some influential factors (such as the energy barrier and the surface adsorption) were identified,[25,47] their effects have not been quantified in an analytical form. (3) Systematic consideration of a library of pore sizes and shapes. Because of (1) and (2) above, only some sample graphene pores were investigated, which does not comprehensively describe the actual experimental graphene system where the pore structure is polydisperse.[149]

With the above in mind, in this chapter, I study the permeation of CO_2, CH_4, and O_2 gases through several sample graphene pores at various temperatures. Particular attention is paid to the separation of CO_2/CH_4 because it constitutes an important step in the processing of natural gas,[5] and is also one of the most well investigated gas pairs for membrane separation.[11] For comparison, I also study the

permeation characteristics of O_2, a representative smaller gas molecule. Calculating and analyzing gas permeation in an MD simulation framework, I show that the permeation of adsorptive gas molecules through sub-nanometer pores can be decoupled into two steps: (1) adsorption to the pore mouth, and (2) translocation through the pore. The rate of translocation can be fitted by an Arrhenius-type equation, whose parameters can be quantitatively predicted using transition state theory.[150,151] In addition, I propose an algorithm to allow rapid calculation of gas permeances per pore for a graphene pore library, including generating a Robeson plot for the CO_2/CH_4 gas pair. Based on the predicted Robeson plot, I obtain an upper bound for the gas permeation performance of porous graphene membranes.

2.2 Analytical Model

In previous work, Drahushuk and Strano analyzed the mechanism of gas permeation through a single layer porous membrane as a series of consecutive kinetic steps, including proposing corresponding theoretical expressions for the cases where some are rate limiting.[152] Specifically, the permeation pathway *via* the surface adsorption layer was modeled as consisting of the following five steps: (1) adsorption of a gas-phase molecule onto the graphene surface, (2) association of the surface-adsorbed gas molecule onto the pore mouth (above the pore), (3) translocation of the pore-associated gas molecule to the other side of the graphene surface, (4) dissociation from the pore mouth to the graphene surface, and (5) desorption from the graphene surface to the bulk. A similar adsorption-translocation model has been proposed by Tian *et al.*[153] Typically, for a sub-nanometer pore and an adsorptive gas, the translocation (step 3) is activated (*i.e.*, the gas molecule needs to overcome an energy barrier to translocate through the pore). As a result, the translocation step is rate-limiting due to its slowest kinetics, and the other four steps are in equilibrium (Figure 2-1a).[152] Therefore, at steady state, the rate of permeation is equal to the rate of translocation. Assuming first-order kinetics (since no intermediate states exist), the permeation rate $\mathrm{d}N/\mathrm{d}t$ (number of permeated gas per unit time per pore) should be proportional to the number of pore-associated gas molecules N_{pore}, that is:

$$\frac{\mathrm{d}N}{\mathrm{d}t} = k_{\mathrm{trans}} N_{\mathrm{pore}} \tag{2-1}$$

where the proportionality constant is referred to as the translocation coefficient k_{trans}. The permeance per pore, Π, can be obtained as the ratio of the permeation rate $\mathrm{d}N/\mathrm{d}t$ to the pressure difference Δp between the feed side and the permeate side, separated by the graphene membrane, that is,

$$\Pi = \frac{1}{\Delta p}\frac{\mathrm{d}N}{\mathrm{d}t} = k_{\mathrm{trans}}\frac{N_{\mathrm{pore}}}{\Delta p} \tag{2-2}$$

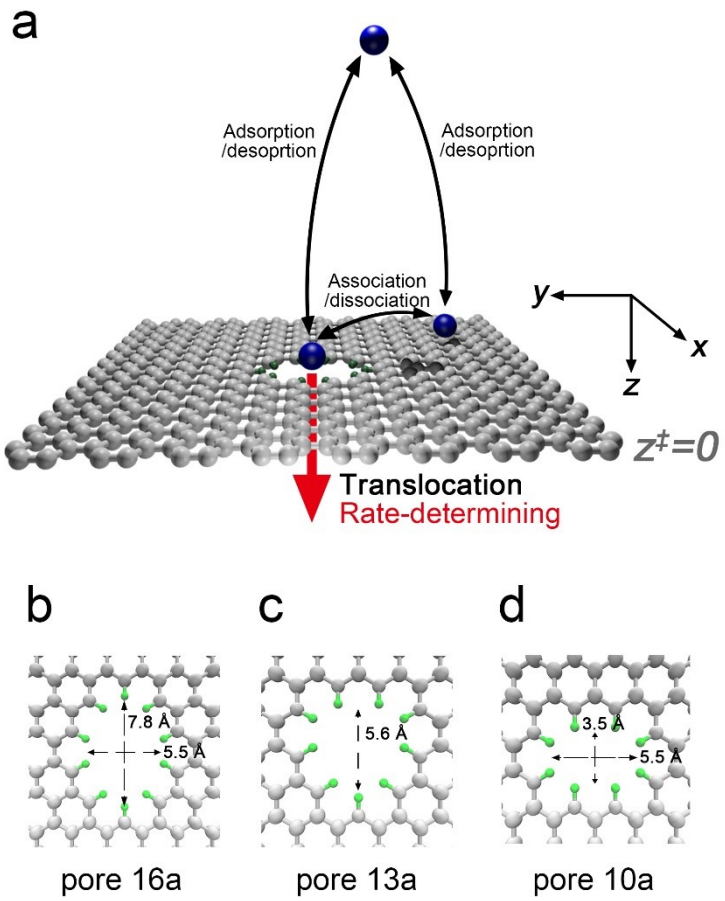

Figure 2-1. (a) Schematic illustration of the mechanism of gas permeation through a sub-nanometer graphene pore. (b-d) Typical graphene pores studied in this chapter: pore 16a, 13a, and 10a. The pores in the chapter are designated in terms of the number of carbon atoms removed; "a" is an identifier. More pore configurations *(e.g.,* pore 16b) will be introduced later. Grey spheres denote carbon atoms, and green spheres denote hydrogen atoms. The pore sizes are given in (b-d) in angstrom. The sizes are measured as the distances between the nuclei of opposite hydrogen atoms.

In this chapter, the permeance per pore, Π, with an SI unit of mol Pa^{-1} s^{-1}, is defined as the pressure-normalized permeation rate for a single pore. Note that this definition is different from the commonly used definition of permeance as the pressure-normalized flux (unit: mol m^{-2} Pa^{-1} s^{-1}). For clarity, the commonly used definition of permeance is referred to as the "permeance per surface area".

In the simulations discussed in this chapter, the permeate side of the membrane is maintained in vacuum to eliminate reverse permeation, and therefore, the pressure difference Δp equals the bulk pressure p on the feed side.

Henry's law states that the amount of dissolved gas in a liquid is proportional to its partial pressure in the gas phase.[41] This proportionality constant, also known as the solubility constant or the Henry's Law Constant, describes the equilibrium of the gas in the liquid and in the gas phases. In the case of gas permeation through a graphene nanopore, the equilibrium between the pore-associated gas molecules and the bulk gas molecules can also be modeled in the context of phase equilibrium. In analogy to the Henry's Law Constant introduced to model liquid-gas phase equilibrium, here, a pore Henry's coefficient H_{pore} is introduced as the ratio of N_{pore} and the bulk pressure p to model the equilibrium of pore association:

$$H_{\mathrm{pore}} = \frac{N_{\mathrm{pore}}}{p} \tag{2-3}$$

Therefore, according to Equations (2-2) and (2-3), and because $\Delta p = p$ in my simulatons, the permeance per pore Π can be expressed as follows:

$$\Pi = k_{\mathrm{trans}} H_{\mathrm{pore}} \tag{2-4}$$

2.3 Model Validation by Molecular Dynamics Simulations

The main hypothesis embodied in Equation (2-4) is that the translocation coefficient k_{trans} only captures the interaction between the pore and a single gas molecule, and is therefore independent of the bulk gas pressure. In order to validate Equation (2-4), I simulated the permeation of CO_2, CH_4, and O_2 through pores 16a and 13a (Figure 2-1b, c) at various temperatures and pressures. The permeances per pore were determined using the escape time method in the context of an MD simulation framework (see Section 2.8 for more details). Note that generally, the MD simulation results could depend on the force fields used. Here, I utilized the Transferable Potential for Phase Equilibria (TraPPE) Force Field[154] to model the non-bonded interactions of CO_2. The TraPPE Force Field was trained to reproduce the vapor-liquid equilibria of CO_2, N_2, and alkanes. To test the sensitivity of the simulated results on the force field chosen, I also used the Elementary Physical Model 2 for comparison, and found that the differences

between the two force fields are minor (Table 2-4 in Appendix 2.9.1).[155] In my simulations, the bulk phase was defined as the region extending beyond 3 nm from the graphene surface, where the gas density profile approaches a constant value (Figure 2-8a, b in Appendix 2.9.2). The pore mouth region was defined as a cylinder with a radius of 0.4 nm and a height of 0.5 nm, whose axis crosses the pore center and is normal to the graphene basal plane. The volume of the pore mouth region was determined based on the gas density profile in the vicinity of the pore (Figure 2-8c, d in Appendix 2.9.2). Note that small variations in the size of the pore mouth region do not affect the validity of the results (Figure 2-9 in Appendix 2.9.2). The number of pore-associated gas molecules and the bulk gas density were calculated as the time average of the number of gas molecules in the pore mouth region and in the bulk region, which are counted during the simulation. The time interval for each counting was 2 ps, and more than 10^5 countings were done during a typical simulation. The simulations were carried out in the NVT ensemble. The bulk pressure p was calculated using the bulk gas density and the temperature in the equation of state for each gas. For this purpose, I utilized the open-source program CoolProp,[156] which integrates the equations of state for CO_2,[157] CH_4,[158] and O_2.[159,160] The pore Henry's coefficients were then deduced using Equation (2-3).

The simulated permeances per pore and pore Henry's coefficients of three gas–pore combinations are shown in Figure 2-2. Figure 2-2a shows the simulated permeances per pore of CO_2 through pore 16a under various feed side pressures at temperatures ranging from 300 K to 700 K. Note that the force field used may not accurately capture the "real" intermolecular interactions at elevated temperatures, because it was originally developed at room temperature. However, by considering a fictitious gas which satisfies the force field used over the entire temperature range studied, valuable mechanistic information can be obtained, including the energy barrier and the heat of adsorption. It is expected that the values of the important energetic terms of the fictitious gas and the "real" gas will converge at room temperature, where the force field was calibrated. Figure 2-2b shows the corresponding simulated pore Henry's coefficients at the same conditions as those in Figure 2-2a. Note that for the CO_2–pore 16a case, the variations of the simulated permeances per pore and pore Henry's coefficients with pressure are very similar, suggesting a proportional correlation between these two quantities. At temperatures higher than 400 K, both the simulated permeances per pore and the pore Henry's coefficients decrease slightly

at low pressures and approach a constant value at high pressures. At 300 K, both of these quantities decrease significantly as the pressure increases from 1×10^5 to 5×10^5 Pa. This result is consistent with the Brunauer–Emmett–Teller (BET) theory, where the heat of adsorption for the first layer is greater than that for the subsequent layers.[161] This implies that gas molecules have a higher tendency to be adsorbed to a solid surface when the surface coverage is low. When the bulk gas pressure is high, the surface coverage increases and the adsorbent–adsorbent interactions hinder additional gas adsorption. Similarly, the tendency of the first molecular association to the pore mouth is greater than that for the subsequent associations. This leads to a higher pore Henry's coefficient in the low pressure range. Note that this behavior is not strictly observed in the CO_2–pore 13a case. This may be because the permeances per pore through pore 13a are much lower than those through pore 16a, and the corresponding error ranges are much larger (Figure 2-2e). The increase of the simulated permeance per pore and pore Henry's coefficient observed at 300 K at pressures which exceed 20×10^5 Pa is due to a substantial reduction in the compressibility factor as the critical point of CO_2 (304 K, 72.8×10^5 Pa) is approached (Figure 2-10 in Appendix 2.9.3). This critical phenomenon-related behavior is reproduced using the force field used.[154]

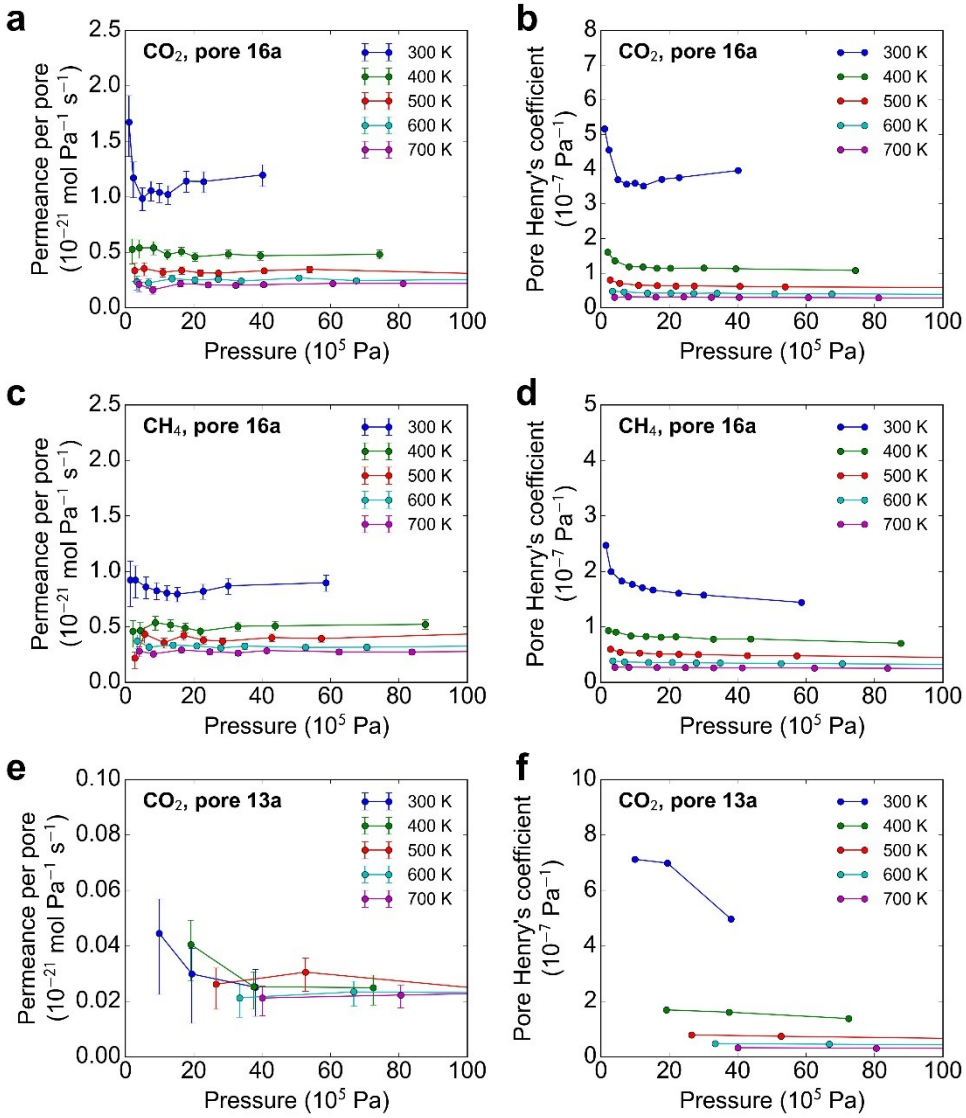

Figure 2-2. (a) Simulated permeances per pore and (b) simulated pore Henry's coefficients of CO_2 through pore 16a at various temperatures and pressures. (c) Simulated permeances per pore and (d) simulated pore Henry's coefficients of CH_4 through pore 16a at various temperatures and pressures. (e) Simulated permeances per pore and (f) simulated pore Henry's coefficients of CO_2 through pore 13a at various temperatures and pressures.

Similar comparisons can be made for CH_4 (Figure 2-2c, d) and O_2 (Figure 2-11 in Appendix 2.9.3), which further confirm the proportional correlation between the simulated permeances per pore and pore Henry's coefficients for these two gases. When the pore shrinks from pore 16a to pore 13a, the simulated permeance per pore of CO_2 decreases by two orders of magnitude, from 10^{-21} to 10^{-23} mol s^{-1} Pa^{-1} (Figure 2-2e vs. Figure 2-2a). However, the pore Henry's coefficient does not significantly change as the pore diameter is reduced (Figure 2-2f vs. Figure 2-2b).

In general, the permeance per pore Π, the pore Henry's coefficient H_{pore}, and the translocation coefficient k_{trans}, all depend on both temperature and pressure. In the high pressure range, these quantities are not pressure-dependent, and therefore, are only functions of temperature. Figure 2-3a shows the temperature dependence of the simulated permeances per pore of CO_2, CH_4, and O_2 through pore 16a averaged over the high pressure range (> 2×10^6 Pa). For these three gases, the permeances per pore are decreasing functions of temperature. The permeance per pore Π can be fitted to an Arrhenius equation, that is:

$$\Pi(T) = A_{\mathrm{app}}\exp\left(-\frac{E_{\mathrm{a,app}}}{RT}\right) \tag{2-5}$$

where $E_{\mathrm{a,app}}$ is the apparent energy barrier, A_{app} is the apparent pre-exponential factor (abbreviated as prefactor in the following), and R is the gas constant. Correspondingly, all energies are expressed on a molar basis in this chapter.

By linear fitting of ln $[\Pi(T)]$ to T^{-1}, the apparent energy barriers $E_{\mathrm{a,app}}$ can be obtained (Figure 2-12a in Appendix 2.9.3). Note that the deduced apparent energy barriers are negative in these cases (*e.g.,* -7.2 kJ mol^{-1} for CO_2), which is different from the normal definition of an energy barrier. This contradiction is resolved as follows. According to Equation (2-4), gas permeation through a pore involves two steps: pore-association and translocation (quantified by H_{pore} and k_{trans}, respectively). Figure 2-3b shows the temperature dependence of the pore Henry's coefficients, which is subsequently fitted to the van't Hoff equation to extract the heat of adsorption ΔH_{ads} (Figure 2-12b in Appendix 2.9.3) as follows:[41]

$$H_{\mathrm{pore}}(T) = A_{\mathrm{pore}}\exp\left(-\frac{\Delta H_{\mathrm{ads}}}{RT}\right) \tag{2-6}$$

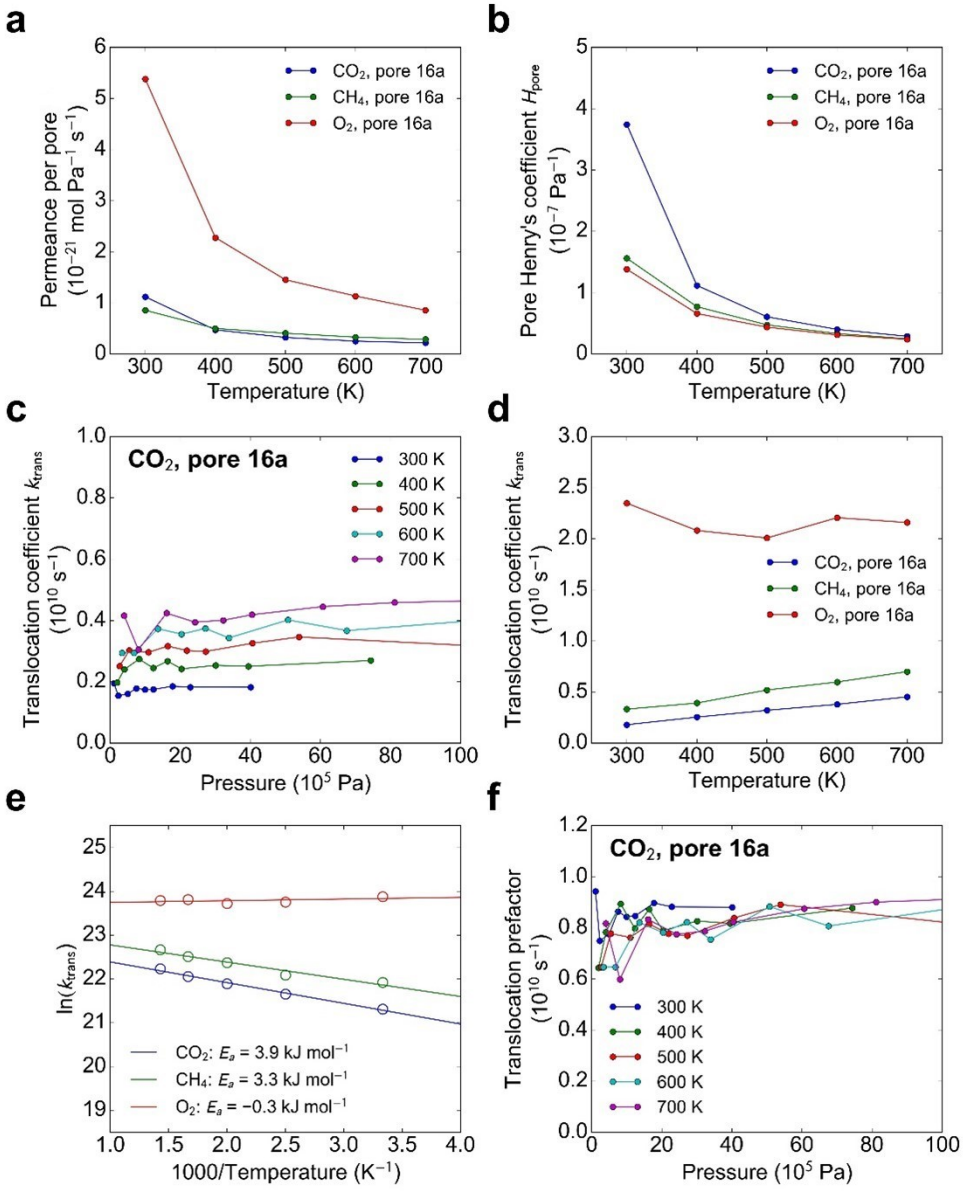

Figure 2-3. (a) Simulated permeances per pore of CO_2, CH_4, and O_2 through pore 16a averaged over the high pressure range at various temperatures. (b) Simulated pore Henry's coefficients of CO_2, CH_4, and O_2 above pore 16a averaged over the high pressure range at various temperatures. (c) Translocation coefficients calculated at various temperatures and pressures for CO_2. (d) Temperature dependence of the translocation coefficients of CO_2, CH_4, and O_2 through pore 16a, and (e) related Arrhenius fitting results. (f) Convergence of the translocation prefactors of CO_2.

Note that the heats of adsorption are typically negative, suggesting an exothermic pore-association step (Table 2-1). I also studied the temperature dependence of the surface adsorption on the graphene lattice away from the pore, and calculated the associated heat of adsorption $\Delta H_{\mathrm{ads}}^{\mathrm{surf}}$. It can be found that the heats of adsorption corresponding to pore association and surface adsorption are similar, supporting the assumption that the permeation steps prior to translocation are at equilibrium (Figure 2-13 in

Appendix 2.9.3). The heat of adsorption on the graphene surface $\Delta H_{\mathrm{ads}}^{\mathrm{surf}}$ is consistent with both experimental and simulation results,[43–45] with a certain overestimation due to entropic effects.

Table 2-1. Apparent energy barrier, heat of adsorption, energy barrier, and translocation prefactor, all deduced from a temperature fitting of the MD simulation results for four gas–pore combinations.

Gas–pore	Apparent energy barrier (kJ mol^{-1})	Heat of adsorption (kJ mol^{-1})	Energy barrier (kJ mol^{-1})	Translocation prefactor (10^{10} s^{-1})
CO_2–16a	-7.2 ± 1.2	-11.1 ± 0.8	3.9 ± 0.6	0.81 ± 0.08
CH_4–16a	-4.7 ± 0.6	-8.0 ± 0.9	3.3 ± 1.3	1.06 ± 0.15
O_2–16a	-7.9 ± 1.0	-7.7 ± 0.4	-0.2 ± 0.9	2.02 ± 0.13
CO_2–13a	-1.8 ± 1.0	-13.1 ± 0.8	11.3 ± 1.7	0.32 ± 0.05

Figure 2-3c shows the translocation coefficients k_{trans} of CO_2 through pore 16a calculated according to Equation (2-4) (for the k_{trans} results corresponding to CH_4 and O_2, see Figure 2-12c, d in Appendix 2.9.3). The translocation coefficient is independent of pressure, further confirming the main hypothesis embodied in Equation (2-4). In addition, the temperature dependence of the translocation coefficient (Figure 2-3d) can be fitted to the Arrhenius equation (Figure 2-3e). Specifically,

$$k_{\mathrm{trans}}(T) = A_{\mathrm{trans}} \exp\left(-\frac{E_{\mathrm{a}}}{RT}\right) \tag{2-7}$$

The deduced "real" energy barriers E_{a} correspond to the activation energy required during translocation from the pore-adsorbed state on one side of the pore to the other side of the pore. The energy barriers for CO_2 and CH_4 are 3.9 kJ mol^{-1} and 3.3 kJ mol^{-1}, respectively (also listed in Table 2-1). In contrast, O_2 exhibits an energy barrier close to zero (-0.2 kJ mol^{-1}) to cross pore 16a. According to Equations (2-4) to (2-7), the apparent energy barrier, the heat of adsorption, and the "real" energy barrier are related as follows:

$$E_{\mathrm{a,app}} = \Delta H_{\mathrm{ads}} + E_{\mathrm{a}} \tag{2-8}$$

For CO_2 and CH_4 across pore 16a, the heat of adsorption of pore association ΔH_{ads} is greater than the "real" energy barrier E_{a} in absolute value (Table 2-1). Therefore, according to Equation (2-8), the apparent energy barriers are negative in these cases. For O_2, the heat of adsorption is close to the apparent energy barrier, implying a zero "real" energy barrier.

Translocation prefactors A_{trans} can be calculated using Equation (2-7). The translocation prefactors of CO_2 are shown in Figure 2-3f, and their values are close to each other, independent of temperature and pressure. Similar results can be observed for CH_4 and O_2 (Figure 2-12e, f in Appendix 2.9.3). Therefore, the translocation prefactor depends solely on the gas type and pore configuration. The translocation prefactor corresponds to the frequency of crossing attempts (in units of s^{-1}), while the translocation coefficient corresponds to the frequency of successful crossing attempts (in units of s^{-1}). Note that the calculated prefactors are of the order of 10^{10} s^{-1}, smaller than previously reported values (10^{13} or 10^{11} s^{-1}).[25,49] It is also noteworthy that a similar overestimation of the prefactors was reported in the case of benzene transport in zeolites.[162] Values of energies and prefactors deduced from the fitting procedures discussed above are reported in Table 2-1. Confidence intervals in this chapter are reported at the 95% confidence level. A detailed analysis of the CO_2–13a gas-pore combination is shown in Figure 2-14 in Appendix 2.9.3.

2.4 Transition State Theory Prediction

In order to efficiently determine the permeance per pore, the pore Henry's coefficient and the translocation coefficient need to be evaluated separately (Equation (2-4)). Adsorption isotherms, which are related to the Henry's coefficient, can be obtained experimentally[45,163] or computationally.[43,44] It is noteworthy that simulation of adsorption is not computationally expensive because it does not involve the detection of a rare event, which is time consuming.

On the other hand, the evaluation of translocation coefficients necessitates an in-depth theoretical understanding to overcome the large computational cost that characterizes rare event simulations. For example, a typical simulation box contains 200 CO_2 molecules and two graphene sheets, corresponding to a gas pressure of ~ 2×10^6 Pa at 300 K. The simulation speed of this box is 0.6 hours (wall time) per nanosecond (simulation time) using 8 processors in parallel. When the energy barrier is 10 kJ mol^{-1}, the expectation value of the elapsed time for one translocation event through pore is ~ 10 ns (simulation time), corresponding to ~ 6 hr (wall time). If the energy barrier is 20 kJ mol^{-1}, each translocation takes

~ 30 days (wall time) on average. The computational cost grows exponentially as the energy barrier increases.

Because the translocation step is associated with an energy barrier, it can be modeled as a chemical reaction in the context of the transition state theory (TST). Recall that TST models the rate constant in a classical barrier crossing event $k_{\mathrm{trans}}^{\mathrm{TST}}$, such as a gas molecule climbing over a one-dimensional barrier, as follows:[150,151,164]

$$k_{\mathrm{trans}}^{\mathrm{TST}} = \frac{1}{2}|\dot{z}(0)|\frac{\exp[-A(z^{\ddagger})/RT]}{\int_{z<z^{\ddagger}}\exp[-A(z)/RT]\mathrm{d}z} = \frac{1}{2}|\dot{z}(0)|\frac{Q(z^{\ddagger})}{Q(z<z^{\ddagger})} \tag{2-9}$$

where z is the coordinate of translocation, which in the porous graphene membrane case under consideration, corresponds to the direction normal to the graphene basal plane (Figure 2-1a), A is the Helmholtz free energy, ‡ denotes the transition state (TS), and $|\dot{z}(0)|$ is the average velocity when a molecule crosses the TS (the dot represents the first derivative with respect to time). The one half factor is introduced because a molecule at the TS can move in both directions. In Equation (2-9), $Q(z)$ is the canonical partition function evaluated at a certain z coordinate, which is defined as follows:

$$Q(z) = \exp\left[-\frac{A(z)}{RT}\right] = \frac{\int \mathrm{d}\vec{r}\int \mathrm{d}\vec{\theta}\iint_{\Omega}\exp\left[-E(x,y,z,\vec{\theta},\vec{r})/RT\right]\mathrm{d}x\mathrm{d}y}{\int \mathrm{d}\vec{r}\int \mathrm{d}\vec{\theta}\iint_{\Omega}\mathrm{d}x\mathrm{d}y} \tag{2-10}$$

where E denotes the potential energy of the gas–graphene system, (x, y, z) indicates the three-dimensional coordinates of the center of mass of the gas molecule, $\vec{\theta} = (\theta_x, \theta_y, \theta_z)$ indicates the rotation angles of a molecule about the *x*, *y*, and *z* axes, and $\vec{r}$ is a vector containing all the positional information of all the atoms of the graphene membrane, which is held constant when the graphene membrane is kept rigid. The kinetic energy contribution is not included in Equation (2-10), because in a classical system, the kinetic energy only depends on the momentum of all atoms, and its contribution in the canonical partition function can be separated out and is identical for all cases. In Equation (2-10), the integrations are carried out within the pore mouth region (denoted as Ω), in order to be consistent with the definition of the translocation coefficient (Equation (2-1)). Because the canonical partition function $Q(z)$ represents the number of available microstates at each translocation coordinate z in the canonical ensemble, it also represents the distribution of the gas molecule along the translocation

trajectory. Therefore, hereafter, $Q(z)$ will be referred to as the relative distribution function of a gas molecule. Note that $Q(z)$ is not a normalized distribution function. Instead, it is the distribution function relative to the zero-free-energy position (by definition in Equation (2-10), $Q(z) = 1$ when $A(z) = 0$).

Accordingly, $Q(z < z^{\ddagger})$ is defined as:

$$Q(z < z^{\ddagger}) = \int_{z<z^{\ddagger}} \exp\left[-\frac{A(z)}{RT}\right] \mathrm{d}z = \frac{\int \mathrm{d}\,\vec{r} \int \mathrm{d}\,\vec{\theta} \iiint_{z<z^{\ddagger},\Omega} \exp\left[-E(x,y,z,\vec{\theta},\vec{r})/RT\right] \mathrm{d}x\mathrm{d}y\mathrm{d}z}{\int \mathrm{d}\,\vec{r} \int \mathrm{d}\,\vec{\theta} \iint_{\Omega} \mathrm{d}\,x\mathrm{d}y} \tag{2-11}$$

The ratio $Q(z^{\ddagger})/Q(z < z^{\ddagger})$ corresponds to the equilibrium constant characterizing the quasi-equilibrium between the TS and the adsorbed state (AS) on the feed side (as $z < z^{\ddagger}$ refers to the feed side). This ratio represents the fraction of pore-associated gas molecules at the TS. The translocation coefficient $k_{\mathrm{trans}}^{\mathrm{TST}}$ can then be predicted by multiplying the ratio $Q(z^{\ddagger})/Q(z < z^{\ddagger})$ by the average velocity corresponding to crossing the TS, $|\dot{z}(0)|$, and the one half factor.

The "real" translocation coefficient k_{trans} and the TST-predicted translocation coefficient $k_{\mathrm{trans}}^{\mathrm{TST}}$ (Equation (2-9)) are related as follows:

$$k_{\mathrm{trans}} = \kappa k_{\mathrm{trans}}^{\mathrm{TST}} \tag{2-12}$$

where the transmission probability κ accounts for recrossing.[164] To further clarify, the transmission probability κ represents the likelihood that a molecule actually arrives at the AS on the permeate side given that it has crossed the TS ($0 \leq \kappa \leq 1$). If the TS is a local energy maximum for a molecule, then that molecule is not likely to recross once it crosses the TS, and κ approaches 1 in Equation (2-12). Therefore, κ can be approximated as 1 if the energy barrier of translocation is substantially greater than zero. On the other hand, if the TS is a local energy minimum (equivalent to a zero energy barrier), the likelihood of recrossing is not negligible and $\kappa < 1$ in Equation (2-12).

The Helmholtz free energy curves $A(z)$ of CO_2 and CH_4 through pore 16a are shown in Figure 2-4a, b (the $A(z)$ curve of O_2 through pore 16a is shown in Figure 2-5a). The potential energy curves $E(z)$ are also shown as a reference. The free energy curves were calculated using the weighted histogram analysis method;[165] the potential energy curves were obtained by directly evaluating Lennard-

Jones and electrostatic pairwise interactions along the translocation trajectory, using the same atomic force field as previously used (see Section 2.8 for more details). Here, the translocation coordinate z is equivalent to the vertical distance from the center of mass of a gas molecule to the pore, and the TS is located at $z = 0$. The free energy curve is different from the potential energy curve in the following aspects: (1) the free energy curve depends on temperature and the potential energy curve does not, (2) the equilibrium distance of the free energy curve (~ 0.3 nm) is larger than that of the potential energy curve (~ 0.1 nm for CO_2 and CH_4, 0 for O_2), indicating that the entropic effect favors a shift away from the pore, and (3) the free energy barrier is higher than the potential energy barrier, again suggesting an entropic penalty for crossing the pore. The gas molecule's geometric arrangement in the AS and the TS depends on the gas type and the pore configuration (Figure 2-15 in Appendix 2.9.3).

The relative distribution functions $Q(z)$ of CO_2 and CH_4 through pore 16a are shown in Figure 2-4c, d (results of O_2 shown in Figure 2-5c). For CO_2 and CH_4, the distribution at the TS is extremely low. The integral term $Q(z < z^{\ddagger})$ is equal to the area under the distribution function on one side of the pore. When $Q(0)$ approaches zero, one can approximate the integral as the area of a triangle, whose height equals the maximum value of the distribution function, and whose base equals $2L$ (L is the half-peak width, as shown in Figure 2-4d):

$$Q(z < z^{\ddagger}) = \int_{z<z^{\ddagger}} \exp\left[-\frac{A(z)}{RT}\right] \mathrm{d}z = \frac{1}{2} \cdot 2L \exp\left[-\frac{A(z_{\mathrm{eqm}})}{RT}\right] = L \exp\left[-\frac{A(z_{\mathrm{eqm}})}{RT}\right] \quad (2\text{-}13)$$

where z_{eqm} is the equilibrium distance. Note that the free energy attains its minimum value, and the distribution function attains its maximum value, at z_{eqm}. Substituting Equation (2-13) in Equation (2-9) yields:

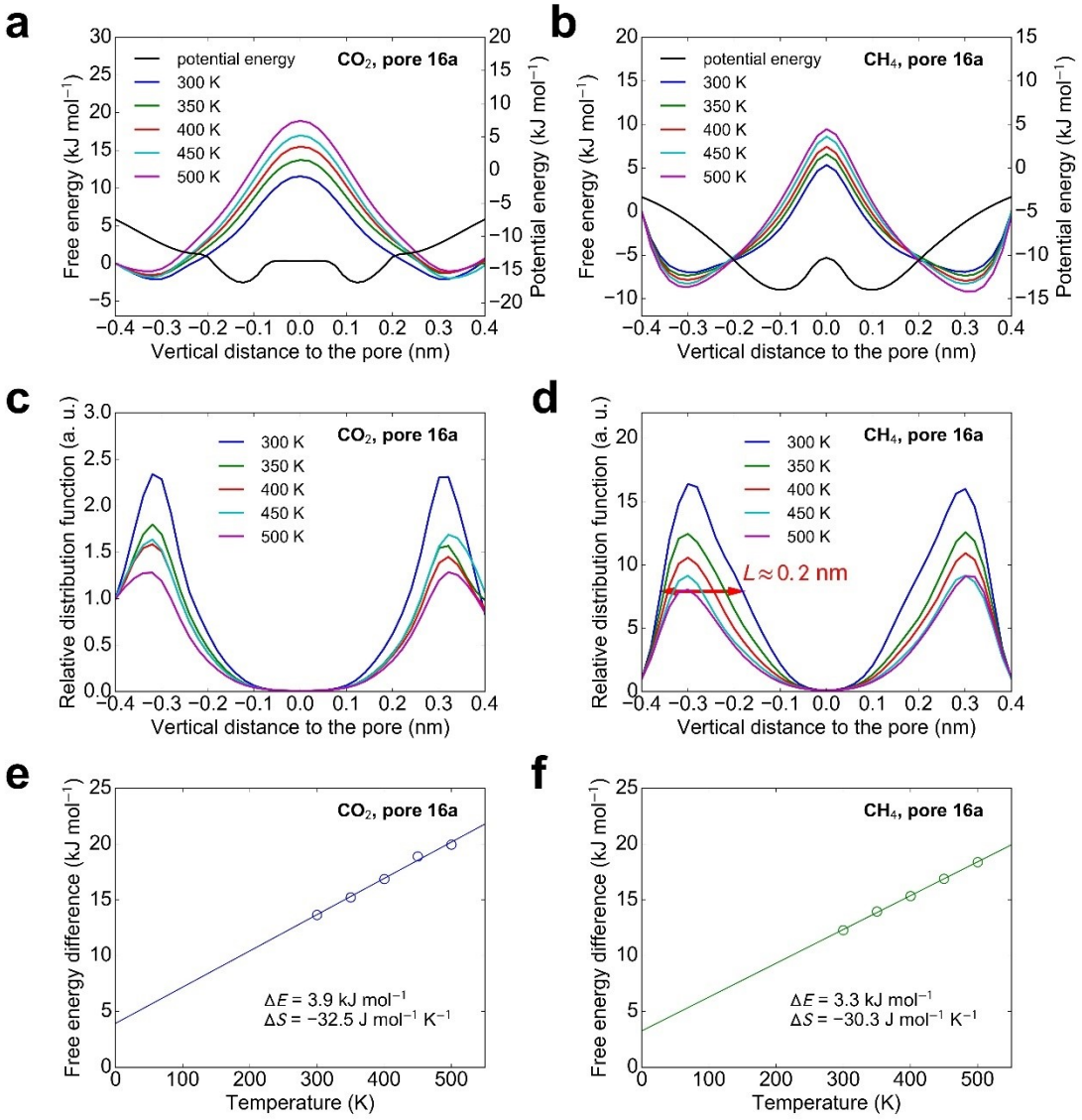

Figure 2-4. (a, b) Free energy curves (left I axes) at 300 to 500 K, and potential energy curves (right I axes) along the translocation trajectories of CO_2 and CH_4 through pore 16a. (c, d) Relative distribution functions along the translocation trajectories of CO_2 and CH_4. (e, f) Linear fitting results of free energy differences to temperature for CO_2 and CH_4.

$$k_{\text{trans}}^{\text{TST}} = \frac{1}{2L}|\dot{z}(0)|\exp\left[-\frac{A(z^{\ddagger}) - A(z_{\text{eqm}})}{RT}\right] = \frac{1}{2L}|\dot{z}(0)|\exp\left(-\frac{\Delta A}{RT}\right) \tag{2-14}$$

where ΔA is the free energy difference from the AS to the TS. In an isothermal environment, the definition of the Helmholtz free energy $A = E - TS$ implies that:

$$\Delta A = \Delta E - T\Delta S \tag{2-15}$$

Therefore,

$$k_{\text{trans}}^{\text{TST}} = \frac{1}{2L}|\dot{z}(0)|\exp\left(\frac{\Delta S}{R}\right)\exp\left(-\frac{\Delta E}{RT}\right) \tag{2-16}$$

Assuming a transmission probability $\kappa = 1$, and comparing Equation (2-16) with Equation (2-7), it is found that ΔE is equivalent to the energy barrier E_{a}, and that the translocation prefactor can be expressed as follows:

$$A_{\text{trans}}^{\text{TST}} = \frac{1}{2L}|\dot{z}(0)|\exp\left(\frac{\Delta S}{R}\right) \tag{2-17}$$

According to Equation (2-15), the energy barriers ΔE and the entropy differences from AS to TS can be obtained by linear fitting of ΔA to temperature (Figure 2-4e, f, Figure 2-5b). The fitted ΔE values are equal to 3.9 kJ mol^{-1} and 3.3 kJ mol^{-1} for CO_2 and CH_4, respectively, which is consistent with the fitted E_{a} values from large-scale MD simulations (Figure 2-3e and Table 2-1). These results confirm the applicability of TST and the validity of assuming that $\kappa \approx 1$.

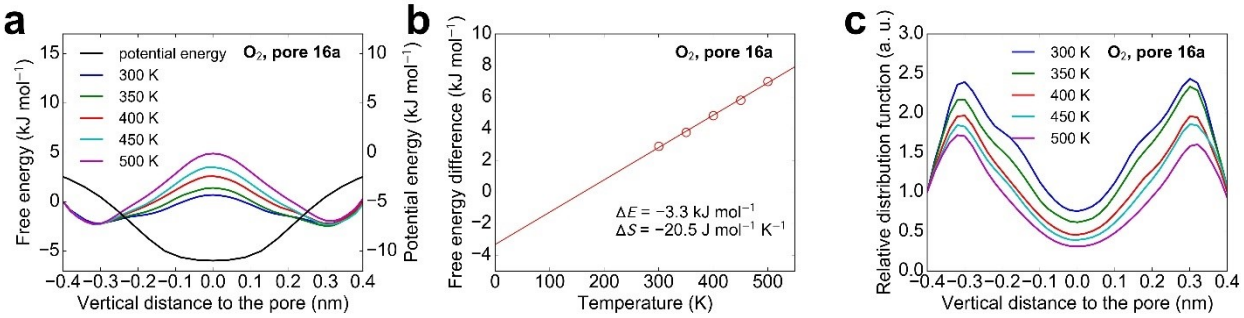

Figure 2-5. (a) Free energy curves (left I axes) at 300 to 500 K, and potential energy curves (right y axes) along the translocation trajectories of O_2 through pore 16a. (b) Linear fitting results of free energy differences to temperature for O_2. (c) Relative distribution functions along the translocation trajectories of O_2.

Note that ΔE is -3.3 kJ mol^{-1} for O_2 (Figure 2-5b), which is different from the zero energy barrier calculated from MD simulations. This is because the recrossing effect is not negligible in the case of O_2, as O_2 experiences a local potential energy minimum at the center of pore 16a and may recross the TS. An O_2 molecule tends to be attracted to the $z = 0$ plane in the energy well, but it needs to overcome another barrier to dissociate from the energy well. These two effects balance each other, resulting in a zero energy barrier. In other words, $\kappa \approx \exp(\Delta E/RT)$, and

$$E_{\text{a}} = \max(\Delta E, 0) \tag{2-18}$$

Although an O_2 molecule faces no potential energy barrier for translocation through pore 16a, a free energy barrier still exists due to the entropic effect (Figure 2-5a), which is also the case for smaller molecules like H_2 (Figure 2-17 in Appendix 2.9.4). This suggests that a gas molecule tends to reside a certain distance away from the pore center at equilibrium, instead of residing at the pore center. This is consistent with the physical meaning of the translocation step from one AS to the other.

The two methods discussed above to calculate the energy barrier (MD simulations and TST) involve fitting of the free energy to temperature. Calculation of free energies requires sampling from the entire phase space. Alternatively, one can directly calculate an energy barrier $E_{\mathrm{a,dir}}$ as the difference between the maximum and the minimum potential energies along the potential energy curve $E(z)$ (direct energy barrier method). More rigorously, the maximum point must be located between the two symmetrical minimum points. Typically, the maximum potential energy is located at $z = 0$.

Table 2-2 reports energy barriers calculated using the three methods discussed above for eight gas–pore combinations (additional details of free energy fitting from TST are presented in Figure 2-18 in Appendix 2.9.4). The configuration of pore 10a is shown in Figure 2-1d. The last four combinations require long computation time to observe translocation through the pore due to the high energy barriers and subsequently low permeances per pore, and therefore were not obtained using large-scale MD simulations. By comparing the direct method with the free energy methods, it is concluded that the direct method can provide satisfactory estimations of the energy barriers. Note that the equilibrium distance of the potential energy is closer to the TS than that of the free energy (Figure 2-4a, b and Figure 2-5a). My results suggest that the observed differences in the equilibrium distances do not undermine the validity of the direct method. This is because the equilibrium distance of the free energy q_{eqm} shifts towards the pore as the temperature decreases (shown in Figure 2-4), and could coincide with the equilibrium distance of the potential energy as one extrapolates ΔA to zero temperature, when $A = E - TS = E$. For those cases involving O_2, for which TST is not perfectly applicable, the direct method still predicts a zero energy barrier by incorporating the recrossing effect implicitly, which is consistent with the MD simulation result. In general, the direct method provides a quick and reliable method to calculate the energy barrier. Other direct energy methods with higher accuracy (*e.g.*, DFT) can also be utilized.

Table 2-2. Comparison of the three methods used here to calculate the energy barrier.

Gas–pore	E_a from MD simulation (kJ mol^{-1})	ΔE from TST (kJ mol^{-1})	$E_{a,dir}$ from direct energy barrier method (kJ mol^{-1})
CO_2–16a	3.9 ± 0.6	3.9 ± 2.0	3.3
CH_4–16a	3.3 ± 1.3	3.3 ± 0.5	3.3
O_2–16a	-0.2 ± 0.9	-3.3 ± 0.8	0.0
CO_2–13a	11.3 ± 1.7	9.6 ± 2.3	10.4
CH_4–13a	n/a	20.0 ± 2.0	22.3
O_2–13a	n/a	-3.5 ± 0.5	0.0
CO_2–10a	n/a	82.4 ± 7.4	82.3
O_2–10a	n/a	66.5 ± 4.3	59.1

2.5 Estimation of Entropy Penalties

Equation (2-17) provides a theoretical expression for the translocation prefactor A_{trans} in Equation (2-7). The average crossing velocity $|\dot{z}(0)|$ can be approximated by the Maxwell-Boltzmann distribution. Specifically,

$$|\dot{z}(0)| = \sqrt{\frac{2k_BT}{\pi m}} \tag{2-19}$$

where k_B is the Boltzmann constant and m is the gas molecular weight. Therefore, Equation (2-17) can be rewritten as follows:

$$A_{\text{trans}}^{\text{TST}} = \frac{1}{L}\sqrt{\frac{k_BT}{2\pi m}}\exp\left(\frac{\Delta S}{R}\right) \tag{2-20}$$

Next, Equation (2-20) is used to quantitatively predict the translocation prefactor. The half-peak width L of the relative distribution function can be estimated from Figure 2-4c, d and Figure 2-5c. At 300 K, L approximately equals to 0.15, 0.2, and 0.3 nm for CO_2, CH_4, and O_2, respectively. The entropy difference ΔS from AS to TS is typically negative, representing the entropy penalty to cross a sub-nanometer graphene pore. The translational, rotational, and vibrational degrees of freedom of a molecule are hindered at the TS due to the restrictions imposed by the pore. The potential energy landscape at the TS is much steeper than that at the AS, indicating stronger steric restriction at the TS

(Figure 2-15c, f in Appendix 2.9.3). The entropy penalties for CO_2, CH_4, and O_2 through pore 16a are -32.5, -30.3, and -20.5 J mol^{-1} K^{-1}, respectively. According to Equation (2-20), I predict that the translocation prefactor through pore 16a is 1.3×10^{10} s^{-1} for CO_2, 2.1×10^{10} s^{-1} for CH_4, and 3.2×10^{10} s^{-1} for O_2. These theoretical estimations are all in good agreement with the MD simulation results (Table 2-1) within order-of-magnitude accuracy. Note that errors could stem from deviations from the Maxwell-Boltzmann distribution, or from an inaccuracy in the estimation of L.

Equation (2-20) can be further validated by adding flexibility to the graphene sheet, which so far, was assumed to be rigid. In large-scale MD simulations, the bond lengths, the angles, and the dihedrals were allowed to fluctuate, while the carbon atoms at the periodic boundary were frozen to keep the graphene sheet in place. As shown in Figure 2-6a, the graphene sheet slightly bends. The energy barrier E_a and the translocation prefactor A_{trans} are calculated for CO_2 and CH_4 through pore 16a using the same method shown previously (details shown in Figure 2-16 in Appendix 2.9.3). When flexibility is added to the graphene sheet, the energy barrier decreases by about 0.7–0.8 kJ mol^{-1} (Figure 2-6b vs. Table 2-1), and the translocation prefactor increases by ~ 50%, compared to the case of rigid graphene (Figure 2-6c vs. Table 2-1). The decrease in the energy barrier can be attributed to the expansion in pore size as the graphene sheet bends. The increase in the prefactor can be explained by a smaller entropy penalty.

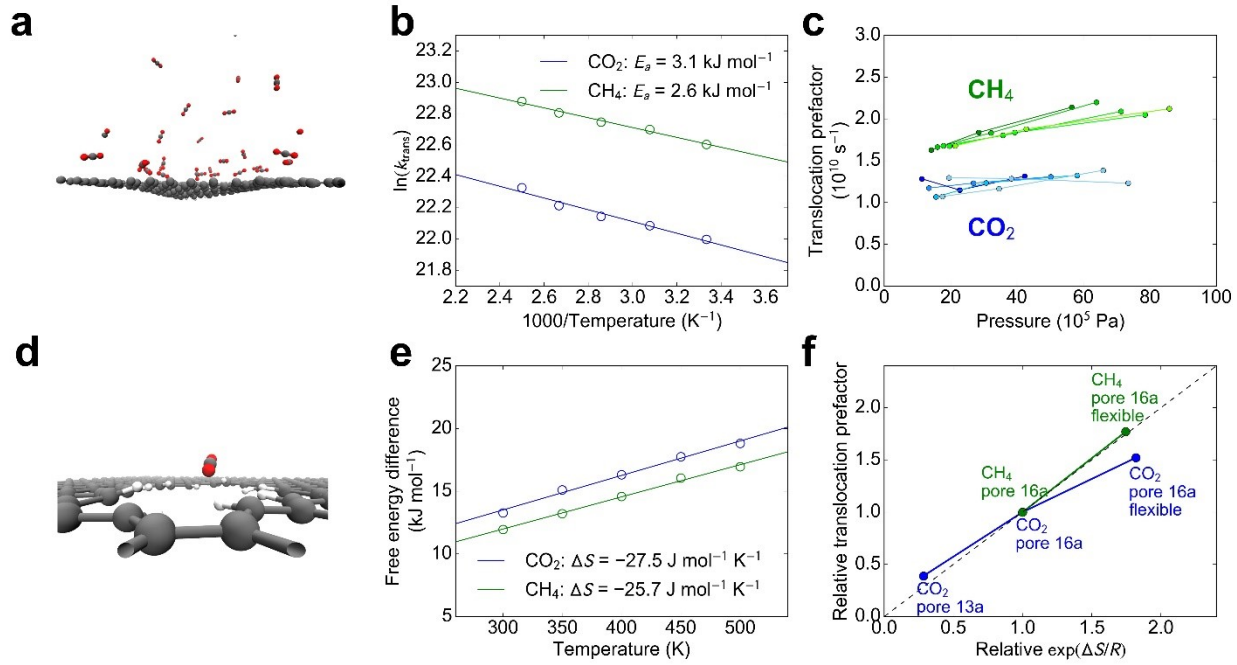

Figure 2-6. (a) Snapshot of an MD simulation, (b) fitting results of the energy barrier, and (c) translocation prefactors of CO_2 and CH_4 through pore 16a on flexible graphene. (d) Snapshot and (e) fitting results of the free energy curve calculation for gas permeation through pore 16a on flexible graphene. (f) The relation between the prefactor and $\exp(\Delta S/R)$.

In order to calculate the entropy penalty for flexible graphene pores, I calculated the free energy curves after unfreezing the hydrogen and carbon atoms at the pore rim (Figure 2-6d). Note that the carbon atoms which are not at the pore rim were kept frozen; otherwise, the configuration space will be too large to be sampled within a reasonable period of time. The entropy penalty equals -27.5 and -25.7 J mol^{-1} K^{-1} for CO_2 and CH_4 to cross flexible pore 16a, respectively (for rigid pore 16a, the entropy penalties are -32.5 and -30.3 J mol^{-1} K^{-1} for CO_2 and CH_4, respectively). Because of the pore flexibility, the system can sample more configurations at the TS, and the magnitude of the entropy penalty is reduced. The ~ 5 J mol^{-1} K^{-1} saved from the entropy penalty is responsible for the increase in translocation prefactors, according to Equation (2-20). As shown in Figure 2-6f, taking rigid pore 16a as a reference, the increase in the prefactor is comparable to the increase in $\exp(\Delta S/R)$.

The relation between the prefactor and the entropy penalty can also be confirmed by shrinking the pore from pore 16a to 13a. The entropy penalty for CO_2 to cross pore 13a is -43.0 J mol^{-1} K^{-1}, which is 10.5 J mol^{-1} K^{-1} higher than that for CO_2 to cross pore 16a (in absolute value). The decrease in $\exp(\Delta S/R)$ is consistent with the decrease in the prefactor (Figure 2-6f).

Table 2-3 reports the entropy penalty values, the translocation prefactors predicted by Equation (2-20), and the prefactors deduced from MD simulations for various gas–pore combinations (additional details of the fitting are shown in Figure 2-18 in Appendix 2.9.4, and the structure of pore 22 is shown in Figure 2-19 in Appendix 2.9.5; some gas–pore combinations were not simulated by MD due to their high demand of computational resources). Note that the half-peak width L of the AS is assumed to remain the same for each type of gas. Table 2-3 reveals that: (1) Equation (2-20) can predict the translocation prefactor with order-of-magnitude precision, (2) for the same pore, a smaller gas molecule such as O_2 incurs a smaller entropy penalty, (3) for a given gas, a smaller pore results in a stronger entropy penalty, and (4) pore flexibiliy reduces the entropy penalty for pore crossing.

Table 2-3. Entropy penalty, translocation prefactor predicted by Equation (2-20), and prefactor derived from MD simulations for various sample gas–pore combinations. "Flex" is an abbreviation for "pore with flexibility".

Gas–pore	Entropy penalty ΔS (J mol^{-1} K^{-1})	$A_{\text{trans}}^{\text{TST}}$ from Equation (2-20) (10^{10} s^{-1})	A_{trans} from MD Simulations (10^{10} s^{-1})
CO_2–16a	-32.5 ± 4.9	1.3	0.81 ± 0.08
CH_4–16a	-30.3 ± 1.3	2.1	1.06 ± 0.15
O_2–16a	-20.5 ± 1.8	3.2	2.02 ± 0.13
CO_2–13a	-43.0 ± 5.8	0.36	0.32 ± 0.05
CH_4–13a	-45.5 ± 4.9	0.33	n/a
O_2–13a	-31.6 ± 1.1	0.83	n/a
CO_2–10a	-64.7 ± 18.2	0.02	n/a
O_2–10a	-44.2 ± 10.5	0.18	n/a
CO_2–22	-21.7 ± 6.0	7.7	n/a
CH_4–22	-17.1 ± 5.8	10.0	n/a
CO_2–16a-flex	-27.5 ± 4.6	2.3	1.23 ± 0.09
CH_4–16a-flex	-25.7 ± 3.3	3.6	1.87 ± 0.19

To theoretically predict the translocation prefactor using Equation (2-20), an algorithm to estimate the entropy penalty is required. This is because, similar to the calculation of free energies, the calculation of entropy requires sampling the entire phase space, and therefore, is computationally demanding. A convenient way to rapidly estimate the entropy penalty for any relatively circular pore involves fitting the known results to a power law which relates the entropy penalty to the pore size, as shown below.

$$\Delta S_{\text{CO}_2} \approx -\frac{1516\ \text{J mol}^{-1}\ \text{K}^{-1}}{(\#\text{of missing C atoms})^{1.380}} \tag{2-21}$$

$$\Delta S_{\text{CH}_4} \approx -\frac{5257\ \text{J mol}^{-1}\ \text{K}^{-1}}{(\#\text{of missing C atoms})^{1.855}} \tag{2-22}$$

$$\Delta S_{\text{O}_2} \approx -\frac{1891\ \text{J mol}^{-1}\ \text{K}^{-1}}{(\#\text{of missing C atoms})^{1.619}} \tag{2-23}$$

The numerators and the powers in the denominators were deduced by linear fitting of $\ln(-\Delta S)$ to ln(number of missing C atoms) (Figure 2-20 in Appendix 2.9.6). The fitted pore size ranges from 10 to 22 removed carbon atoms. The power law fittings make sense considering the following two limits: (1) in the limit when no carbon atom is removed, the entropy penalty goes to infinity due to the

impermeability of a perfect graphene lattice, and (2) in the limit when the number of removed carbon atoms goes to infinity, the entropy penalty approaches zero because of the absence of any constraints imposed by the pore edge.

2.6 Prediction of Gas Separation through Graphene Nanopores

Using Equations (2-21) and (2-22), along with Equations (2-7) and (2-20) and the direct energy barrier calculation method, one can predict the CO_2 and CH_4 permeances per pore through a series of pores in the pore library (Figure 2-19 in Appendix 2.9.5). The predicted pore sizes range from 13 to 24 removed carbon atoms, which are mainly included in the pore size range fitted to obtain Equations (2-21) and (2-22). These pores are small enough so that the gas transport is translocation limited (Appendix 2.9.7). The pore Henry's coefficients from previous MD simulations were used. Figure 2-7a shows the performance of some sub-nanometer graphene pores in terms of the CO_2 permeance per pore and the CO_2/CH_4 separation factor. The separation factor here is defined as the ratio of the permeances per pore of the pure CO_2 to the pure CH_4 inlets. To investigate the gas permeation behavior of a mixed gas inlet, I also simulated an equimolar mixture of CO_2 and CH_4 on the feed side. No major difference in energy barrier was observed between the mixture gas inlet and the pure gas inlet (Figure 2-21 and Table 2-5 in Appendix 2.9.8). This supports the argument that the translocation of gas through a sub-nanometer pore is a single-molecule event, because the pore is too small for two gas molecules to translocate simultaneously. However, I observed a lower heat of adsorption (in absolute value) of CO_2 adsorbing to pore 16a in an equimolar CO_2/CH_4 mixture when compared to pure CO_2 (Table 2-5 in Appendix 2.9.8). This is due to competitive adsorption of different gases at the pore mouth when the gas pressure is high (> 50 bar). Note that in practical situations used to test gas permeation through single-layer or few-layer graphene, the pressure of the gas phase is typically lower than 5 bar.[109–111] In this case, the number of gas molecules adsorbed at the pore mouth is typically less than one (< 0.2, Figure 2-22 in Appendix 2.9.10), and the effect of competitive adsorption is minor. In summary, at a relatively low pressure, gas permeation behaves similarly for a pure gas inlet and for a mixed gas inlet.

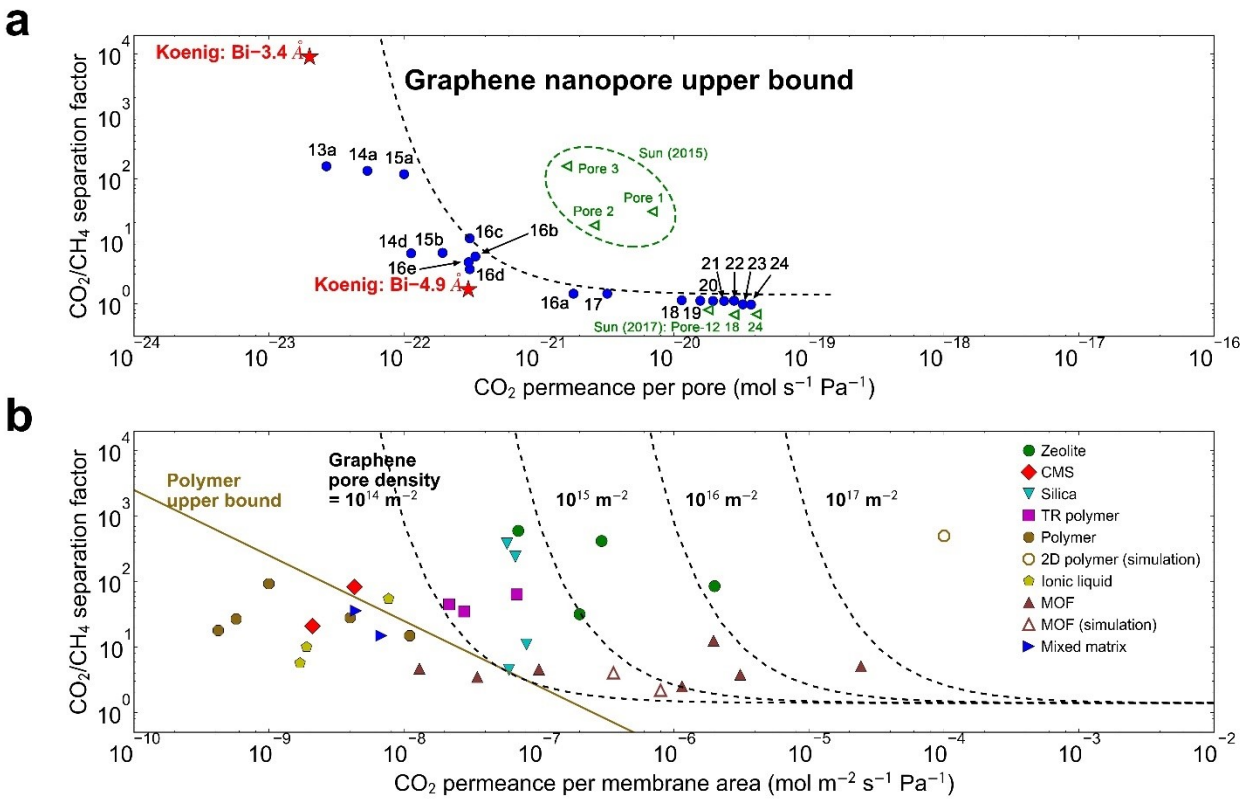

Figure 2-7. (a) Robeson plot (separation factor vs. permeance per pore) characterizing the CO_2/CH_4 separation through various graphene sub-nanometer pores at 300 K. Pore configuration identifiers are annotated beside each data point. Experimental data obtained by Koenig *et al.*[109] and results from several MD simulations[48,75] are also plotted. (b) Comparison between a porous graphene membrane and other membranes for CO_2/CH_4 separations. Hollow markers correspond to simulation results. The references are listed in Table 2-6 in Appendix 2.9.9. For the MOF membrane simulation work,[166] the MOF membranes are only ~ 5-nm thick in simulation. From a practical perspective, the permeance is calculated assuming a typical MOF membrane thickness of 5 μm.[143]

Figure 2-7a shows a negative correlation between permeance per pore and selectivity. Pores with CO_2/CH_4 separation factors which are higher than 10^2 have CO_2 permeances per pore lower than 10^{-22} mol s^{-1} Pa^{-1}. Further, pores with separation factors of ~ 10 have permeances per pore between 10^{-22} and 10^{-21} mol s^{-1} Pa^{-1}. Note that when the CO_2 permeance per pore is higher than 10^{-21} mol s^{-1} Pa^{-1}, the CO_2/CH_4 the selectivity approaches 1. Therefore, the graphene perforation should be carefully engineered in order to attain a satisfactory separation factor.

The trade-off between permeability and selectivity is widely observed in the permselective membrane literature. The upper bound for polymer membranes was discussed by Robeson.[10,11] Taking membrane thickness into consideration, some literature replaced permeability by permeance as the *x* axis in the Robeson plot (permeance = permeability / membrane thickness).[111,167] Analogously, an upper

bound for hydrogen-terminated graphene nanopores is drawn (Figure 2-7a). This upper bound is in good agreement with the experimental results obtained by Koenig *et al.*[109] Indeed, the performances of the two graphene membranes studied by Koenig *et al.* lie within the upper bound (stars in red in Figure 2-7a).[109] The graphene nanopore upper bound is also compared to results from previous MD simulation studies (triangles in green in Figure 2-7a; note that the designation scheme for pore sizes used here is different from the one used in ref. 48 and 75). It is noteworthy that the simulated CO_2 permeances per pore from three types of the graphene pores considered exceed the predicted upper bound by one order of magnitude. This may be due to the different force field models and graphene flexibility conditions used.[75]

Despite the existence of such an upper bound, porous graphene membranes are still highly promising because of the potentially tunable pore density.[72] The permeance of porous graphene per membrane surface area is the product of the permeance per pore and the pore density per membrane surface area, assuming a monodisperse pore distribution. Figure 2-7b compares the graphene nanopore upper bound at different pore densities with the previously reported permselective membranes for CO_2/CH_4 separations (Table 2-6 in Appendix 2.9.9). At a pore density of 10^{14} m^{-2}, which has been experimentally realized,[131] the upper limit of a porous graphene membrane can exceed the polymer upper bound. Therefore, as perforation techniques continue to improve, porous graphene membranes can potentially outperform other permselective membranes.

2.7 Conclusions

In this chapter, I used MD simulations to validate the decoupling of gas permeation through sub-nanometer graphene pores into adsorption to the pore mouth and translocation through the pore. The adsorption was quantified by the pore Henry's coefficients, which follows the van't Hoff equation. The translocation was described by the translocation coefficient, which follows an Arrhenius equation. I utilized transition state theory to predict the translocation coefficient, showing good agreement with the simulated values. By calculating the free energy curves of gas molecules translocating through sub-nanometer graphene pores, I showed that when the free energy barrier is relatively high, entropy and energy terms can be decoupled, and the prefactor for translocation is related to the entropy penalty for

crossing the pore. I developed efficient algorithms to predict the energy barrier and the entropy penalty for translocation, and then calculated gas permeances per pore through a range of pores. For the CO_2/CH_4 gas mixture, the simulated results exhibit a trade-off between the CO_2 permeance and the CO_2/CH_4 selectivity, represented by an upper bound for sub-nanometer hydrogen-terminated graphene pores in a Robeson plot. By comparing the performance predicted for porous graphene with those reported for permselective membranes, I show that porous graphene is promising for gas separation, because it can potentially outperform other materials, given a high pore density.

In the next chapter, I will extend the nanopore size range investigated beyond sub-nanometer, where the energy barrier associated with pore translocation decreases to zero and Equation (2-4) is no longer valid.

2.8 Methods

2.8.1 Force Field

An all-atom force field was utilized to carry out the simulations reported in this chapter. The potential energy of the graphene–gas system consists of bonded potentials and non-bonded potentials. The bonded potentials include harmonic bonds, harmonic valence angles, and dihedral potentials in a cosine form. Bond stretching and bending force constants of CO_2 and CH_4 are given by the elementary physical model 2 (EPM2 Model),[155] and the all-atom optimized potentials for liquid simulations (OPLS-AA Model).[168] CHARMM27 force field parameters[169,170] were used to construct the bonded interactions of the graphene sheet.

Non-bonded interactions include Lennard-Jones potentials and electrostatic potentials. The Lennard-Jones parameters of graphene were reported by Cheng and Steele.[171] The transferable potential for phase equilibria (TraPPE) force field[154] and the OPLS-AA force field were used for CO_2 and CH_4, respectively. The force field for O_2 was developed by Perng *et al*.[172] The cutoff distance of the Lennard-Jones interactions was set as 1.2 nm. Long-range electrostatics were handled using the Particle-Particle-Particle Mesh (PPPM) method. Periodic boundary conditions were utilized in all directions.

Force field parameters for the carbon and hydrogen atoms residing at the edge of the graphene nanopore were approximated by aromatics in the AMBER force field, because graphene can be approximated as a very large polycyclic aromatic molecule.[173]

2.8.2 Escape Time Calculation

All molecular dynamics simulations were carried out using the Large-Scale Atomic/Molecular Massively Parallel Simulator (LAMMPS).[174] Two porous graphene sheets with a hydrogen-terminated pore in each were placed parallel to each other at a distance of 20 nm, separating the periodic simulation box into two compartments. Gas molecules were placed in one compartment, and the other one consisted of vacuum. The system was simulated in the NVT ensemble using the Nose-Hoover thermostat with a time constant of 0.2 ps.[175] The simulation time step was 2 fs. The gas molecules were allowed to diffuse, and the time elapsed before all the atoms of a molecule appeared in the other compartment (escape time) was recorded. Once a translocation event took place, the system was reverted to the state before translocation, and all the molecules were assigned new, random Maxwell-Boltzmann-distributed velocities, and were shifted by a random (x, y) displacement, so that the system was uncorrelated with its previous state. Note that this lack of correlation between each run is required to guarantee unbiased results. Escape times were recorded repeatedly following this procedure. Some time was needed for the simulation system to equilibrate. However, the equilibration time was far less than the overall simulation time, and therefore, did not affect the estimation accuracy of the permeation rate (Figure 2-22 in Appendix 2.9.10).

Due to the lack of memory of the system, the escape times follow an exponential distribution (Figure 2-23 in Appendix 2.9.10),[176]

$$f(t) = \lambda \exp(-\lambda t) \tag{2-24}$$

The parameter λ in Equation (2-24) can be estimated using the maximum likelihood estimation from *M* escape time records, and it is the rate of permeation from two graphene nanopores (because of the use of two graphene sheets in the simulation). The estimated value $\hat{\lambda}$ can be calculated as follows:[177]

$$\hat{\lambda} = \left(\frac{\Sigma_{i=1}^{M} t_i}{M} \right)^{-1} \tag{2-25}$$

The $100(1-\alpha)\%$ confidence interval of the parameter λ can be obtained as follows:[177]

$$\frac{\hat{\lambda}\,\chi^2_{\frac{\alpha}{2},2M}}{2M} < \lambda < \frac{\hat{\lambda}\,\chi^2_{1-\frac{\alpha}{2},2M}}{2M} \tag{2-26}$$

where $\chi^2_{q,v}$ is the $100q$ percentile of the χ^2 distribution with v degrees of freedom.

2.8.3 Free Energy Curve Calculation

Free energy calculations were carried out using LAMMPS to obtain the free energy barrier of a gas molecule crossing a sub-nanometer graphene pore. The gas molecule was held at vertical distances above and below the graphene basal plane by a harmonic biasing force along the direction normal to the graphene basal plane. In order to match the definition of a pore-associated molecule, the gas molecule was enclosed in the pore mouth region by reflective walls. The gas molecule was equilibrated at each biasing point for 1 ns. Subsequently, histograms of the distances between the center of mass of the gas molecule and the graphene basal plane were recorded during 4 ns. The free energy curves were calculated using the weighted histogram analysis method[53] by the WHAM code[178], with a tolerance of 10^{-6}. The histograms at each biasing point for CO_2 through pore 16a at 300 K are shown in Figure 2-24 in Appendix 2.9.11. The simulation could be carried out both with or without the presence of other molecules in the simulation box. The results are similar for the two situations (Figure 2-25 in Appendix 2.9.11), indicating that the interactions between a gas molecule and the pore are not affected by other gas molecules, especially when considering translocation. Therefore, for simplicity and computational accuracy, I carried out free energy simulations with a single gas molecule.

2.8.4 Direct Energy Barrier Calculation

The energy barriers corresponding to the gas permeation through graphene sub-nanometer pores were calculated directly using the same force field of non-bonded interactions as discussed above. The graphene sheet and the molecule were both held rigid. The algorithm was implemented in MATLAB. Firstly, I obtained the (x, y) coordinates of the gas molecule at the transition state (the x and y axes are

parallel to the graphene basal plane, and the z axis is normal to the basal plane). I optimized the molecule's (x, y) coordinates and its three-dimensional rotation to find the potential energy minimum, while enforcing the constraint that the center of mass of the molecule should lie on the graphene basal plane. Secondly, I calculated the potential energy at a series of vertical distances z along the translocation trajectory, which is assumed to be perpendicular to the graphene basal plane. In my algorithm, a gas molecule was allowed to rotate in all directions. In that way, the potential energy curve is obtained. The minimum potential energy in the curve corresponds to the pore association site, and the maximum corresponds to the transition state (usually located at $z = 0$). The direct energy barrier is then obtained as the difference between the maximum and the minimum potential energy values.

2.9 Appendices

2.9.1 Molecular Dynamics Simulation Results of CO_2 Permeation Using the EPM2 Force Field

The permeation of CO_2 through graphene pore 16a was simulated using the Elementary Physical Model 2 (EPM2) to investigate the sensitivity of the permeation results on the force field.[155]

The main hypothesis – $\Pi = k_{\mathrm{trans}} H_{\mathrm{pore}}$ – and its related temperature dependence remain valid even if another force field is utilized. A comparison of fitting results from MD simulations using two CO_2 force fields is presented in Table 2-4. Only minor differences are observed, and therefore, the validity of the theory is relatively insensitive to the chosen force field.

Table 2-4. Apparent energy barrier, adsorption heat, energy barrier, and translocation prefactor derived from temperature fitting of MD results for CO_2–pore 16a using the TraPPE and EPM2 force fields.

Force field	Apparent energy barrier (kJ mol^{-1})	Adsorption heat (kJ mol^{-1})	Energy barrier (kJ mol^{-1})	Translocation Prefactor (10^{10} s^{-1})
TraPPE	-7.2 ± 1.2	-11.1 ± 0.8	3.9 ± 0.6	0.81 ± 0.08
EPM2	-7.4 ± 0.7	-10.8 ± 0.1	3.4 ± 0.6	0.85 ± 0.06

2.9.2 Definitions for the Bulk and the Pore Mouth Region

As shown in Figure 2-8a, b, the adsorption layers of CO_2 and CH_4 on graphene are located between 0.25 and 0.5 nm away from the pore. Hence, setting the vertical range of 0–0.5 nm would be sufficient to capture the adsorption behavior. Concomitantly, the density profile approaches a constant value when the distance from the graphene basal plane is 1 nm or greater. Therefore, it is reasonable to define the bulk as the region which lies 3 nm or farther away from the graphene basal plane.

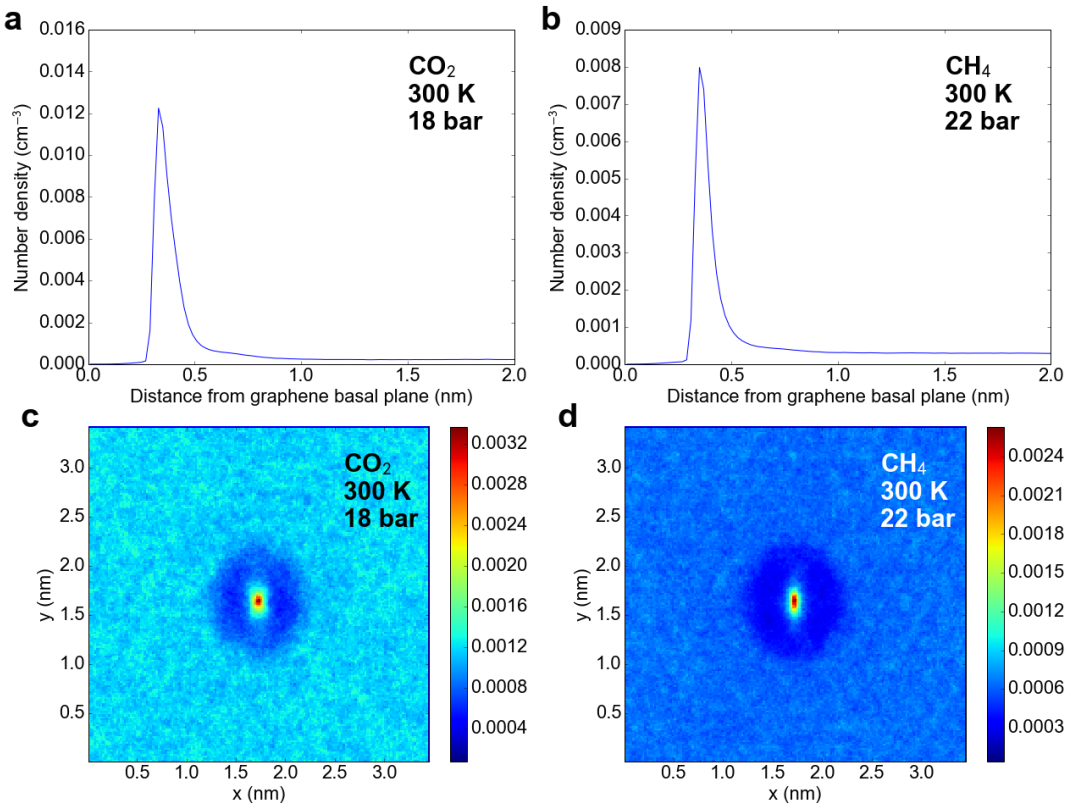

Figure 2-8. Number density distributions in the z direction away from the graphene basal plane of (a) CO_2 at 300 K and 18 bar, and (b) CH_4 at 300 K and 22 bar. Number density distributions within the adsorption layer in the (x, y) plane of (c) CO_2 and (d) CH_4 at the same conditions as above. The pore is pore 16a.

As shown in Figure 2-8c, d, within the adsorption layer, the gas molecules have a uniform distribution away from the pore, which is located at (x, y) = (1.7 nm, 1.6 nm). However, the (x, y) density profile shows a high peak (denoted in red) at the pore center, suggesting strong adsorption at the pore mouth. Concomitantly, a depletion region with a radius of ~ 0.5 nm (denoted in dark blue) is observed, where the gas molecules are not likely to reside. The depletion region is concentric with the pore, and is of approximately the same size as that of pore 16a. The depletion region occurs because

the gas molecule loses attractive forces from below due to the removed carbon atoms in the pore. As a result, there is an energy barrier to approach the pore from the graphene surface. Because of the depletion region, it is reasonable to define a pore mouth region with a radius of 0.4 nm, which is enough to encompass the density peak at the pore center.

The energy barrier to approach the pore has been investigated by Drahushuk and Strano.[152] A typical barrier height is less than 4 kJ mol^{-1}, corresponding to an exponential Boltzmann factor of > 0.2 at 300 K. It is expected that, when transport through the pore is translocation-limited, the surface influx should be much greater than the total flux, thereby providing sufficient feed for translocation. Therefore, in the translocation-limited regime, the energy barrier to approach the pore from the surface adsorption layer should have a minor effect.

As shown in Figure 2-9, I varied the cylinder radius r and the cylinder height h of the pore mouth region from the value used above ($r = 0.4$ nm, $h = 0.5$ nm). The corresponding pore Henry's coefficients follow an identical trend, only deviating by a constant ratio. Therefore, the results for the adsorption heat and the energy barrier would not change.

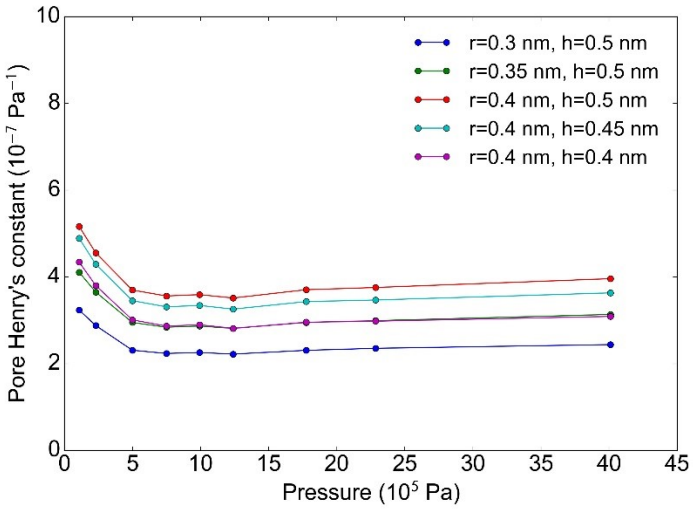

Figure 2-9. Pore Henry's coefficients of CO_2 above pore 16a at 300 K with different sizes of the pore mouth region.

2.9.3 Details of the Molecular Dynamics Simulation Results and Analyses

Figure 2-10 shows the compressibility factor of CO_2 at various pressures and temperatures based on the equation of state reported by Span and Wagner.[157] At 300 K, the compressibility factor decreases below

0.9 as the pressure increases above 20×10^5 Pa. Note that lower compressibility factors correspond to smaller pressure values. This is in accordance with the increase in the simulated permeance per pore and in the pore Henry's coefficient observed at 300 K at pressures above 20×10^5 Pa.

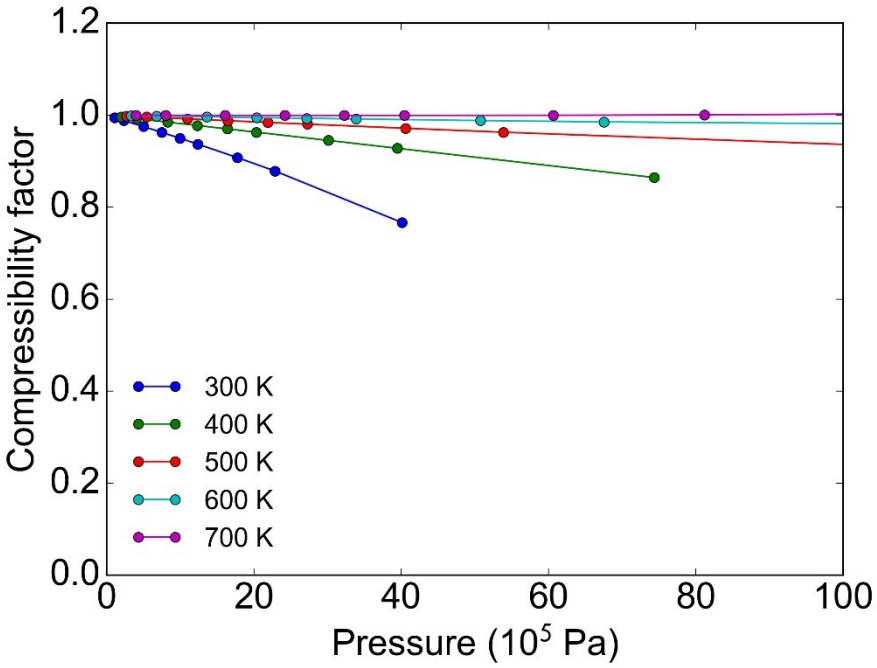

Figure 2-10. Compressibility factor of CO_2 at various temperatures and pressures according to the equation of state provided in ref. 157.

The simulated permeances per pore and pore Henry's coefficients of O_2 through pore 16a are shown in Figure 2-11. The proportional correlation between the simulated permeances per pore and the pore Henry's coefficients can be further confirmed.

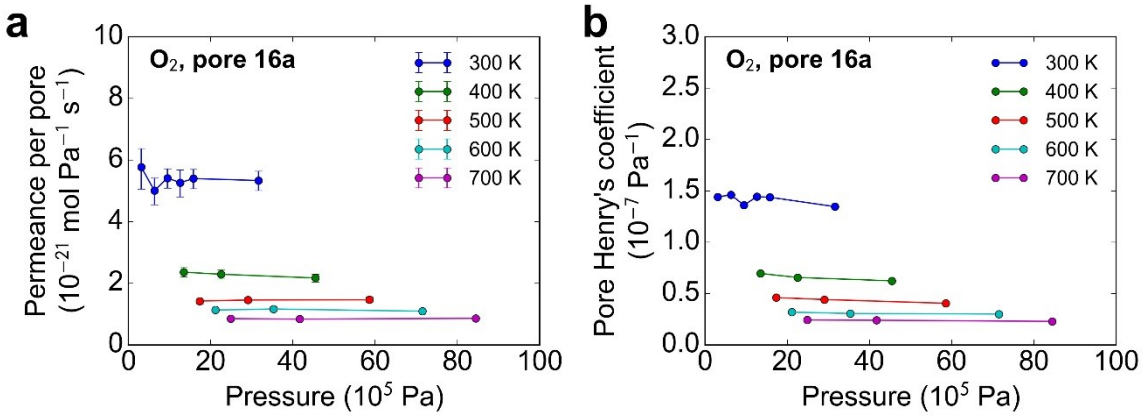

Figure 2-11. (a) Simulated permeances per pore and (b) simulated pore Henry's coefficients of O_2 through pore 16a at various temperatures and pressures.

Figure 2-12 shows additional details about analyzing the temperature dependence of the simulated permeances per pore and pore Henry's coefficients. Linear fitting results according to the Arrhenius equation and the van't Hoff equation are shown in Figure 2-12a, b, respectively. Apparent energy barriers and heats of adsorption for CO_2, CH_4, and O_2 across pore 16a are obtained. Figure 2-12c, d show the translocation coefficients k_{trans} of CH_4 and O_2 through pore 16a, respectively, and the corresponding translocation prefactors A_{trans} are shown in Figure 2-12e, f. The translocation prefactors have similar values as expected.

I studied the surface adsorption of CO_2 on the graphene lattice away from the pore at various conditions, and calculated the areal number densities c of the adsorption layer, with a unit of Pa^{-1} nm^{-2} (Figure 2-13). Similar to the pore Henry's coefficient, a surface Henry's coefficients H_{surf} is defined as the ratio of the areal density c and the bulk pressure p. By fitting H_{surf} to the van't Hoff equation, I obtain the adsorption heat of CO_2 to the graphene surface $\Delta H_{\mathrm{ads}}^{\mathrm{surf}}$ (Figure 2-13b, c).[41] The surface adsorption region is defined as the region located less than 0.5 nm away from the graphene basal plane, and more than 1 nm away from the center of the pore. Note that the heats of adsorption corresponding to association and to surface adsorption are similar (-11.1 vs. -10.6 vs. kJ mol^{-1}), suggesting that the permeation steps prior to translocation are at equilibrium.

Figure 2-14 shows simulation results of CO_2 through pore 13a and related analyses. The analytical method used is the same as that used to generate Figure 2-3 and Figure 2-12. Note that the permeances per pore are significantly reduced when the pore shrinks from 16a to 13a, while the energy barrier increases substantially. However, the pore Henry's coefficients and the heat of adsorption exhibit no apparent changes.

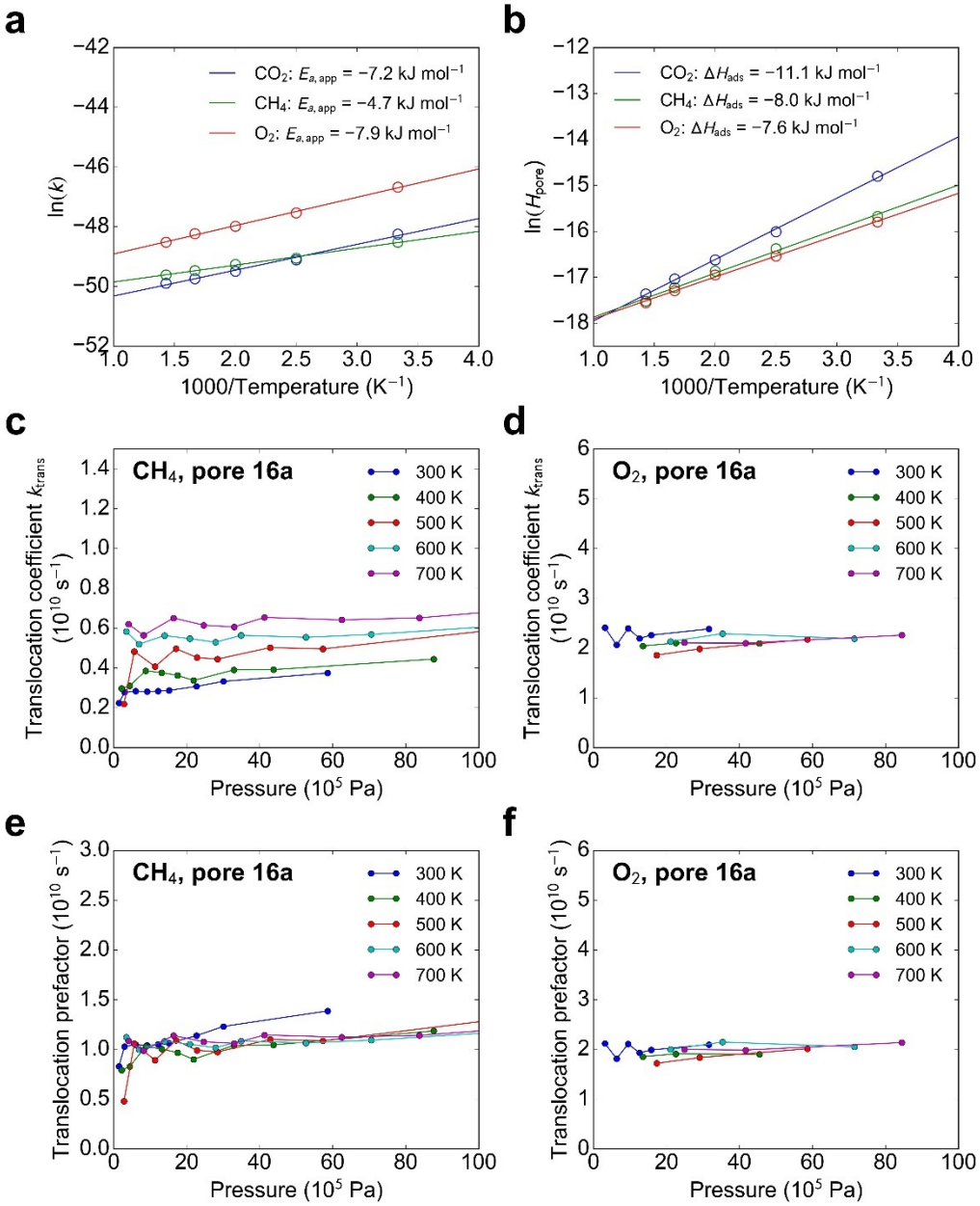

Figure 2-12. (a) Fitting results of simulated permeances per pore of CO_2, CH_4, and O_2 through pore 16a according to the Arrhenius equation. (b) Fitting results of simulated pore Henry's coefficients of CO_2, CH_4, and O_2 above pore 16a according to the van't Hoff equation. (c, d) Translocation coefficients calculated at various temperatures and pressures for CH_4 and O_2, respectively. (e, f) translocation prefactors of CH_4 and O_2, respectively.

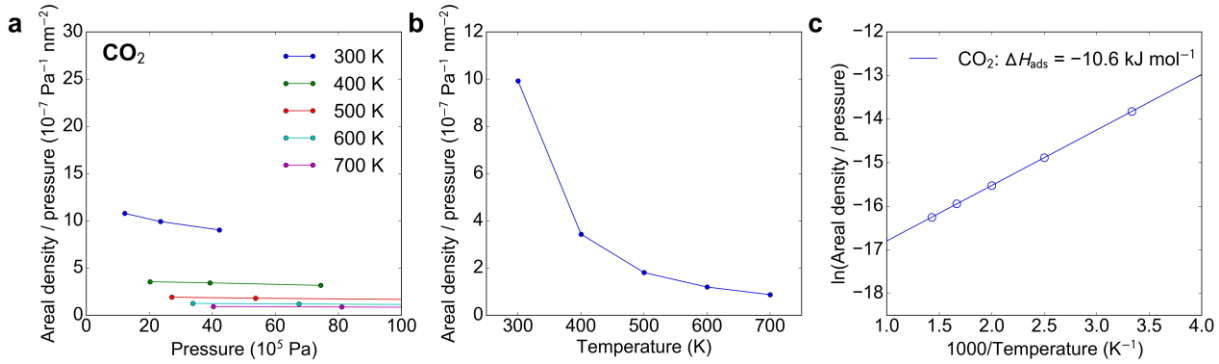

Figure 2-13. (a) Pressure-normalized areal number density of adsorbed CO_2 on the graphene surface at various temperatures and pressures. (b) Temperature dependence of the pressure-normalized areal number density of adsorbed CO_2, and (c) related fitting results for the adsorption heat $\Delta H_{\mathrm{ads}}^{\mathrm{surf}}$.

The gas molecule's geometric arrangement in the adsorbed state (AS) and the transition state (TS) depends on the gas type and the pore configuration. For example, the C=O bond forms an angle of 56.5° with the normal to the graphene sheet when CO_2 is at the TS in pore 16a (Figure 2-15a). The angle decreases to 9.9° when the pore shrinks to pore 13a (Figure 2-15b). Note that pore 13a imposes stronger steric restriction from its edges compared to pore 16a, due to its smaller size, thereby leading to an almost perpendicular alignment of CO_2 at the TS. Regarding the AS, the potential energy between CO_2 and pore 16a is minimized when the CO_2 molecule is aligned parallel to the graphene basal plane (Figure 2-15d). On the other hand, the CO_2 molecule is vertically aligned at the AS above pore 13a (Figure 2-15e). The AS and TS configurations are obtained by minimizing and maximizing the potential energy along the translocation trajectory.

It is noteworthy that the potential energy landscape at the TS is much steeper than that at the AS (Figure 2-15c, f). As a result, the location of a gas molecule at the AS is more evenly distributed in the molecular coordinate space, while the gas molecule's location at the TS is sharply peaked.

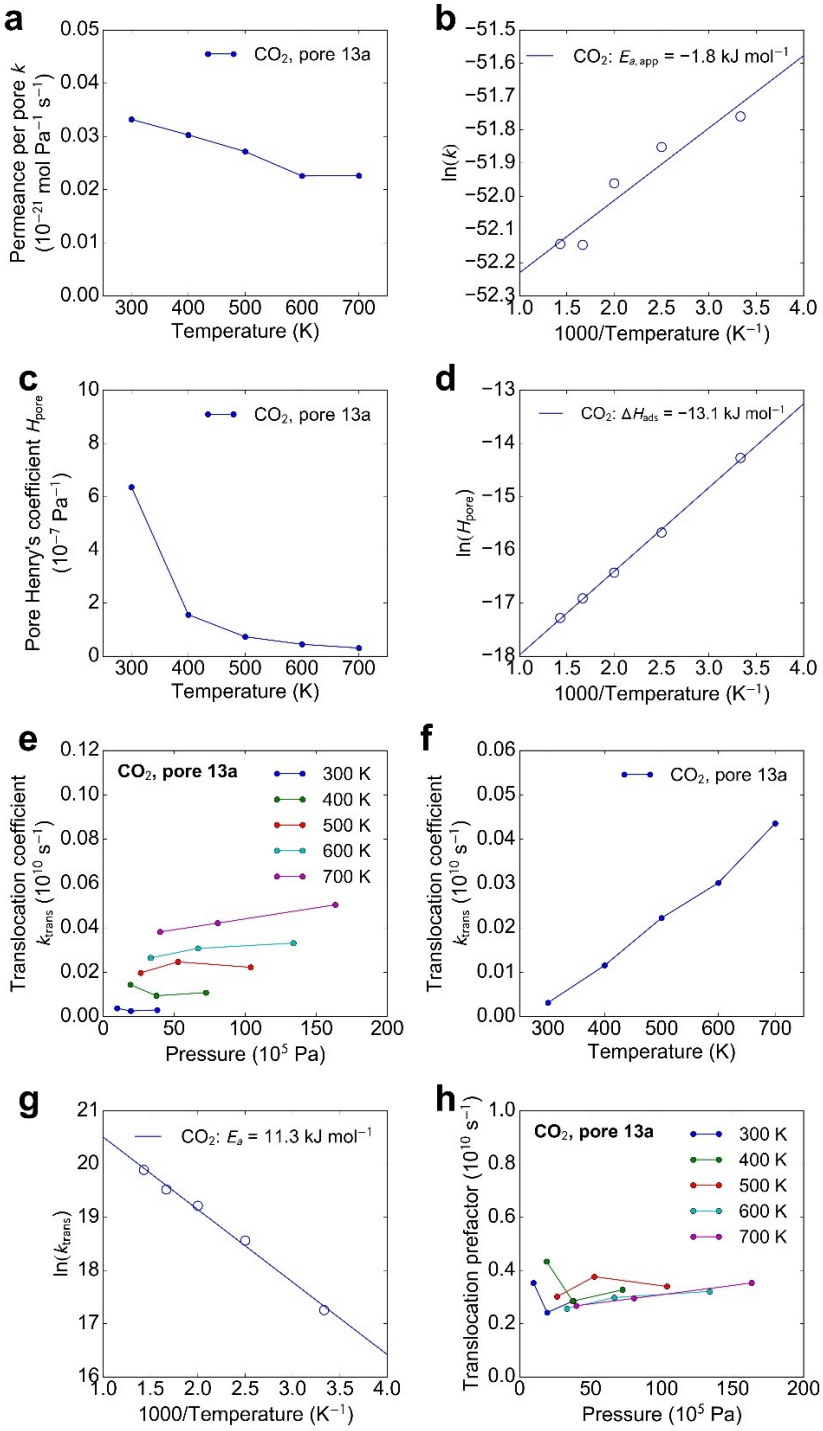

Figure 2-14. (a) Simulated permeances per pore of CO_2 through pore 13a at various temperatures, and (b) related Arrhenius fitting results. (c) Pore Henry's coefficients of CO_2 above pore 13a at various temperatures, and (d) related fitting results for heat of adsorption. (e) Translocation coefficient of CO_2 through pore 13a calculated at various temperatures and pressures. (f) Temperature dependence of the translocation coefficient, and (g) related Arrhenius fitting results for the energy barrier. (h) The translocation prefactors of CO_2 through pore 13a.

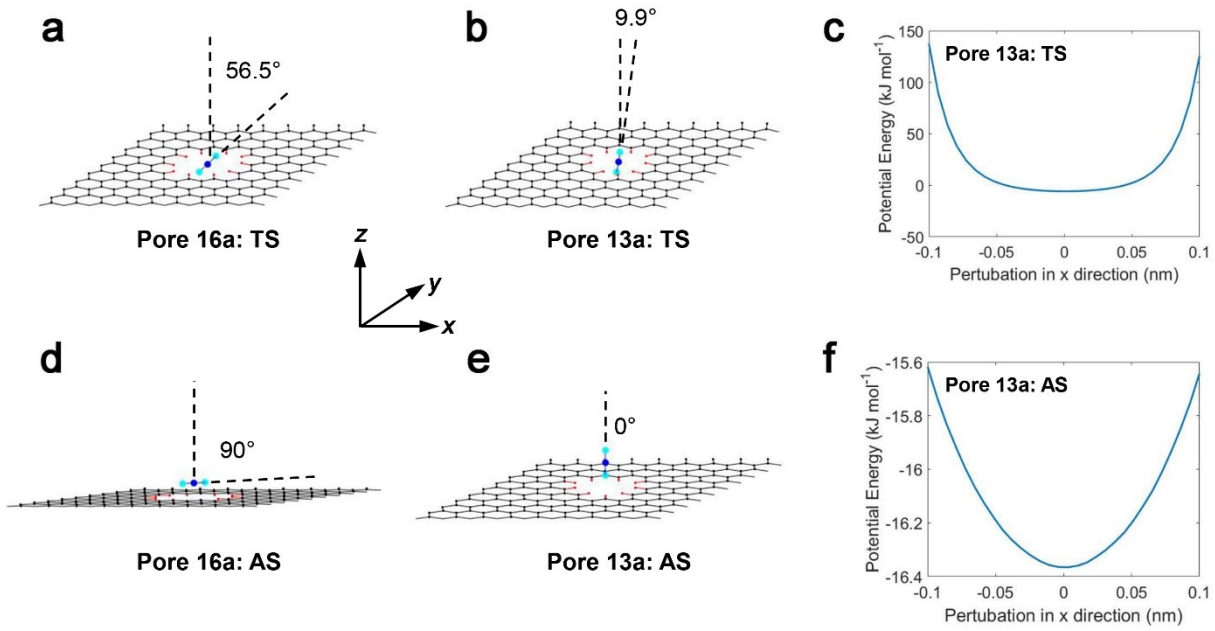

Figure 2-15. Geometric arrangement of CO2 at the transition state (TS) of (a) pore 16a and (b) pore 13a. Potential energy landscape of CO_2 in the *x* direction at the TS inside pore 13a. Geometric arrangement of CO_2 at the adsorbed state (AS) of (d) pore 16a and (e) pore 13a. Potential energy landscape of CO_2 in the *x* direction at the AS above pore 13a. Color code: black – carbon in graphene, red – hydrogen in graphene, blue – carbon in CO_2, cyan – oxygen in CO_2.

Figure 2-16 shows simulation results and related analyses of CO_2 and CH_4 through pore 16a in a flexible graphene membrane. The analytical method used is the same as introduced previously. The heats of adsorption do not change significantly upon the addition of flexibility.

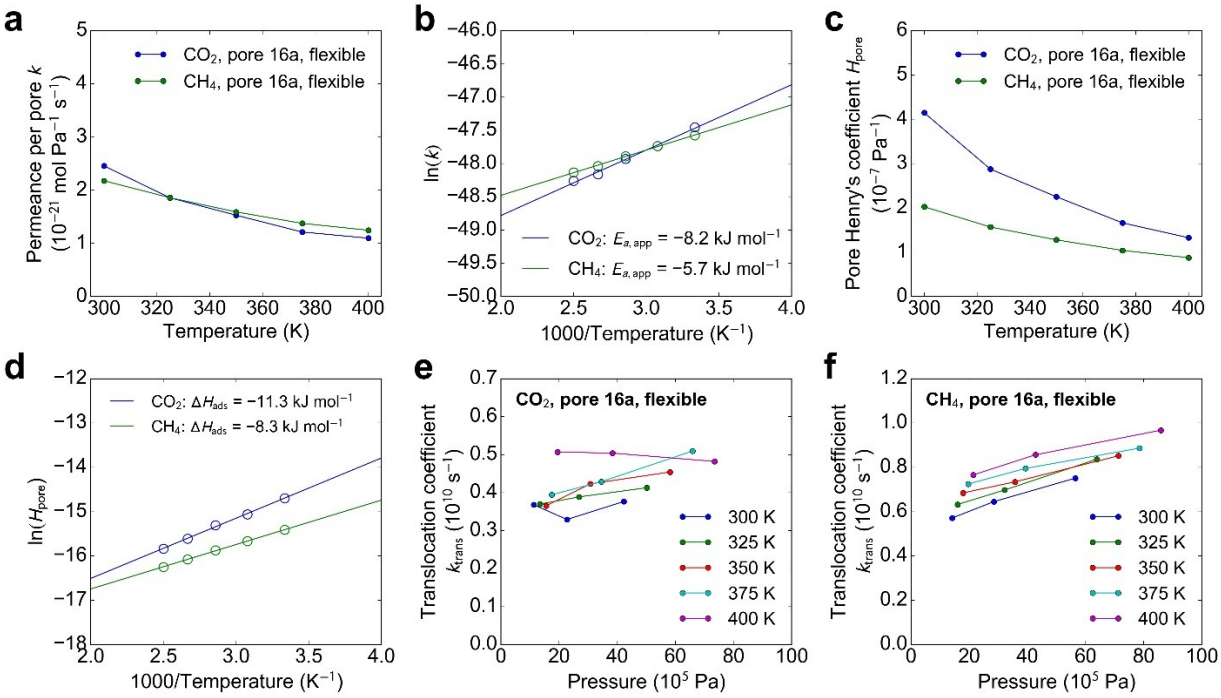

Figure 2-16. (a) Simulated permeances per pore of CO_2 and CH_4 through flexible pore 16a at various temperatures, and (b) related Arrhenius fitting results. (c) Pore Henry's coefficients of CO_2 and CH_4 above flexible pore 16a at various temperatures, and (d) related fitting results for heat of adsorption. Translocation coefficient of (e) CO_2 and (f) CH_4 through flexible pore 16a calculated at various temperatures and pressures.

2.9.4 Free Energy Curves and Related Analyses

Figure 2-17 shows the free energy curve and the potential energy curve of H_2 through pore 16a. No potential energy barrier exists for H_2 to cross pore 16a. However, a free energy barrier exists due to the entropic effect.

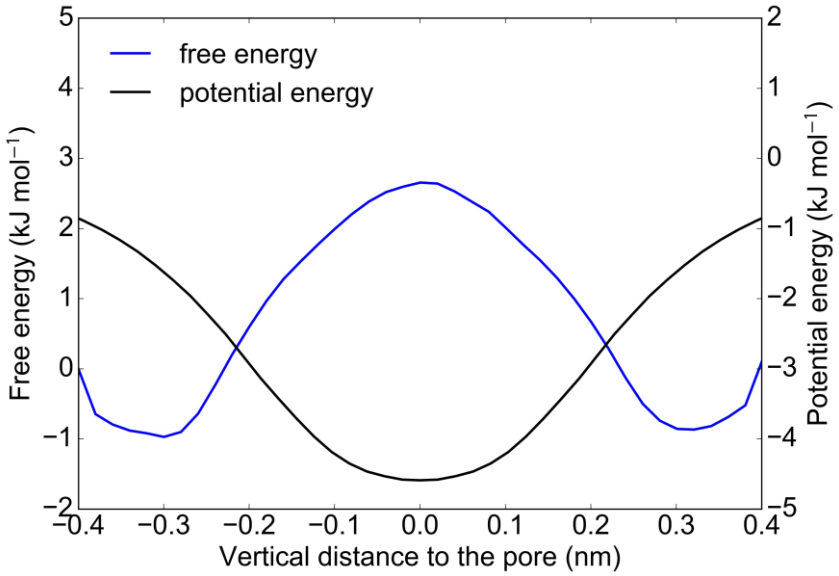

Figure 2-17. Free energy curve (left axis) at 300 K and potential energy curve (right axis) along the translocation trajectories of H_2 through pore 16a. Force field adapted from Bouanich.[179]

Figure 2-18 shows the linear fitting results of the free energy barrier ΔA vs. temperature T for various gas molecules through pore 10a, 13a, and 22. The results exhibit good linearity, suggesting that the entropic contribution to the free energy barrier is independent of temperature.

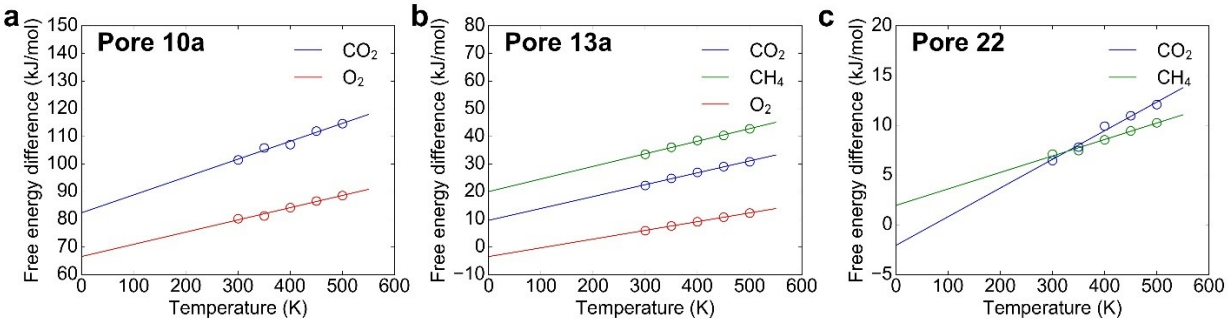

Figure 2-18. Linear fitting of free energy differences to temperature of (a) pore 10a, (b) pore 13a, and (c) pore 22.

2.9.5 Pore Library

Figure 2-19 shows the atomic structures of the pores studied in this chapter.

Figure 2-19. Atomic Structures of the hydrogen-terminated pores investigated. The pore size ranges from 13 to 24. Black dots represent carbon atoms, and red dots represent hydrogen atoms.

2.9.6 Power Law Fitting of Entropy Penalty to Pore Size

Figure 2-20 shows the linear fitting results relating the entropy penalties ΔS to the pore size based on power law estimations. The depicted error ranges are listed in Table 2-3.

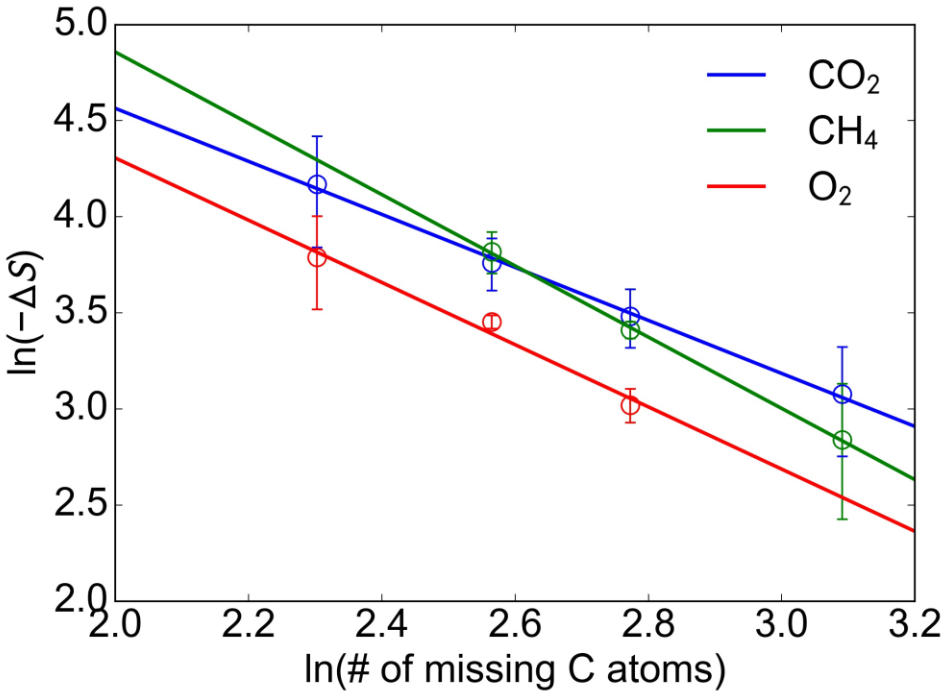

Figure 2-20. Linear fitting results of $\ln(-\Delta S)$ vs. $\ln(\text{number of missing C atoms})$ for CO_2, CH_4, and O_2.

2.9.7 Justification of Translocation-Limited Transport

When the pore size increases, the rate of translocation rapidly increases. At a certain pore size, the translocation step is no longer rate-limiting. To be more precise, when the pore size is sufficiently large, gas molecules at the pore mouth translocate through the pore so fast that the bulk gas phase and the surface adsorption layer cannot supply gas molecules sufficiently fast. In other words, the assumption of equilibrium between the pore mouth adsorbate and the other phases (bulk gas and surface adsorbate) is no longer valid. As a result, the number of pore-associated gas molecules should be smaller than its equilibrium value. Beyond this critical pore size, the pore Henry's coefficient no longer controls the total gas flow.

This critical pore size, D_c, depends on the gas. For example, in the case of CO_2, by equating the maximum translocation rate ($\Delta E = 0, \Delta S = 0$) to the impingement rate from bulk gas given by the kinetic theory of gases ($\dot{n}_{\mathrm{dir}} = A_{\mathrm{pore}} \frac{\Delta p}{\sqrt{2\pi MRT}}$, where A_{pore} is the area of the pore, Δp is the pressure difference, M is the gas molar weight, R is the gas constant, and T is the absolute temperature), a critical pore diameter is found to be D_c = 3.8 nm, corresponding to the removal of ~400 carbon atoms, which is significantly larger than the pores investigated in this chapter (13 to 24 removed carbon atoms). This means that the translocation-limited transport assumption is valid for the pores studied. Note that because CO_2 is an adsorptive gas, the surface influx may be greater than the direct influx for a small pore diameter, thereby decreasing the critical pore size.

2.9.8 CO_2/CH_4 Mixture Separation

MD simulation results of CO_2/CH_4 mixture separation through pore 16a are shown in Figure 2-21 and Table 2-5. The analytical method used is the same as that described in the main text. The permeation behavior of a gas component does not change significantly when it is moved from a pure feed phase to a mixed feed phase. The energy barriers remain unchanged, suggesting that the permeation of gas through a sub-nanometer pore is a single-molecule event. The heat of adsorption of CO_2 changes slightly, which may be attributed to the CO_2–CH_4 interactions.

Table 2-5. Apparent energy barrier, heat of adsorption, energy barrier, and translocation prefactor derived from temperature fitting of the MD results for CO_2 and CH_4–pore 16a in mixed and pure inlets.

Gas	Apparent energy barrier (kJ mol^{-1})	Heat of adsorption (kJ mol^{-1})	Energy barrier (kJ mol^{-1})	Translocation prefactor (10^{10} s^{-1})
CO_2 in mixture	-6.0 ± 0.9	-9.8 ± 1.8	3.8 ± 1.2	0.89 ± 0.11
Pure CO_2	-7.2 ± 1.2	-11.1 ± 0.8	3.9 ± 0.6	0.81 ± 0.08
CH_4 in mixture	-4.3 ± 1.4	-7.7 ± 1.5	3.3 ± 1.6	1.36 ± 0.24
Pure CH_4	-4.7 ± 0.6	-8.0 ± 0.9	3.3 ± 1.3	1.06 ± 0.15

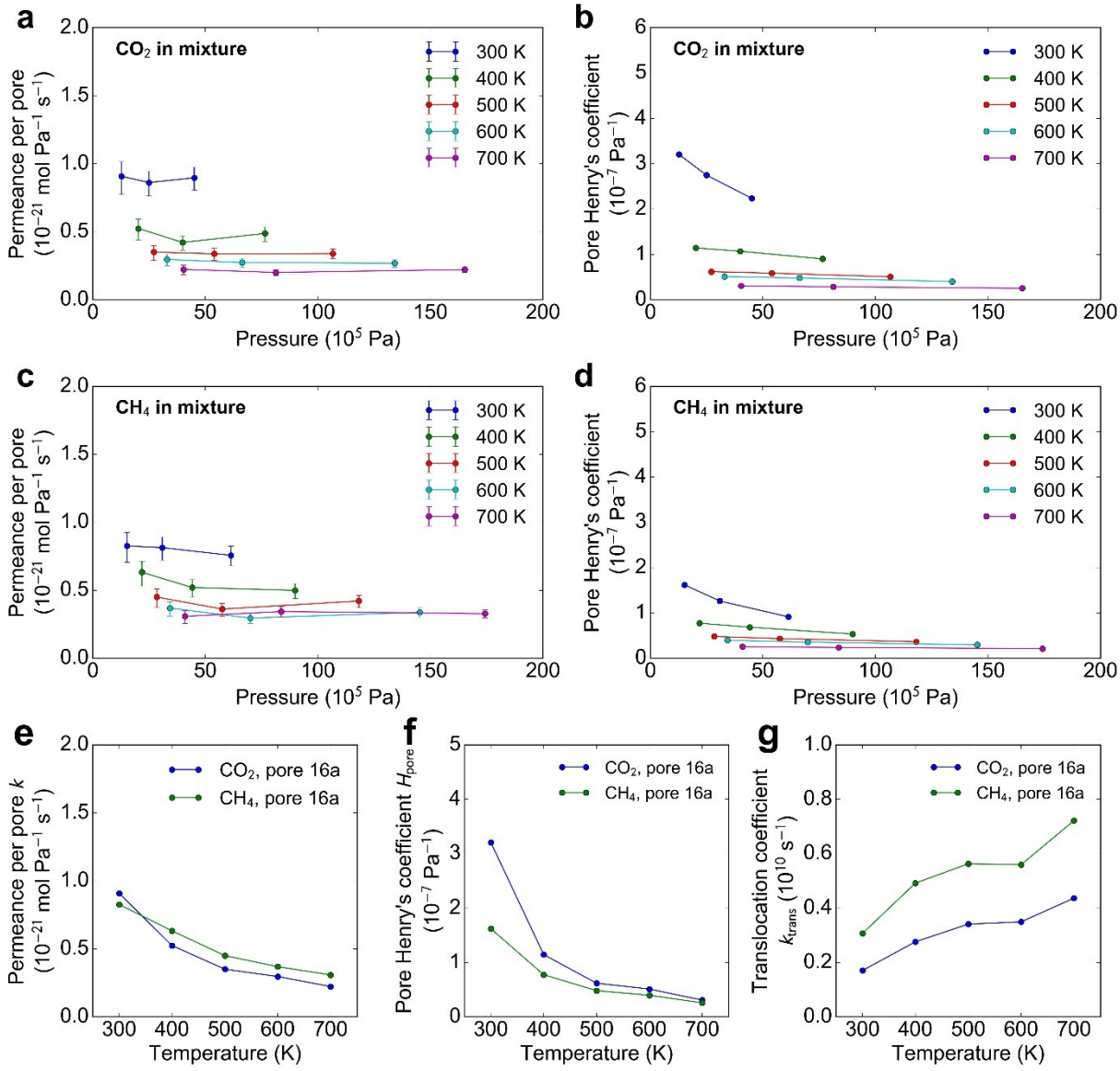

Figure 2-21. Simulated permeances per pore of (a) CO_2 and (c) CH_4 through pore 16a in an equimolar CO_2/CH_4 mixture. Pore Henry's coefficients of (b) CO_2 and (d) CH_4 above pore 16a in the mixture. (e) Simulated permeances per pore, (f) pore Henry's coefficients, and (g) translocation coefficients through and above pore 16a as functions of temperature.

2.9.9 Previously Reported Membrane Performance for CO_2/CH_4 Separation

Table 2-6. Data from the literature on various membranes in the separation of CO_2/CH_4 mixture.

Material	CO_2 Permeance (mol m^{-2} s^{-1} Pa^{-1})	Separation Factor	Reference
Zeolites	2.9×10^{-7}	420	[14]
	2.0×10^{-6}	86	[142]
	7.0×10^{-8}	600	[13]
	2.0×10^{-7}	32	[180]
Carbon molecular sieves (CMS)	4.3×10^{-9}	83	[181]
	2.1×10^{-9}	21	[182]
Silica	6.0×10^{-8}	4.5	[183]
	8.1×10^{-8}	11	[184]
	6.7×10^{-8}	240	[185]
	5.8×10^{-8}	380	[186]
Thermally rearranged (TR) polymer	6.8×10^{-8}	64	[141]
	2.2×10^{-8}	45	[141]
	2.8×10^{-8}	35	[141]
Polymer	5.7×10^{-10}	27	[187]
	4.2×10^{-10}	18	[188]
	4.0×10^{-9}	28	[189]
	1.0×10^{-9}	93	[190]
	1.1×10^{-8}	15	[191]
2D polymer (simulation)	1.0×10^{-4}	500	[73]
Mixed matrix membranes	4.4×10^{-9}	36	[21]
	6.8×10^{-9}	15	[192]
Ionic	7.7×10^{-9}	55	[193]
	1.7×10^{-9}	5.7	[194]
	1.9×10^{-9}	10	[195]
Metal organic frameworks (MOF)	2.4×10^{-5}	5.1	[143]
	1.0×10^{-7}	4.6	[196]
	1.2×10^{-6}	2.5	[16]
	3.1×10^{-6}	3.8	[15]
	2.0×10^{-6}	12.6	[197]
	3.5×10^{-8}	3.5	[198]
	1.3×10^{-8}	4.7	[199]
MOF (simulation)	1.8×10^{-5}	4.1	[166]
Assume thickness = 100 nm	4.0×10^{-5}	2.2	[166]

2.9.10 Justification of the Escape Time Method

In Figure 2-22, the instantaneous, cumulative average, and overall average values of the bulk gas density, pore-associated gas number, and areal density of surface-adsorbed gas from 0 to 5 ns in the simulation are depicted. The system equilibrates within 5 ns, which is short compared to the overall simulation time (~450 ns). Therefore, the equilibration period has negligible effect on the simulation results.

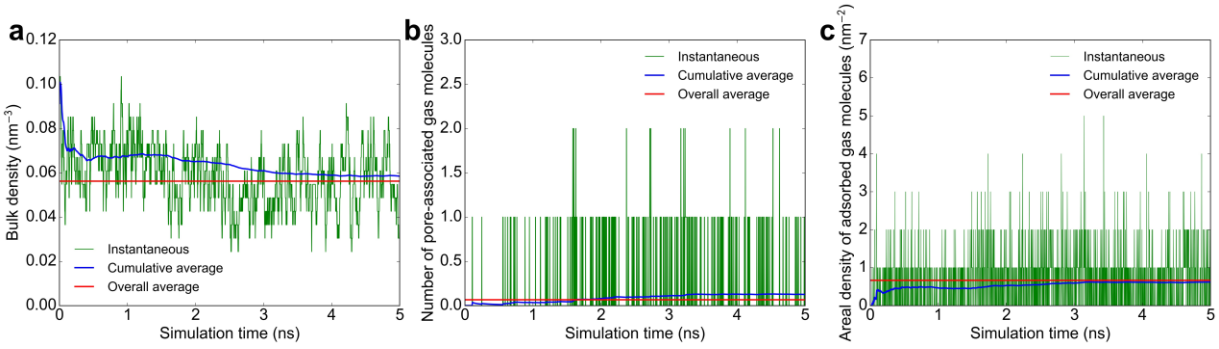

Figure 2-22. The instantaneous, cumulative average and overall average values of (a) bulk gas density, (b) pore-associated gas number, and (c) areal density of surface-adsorbed gas from 0 to 5 ns in the simulation. The simulated gas is CO_2. The temperature is 300 K and the bulk pressure is 2.3 bar. The cumulative average is the average value of all the previous data points. The overall average is taken over a ~450 ns period. The equilibration time is below 5 ns, and therefore, the initial equilibration process does not affect the overall result.

The histogram of escape times of CO_2 through pore 16a is shown in Figure 2-23a. Figure 2-23b further validates the exponential distribution of the escape time by taking the natural logarithm of the probability distribution and fitting it to a linear variation with respect to time.

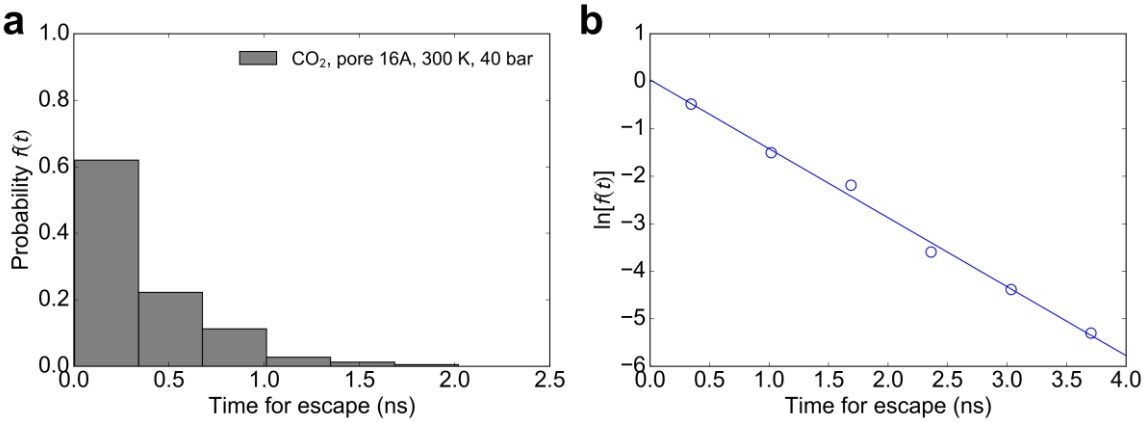

Figure 2-23. (a) The probability distribution $f(t)$ of the escape times of CO_2 crossing pore 16a at 300 K and 40 bar. (b) The linear relation between ln[$f(t)$] and the escape time t, proving the exponential distribution.

2.9.11 Justification of the Free Energy Calculation

The histograms for CO_2 through pore 16a at 300 K at every biasing point are shown in Figure 2-24. The significant overlap between adjacent histograms guarantees a reliable free energy curve.

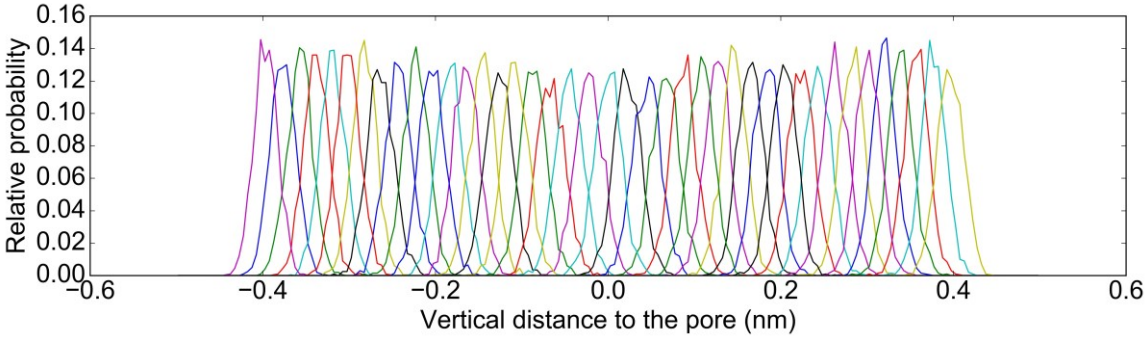

Figure 2-24. Histograms at each biasing point for CO_2 through pore 16a at 300 K. Adjacent histograms have significant overlap.

Figure 2-25 shows the free energy differences of CO_2 through pore 16a with or without the presence of other CO_2 molecules in the simulation box at various temperatures. The interactions between a gas molecule and the pore are not affected by other molecules.

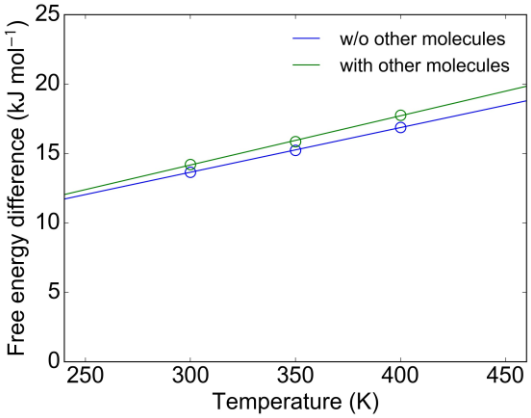

Figure 2-25. Free energy differences of CO_2 through pore 16a with or without the presence of other CO_2 molecules in the simulation box at various temperatures. Despite the presence of the other 99 CO_2 molecules, the free energy differences do not change significantly.

3 Mechanism of Gas Permeation through Graphene Nanopores across Multiple Regimes

3.1 Introduction

The atomic thickness of graphene endows it with tremendous potential for membrane separation.[200,201] For conventional polymeric membranes, the cross-membrane transport resistance is proportional to the membrane thickness, limiting their trans-membrane gas flux.[25] In contrast, nanoporous graphene membranes are anticipated to have extremely small molecular transport resistances and high fluxes.[25,140] The concept of membrane separation using nanoporous graphene has been demonstrated for diverse applications, such as, gas separation,[113,126] seawater desalination,[133,202] nanofiltration,[149,203] and ion separation.[131,204]

The application of permselective membranes, *i.e.*, membranes demonstrating high selectivities for gas separation processes, is currently underdeveloped, with several challenges remaining to be surmounted.[1,5,139] For conventional polymeric membranes, the permeability and selectivity of a given gas pair demonstrate a trade-off relationship, referred to as the Robeson upper bound.[11] This upper bound limits the overall applicability of polymeric membranes for gas separation applications. Graphene, however, has the potential to surpass the upper bound limit due to its atomic thickness and much reduced gas transport resistance.[49] In addition, the gas permeance (defined as the gas flux normalized by the driving force, *i.e.*, the pressure drop) of a nanoporous graphene membrane is linearly correlated to the areal pore density of the membrane, further boosting its potential performance, as discussed in Section 2.6.

In order to achieve high selectivity for gas separation, the graphene pore diameter (D_p) should be commensurate with the collision diameter, also known as the kinetic diameter (D_m) of the gas molecules, which is typically around a few Angstroms.[6] Graphene nanopores have been experimentally created using various strategies, and the gas separation performances of the resulting nanopores have been tested in several experimental studies. Koenig *et al*. used ultraviolet-induced oxidative etching to

introduce nanopores in pristine graphene.[109] A smaller nanopore (3.4 Å in diameter) exhibited pressure-normalized H_2 and CO_2 flow rates of ~ 10^{23} mol s^{-1} Pa^{-1}, but the flow rates of Ar, N_2, and CH_4 were 3–4 orders of magnitude lower. A larger nanopore (4.9 Å in diameter) exhibited higher flow rates but lower separation factors among H_2, CO_2, N_2, and CH_4, while rejecting SF_6. Boutilier *et al*. created graphene nanopores with diameters below 7 Å using ion bombardment followed by oxygen plasma treatment.[115] With an appropriate amount of oxygen plasma exposure, the nanoporous graphene membrane demonstrated a gas selectivity that surpassed the Knudsen effusion selectivity, suggesting a contribution of molecular sieving resulting from nanometer-sized pores. The Knudsen effusion is also known as Graham's Law of effusion, where the rate of effusion of a gas is inversely proportional to the square root of its molecular mass.[42] I (see Chapter 5) and Huang *et al*.[120] observed gas separation beyond the Knudsen selectivity limit through graphene nanopores formed spontaneously during the chemical vapor deposition (CVD) of single-layer graphene, with pore diameters ranging from ~ 1 to 2.5 nm.

These experimental datasets[109,115,120] span wide ranges of gas flow rates and separation factors, as well as of graphene nanopore diameters, and are likely to be governed by different gas permeation mechanisms.[152] In theory, given complete knowledge of the gas permeation mechanism, it should be possible to analytically model the mathematical relation between the gas flow rate, the pore size (and shape), and the properties of the gas species, including the molecular weight and the kinetic diameter. Such a model could then be used to fit the experimentally measured gas flow rates to predict the pore size distribution, or at least a representative pore structure. Wang *et al*. proposed two gas transport regimes, the activated regime and the steric regime, determined by the relative magnitudes of the pore diameter D_p and the gas kinetic diameter D_m.[26] Specifically, in the activated regime, D_p is smaller than, or approximately equal to D_m, and the gas molecule needs to overcome an energy barrier imposed by the pore rim atoms. Previous studies have utilized *ab initio* simulations to estimate the energy barrier for a gas molecule to translocate through graphene membranes.[25,66,95] In Chapter 2, I investigated in detail gas permeation in the activated regime using molecular dynamics (MD) simulations, and have shown that the rate of barrier crossing can be described accurately using transition state theory.

On the other hand, when the pore size D_p is larger than the gas kinetic diameter D_m, the energy barrier decreases and the gas permeation is non-activated. Wang *et al*. designated this regime as "the

steric regime" exhibiting an effusion-like mechanism.[26] Gas effusion through a pore occurs when the pore size is smaller than the gas mean free path, and the effusion rate of the gas depends on its rate of direct impingement from the bulk.[113] However, various studies have demonstrated the significance of another pathway: surface diffusion.[46–48,152] The carbon atoms in graphene exert attractive van der Waals forces on the gas molecules, which in turn, get adsorbed on the graphene surface, thereby forming an adsorption layer. The adsorbed gas molecules then diffuse to the pore region and subsequently permeate to the other side of the membrane. This surface diffusion pathway occurs simultaneously with the direct impingement pathway, and can be important, or even dominant, when the local density of gas molecules adsorbed on the graphene basal plane is high.[47]

Despite the research efforts mentioned above, a comprehensive mechanism that unifies the different gas transport regimes has not yet been advanced. More specifically, the following challenges remain. First, the direct impingement pathway, the surface diffusion pathway, and the activated permeation have not been integrated into a general analytical equation. Second, the governing equations of the direct impingement and surface diffusion pathways, although recognized, have not been refined and validated using simulation tools. With the above two points in mind, in this chapter, I propose to formulate a model that incorporates all the different transport regimes, including deriving a general analytical expression to predict the gas permeance through different sizes of graphene nanopores based on the model. In addition, I utilize MD simulations to refine the expression derived from the model, and discuss the origins of these refinements. Based on the model, I study the contributions, from the direct impingement and the surface diffusion pathways in quantitative detail, and analytically model the transition between different transport regimes. Furthermore, I predict the graphene nanopore size limit that is required to achieve meaningful gas separation performances.

3.2 Theoretical Model

Based on the modeling study by Drahushuk and Strano,[152] the gas permeation process is described by a three-state reaction kinetics model (Figure 3-1). The three states which a gas molecule can occupy include (1) the bulk gas state, characterized by the bulk pressure p, (2) the surface adsorption state, characterized by the areal number density of adsorbed gas molecules C_{surf}, and (3) the pore mouth state,

characterized by the number of gas molecules at the pore mouth N_{pore}. The height of the adsorption layer is a parameter in my model that can be determined using MD simulations, which will be discussed in the next section. The pore mouth state is defined as the cylinder depicted in red in Figure 3-1, which has the pore area as its base and the same height as the adsorption layer.

The transport rates to, or from, the three states can be modeled as first order reactions (Figure 3-1b). The first order assumption is based on the linear dependence of the rate of diffusion on the concentration gradient (Fick's first law). Because the bulk state and the adsorption state have a large area of contact, the molecular exchange between the two states is rapid. Therefore, the bulk pressure p and the adsorbed areal density C_{surf} can be assumed to be in equilibrium:

$$C_{\text{surf}} = H_{\text{surf}} \cdot p \tag{3-1}$$

where H_{surf} is the equilibrium constant and is referred to hereafter as the surface Henry's coefficient, because the equilibrium between the bulk gas and the adsorbed phase resembles Henry's law.[41] The surface Henry's coefficient H_{surf} is constant if the linear adsorption isotherm in Equation (3-1) holds. In the case of other adsorption isotherms, such as, the Langmuir isotherm or the Brunauer–Emmett–Teller isotherm,[161] H_{surf} depends on the bulk pressure. In this chapter, the bulk pressure is lower than 15 bar, and therefore, the surface adsorption occupancy is low (Appendix 2.9.10). As a result, the adsorption isotherms of the gases studied here are in the linear regime (Figure 3-9 in Appendix 3.10.1).

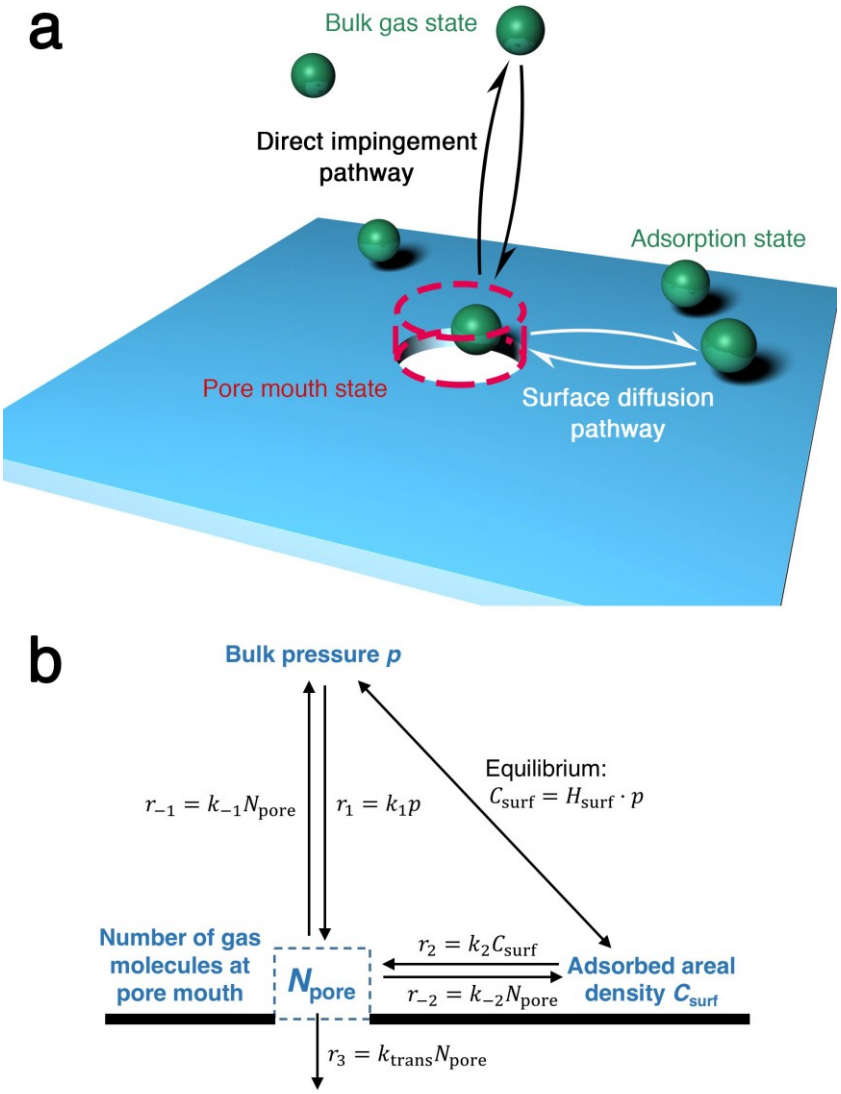

Figure 3-1. (a) Schematic illustration of the three-state gas permeation model, and (b) its transport rates. The symbols utilized are explained in the main text.

The total gas permeation rate, or the rate of translocation, r_3 is the product of N_{pore} and the translocation coefficient k_{trans} (Figure 3-1b, $r_3 = k_{trans}N_{pore}$, Equation (2-1)). The translocation coefficient k_{trans} can be predicted using an algorithm based on the transition state theory developed in Chapter 2. I predict that k_{trans} is proportional to $\exp(-E_a/k_B T)$, where E_a is the energy barrier of translocation through the nanopore, k_B is the Boltzmann constant, and T is the absolute temperature. Note that in the current model, I assume that the permeate side is vacuum, so that only the feed side pressure needs to be considered. Note also that if the permeate side has a finite pressure, the back-permeance from the permeate side to the feed side can also be treated using the same model.[46]

To fully determine the gas permeation rate r_3, the rate constants k_1, k_{-1}, k_2, and k_{-2} in Figure 3-1 need to be specified. The forward rate constant k_1 from the bulk to the pore mouth can be predicted using the kinetic theory of gases. According to the kinetic theory of gases, the impingement rate, r_1, of an ideal gas onto the pore area is expressed as follows:[41]

$$r_1 = A_{\text{pore}}\rho\sqrt{\frac{k_{\text{B}}T}{2\pi m}} \tag{3-2}$$

where A_{pore} is the pore area, m is the gas molecular weight, and ρ is the volumetric number density of the bulk gas. In the ideal gas limit, $p = \rho k_B T$. Otherwise, to model a non-ideal gas, the compressibility factor Z needs to be included: $p = Z\rho k_B T$.[41] Continuing with a non-ideal gas and considering a circular pore with diameter D_{p}, the forward rate constant k_1 can be derived based on Equation (3-2), $p = Z\rho k_B T$, and $A_{\text{pore}} = \pi D_{\text{p}}^2/4$:

$$k_1 = \frac{r_1}{p} = \frac{A_{\text{pore}}\rho}{Z\rho k_{\text{B}}T}\sqrt{\frac{k_{\text{B}}T}{2\pi m}} = \frac{A_{\text{pore}}}{Z\sqrt{2\pi m k_{\text{B}}T}} = \sqrt{\frac{\pi}{2mk_{\text{B}}T}}\frac{D_{\text{p}}^2}{4Z} \tag{3-3}$$

The expression for the backward rate from the pore mouth to the bulk can be derived as follows. For an elementary reaction, the equilibrium constant is equal to the forward rate constant divided by the reverse rate constant. Therefore, $N_{\text{pore}}^{\text{eqm}}/p = k_1/k_{-1}$, where $N_{\text{pore}}^{\text{eqm}}$ is the number of gas molecules at the pore mouth under the equilibrium condition (Section 2.2). Pore Henry's coefficient $H_{\text{pore}} = N_{\text{pore}}^{\text{eqm}}/p$ is defined as the equilibrium constant. Following this, the backward rate constant k_{-1} can be derived based on Equation (3-3):

$$k_{-1} = k_1\frac{p}{N_{\text{pore}}^{\text{eqm}}} = \frac{k_1}{H_{\text{pore}}} = \sqrt{\frac{\pi}{2mk_{\text{B}}T}}\frac{D_{\text{p}}^2}{4H_{\text{pore}}Z} \tag{3-4}$$

Regarding the surface diffusion pathway, Drahushuk and Strano proposed an estimation where the rate of injection from the adsorption layer to the pore r_2 has a similar expression as that in Equation (3-2), except that it is proportional to the circumference of the pore, instead of to the pore area, that is:[152]

$$r_2 \propto D_{\text{p}} \tag{3-5}$$

In fact, the logic behind the kinetic theory of gases in three-dimensions (3D) can be applied to a two-dimensional (2D) gas system, if the adsorbed gas molecules are simplified as a two-dimensional gas. This simplification is based on the following assumptions: (1) the adsorbed gas molecules have relatively long residence times on the graphene sheet, (2) the adsorbed gas molecules follow the Maxwell-Boltzmann velocity distribution, and (3) the adsorbed gas molecules are evenly distributed on the graphene sheet, excluding the pore mouth area, where the concentration of the gas molecules is lower, leading to surface diffusion of the gas molecules towards the pore mouth area.

Assumption (1) is supported by the simulation study of Sun and Bai,[205] who found that the in-plane diffusion coefficient of the adsorbed gas molecules is lower than that of the gas molecules in the bulk, due to the gas molecule-graphene interactions. Assumption (2) can be directly confirmed by the Maxwell-Boltzmann velocity distribution of the adsorbed gas molecules observed in the MD simulations (Figure 3-10 in Appendix 3.10.2). Assumption (3) will, in fact, be violated due to the existence of the pore, which complicates the problem. For the sake of simplicity, as a first approximation, I assume that the gases adsorbed on the graphene layer are evenly distributed. However, a more detailed analysis of this underlying assumption will be presented in the next section. Assuming a 2D-gas model for the adsorbed layer, one can neglect the movement of gas molecules in the direction normal to the graphene plane (denoted hereafter as the *z* direction), and only need to consider the movement of gas molecules parallel to the graphene sheet (denoted hereafter as the *x*-*y* plane).

As shown in Figure 3-2a, consider a differential length dL along the circumference of the pore in the *x*-*y* plane. Define the direction tangential to dL as *x*, and the direction normal to dL as *y*. According to the Maxwell-Boltzmann distribution, in an orthogonal coordinate system, the velocities of each gas molecule in the *x* and *y* directions, v_x and v_y, follow a Gaussian distribution and are independent of each other,[41] that is,

$$f_{v_i}(v_i) = \sqrt{\frac{m}{2\pi k_B T}} \exp\left(-\frac{m v_i^2}{2 k_B T}\right) \tag{3-6}$$

where $f_{v_i}(v_i)$ is the probability density function of v_i, and i corresponds to either the x or the y directions. Using MD simulations, it is found that the correlation coefficient of v_x and v_y in the adsorption layer is 0.003, indicating independent velocity distributions in the x and y directions (Appendix 3.10.2).

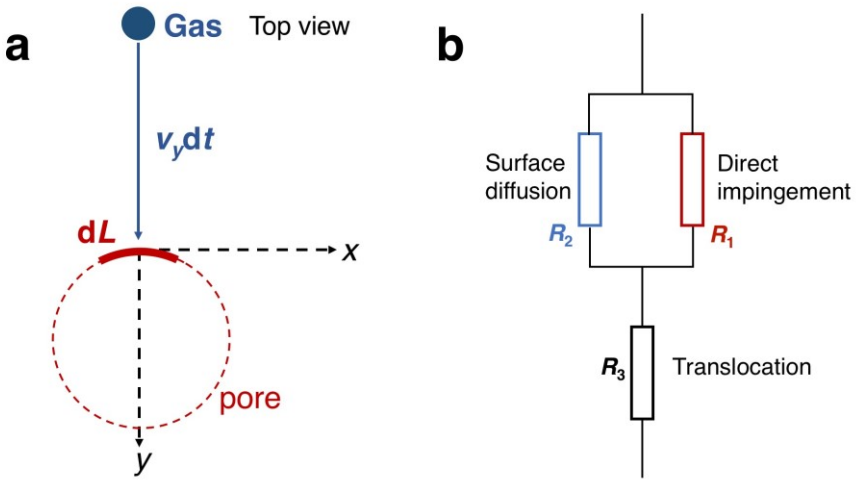

Figure 3-2. (a) Derivation of the rate of injection from the adsorption layer to the pore. Injection is an essential step in the surface diffusion pathway. (b) Transport resistances associated with the translocation, the surface diffusion, and the direct impingement steps are represented in an analogous electric circuit form.

Note that because the velocities v_x and v_y are independent, only v_y matters when considering gas molecules crossing dL in the +y direction (Figure 3-2a). For a gas molecule with $v_y > 0$, it can cross dL within a differential time interval dt if the y-projection of its distance to dL is less than v_ydt. In other words, only the molecules in the area $v_y \mathrm{d}t\mathrm{d}L$ are available to be transported across dL. Given the areal density of gas molecules, C_{surf}, the differential number of gas molecules $\mathrm{d}^2 n_2$ crossing dL in the +y direction during the time interval dt can be integrated from $v_y = 0$ to $+\infty$:

$$\mathrm{d}^2 n_2 = \int_0^{+\infty} \left[(v_y \mathrm{d}t) C_{\mathrm{surf}} \mathrm{d}L f_{v_y}(v_y) \right] \mathrm{d}v_y = \sqrt{\frac{k_\mathrm{B}T}{2\pi m}} C_{\mathrm{surf}} \, \mathrm{d}t \, \mathrm{d}L \tag{3-7}$$

Note that the second differential $\mathrm{d}^2 n_2$ is used because the orders of the differential on both sides of Equation (3-7) need to match. According to Equation (3-7), the rate of surface inward diffusion dr_2 across the differential length dL can be expressed as follows ($r_2 = \mathrm{d}n_2/\mathrm{d}t$):

$$\mathrm{d}r_2 = \mathrm{d}\left(\frac{\mathrm{d}n_2}{\mathrm{d}t}\right) = \sqrt{\frac{k_\mathrm{B}T}{2\pi m}} C_{\mathrm{surf}} \, \mathrm{d}L \tag{3-8}$$

Equation (3-8) is valid for any differential length dL along the pore rim. Therefore, by integrating dr_2 over the circumference of the pore $L = \pi D_p$, it is derived that:

$$r_2 = \oint_L \mathrm{d}r_2 = \oint_L \sqrt{\frac{k_\mathrm{B}T}{2\pi m}} C_\mathrm{surf}\,\mathrm{d}L = \sqrt{\frac{k_\mathrm{B}T}{2\pi m}} C_\mathrm{surf} L = \sqrt{\frac{\pi k_\mathrm{B}T}{2m}} C_\mathrm{surf} D_\mathrm{p} \tag{3-9}$$

Equation (3-9) is consistent with Equation (3-5). Accordingly, the forward rate constant associated with the surface diffusion pathway k_2 is therefore given by:

$$k_2 = \frac{r_2}{C_\mathrm{surf}} = \sqrt{\frac{\pi k_\mathrm{B}T}{2m}} D_\mathrm{p} \tag{3-10}$$

The backward rate constant k_{-2} from the pore to the adsorption layer can be derived in a manner similar to that used to derive k_{-1} in the direct impingement pathway. The equilibrium constant between the surface adsorption state (areal adsorption density C_surf) and the pore mouth state (pore mouth molecular number N_pore) is equal to the forward rate constant k_2 divided by the reverse rate constant k_{-2}. Therefore, $N_\mathrm{pore}^\mathrm{eqm}/C_\mathrm{surf} = k_2/k_{-2}$, where $N_\mathrm{pore}^\mathrm{eqm}$ is the number of gas molecules at the pore mouth under the equilibrium condition. Recall the surface Henry's coefficient $H_\mathrm{surf} = C_\mathrm{surf}/p$ (Equation (3-1)) and the pore Henry's coefficient $H_\mathrm{pore} = N_\mathrm{pore}^\mathrm{eqm}/p$. Therefore, the backward rate constant k_{-2} can be derived as follows:

$$k_{-2} = k_2 \frac{C_\mathrm{surf}}{N_\mathrm{pore}^\mathrm{eqm}} = k_2 \frac{C_\mathrm{surf}/p}{N_\mathrm{pore}^\mathrm{eqm}/p} = k_2 \frac{H_\mathrm{surf}}{H_\mathrm{pore}} = \sqrt{\frac{\pi k_\mathrm{B}T}{2m}} \frac{H_\mathrm{surf}}{H_\mathrm{pore}} D_\mathrm{p} \tag{3-11}$$

Knowing the rate constants k_1, k_{-1}, k_2, and k_{-2}, the overall gas permeation rate can be derived as follows. At steady state, the number of gas molecules at the pore mouth should be time invariant:

$$\frac{\mathrm{d}N_\mathrm{pore}}{\mathrm{d}t} = r_1 - r_{-1} + r_2 - r_{-2} - r_3 = 0 \tag{3-12}$$

where

$$r_1 = k_1 p = \sqrt{\frac{\pi}{2mk_\mathrm{B}T}} \frac{D_\mathrm{p}^2}{4Z} p \tag{3-12a}$$

$$r_{-1} = k_{-1} N_\mathrm{pore} = \sqrt{\frac{\pi}{2mk_\mathrm{B}T}} \frac{D_\mathrm{p}^2}{4H_\mathrm{pore}Z} N_\mathrm{pore} \tag{3-12b}$$

$$r_2 = k_2 C_{\text{surf}} = k_2 H_{\text{surf}} p = \sqrt{\frac{\pi k_{\text{B}} T}{2m}} D_{\text{p}} H_{\text{surf}} p \tag{3-12c}$$

$$r_{-2} = k_{-2} N_{\text{pore}} = \sqrt{\frac{\pi k_{\text{B}} T}{2m}} \frac{H_{\text{surf}}}{H_{\text{pore}}} D_{\text{p}} N_{\text{pore}} \tag{3-12d}$$

$$r_3 = k_{\text{trans}} N_{\text{pore}} \tag{3-12e}$$

Using Equations (3-12a)–(3-12e) in Equation (3-12), it is derived that:

$$k_1 p - k_{-1} N_{\text{pore}} + k_2 H_{\text{surf}} p - k_{-2} N_{\text{pore}} - k_{\text{trans}} N_{\text{pore}} = 0 \tag{3-12f}$$

$$N_{\text{pore}} = p \frac{k_1 + k_2 H_{\text{surf}}}{k_{-1} + k_{-2} + k_{\text{trans}}} \tag{3-12g}$$

Using the relations $k_{-1} = k_1 / H_{\text{pore}}$ (Equation (3-4)) and $k_{-2} = k_2 H_{\text{surf}} / H_{\text{pore}}$ (Equation (3-11)), Equation (3-12g) can be rewritten as follows:

$$\begin{aligned} N_{\text{pore}} &= p \frac{k_1 + k_2 H_{\text{surf}}}{\frac{k_1 + k_2 H_{\text{surf}}}{H_{\text{pore}}} + k_{\text{trans}}} = p \frac{1}{\frac{1}{H_{\text{pore}}} + \frac{k_{\text{trans}}}{k_1 + k_2 H_{\text{surf}}}} \\ &= \frac{1}{\frac{1}{k_1 + k_2 H_{\text{surf}}} + \frac{1}{k_{\text{trans}} H_{\text{pore}}}} \cdot \frac{p}{k_{\text{trans}}} \end{aligned} \tag{3-13}$$

The overall transport resistance R is defined as the ratio between the pressure p and the overall transport rate r_3. Note that R can be interpreted as the inverse of the pressure-normalized flow rate. Using the expression for N_{pore} given in Equation (3-13), it is derived that:

$$R = \frac{p}{r_3} = \frac{p}{k_{\text{trans}} N_{\text{pore}}} = \frac{1}{k_1 + k_2 H_{\text{surf}}} + \frac{1}{k_{\text{trans}} H_{\text{pore}}} \tag{3-14}$$

Note that each term in the denominators of the fractions in Equation (3-14) can be regarded as a transport resistance, corresponding to each transport step, that is,

$$R_1^{-1} = k_1 = \sqrt{\frac{\pi}{2mk_{\text{B}}T}} \frac{D_{\text{p}}^2}{4Z} \tag{3-15}$$

$$R_2^{-1} = k_2 H_{\text{surf}} = \sqrt{\frac{\pi k_{\text{B}} T}{2m}} D_{\text{p}} H_{\text{surf}} \tag{3-16}$$

$$R_3^{-1} = k_{\text{trans}} H_{\text{pore}} \tag{3-17}$$

Based on Equations (3-15)–(3-17), Equation (3-14) can be conveniently rewritten as follows:

$$R = R_3 + \frac{1}{\frac{1}{R_1} + \frac{1}{R_2}} \tag{3-18}$$

Note that R_1, R_2, and R_3 represent the innate kinetics associated with each transport step. Indeed, R_1 is the resistance associated with the direct impingement step, R_2 is the resistance associated with the surface diffusion step, and R_3 is the resistance associated with the translocation step. Therefore, the overall resistance associated with these three steps is modeled by R_1 and R_2 being in parallel, and their combination being in series with R_3 (Figure 3-2b).

Equations (3-14)–(3-18) provide important insights into the dependence of the gas flow rate on the pore diameter D_p. When D_p is approximately equal to the gas kinetic diameter D_m, the translocation energy barrier E_a leads to an extremely small translocation coefficient k_{trans}, where $k_{\text{trans}} \propto \exp(-E_a/k_B T)$ and a large R_3. Wang *et al.* proposed that the energy barrier $E_a \approx \sqrt{4\pi\varepsilon D_p/a}\left(2\sigma/D_p\right)^{12}$, where ε and σ are Lennard-Jones parameters that approximate the gas molecule-pore interaction, and a is the distance between adjacent atoms on the pore rim.[26] The distance parameter σ in the Lennard-Jones potential is strongly correlated to the gas kinetic diameter D_m, and therefore, the energy barrier increases significantly as D_m approaches, or even exceeds, D_p. For better accuracy, k_{trans} and R_3 should be treated as implicit functions of D_m and D_p, and these values can be obtained using all-atomistic MD simulations (Chapter 2). In cases where R_3 is large, the translocation resistance R_3 is dominant ($R \approx R_3$) because it is much greater than both R_1 and R_2, and my model can reproduce the activated regime in the small pore limit. In the activated regime, the size of the pore becomes discretized, and pore features like shape and eccentricity can strongly affect its barrier properties.

On the other hand, when D_p is sufficiently large relative to D_m (but still smaller than the gas mean free path), the pore edge no longer imposes a translocation energy barrier and R_3 is small and negligible. As $D_m/D_p \to 0$, $\sigma/D_p \to 0$, and the energy barrier $E_a \to 0$. Considering the direct impingement (R_1^{-1}) and surface diffusion (R_2^{-1}) pathways, R_1^{-1} scales as D_p^2 (Equation (3-15)) and R_2^{-1} scales as D_p (Equation (3-16)). Therefore, in the large pore limit, $R_1^{-1} \gg R_2^{-1}$, and the direct impingement pathway is dominant ($R \approx R_1$), which reproduces the effusion mechanism. It is noteworthy that R_1, R_2, and R_3

exhibit different temperature dependences. To further study the role of temperature on gas permeation, I carried out MD simulations at different temperatures to probe the physical nature of the transport steps (see the sections below).

The theoretical permeation model introduced above was based on several assumptions, including 100% permeation success probability, and is expected to demonstrate deviations from real practical situations. More specifically, the permeation model requires revision, validation, and calibration due to the following reasons. First, the rate of surface diffusion depends on the value of the surface Henry's coefficient H_{surf}. It is still an open question whether the surface diffusion step is rate determining, and if it is, under what conditions. Second, the equations proposed above may require some corrections associated with potential nonidealities of the gases considered which need to be accounted for. For example, the diffusion of a gas molecule from the adsorption layer to the pore mouth could also require overcoming an energy barrier (Appendix 2.9.2).[152] This energy barrier along the surface diffusion path, in turn, would reduce the flow rate of gas from the adsorption layer to the pore mouth. Third, there may be additional pathways, or mechanisms, that were not considered in my model. For example, the direct impingement and the surface diffusion pathways can potentially interfere with each other. In the following sections, I will utilize MD simulations to test the validity of my gas permeation model, including refining it as needed.

3.3 Overview of Molecular Dynamics Simulations

In order to test the validity of my transport model, I carried out MD simulations to estimate the gas permeation rate and to study its dependence on the pore size (see Section 3.9 for more details). As shown in Figure 3-3a, a typical simulation run was carried out in a $10 \times 10 \times 80$ nm^3 simulation box, separated into two identical compartments by two 10×10 nm^2 graphene sheets placed parallel to each other, with one hydrogen-terminated pore on each sheet. The two compartments had the same number of gas molecules and were in equilibrium at the beginning of the simulation (Figure 3-3a). The number of permeation events in both directions was counted by analyzing the trajectories of all the gas molecules. Due to the rarity of gas-gas collisions in the dilute gas limit, the one-sided non-equilibrium permeation rate is one half of the two-sided equilibrium permeation rate. This strategy was introduced

and justified by Sun *et al*.[46] Because the simulation box contains two porous graphene sheets, the one-sided gas flow rate through one membrane was one quarter of the two-sided flow rate in the entire simulation box.

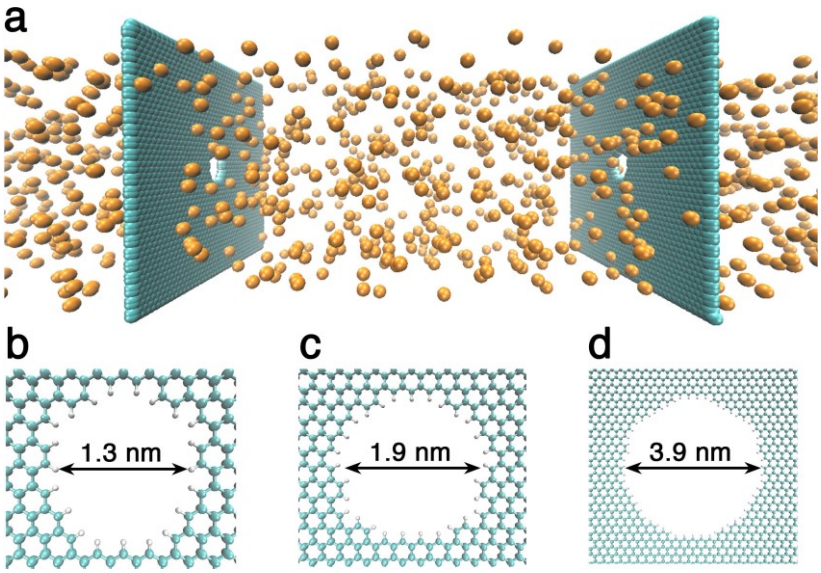

Figure 3-3. (a) Snapshot of the MD simulation measuring Ar permeation through graphene pores of 1.3 nm diameter. (b-d) Atomic structures of the 1.3 nm, 1.9 nm, and 3.9 nm diameter graphene nanopores, respectively. Color code: cyan–C, white–H, orange–Ar.

I simulated gas permeation through three types of nanopores, with diameters of 1.3, 1.9, and 3.9 nm, respectively (Figure 3-3b-d). These pores are sufficiently large relative to the kinetic diameters of the three gases considered (CO_2: 0.33 nm, Ar: 0.34 nm, and CH_4: 0.38 nm).[6] As a result, there is no translocation energy barrier, resulting in a low translocation resistance ($R_3 \approx 0$). Therefore, Equation (3-18) can be rewritten as follows:

$$R^{-1} = R_1^{-1} + R_2^{-1} = k_1 + k_2 H_{\text{surf}} = \sqrt{\frac{\pi}{2mk_{\text{B}}T}}\frac{D_{\text{p}}^2}{4Z} + \sqrt{\frac{\pi k_{\text{B}}T}{2m}} D_{\text{p}} H_{\text{surf}} \qquad (3\text{-}19)$$

where Equation (3-15) and (3-16) were used. Note that R^{-1} is also defined as the pressure-normalized permeation rate, with a unit of mol s^{-1} Pa^{-1} (or molecule s^{-1} Pa^{-1}). Because in the following discussions, the transport resistances R, R_1, and R_2 will be referred to mainly in the inverse form, for simplicity, I introduce the total permeance per pore $\Pi = R^{-1} = r_3/p$. It is worth noting that the definition of "permeance per pore" adopted here is different from the common definition of permeance as the pressure-normalized gas flux (with a unit of mol s^{-1} Pa^{-1} m^{-2}). Note also that the conventional permeance, as well as the permeance per pore, are simply related through the areal pore density.

Following my definition, I define the permeance per pore associated with the direct impingement pathway as Π_1, and that associated with the surface diffusion pathway as Π_2. According to my model, the total permeance per pore is partitioned into its two contributions, Π_1 and Π_2, as follows (derived from Equation (3-19)):

$$\Pi = R^{-1} = R_1^{-1} + R_2^{-1} = k_1 + k_2 H_{\text{surf}} = \Pi_1 + \Pi_2 \tag{3-20}$$

$$\Pi_1 = k_1 = \sqrt{\frac{\pi}{2mk_{\text{B}}T}} \frac{D_{\text{p}}^2}{4Z} \tag{3-21}$$

$$\Pi_2 = k_2 H_{\text{surf}} = \sqrt{\frac{\pi k_{\text{B}} T}{2m}} D_{\text{p}} H_{\text{surf}} \tag{3-22}$$

In order to compare my simulation results with Equations (3-20)–(3-22), the permeation events observed in the MD simulations need to be partitioned into those associated with the direct impingement pathway (referred to as the "direct pathway" in the figures) and with the surface diffusion pathway (referred to as the "surface pathway" in the figures). To this end, a permeation event is considered to be associated with the direct impingement pathway if the gas molecule moves into the pore mouth cylinder state from the top and then crosses the pore (Figure 3-1). Otherwise, if the gas molecule moves into the pore mouth cylinder state from the side and then crosses the pore, the permeation event is associated with the surface diffusion pathway. The height of the cylinder pore mouth state was set at 0.7 nm, which is consistent with the thickness of the surface adsorption layer (Figure 3-11 in Appendix 3.10.3). Although the choice of this height can affect the partition of the permeation events, the effect is minor (Figure 3-12 in Appendix 3.10.3). The pressure and the compressibility factor resulting from each simulation were calculated by the equations of state provided by the open source program CoolProp.[156] In my simulations, the most non-ideal compressibility factor Z is 0.96, obtained for CO_2 at T = 300 K and p = 7.2 bar, which is close to the ideal gas limit (Z = 1). This finding indicates that all my MD simulations were carried out near the ideal gas condition.

Figure 3-4 shows how the gas permeation depends on pressure, temperature, and pore diameter, as well as on the contributions from the direct impingement and the surface diffusion pathways, all obtained from the MD simulations. As shown in Figure 3-4a, the total permeances per pore of the three

gases considered are independent of pressure up to ~10 bar. This suggests that the parameters in Equations (3-20)–(3-22) are independent of pressure. The error bars (95% confidence intervals) were obtained by assuming that each permeation event occurs independently and randomly, and that the total number of permeation events follows a Poisson distribution. The equation used to calculate the confidence interval (Appendix 3.10.4) indicates that a greater number of total permeation events leads to a lower error. Accordingly, in the remainder of this chapter, unless stated specifically, because the total number of permeation events is proportional to the pressure, the highest pressure for each gas is chosen in order to minimize the relative errors (Figure 3-4a). Figure 3-4b shows that the gas permeance per pore decreases as the temperature increases. This is because the contributions from the direct impingement and the surface diffusion pathways are both decreasing functions of temperature (see the following sections for more discussions). Note that the gas permeance per pore increases non-linearly with the pore diameter (Figure 3-4c), and that the contributions from the direct impingement and the surface diffusion pathways increase differently with increasing pore diameter (Figure 3-4d). Specifically, the direct impingement pathway permeance per pore scales non-linearly with pore diameter (as predicted by Equation (3-21)), while the surface diffusion pathway permeance per pore scales nearly linearly with pore diameter (as predicted by Equation (3-22), and shown by the blue dashed line, Figure 3-4d). The cases corresponding to CH_4 and Ar are similar, and are shown in Figure 3-13 (Appendix 3.10.5).

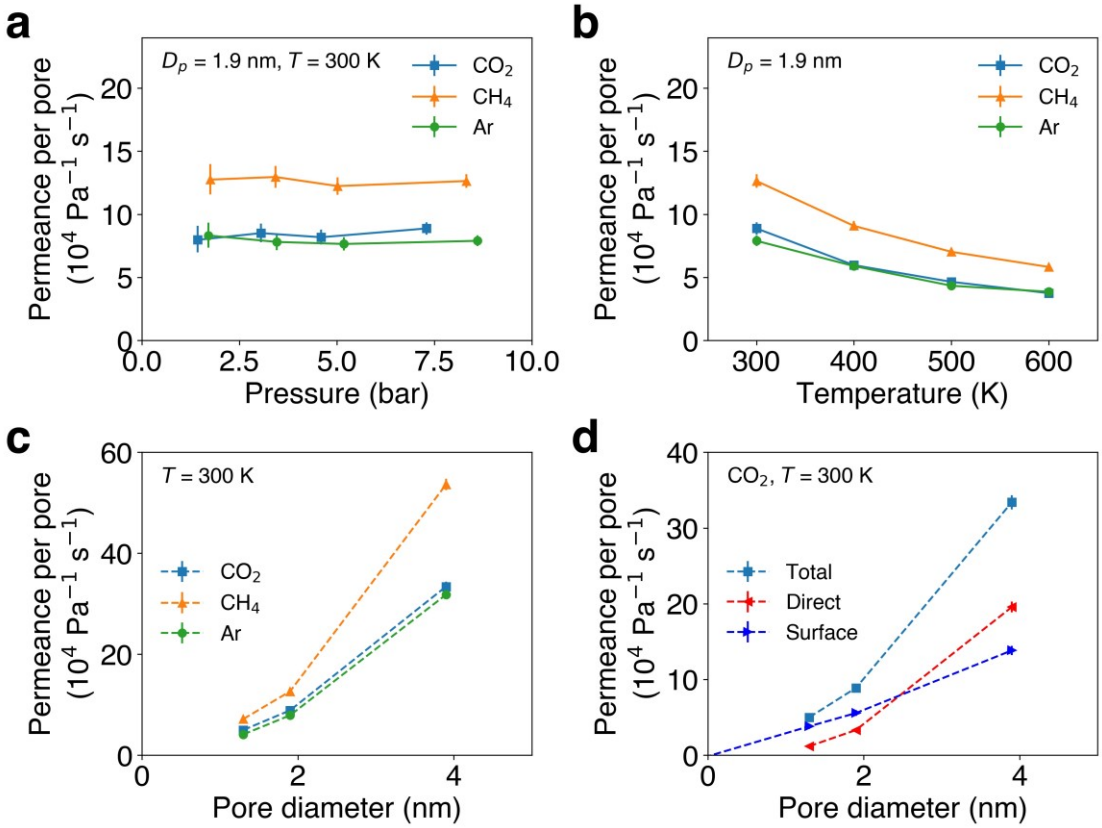

Figure 3-4. Total permeances per pore of CO_2, CH_4, and Ar through 1.9-nm pore at (a) various pressures and (b) various temperatures. (c) Permeances per pore of CO_2, CH_4, and Ar as functions of the pore diameter at 300 K. (d) Contributions of the direct impingement and the surface diffusion pathways to the total CO_2 permeance per pore as a function of the pore diameter at 300 K.

3.4 Direct Impingement Pathway

Figure 3-5 provides additional details about the direct impingement pathway. The permeance per pore contributed by the direct impingement pathway mildly decreases with increasing temperature (Figure 3-5a), which is consistent with the theoretical prediction (Equation (3-21)). Furthermore, Equation (3-21) (green dashed line, Figure 3-5b) can predict the rate of direct impingement attempts of CO_2 with a slight underestimation relative to the MD simulation result (orange dashed line). However, the theory (green dashed line) overpredicts the actual permeance per pore (blue dashed line), because only a fraction of the direct impingement attempts results in successful permeation. In fact, the majority of the direct impingement attempts to the pore mouth area do not lead to permeation. The situation is similar for CH_4 and Ar (Figure 3-14a, b in Appendix 3.10.5).

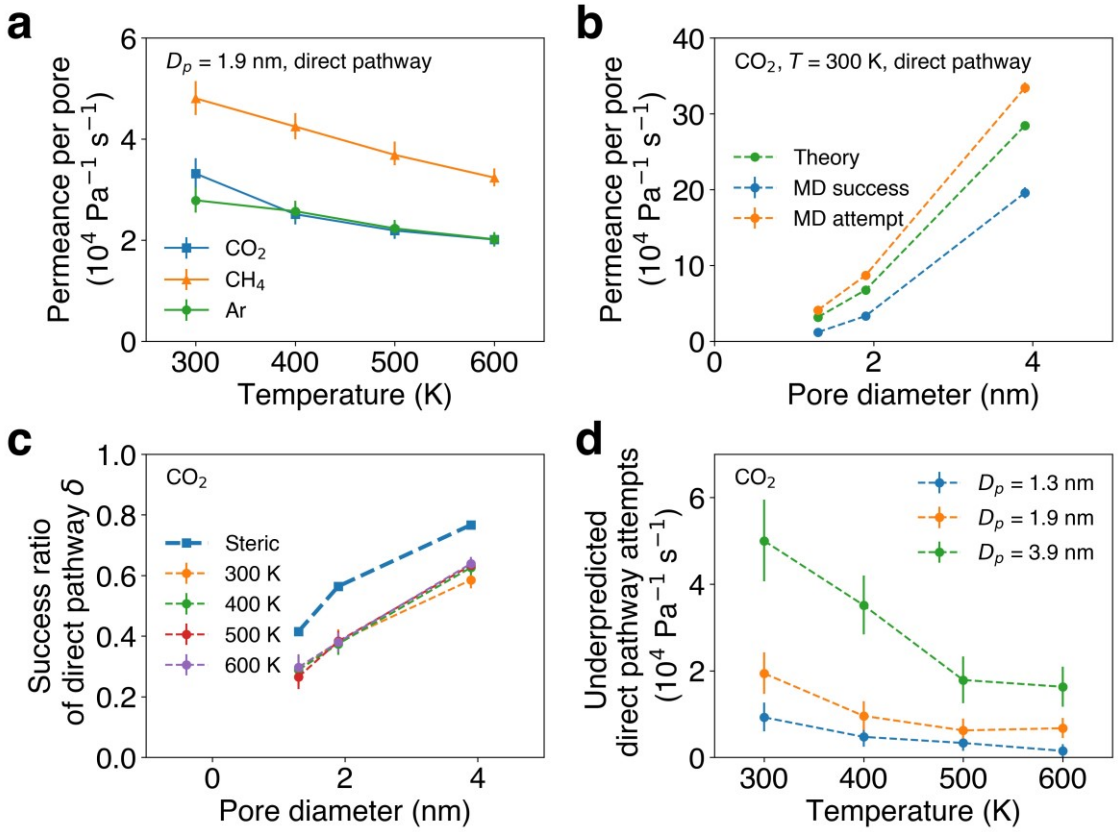

Figure 3-5. (a) Permeance per pore contributed by the direct impingement pathway as a function of temperature for CO_2, CH_4, and Ar. (b) Comparison of the permeance per pore contributed by the direct impingement pathway obtained using MD simulations and the theory (Equation (3-21)) for CO_2 at 300 K. (c) Comparison of the success ratio of the direct impingement pathway obtained using MD simulations and the steric selectivity theory proposed in Chapter 5 (Appendix 5.6.1) for CO_2 as a function of pore diameter at various temperatures. (d) Deviation of the theoretical predictions (Equation (3-21)) from the MD simulation-observed permeation attempts for CO_2 as a function of temperature for various pore diameters.

The discrepancy between the permeation rate and the attempt rate observed in MD simulations indicates that a factor δ which is smaller than unity needs to be introduced to correct the theoretical prediction associated with the direct impingement rate. Indeed, a fraction of these attempts fail because a gas molecule can collide with the pore edge and bounce off.[26] Therefore, δ is defined as the ratio between the successful permeation rate and the attempt rate associated with the direct impingement pathway obtained in the MD simulations. For a given gas, this effect is expected to be less pronounced as the pore diameter increases. The success ratio δ of CO_2 increases from 0.3 to 0.6 as the pore diameter increases from 1.3 to 3.9 nm (Figure 3-5c). As the pore diameter increases further, for a given gas, δ should approach unity. This correlation is independent of temperature (see the four curves corresponding to 300, 400, 500, and 600 K for CO_2 in Figure 3-5c). A similar trend holds in the case of

CH_4 and Ar (Figure 3-14c, d in Appendix 3.10.5). In fact, this phenomenon will be deeply explored in great detail in my experimental study reported in Chapter 5, and is referred to as the steric selectivity mechanism (Appendix 5.6.1). It is shown that the success ratio δ can be approximated as follows:

$$\delta = \left(1 - \frac{D_\mathrm{m}}{D_\mathrm{p}}\right)^3 \tag{3-23}$$

The prediction made using Equation (3-23), denoted as "steric" in Figure 3-5c, considers the distribution of the angle of incidence. Alternatively, if all the impingement attempts are assumed to be normal to the graphene plane, the success ratio can be approximated as $\delta = (1 - D_\mathrm{m}/D_\mathrm{p})^2$. However, Figure 3-5c shows that Equation (3-23) (the blue dashed line) overestimates the success ratio δ relative to the MD simulation results (the other four almost overlapping lines), suggesting that additional factors reduce the success ratio. For example, the trajectory of an impingement attempt may be distorted towards the pore edge due to the van der Waals interactions exerted by the pore edge atoms, which would decrease the likelihood of a successful crossing. Note that in the steric selectivity mechanism (Appendix 5.6.1), the impingement trajectories of the gas molecules are assumed to be straight and unaffected by the van der Waals attractive forces. Because of the expected molecular-level complexity of the gas–pore interaction, I propose a semi-empirical equation for the success ratio, inspired by Equation (3-23):

$$\delta = \left(1 - \frac{D_\mathrm{m}}{D_\mathrm{p}}\right)^\alpha \tag{3-24}$$

Interestingly, the proposed equation can reproduce the limiting cases: (i) $D_\mathrm{m} = 0$ leads to $\delta = 1$ (no reduction in the success ratio due to gas molecule-pore collision), and (ii) $D_\mathrm{m} = D_\mathrm{p}$ leads to $\delta = 0$ (zero success ratio due to 100% likelihood of collision). I fit $\ln(\delta)$ *vs.* $(1 - D_\mathrm{m}/D_\mathrm{p})$ using a linear correlation, and the fitting results show that the exponent α in Equation (3-24) is different for the three gases considered: $\alpha(CO_2) = 4.58$ ($R^2 = 0.93$), $\alpha(CH_4) = 3.68$ ($R^2 = 0.95$), and $\alpha(\mathrm{Ar}) = 4.32$ ($R^2 = 0.97$). No obvious correlation is found between the value of α and the properties of the three gases considered, including their kinetic diameters and Lennard-Jones parameters. Nevertheless, all the three α values are greater than 3 in the steric selectivity mechanism (Appendix 5.6.1), indicating an enhanced gas molecule-pore edge interaction relative to that predicted by the original steric selectivity mechanism.

It is also noteworthy that Equation (3-21) underestimates the rate of direct impingement attempts relative to the MD simulation results. Indeed, in Figure 3-5d, the difference between the simulated and the predicted direct pathway impingement attempts is plotted as a function of temperature for CO_2 and three pore diameters. Interestingly, Figure 3-5d shows that the difference is a decreasing function of temperature and an increasing function of the pore diameter, instead of being random. This trend is also observed for CH_4 and Ar (Figure 3-14e, f in Appendix 3.10.5). This difference (Figure 3-5d) is one order of magnitude lower than the rate of the simulated direct impingement attempts (Figure 3-5b). This finding suggests that the difference between the simulated and the theoretical results reflects the existence of a separate minor permeation pathway, which will be discussed in Section 3.6.

3.5 Surface Diffusion Pathway

The gas permeance contributed by the surface diffusion pathway decays rapidly with increasing temperature for D_p = 1.9 nm (Figure 3-6a). This is mainly due to the exothermic gas molecule-graphene adsorption contributed by the van der Waals interaction. Similar observations can be made for D_p = 1.3 nm and D_p = 3.9 nm (Figure 3-15a, b in Appendix 3.10.5). The surface Henry's coefficient H_{surf} represents the magnitude of the gas adsorption on the graphene surface, and it is correlated to temperature according to the van't Hoff equation, involving the heat of adsorption ΔH_{ads}.[41] Specifically,

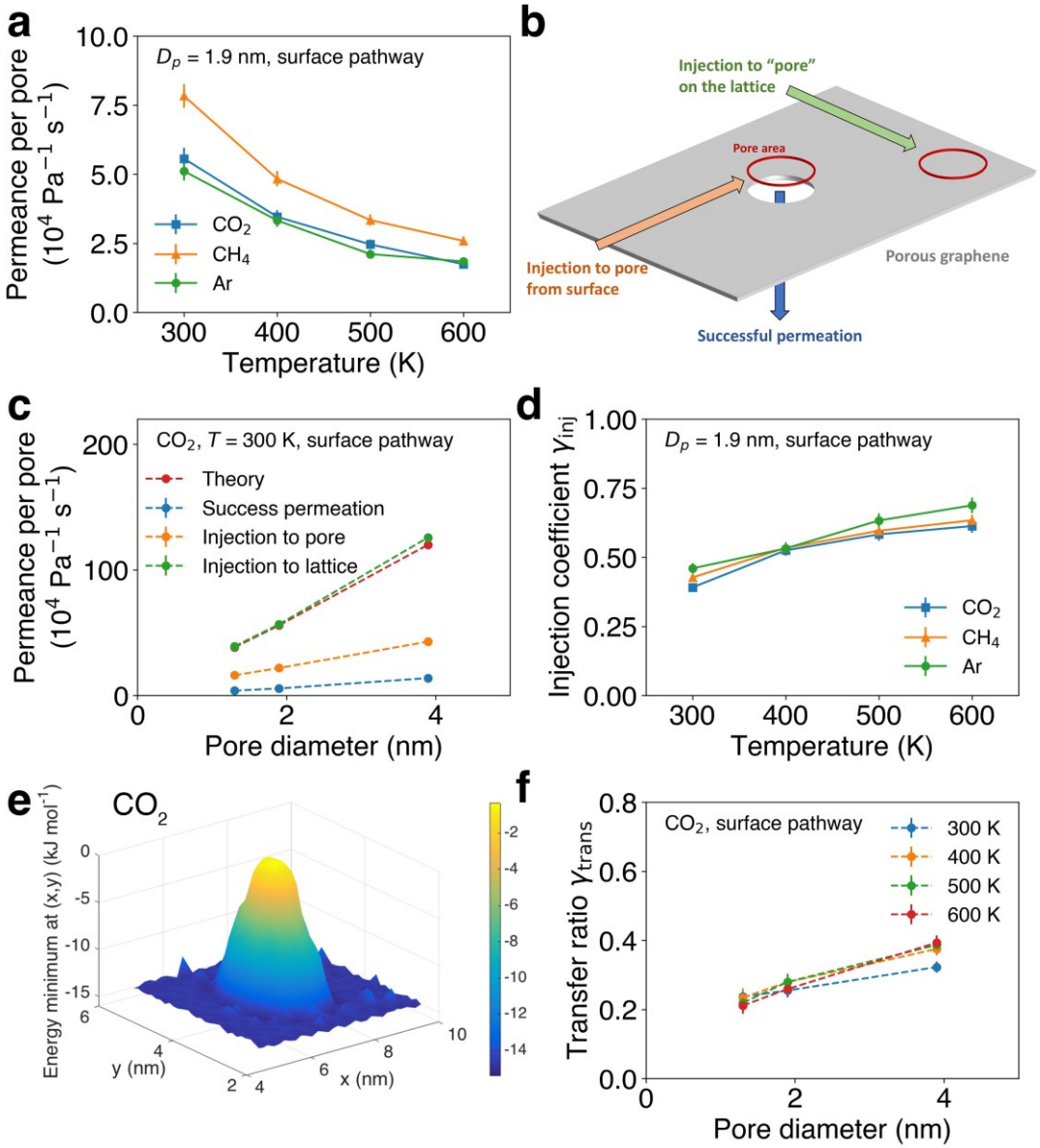

Figure 3-6. (a) Permeance per pore contributed by the surface diffusion pathway as a function of temperature for CO_2, CH_4, and Ar. (b) Schematic illustration of monitored transport rates associated with the surface diffusion pathway. (c) Comparison of the permeance per pore contributed by the surface diffusion pathway obtained using MD simulations and my theoretical predictions as a function of pore diameter for CO_2 at T = 300 K. (d) Injection coefficient corresponding to the surface diffusion pathway γ_{inj} as a function of temperature for the three gases considered for D_p = 1.9 nm. (e) Potential energy landscape of a CO_2 molecule near the 1.9-nm diameter graphene pore. The peak represents a rise in energy above the pore. (f) Transfer ratio corresponding to the surface diffusion pathway γ_{trans} as a function of pore diameter for CO_2 at various temperatures.

$$H_{\mathrm{surf}}(T) = H^0_{\mathrm{surf}} \exp\left(-\frac{\Delta H_{\mathrm{ads}}}{k_{\mathrm{B}} T}\right) \tag{3-25}$$

where H^0_{surf} is the prefactor. Heat of adsorption values for the three gases considered were derived by fitting $H_{\mathrm{surf}}(T)$ obtained from MD simulations to Equation (3-25), within the temperature range from 300 to 600 K, and are listed in Table 3-1.

Table 3-1. Heats of adsorption and energy barriers of injection for CO_2, CH_4, and Ar within the temperature range T = 300 to 600 K.

	Heat of adsorption ΔH_{ads} (kJ mol^{-1})	Energy barrier associated with injection $E_{a,\mathrm{inj}}$ (kJ mol^{-1})		
		D_{p} = 1.3 nm	D_{p} = 1.9 nm	D_{p} = 3.9 nm
CO_2	-10.7 ± 0.5	2.2	2.3	2.7
CH_4	-9.2 ± 0.6	1.9	2.0	2.2
Ar	-7.9 ± 1.0	2.2	2.0	2.4

In order to analyze the surface diffusion pathway, two individual steps can be identified along this pathway (orange and blue arrows in Figure 3-6b). Firstly, a gas molecule adsorbed on the graphene surface injects into the pore mouth area (orange arrow in Figure 3-6b, denoted as "injection to pore" in Figure 3-6c). Subsequently, the injected molecule permeates through the pore (blue arrow in Figure 3-6b, denoted as "success permeation" in Figure 3-6c). It is worth noting that the rates of both steps are significantly lower than the theoretical prediction provided by Equation (3-22) (denoted as "theory" in Figure 3-6c). Interestingly, if the "pore area" is moved away from the physical pore in the graphene lattice and the gas injection rate is monitored as if the pore were located at a new location (green arrow in Figure 3-6b), the rate of injection to the "fictitious pore" in the lattice (denoted as "injection to lattice", green dashed curve in Figure 3-6c) matches the theoretical prediction (denoted as "theory", red dashed curve in Figure 3-6c). Note that this fictitious pore injection rate is independent of the fictitious pore–real pore distance when it is greater than 5 nm. Therefore, in the first step along the surface diffusion pathway, a fraction of the injection attempts is rejected. In addition, in the second step, among the gas molecules that arrive at the pore mouth area, only a fraction permeates through the pore. This behavior is similar for CH_4 and Ar (Figure 3-15c, d in Appendix 3.10.5). Here, the first success ratio is denoted as the injection coefficient γ_{inj}, and the second success ratio is denoted as the transfer ratio γ_{trans}.

As shown in Figure 3-6d, the injection coefficient γ_{inj} for D_p = 1.9 nm is an increasing function of temperature, indicating that the injection step is associated with climbing an energy barrier (similar results are obtained for the other two pore diameters, see Figure 3-15e, f in Appendix 3.10.5). Figure 3-6e shows the potential energy landscape of CO_2 adsorbing on graphene in the vicinity of the pore. The potential energy increases as the CO_2 molecule moves above the pore region, because the carbon atoms missing from the graphene lattice, due to the presence of the pore, are not able to interact favorably with the gas molecules *via* van der Waals interactions. In other words, an adsorbed gas molecule needs to "desorb" from the graphene lattice to enter the pore area, which involves an energy barrier. In the case of CH_4 and Ar, as well as of the other two pore sizes considered, the potential energy landscapes are similar to that in Figure 3-6e, with varying heights and basal areas of the potential energy protrusion. This energy barrier violates the assumptions underlying Equation (3-22) because the gradient in the potential energy landscape felt by the gas molecules disrupts their in-plane distribution. The energy barriers associated with injection $E_{a,inj}$ for the three gases considered can be derived by fitting the three injection coefficients γ_{inj} to temperature according to an Arrhenius equation. Specifically,

$$\gamma_{\mathrm{inj}} = \gamma_{\mathrm{inj}}^{0} \exp\left(-\frac{E_{\mathrm{a,inj}}}{k_{\mathrm{B}}T}\right) \tag{3-26}$$

where $\gamma_{\mathrm{inj}}^{0}$ is the prefactor. The energy barriers associated with injection into pores for the three gases considered having values of D_p equal to 1.3, 1.9, and 3.9 nm, respectively, are listed in Table 3-1. Because of the "desorbing" nature of the injection step, the energy barrier associated with injection should be correlated to the heat of adsorption. Note that for the three pore diameters considered, the energy barrier associated with injection $E_{\mathrm{a,inj}}$ is 20–30% of the heat of adsorption ΔH_{ads} (absolute value). This is because the gas molecule only needs to climb less than halfway on the energy bump to enter the pore region. The fitted values of the prefactor $\gamma_{\mathrm{inj}}^{0}$ in Equation (3-26) for the nine cases considered (three gases and three pores) are close to 1 (1.00 ± 0.11). Therefore, $\gamma_{\mathrm{inj}}^{0} \approx 1$. If $E_{a,inj}$ approaches 0, γ_{inj} approaches its maximum value of 1, which is consistent with the definition of γ_{inj} as a success ratio between 0 and 1.

The transfer ratio γ_{trans} characterizes the success ratio associated with a gas molecule crossing the membrane if it has entered the pore area. Although some gas molecules may have entered the pore area,

they could have slided across the pore without permeating through the pore. As shown in Figure 3-6f, γ_{trans} for CO_2 is nearly independent of temperature, and therefore, this second step does not involve climbing an energy barrier. For CH_4 and Ar, similar observations can be made (Figure 3-15g, h in Appendix 3.10.5). In addition, γ_{trans} is positively correlated to the pore diameter (Figure 3-6f, also Figure 3-15g, h), which is expected because a larger pore is more likely to allow gas permeation. It is noteworthy that a theoretical prediction of γ_{trans} is challenging, because the momentum change which drives a gas molecule to cross the pore involves complex gas–pore and gas–gas collisions. Nevertheless, additional insight can be gained by considering the following two limiting cases: (1) when D_p approaches 0 (D_m/D_p approaches infinity), γ_{trans} should approach 0 because the pore is closed, and (2) when D_p approaches infinity (D_m/D_p approaches 0), γ_{trans} is expected to approach 0.5 because the gas molecule has equal probability to move towards, or to move away from, the pore in the z direction.

3.6 Minor Spillover Pathway

Recall that in the direct impingement pathway analysis, Equation (3-21) underpredicts the rate of the direct impingement attempts relative to the simulation results, with the deviation showing a sharp decrease with increasing temperature (Figure 3-5d). This negative correlation with temperature resembles the temperature dependence of the permeance *via* the surface diffusion pathway (Figure 3-6a). Therefore, it is hypothesized that the surplus direct impingement attempts observed in my MD simulations originate from the adsorption layer. In order to test this hypothesis, I analyzed the angle of incidence distribution among all the permeation events as follows. The angle of incidence is defined as the angle formed between the direction normal to the graphene plane (+z) and the tangent to the molecule's trajectory at the point of crossing the graphene basal plane (z = 0), as shown in the inset at the top-right in Figure 3-7a. Assume that the crossing occurs at time t_0. In this case, the angle of incidence θ can be derived from the velocity $\vec{v}$ of a gas molecule at the crossing point:

$$\theta = \tan^{-1}\left(\frac{|v_z|}{\sqrt{v_x^2 + v_y^2}}\right) \tag{3-27}$$

Because the trajectories recorded in the MD simulations are discretized in time, the secant between times t_0 and $t_0-\Delta t$ is used to replace the tangent at t_0, where Δt is a small time interval. Therefore, the angle of incidence obtained from my simulations should be calculated as follows:

$$\theta = \tan^{-1}\left\{\frac{\frac{z(t_0)-z(t_0-\Delta t)}{\Delta t}}{\sqrt{\left[\frac{x(t_0)-x(t_0-\Delta t)}{\Delta t}\right]^2+\left[\frac{y(t_0)-y(t_0-\Delta t)}{\Delta t}\right]^2}}\right\} \tag{3-28}$$

Note that in the limit of $\Delta t \to 0$, Equation (3-28) reduces to Equation (3-27). Interestingly, Δt can be carefully tuned to reveal additional mechanistic details. For example, the angle of incidence can be used to determine whether a permeated gas molecule originates from the bulk gas phase or from the adsorption layer. To this end, the average distance $\overline{v}\Delta t$ traversed by a gas molecule having average speed $\overline{v}$ during time Δt should satisfy the following requirements. First, $\overline{v}\Delta t$ should be greater than the pore diameter D_p. Otherwise, the gas molecule's traveling trajectory before entering the pore mouth region is not recorded, because the entering event occurred longer than Δt ago, and the information is lost about whether the gas molecule comes from the bulk gas or from the surface adsorption layer. Second, $\overline{v}\Delta t$ should be less than the gas mean free path λ to ensure that gas–gas collisions do not confound the angle of incidence distribution. Accordingly, the following inequality should be satisfied by $\overline{v}\Delta t$: $D_p < \overline{v}\Delta t < \lambda$. According to the Maxwell-Boltzmann distribution, $\overline{v} = \sqrt{8k_B T/\pi m}$.[41] The gas mean free path is given by $\lambda = (\sqrt{2}\pi D_m^2 \rho)^{-1}$, where ρ is the volumetric number density of the bulk gas.[41] Consider one of the simulation cases for CO_2, where the gas pressure is 7.4 bar, the temperature is 300 K, and the pore diameter is 3.9 nm. In this case, Δt should satisfy 10 ps < Δt < 30 ps. For the other two gases and the other two pore sizes considered in this chapter, the upper and lower bounds for Δt may differ, and the corresponding Δt value can be carefully chosen in order to carry out a similar analysis as shown below.

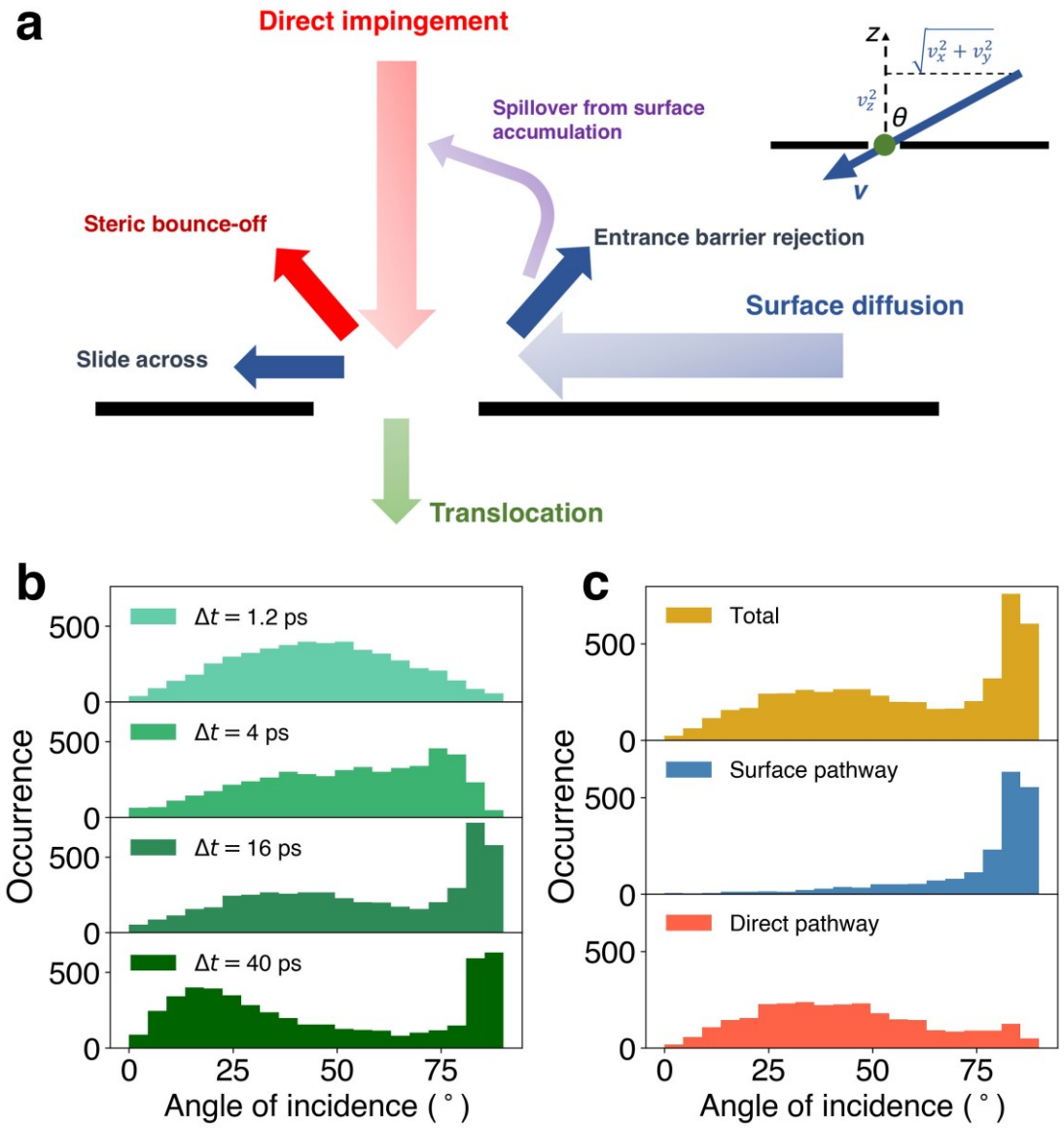

Figure 3-7. (a) Schematic illustration of the gas permeation mechanism through a graphene nanopore. (b) Angle of incidence distribution of a CO_2 molecule crossing a 3.9-nm-diameter graphene pore with Δt ranging from 1.2 ps to 40 ps. (c) Angle of incidence distribution of a CO_2 molecule crossing a 3.9-nm-diameter pore from the direct impingement and the surface diffusion pathways, where Δt = 16 ps. The minor peak at high angle of incidence in the direct impingement pathway represents a minor spillover pathway.

Figure 3-7b shows the angle of incidence distribution corresponding to the above-mentioned simulation case. The *y* axis represents the number of occurrences during the 5 ns simulation for each bin of the angle of incidence on the *x* axis. When Δt = 1.2 ps, only a very short length of the molecular trajectory close to the pore mouth is recorded, and the angle of incidence follows the distribution $f \propto \sin\theta\cos\theta$ (top panel in Figure 3-7b), indicating an entirely random angular distribution (Appendix

5.6.1).[46] In other words, this distribution shows no memory regarding the pore. As the time interval Δt increases, a peak at high angle of incidence emerges, reflecting the contribution from the surface adsorption layer. At a time interval of 16 ps, the angle of incidence distribution exhibits both a broad direct impingement peak at 45° and a sharp surface diffusion peak at near 90° (second to bottom panel in Figure 3-7b). As Δt is further increased to 40 ps, which is higher than the upper limit of 30 ps determined by the relation $\overline{v}\Delta t < \lambda$, the direct impingement peak becomes biased as it shifts to the low angle of incidence direction, due to gas–gas collisions (bottom panel in Figure 3-7b). Considering that Δt should satisfy the constraint, 10 ps < Δt < 30 ps, for CO_2 for a pore with D_p equal to 3.9 nm, Δt = 16 ps is chosen as the most appropriate choice for later analysis (top panel in Figure 3-7c).

The above-mentioned methodology is used to analyze the angle of incidence distribution of the permeation events which were previously classified into the surface diffusion or the direct impingement pathways. Note that the pathway of a permeation event is determined by examining whether the gas molecule entered the pore mouth region from the top or from the side. As shown in the middle panel in Figure 3-7c, the angle of incidence distribution corresponding to the surface diffusion pathway shows a single peak at high angle, because the trajectories of the surface diffusion pathway are parallel to the graphene plane and perpendicular to the z direction. On the other hand, as shown in the bottom panel in Figure 3-7c, the angle of incidence distribution corresponding to a direct impingement pathway exhibits a minor peak at high angle, along with a broad $\sin\theta\cos\theta$ peak at 45° associated with random impingement. This minor peak indicates that a fraction of the direct impingement events originated from the surface adsorption layer (Figure 3-7a), and therefore, could not be predicted by the original bulk-gas-based theory (Equation (3-21)). This additional minor pathway explains well the surplus of MD simulation-observed direct impingement attempts over those predicted by the original theory.

Figure 3-7a illustrates this additional minor pathway as a spillover resulting from surface accumulation (the purple arrow). As shown previously, the majority of the surface injection attempts into the pore area are rejected (the blue arrows). These rejected gas molecules create a local high gas density in the vicinity of the pore, and get recirculated as direct impingement (the red arrow). Therefore,

the minor spillover pathway possesses characteristics of both the direct and the surface pathways, which motivates the following power law estimation:

$$K_{\text{minor}} = aK_{1,\text{theory}}^{b}K_{2,\text{theory}}^{c} \tag{3-29}$$

where a, b, and c are fitting parameters, and $K_{1,\text{theory}}$ and $K_{2,\text{theory}}$ are the theory-predicted permeances per pore corresponding to the direct impingement (Equation (3-21)) and the surface diffusion pathways (Equation (3-22)), respectively. The fitted results for CO_2, CH_4, and Ar at different temperatures are: $a = 2.76 \times 10^{-3}$, $b = 0.31$, and $c = 0.91$ ($R^2 = 0.88$, Figure 3-16 in Appendix 3.10.6). The unit for the permeances per pore appearing in Equation (3-29) is molecule Pa^{-1} s^{-1}. Because $c > b$, the minor spillover pathway depends more strongly on the surface diffusion pathway, and demonstrates a pore size dependence of $(D_p^2)^{0.31}(D_p)^{0.91} = (D_p)^{1.53}$.

3.7 Transition between Regimes

Combining Equations (3-20)–(3-29), when the translocation resistance is negligible, the predicted permeance per graphene nanopore is given by:

$$K = \delta K_{1,\text{theory}} + \gamma_{\text{inj}}\gamma_{\text{trans}}K_{2,\text{theory}} + 2.76 \times 10^{-3}K_{1,\text{theory}}^{0.31}K_{2,\text{theory}}^{0.91} \tag{3-30}$$

Note that the gas permeance contribution from the minor spillover pathway (the third term on the right hand side of Equation (3-30)) is orders of magnitude smaller than the contributions from the direct impingement pathway (the $\delta K_{1,\text{theory}}$ term in Equation (3-30)) and the surface diffusion pathway (the $\gamma_{\text{inj}}\gamma_{\text{trans}}K_{2,\text{theory}}$ term in Equation (3-30)). Accordingly, in the following discussions regarding gas permeation through graphene nanopores, it is safe to neglect the spillover pathway. Note that, for other 2D materials, other pore sizes/densities, or other gases, the value of a in Equation (3-29) may be non-negligible, and the spillover pathway should be considered. In the current case of graphene, $K \approx \delta K_{1,\text{theory}} + \gamma_{\text{inj}}\gamma_{\text{trans}}K_{2,\text{theory}}$. Comparing this equation with the purely theoretical model, $K = K_1 + K_2$ (Equation (3-20)), it is observed that the gas permeances per pore from the direct impingement pathway and the surface diffusion pathway need to be corrected by three factors: δ, γ_{inj}, and γ_{trans}. The three correction factors are then inserted into the original theoretical prediction in Equation (3-14),

which includes the translocation step. Therefore, the overall gas permeation resistance for a wider pore diameter range, including the activated (translocation-limited) regime can be expressed as follows:

$$R = R_3 + \frac{1}{\frac{1}{R_1} + \frac{1}{R_2}} = \frac{1}{\delta k_1 + \gamma_{\text{inj}}\gamma_{\text{trans}} k_2 H_{\text{surf}}} + \frac{1}{k_{\text{trans}} H_{\text{pore}}} \quad (3\text{-}31)$$

In Chapter 2, I derived an expression for the transport resistance of the translocation step R_3 based on transition state theory and MD simulations. Accordingly, all the relevant expressions can be combined, including using relevant numbers for the translocation ($k_{\text{trans}} H_{\text{pore}}$ in Equation (3-31)), the direct impingement pathway (δk_1 in Equation (3-31)), and the surface diffusion pathway ($\gamma_{\text{inj}}\gamma_{\text{trans}} k_2 H_{\text{surf}}$ in Equation (3-31)), to predict the gas permeance per pore for graphene pores ranging from 0.5 to 6 nm in diameter for CO_2 (Figure 3-8, Figure 3-17c in Appendix 3.10.7), CH_4 (Figure 3-17a), and Ar (Figure 3-17b). Because the exact mathematical expressions to predict γ_{inj} and γ_{trans} is not available, some approximations need to be made to estimate their values for other pore diameters. In order to calculate γ_{inj}, $E_{\text{a,inj}}$ needs to be first obtained using Equation (3-26). To this end, it is noticed that $E_{\text{a,inj}}/|\Delta H_{\text{ads}}| \approx 0.25$, as seen from the empirical relation between the two energetic terms (Table 3-1). It is noteworthy that the value of $E_{\text{a,inj}}/|\Delta H_{\text{ads}}|$ could change as a function of pore functionalization. For example, oxygen termination would attract CO_2 molecules into the pore due to stronger electrostatic and dispersion interactions, thereby reducing $E_{\text{a,inj}}$. In the case of γ_{trans}, the values of γ_{trans} are estimated by linear interpolation of the MD simulation results. Note that it is assumed that my predictions of the correction factors, δ, γ_{inj}, and γ_{trans}, can be extrapolated to the small pore limit. However, the exact values of the three correction factors in the small pore limit, corresponding to the activated gas transport, are difficult to obtain because their respective effects will be obscured by the rejections from the energy barrier for translocation.

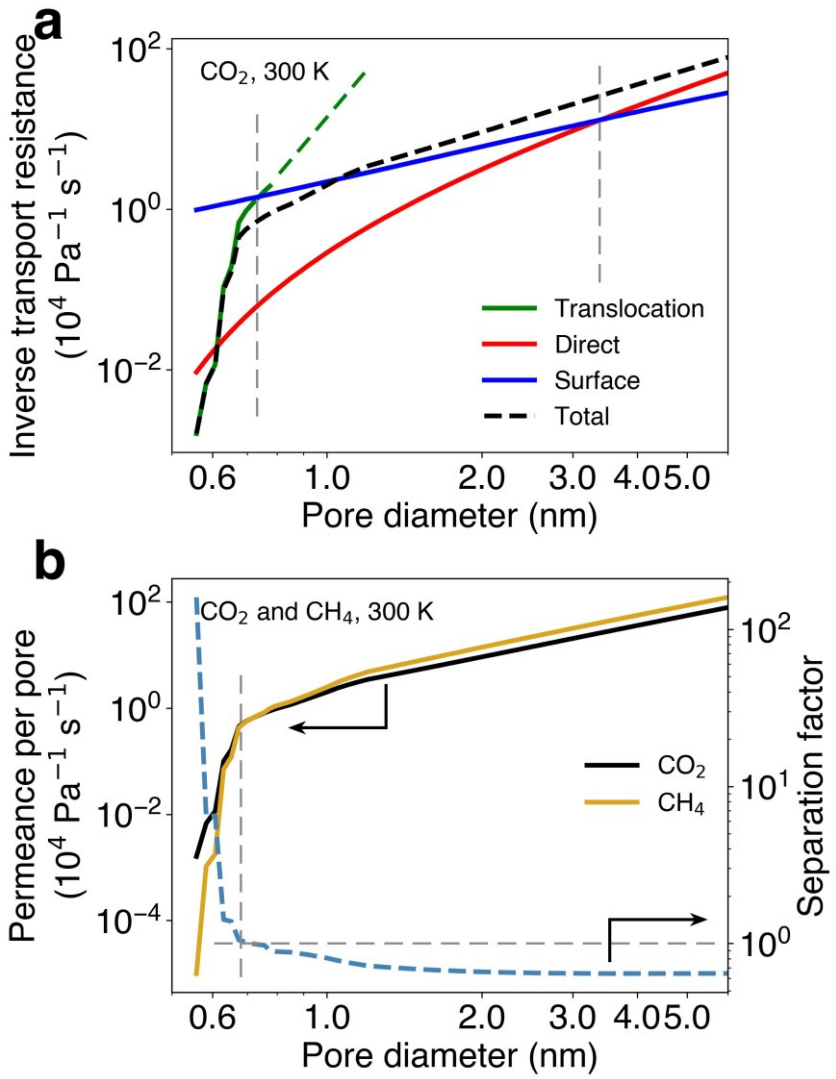

Figure 3-8. (a) Inverse transport resistances associated with the translocation (green), the direct impingement (red), and the surface diffusion (blue) pathways, and the overall permeance per pore (black) as a function of pore diameter for CO_2 at 300 K. The two perpendicular grey dashed lines separate three transport regimes, from left to right: translocation dominated, surface diffusion pathway dominated, and direct impingement pathway dominated, from left to right. (b) Permeance per pore of CO_2 and CH_4 (black and yellow curves, respectively) and corresponding CO_2/CH_4 separation factor (blue dotted curve) as a function of pore diameter at 300 K. The horizontal and perpendicular grey dashed lines denote the pore diameter value at which the values of the CO_2 and CH_4 permeances per pore are equal, and consequently, the separation factor is equal to 1.

Figure 3-8a shows the various contributions to the permeance per pore for CO_2 permeating through a circular pore of diameter ranging between 0.5 to 6 nm at 300 K, predicted using Equation (3-31). The translocation (R_3^{-1}), direct impingement pathway (R_1^{-1}), and surface diffusion pathway (R_2^{-1}) transport kinetics scale differently with the pore diameter. For pores with D_p < 0.72 nm, the energy barriers associated with crossing the pore are greater than 2 kJ mol^{-1}, which impedes the translocation step. In this regime, the translocation step (solid green curve in Figure 3-8a, taken from Chapter 2) is slower

than the surface diffusion step (blue curve in Figure 3-8a): $R_3^{-1} < 1.4 \times 10^4$ Pa^{-1} s$^{-1} < R_2^{-1}$. The critical transition pore diameter D_p^* can be calculated by equating the translocation and the surface pathway resistances:

$$k_\mathrm{trans}(D_\mathrm{p}^*)H_\mathrm{pore} = R_3^{-1} = R_2^{-1} = \gamma_\mathrm{inj}\gamma_\mathrm{trans}(D_\mathrm{p}^*)k_2(D_\mathrm{p}^*)H_\mathrm{surf} \quad (3\text{-}32)$$

According to Equation (3-31), R_3 dominates the overall gas permeation (dashed black curve in Figure 3-8a) in this translocation-dominated regime (see the overlap of the green and black curves), in accordance with the activated regime discussed in Chapter 2. Note that in this regime, the direct impingement step (red curve in Figure 3-8a) is much slower than the surface diffusion step (blue curve), and does not contribute much to the overall gas permeance. As the pore diameter increases beyond 0.72 nm, the energy barrier decreases to 0, and the translocation rate increases rapidly. This rapid increase is shown in Figure 3-8a by the green dashed line extended out from the green solid curve as an estimated trend. When D_p > 0.72 nm, R_3^{-1} is greater than both R_1^{-1} and R_2^{-1}, and becomes increasingly less important in dictating the overall permeance per pore (Equation (3-31)). As shown in Figure 3-8a, the overall permeance per pore (dashed black curve) makes a transition from the translocation dominated (solid green curve) to the surface diffusion dominated (blue curve) from D_p = 0.72 nm to 1 nm. For 1 nm < D_p < 2 nm, the surface diffusion pathway dominates the overall permeance per pore, as shown by the close correlation of the dashed black curve and the blue curve between the two grey dashed lines in Figure 3-8a. Another regime transition occurs at D_p^* = 3.4 nm, where the direct impingement step (red curve) and the surface diffusion step (blue curve) have the same rates: $\delta(D_\mathrm{p}^*)k_1(D_\mathrm{p}^*) = R_1^{-1} = R_2^{-1} = \gamma_\mathrm{inj}\gamma_\mathrm{trans}(D_\mathrm{p}^*)k_2(D_\mathrm{p}^*)H_\mathrm{surf}$. For a graphene pore larger than 4 nm in diameter, the direct impingement pathway dominates, which is consistent with the steric regime proposed by Wang *et al*.[26] The three regimes are separated by the two vertical grey dashed lines as shown in Figure 3-8a.

The cross-regime transition point for the graphene nanopore diameter depends on the permeating gas. The pore diameter at the transition point from the translocation-dominated regime to the surface diffusion pathway-dominated regime is more important because it is the upper limit of highly selective molecular sieving. As shown in Figure 3-17a, b (Appendix 3.10.7), this transition pore diameter is 0.76 and 0.78 nm for CH_4 and Ar, respectively. This transition pore diameter is greater for larger gas

molecules (CH_4, Ar), because for larger gas molecules, the translocation energy barrier remains significant for the graphene pores of larger sizes.

My prediction indicates that the surface diffusion mechanism can dominate for a certain pore size range, albeit a relatively narrow one. It is worth noting that my simulations assume that the graphene surface is perfectly clean. However, experimentally, the graphene surface is susceptible to the adsorption of organic molecules from the gas phase, and of polymer residues from the graphene transfer process (see Chapters 4 and 6 for more discussion).[206] These factors will likely reduce the surface pathway transport rate by decreasing the heat of adsorption or the in-plane diffusivity. Therefore, this chapter represents a potential upper bound for the surface diffusion pathway rate.

By dividing the CO_2 permeance per pore in Figure 3-8a by the CH_4 permeance per pore in Figure 3-17a (Appendix 3.10.7), the CO_2/CH_4 separation factor can be obtained as a function of the pore diameter at 300 K (Figure 3-8b). This gas pair is of high interest because CO_2/CH_4 separation is crucial in many industrial processes such as natural gas sweetening and oil recovery.[207] As shown in Figure 3-8b, a reasonable separation factor (> 5) can only be attained with a pore diameter less than 0.60 nm. This implies that Angstrom-scale precision is required in the nanopore fabrication process in order for the nanoporous graphene membrane to achieve a reasonably good CO_2/CH_4 separation performance.[122] The effect of temperature is also studied (Figure 3-17c in Appendix 3.10.7). The pore diameter restriction for CO_2/CH_4 separation is further tightened to 0.56 nm at 400 K (Figure 3-17d in Appendix 3.10.7), because a higher temperature attenuates the energy barrier difference between CO_2 and CH_4. At 300 K, the CO_2/CH_4 separation factor is 1 when D_p = 0.7 nm (Figure 3-8b). This pore diameter is determined by a competition between the size and the mass of the gas molecules. On the one hand, CO_2 has a smaller gas kinetic diameter than CH_4, and therefore, has an edge over CH_4 when the pore size is small and the translocation step is dominant ($r_3 = k_{trans}N_{pore} \propto \exp(-E_a/k_BT)$). On the other hand, CH_4 has a smaller molecular weight and a higher average velocity. As a result, CH_4 gains the advantage in the large pore size limit where the surface diffusion and the direct impingement steps are dominant ($R_1^{-1} \propto m^{-1/2}$, and $R_2^{-1} \propto m^{-1/2}$, Equations (3-21) and (3-22)). As D_p continues to increase, the direct

impingement pathway dominates, and the separation factor approaches the Knudsen effusion selectivity limit ($K \propto m^{-1/2}$).

3.8 Conclusions

This chapter presents a comprehensive theoretical framework to model gas permeation through graphene nanopores of any given diameter. Specifically, I derived analytical equations to predict the transport rates associated with the direct impingement and the surface diffusion steps, and then integrated them with the translocation step to formulate the overall gas permeation rate per pore. The transport resistances associated with the direct impingement and the surface diffusion steps are in parallel, and that the translocation step resistance is in series with the parallel combination. I then used molecular dynamics simulations to validate and refine the analytical model. Firstly, I showed that the direct impingement rate should be corrected by a success ratio δ. Secondly, I demonstrated that the surface diffusion rate to the pore should be corrected by two correction factors, γ_{inj} and γ_{trans}, characterizing the success ratio associated with diffusing into the pore area and crossing the pore, respectively. Finally, I identified a minor spillover pathway from the surface adsorption layer using an angle of incidence analysis. Based on these corrections, I predicted that the gas permeation through a graphene pore begins from a translocation-dominated regime, followed by a surface-pathway dominated regime, and finally by a direct-pathway dominated regime, as the pore diameter increases. My modeling approach is applicable not only to nanopores in graphene, but also to nanopores in other two-dimensional materials, including hexagonal boron nitride and transition metal dichalcogenides (*e.g.*, molybdenum disulfide). This chapter provides insights into the use of nanoporous 2D materials containing nanopores of varying sizes, for gas separation applications.

In the next chapter, I will further extend the theoretical prediction of gas permeation through a single graphene nanopore to that through a large pore ensemble with a realistic pore size distribution, including comparing with the experimental results to gain a deeper insight.

3.9 Methods

MD simulations were carried out using the large-scale atomic/molecular massively parallel simulator (LAMMPS).[174] The structures of the graphene pores are shown in Figure 3-3b, c, d. These pores are chosen to be circular because a circular pore shape is preferred during the etching of graphene.[35] Further, these pores are also considerably larger than the gas kinetic diameters because this chapter focuses on the non-activated transport regime, and the effect of the energy barrier associated with crossing the pore needs to be avoided. The diameter of the pore is defined as the in-plane distance between two opposing hydrogen atoms minus the van der Waals diameter of a hydrogen atom (0.22 nm).[208] The atoms in the porous graphene sheets were kept frozen during the simulation in order to clearly identify the positions of different regions (the bulk, the adsorption layer, and the pore mouth) with respect to the pore. Note that, in practice, graphene has out-of-plane thermal fluctuations of ~ 0.5 nm in amplitude and ~ 50 nm in wavelength,[209,210] corresponding to a tilting angle within 2°. Because the graphene pores investigated in this chapter contain a large number of missing hexagons, the thermal fluctuations are considered as a minor perturbation, which should not affect the validity of the results. Even for small sub-nanometer graphene pores where thermal fluctuation effects should be more pronounced, freezing the motion of the carbon atoms in the graphene layer does not lead to a significant change in gas permeance (Section 2.5). Several gas molecules (200, 400, 600, or 1000) were evenly distributed in the two compartments and then allowed to diffuse through the nanopores. The simulated gases include CO_2, CH_4, and Ar. The simulations were carried out in the NVT ensemble using the Nose-Hoover thermostat with a time constant of 0.2 ps, within the temperature range of 300 K to 600 K.[175] The time step was 2 fs. The trajectories of all the gas molecules were recorded every 0.4 ps for a total simulation time of 5 ns.

All-atom force fields were used to describe the atomic interactions in the simulation, including bonded and non-bonded interactions. Bonded interactions include harmonic bonds and harmonic valence angles. The elementary physical model 2 (EPM2 model) was used for the stretching and the bending constants of CO_2,[155] and the all-atom-optimized potentials for liquid simulations (OPLS-AA model) was used for CH_4.[168] Non-bonded interactions include Lennard-Jones potentials and point-charge-based electrostatic potentials. The transferable potential for phase equilibria (TraPPE) force

field[154] is adopted for the non-bonded interaction parameters of CO_2, and the OPLS-AA force field[168] for Ar. These force fields can reproduce the liquid-vapor equilibrium of the gas species, which is required in order to simulate the condensed adsorption phase on the graphene surface. The carbon atoms in the graphene lattice were modeled as uncharged atoms using the Lennard-Jones parameters reported by Cheng and Steele.[171] The carbon and the hydrogen atoms at the pore edge were modelled as charged, and their Lennard-Jones parameters and Coulombic partial charges were assigned values corresponding to the aromatic carbon (sp^2 carbon) in the AMBER force field.[173] The cutoff distance for the Lennard-Jones interactions was 1.2 nm. Long-range electrostatic interactions were treated using the Particle-Particle-Particle Mesh (PPPM) method.[211] Periodic boundary conditions were utilized in all directions. Geometric combining rules were implemented to describe the non-bonded interactions between different atoms.

3.10 Appendices

3.10.1 Adsorption Isotherms of Gases on Graphene

Figure 3-9 shows the adsorption isotherms of CO_2, CH_4, and Ar on the graphene basal plane at 300 K. No saturation behavior is observed in the pressure range studied. Therefore, the surface adsorption concentration can be treated as a linear function of pressure, and the surface Henry's coefficient (the slope) can be treated as a being constant. The surface Henry's coefficients of CO_2, CH_4, and Ar at 300 K are 9.8×10^{11}, 6.3×10^{11}, and 5.6×10^{11} molecule m^{-2} Pa^{-1}, respectively.

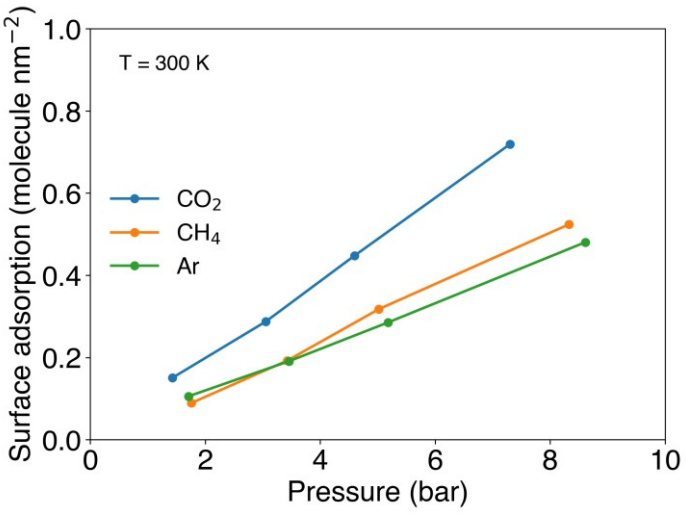

Figure 3-9. Adsorption isotherms of CO_2, CH_4, and Ar on the graphene surface at 300 K.

3.10.2 Velocity Distribution of Adsorbed Gas on Graphene

Figure 3-10 shows the velocity distributions of CO_2 molecules adsorbed on the graphene surface in the *x*, *y*, and *z* directions at 300 K. The red curves are fitting results following normal distributions. The *x* and *y* velocities follow the Maxwell-Boltzmann distribution, which is a normal distribution. The mean is close to 0, and the standard deviation is close to $\sqrt{k_B T/m}$ (238 m s^{-1} for CO_2 at 300 K), where k_B is the Boltzmann constant, T is the absolute temperature, and m is the molecular mass. However, the velocity distribution in the *z* direction is distorted from a normal distribution due to the van der Waals gas-graphene interaction operating in the *z* direction.

The correlation coefficient of the *x* and *y* velocities is then evaluated with corresponding random variables v_x and v_y, respectively. The correlation coefficient ρ_{xy} between v_x and v_y is given by:

$$\rho_{xy} = \frac{\mathrm{cov}(v_x, v_y)}{\sigma_x \sigma_y} = \frac{E(v_x v_y) - E(v_x)E(v_y)}{\sigma_x \sigma_y} \tag{3-33}$$

where E denotes the expectation value, and σ_i denotes the standard deviation of v_i, where $\sigma_i = \sqrt{E(v_i^2) - E(v_i)^2}$. The correlation coefficient between v_x and v_y is 0.003, indicating that the *x* and *y* velocities are independent variables.

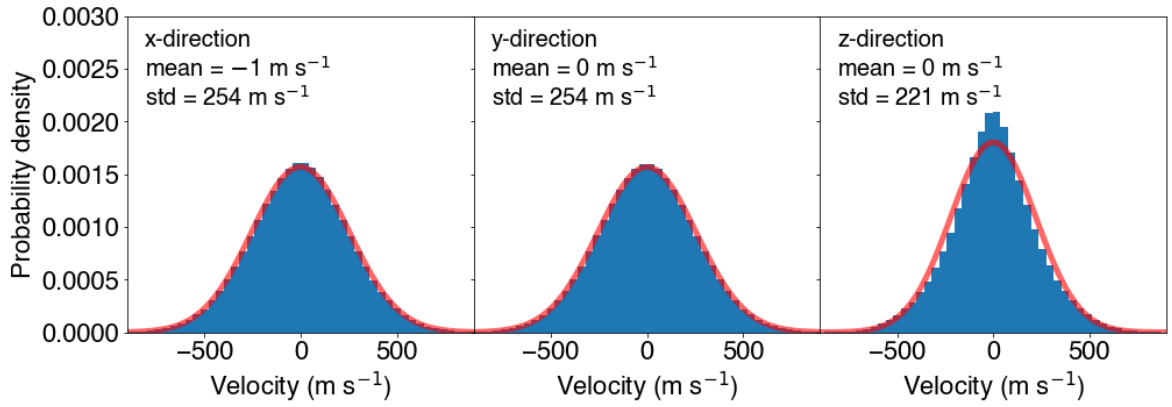

Figure 3-10. Velocity distributions of CO_2 molecules adsorbed on the graphene surface in the *x*, *y*, and *z* directions at 300 K.

3.10.3 Selection of the Gas Adsorption Layer Thickness on Graphene

Figure 3-11 shows the density distribution of CO_2, CH_4, and Ar near the graphene plane. The density in the adsorption layer peaks at ~0.35 nm, and approaches bulk density at around 0.6 nm. Therefore, 0.7 nm is chosen as the thickness of the adsorption layer for all the three gases.

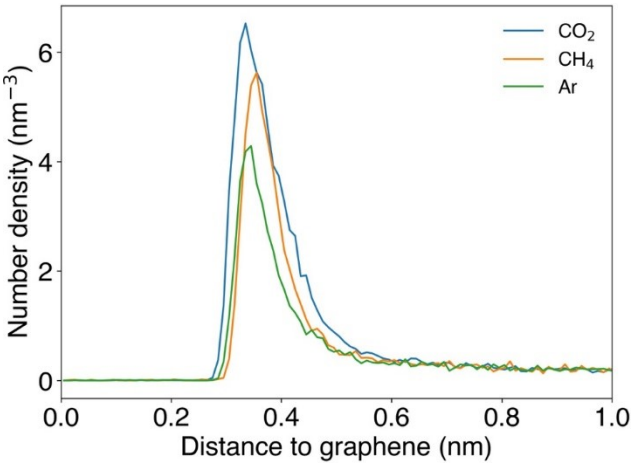

Figure 3-11. Number densities of CO_2, CH_4, and Ar as a function of the vertical distance to the graphene plane.

Figure 3-12 shows that, at 300 K, the direct impingement and the surface diffusion pathways contributions to the total CO_2 permeation per pore are slightly affected by the thickness h of the adsorption layer. This indicates that my analysis of the direct impingement and the surface diffusion pathways is relatively insensitive to the choice of the adsorption layer thickness h. In Chapter 3, h = 0.7 nm (Figure 3-11).

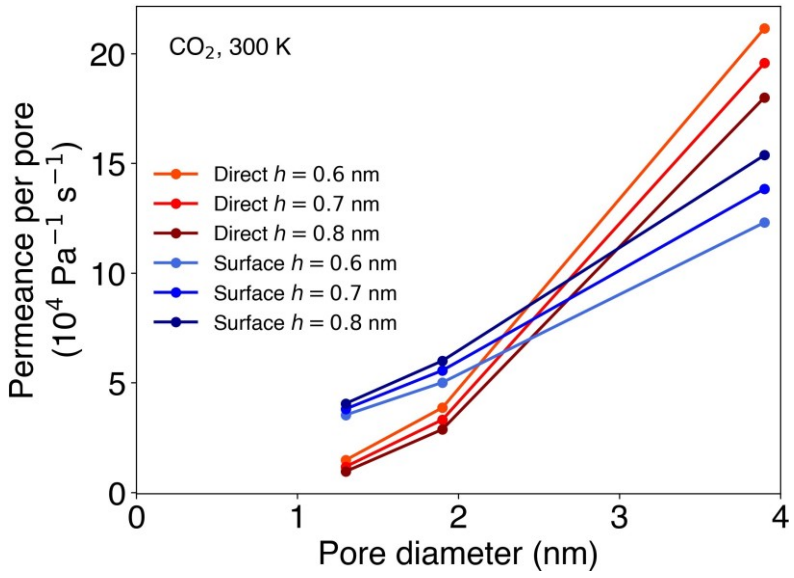

Figure 3-12. Contributions of the direct impingement and the surface diffusion pathways to the CO_2 permeance per pore for different adsorption layer thickness choices at 300 K.

3.10.4 Confidence Interval Calculation

In this chapter, it is assumed that each permeation event occurs independently and randomly because the time interval between each permeation event through one pore is at most 3.5 ps. As a reference, the characteristic time scale for a gas molecule to collide with another is ~ 30 ps, given that the mean free path at 10 bar is ~10 nm, and that the average velocity is ~300 m s^{-1}. Therefore, each permeation event is treated as being unaffected by other gas molecules.

The total occurrence number k of a random event with a given rate in a period of time follows the Poisson distribution with a single rate parameter λ. The probability distribution function f can be expressed as follows:

$$f(k) = \frac{\lambda^k e^{-\lambda}}{k!} \tag{3-34}$$

The expectation value $E(k) = \lambda$. In turn, the maximum likelihood estimation of λ is k.

In my MD simulations, I count the total occurrence number k of a particular event (*e.g.,* gas permeation through graphene nanopores). The confidence interval for λ with confidence level $1 - \alpha$ can be estimated as:

$$\frac{1}{2}\chi^2(\alpha/2; 2k) \leq \lambda \leq \frac{1}{2}\chi^2(1-\alpha/2; 2k+2) \tag{3-35}$$

where $\chi^2(p; n)$ is the quantile function of the χ^2 distribution with n degrees of freedom.[212] I then derive the rate according to the confidence interval of the rate parameter λ.

3.10.5 Details of the Gas Permeation Analysis

Figure 3-13 shows the contributions of the direct impingement and the surface diffusion pathways to the total gas permeance per pore for (a) CH_4 and (b) Ar. Similar to the CO_2 case, the direct impingement pathway portion scales non-linearly with the pore diameter, while the surface diffusion pathway portion scales nearly linearly with the pore diameter (auxiliary lines to the origin are drawn to show the linearity). This is consistent with my theoretical prediction in Equations (3-21) and (3-22).

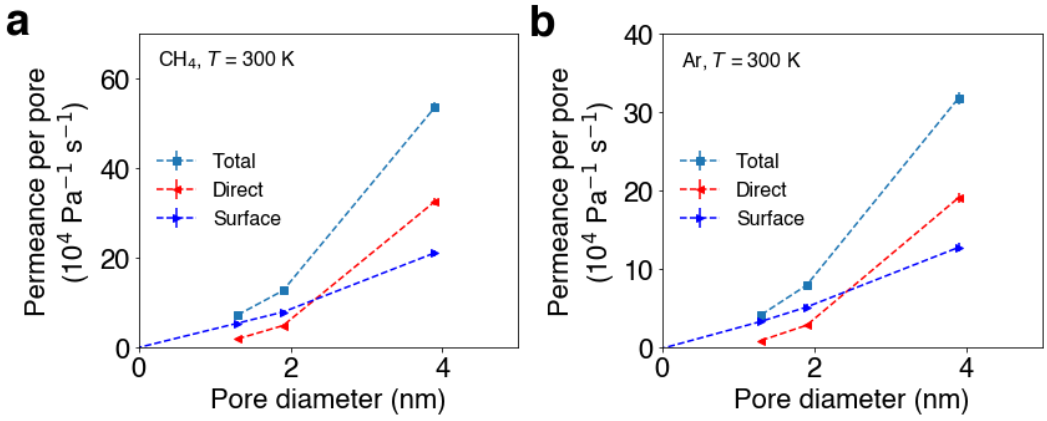

Figure 3-13. Contributions of the direct impingement and the surface diffusion pathways to the total (a) CH_4 and (b) Ar permeances per pore at 300 K.

Figure 3-14 provides supplementary information of the CH_4 and Ar gases for Figure 3-5 in the main text. Figure 3-14a, b are similar to Figure 3-5b. The theory (Equation (3-21)) slightly underpredicts the rate of direct impingement attempts (green vs. orange dashed curves), and only a fraction of the direct impingement attempts results in successful permeation (blue dashed curve). Figure 3-14c, d show the positive correlation between the success ratio δ of the direct impingement pathway and the pore diameter for CH_4 and Ar, respectively. The correlation is not affected by the temperature. In Figure 3-14e, f, the difference between the simulated and the predicted direct pathway impingement attempts is plotted as a function of temperature for CH_4 and Ar, respectively. Note that the difference is a decreasing function of temperature and an increasing function of the pore diameter, instead of being random, similar to the CO_2 case (Figure 3-5d). In the Ar case (Figure 3-14f), due to its low adsorption on graphene (compared to CO_2, Figure 3-11) and its high molecular weight (compared to CH_4), Ar has a low surface diffusion rate. As discussed in the main text, the difference observed in Figure 3-14f is related to the surface diffusion pathway. As a result, the weak surface diffusion of Ar leads to a high error in Figure 3-14f.

Figure 3-15 provides supplementary information for Figure 3-6 in the main text. Figure 3-15a, b are similar to Figure 3-6a, and show that the gas permeance contributed by the surface diffusion pathway decays rapidly with increasing temperature. Figure 3-15c, d are similar to Figure 3-6c, and show that the rates of both steps along the surface diffusion pathway are significantly lower than the theoretical prediction shown in Equation (3-22). Figure 3-15e, f show that the injection coefficients γ_{inj}, for both

D_p = 1.3 and 3.9 nm, are increasing functions of temperature, indicating that the injection step is associated with climbing an energy barrier. Figure 3-15g, h show that the transfer ratios γ_{trans}, for both CH_4 and Ar, are independent of temperature and positively correlated to the pore diameter, similar to Figure 3-6f.

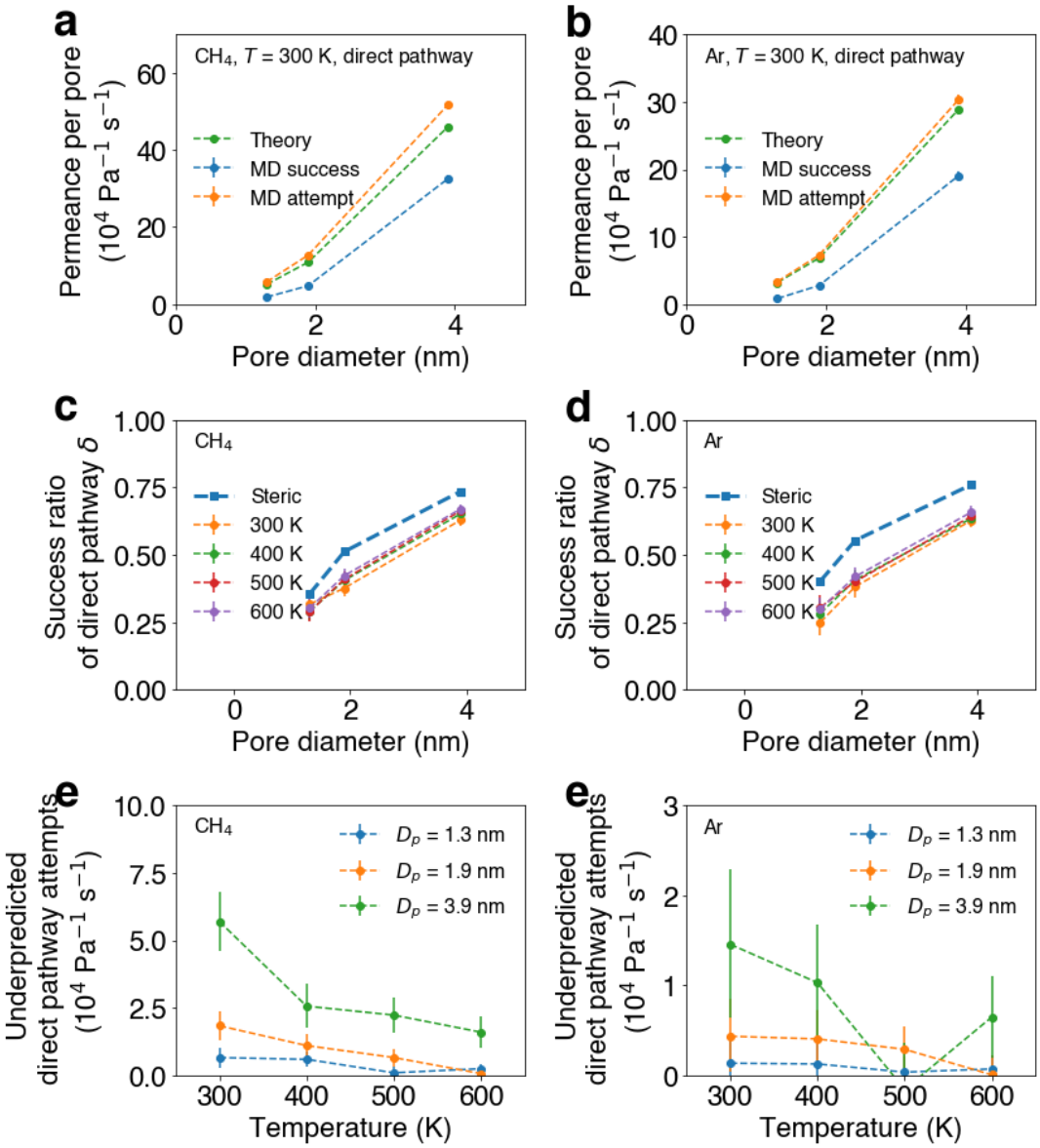

Figure 3-14. Comparison of the permeances per pore contributed by the direct impingement pathway obtained using MD simulations and the theory for (a) CH_4 and (b) Ar at 300 K. Comparison of the success ratios of the direct impingement pathway obtained using MD simulations and the steric selectivity theory reported in Chapter 5 (Appendix 5.6.1) for (c) CH_4 and (d) Ar as functions of pore diameter at various temperatures. Deviations of the theoretical predictions (Equation (3-21)) from the MD simulation-observed permeation attempts for (e) CH_4 and (f) Ar as functions of temperature for various pore diameters.

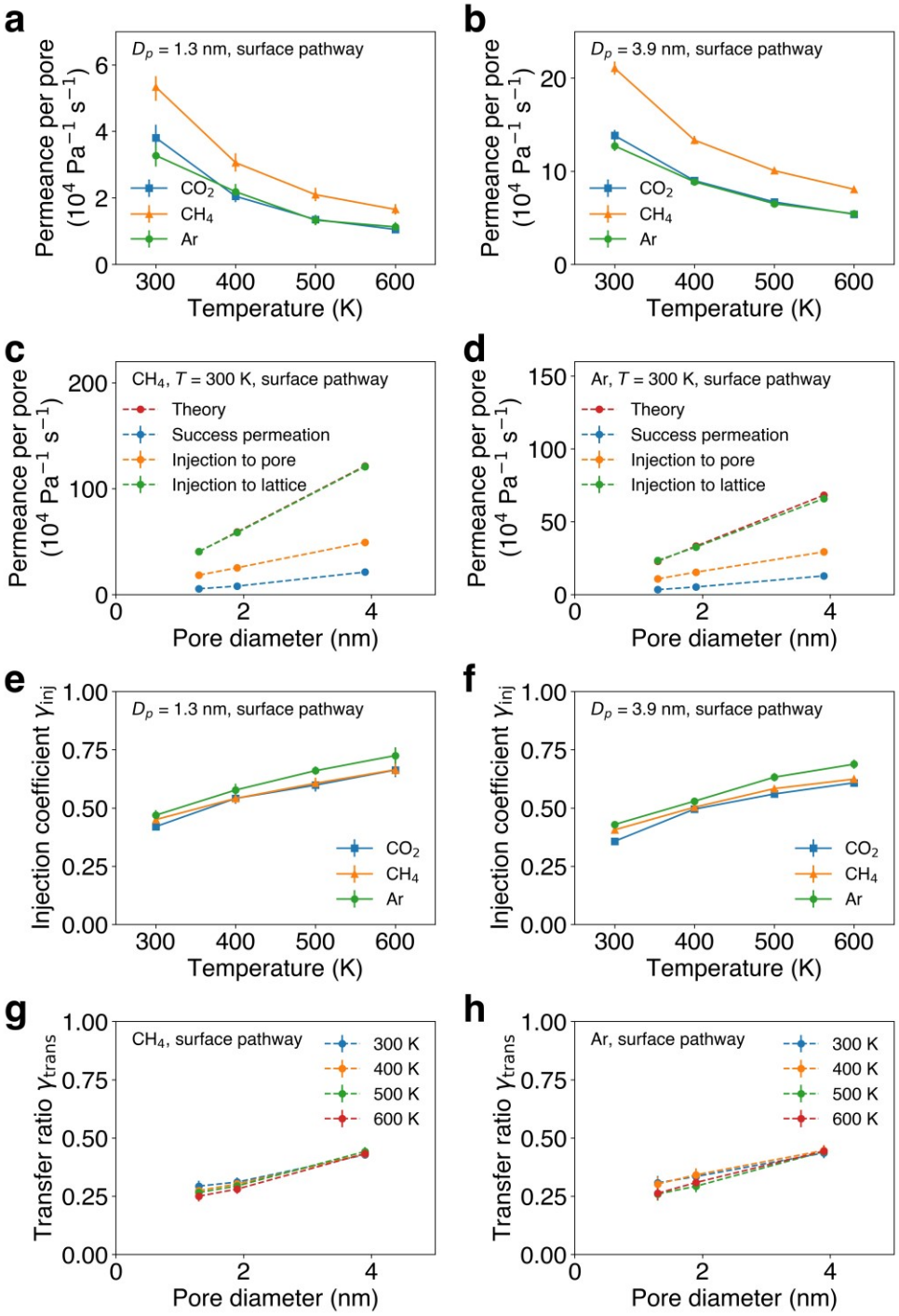

Figure 3-15. Permeance per pore contributed by the surface diffusion pathway as a function of temperature for CO_2, CH_4, and Ar when the pore diameter is (a) 1.3 nm and (b) 3.9 nm. Comparison of the permeance per pore contributed by the surface diffusion pathway obtained using MD simulations and the theoretical predictions as a function of pore diameter for (c) CH_4 and (d) Ar at T = 300 K. Injection coefficient corresponding to the surface diffusion pathway γ_{inj} as a function of temperature for the three gases considered for (e) D_p = 1.3 nm and (f) D_p = 3.9 nm. Transfer ratio corresponding to the surface diffusion pathway γ_{trans} as a function of pore diameter for (g) CH_4 and (h) Ar at various temperatures.

3.10.6 Fitting Process for the Minor Spillover Pathway

Figure 3-16 shows the fitting process of the power law estimation $K_{\text{minor}} = aK_{1,\text{theory}}^{b}K_{2,\text{theory}}^{c}$, where the gas permeance per pore associated with the minor spillover pathway K_{minor} depends on both the direct impingement pathway ($K_{1,\text{theory}}$) and the surface diffusion pathway ($K_{2,\text{theory}}$). In Figure 3-16, K_{minor} (z axis), $K_{1,\text{theory}}$ (x axis), and $K_{2,\text{theory}}$ (y axis) data points of all the {gas, pore, temperature} combinations are plotted in logarithmic scale. A power law indicates that the data points align on a certain plane.

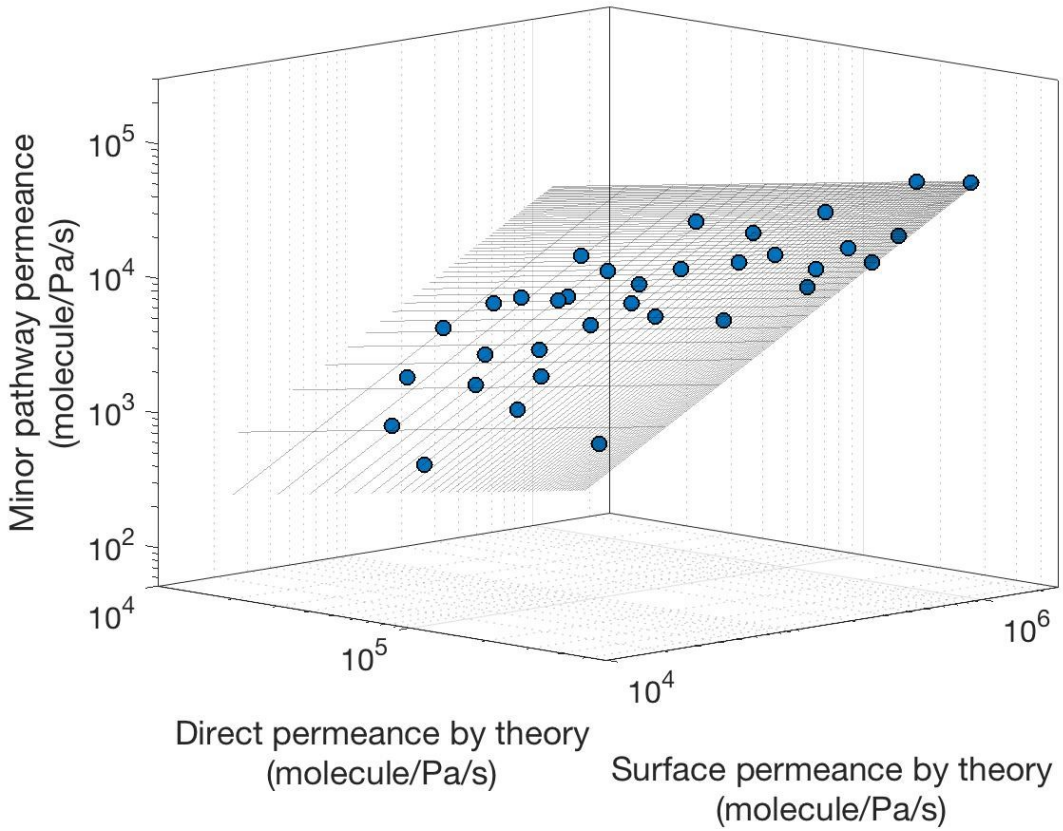

Figure 3-16. Gas permeances per pore associated with the minor spillover pathway K_{minor} (z axis), with the direct impingement pathway predicted by theory $K_{1,\text{theory}}$ (x axis), and with the surface diffusion pathway predicted by theory $K_{2,\text{theory}}$ (y axis) plotted in logarithmic scale. Each data point corresponds to one type of gas molecule, one temperature, and one pore diameter.

3.10.7 Overall Permeance Prediction of Other Gases and Temperatures

Figure 3-17 provides supplementary information for Figure 3-8 in the main text. Figure 3-17a, b show the deconvolution of the permeance per pore of CH_4 and Ar at 300 K into its translocation, direct impingement, and surface diffusion components. As shown in Figure 3-17a, b, the transition pore diameter from the translocation-dominated regime to the surface diffusion-dominated regime is 0.76 and 0.78 nm for CH_4 and Ar, respectively. This transition pore diameter is greater for larger gas molecules (CH_4, Ar), because the translocation energy barrier is present up to this transition point. In addition, this transition pore diameter increases as the temperature increases, because higher temperatures mitigate the effect of the energy barrier according to the Arrhenius equation. As shown in Figure 3-17c, the transition pore diameter from the translocation-dominated regime to the surface diffusion pathway-dominated regime for CO_2 at 400 K is 0.78 nm as compared to 0.72 nm at 300 K (Figure 3-8a). Figure 3-17d shows that a reasonable separation factor (> 5) can only be attained with a pore diameter less than 0.56 nm, which is more stringent compared to 0.60 nm at 300 K (Figure 3-8b).

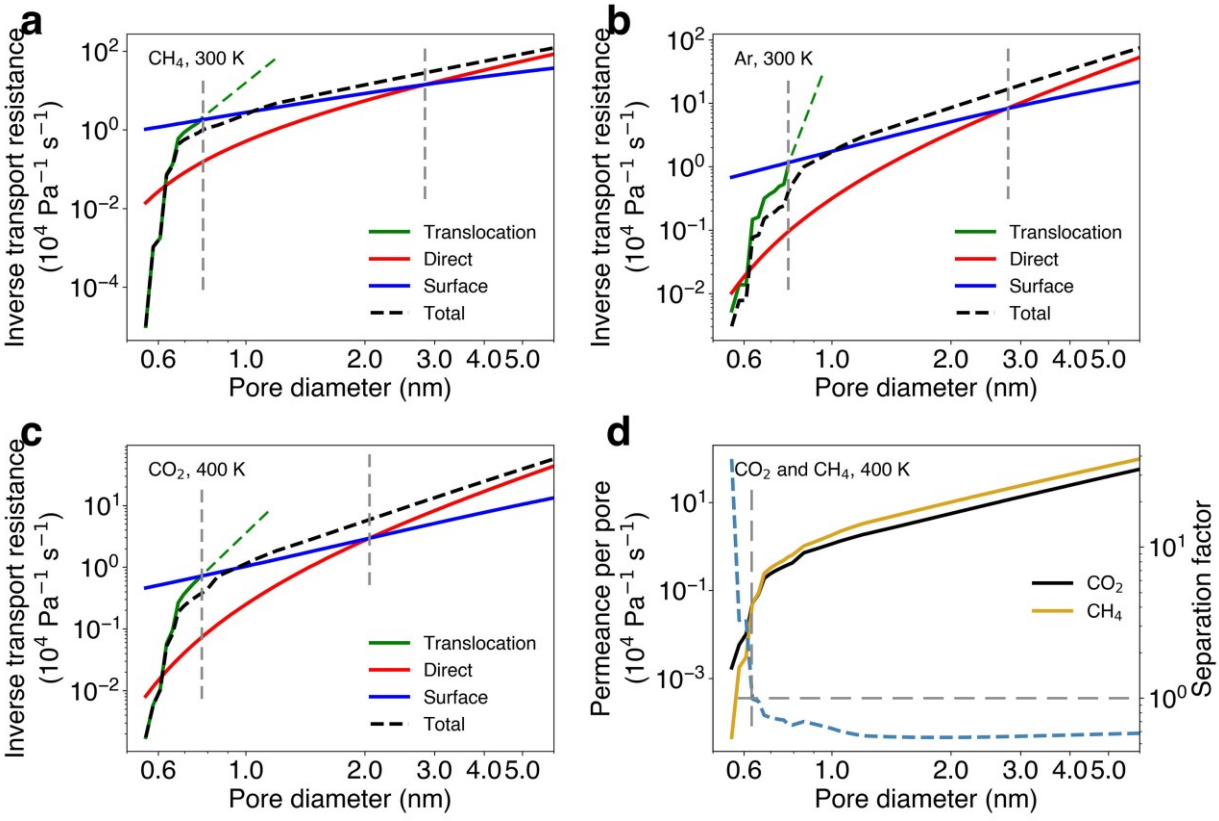

Figure 3-17. Inverse transport resistances associated with the translocation (green), the direct impingement (red), and the surface diffusion (blue) pathways, and the overall permeance per pore (black) as a function of pore diameter for (a) CH_4 at 300 K, (b) Ar at 300 K, and (c) CO_2 at 400 K. The two

perpendicular grey dashed lines separate three transport regimes, from left to right: translocation dominated, surface diffusion pathway dominated, and direct impingement pathway dominated, from left to right. (d) Permeance per pore of CO_2 and CH_4, and corresponding separation factor as a function of pore diameter at 400 K. The horizontal and perpendicular grey dashed lines denote the pore diameter value at which the permeances per pore for CO_2 and CH_4 are equal.

4 Predicting Gas Separation through Graphene Nanopore Ensembles with Realistic Pore Size Distributions

4.1 Introduction

Nanoporous single-layer graphene shows high promise as a next-generation gas separation membrane, primarily due to its atomic thickness.[24,26,27] Compared to the pore matrices inside conventional polymer membranes, nanopores in single-layer graphene have negligible pore lengths. As a result, gas transport through graphene nanopores experiences minimal internal resistance, and is instead dominated by the transport resistances at the pore entrance and the pore exit (Chapters 2 and 3). The minimal internal transport resistance across the pore makes nanoporous single-layer graphene potentially highly permeable to gases.[25] With an appropriate pore size distribution and a high areal pore density, a nanoporous single-layer graphene membrane can surpass the permeance-selectivity Robeson upper bound (Figure 2-7) for conventional polymer membranes,[122] thereby highlighting its potential for gas separation applications.[1,5]

The dominance of the entrance/exit transport resistances leads to a fundamentally different theoretical description of gas permeation through a graphene nanopore compared to that through a thick polymer membrane. The solution-diffusion model describes the permeation of gas molecules through polymer membranes, where the interior diffusive resistance is dominant.[34] In contrast, for graphene nanopores, Chapter 3 shows that the total gas transport resistance can be decomposed into three components: the translocation resistance related to the cross-pore energy barrier, the direct impingement resistance, and the surface diffusion resistance. Specifically, I demonstrate that the diameter of a graphene nanopore needs to be lower than 0.6 nm in order to achieve a moderate CO_2/CH_4 selectivity greater than 5 (Figure 3-8). Below this diameter threshold, gas permeation through graphene nanopores is governed by the translocation energy barrier, which can be predicted by the transition state theory, given an all-atom force field (Chapter 2). Using this theoretical framework, I show that the gas separation performances of two individual graphene nanopores fabricated by Koenig *et al.*[109] are close

to, albeit lower than, the permeance-selectivity upper bound predicted for graphene nanopores (Figure 2-7).

Interestingly, as the relevant datasets transition from investigating individual nanopores to investigating a large number of nanopores in a membrane, and from measurements at room temperature to measurements at a series of temperatures, my theoretical predictions face challenges in matching every experimental observation. The first challenge is that there is not always a representative nanopore structure that yields a similar selectivity of a gas pair as that observed experimentally. For example, Huang *et al.* and Zhao *et al.* measured H_2/CH_4 selectivities ranging from 5 to 25 using single-layer graphene membranes containing millions to billions of nanopores.[120,122] However, my theory cannot assign every selectivity value to an individual nanopore structure, because nanopores are formed in specific shapes and sizes and their selectivities vary discretely, rather than in a continuous manner.[35] Another challenge is that my theory cannot reproduce the apparent energy barriers that are directly derived by fitting experimentally measured gas permeances at different temperatures to the Arrhenius equation. To be more precise, multiple studies conducted by myself (Chapter 5) and others[120,122] have shown that almost all the experimental gas permeances increase as a function of temperature, which is indicative of positive apparent energy barriers based on the Arrhenius equation. Specifically, apparent energy barriers between 10 and 30 kJ mol^{-1} have been measured for He, H_2, CO_2, and CH_4, respectively, and their values appear invariant regardless of how the nanopores were created.[120,122,128] Unfortunately, my previous theoretical calculation results cannot identify a nanopore that matches all the apparent energy barriers simultaneously, assuming that the nanopore structure does not change as a function of temperature.

The two challenges discussed above clearly indicate that it is not sufficient to approximate a large pore ensemble as a single pore. When created randomly in a graphene lattice by an etching method (the most common scalable way to create nanopores), the nanopores are distributed in terms of their sizes and shapes, instead of being identical.[35,115,131,137] Here, the nanopore size refers to the number of carbon atoms removed from the pristine graphene lattice. Due to the randomness of the etching events, when the pore diameter is within 1 nm, the pore size distribution is usually positively skewed (*i.e.*, the right tail is longer), and is typically fitted to a lognormal or Poisson distribution.[121,132] In addition, Rajan *et*

al. has previously shown that multiple nanopore isomers with different pore shapes may exist for the same pore size, and that their relative populations can be predicted by a Kinetic Monte Carlo (KMC) algorithm.[35] The predicted most-probable isomers match transmission electron microscopy (TEM) images of graphene nanopores with high consistency for each pore size, demonstrating the ability of the KMC algorithm to model the real pore etching kinetics encountered in the experiments.[35]

The pore size and pore shape distributions result in variations in the gas permeance through the nanopores in a nanopore ensemble. Accordingly, in this chapter, in order to predict the overall gas permeance through a nanopore ensemble, I propose to (i) simulate the pore size and shape distributions of nanopores generated by graphene etching, (ii) predict the gas permeance through each nanopore, (iii) add up the permeances, and (iv) compare the predicted total gas permeances and selectivities to those measured experimentally. In more detail, I generate a large number of graphene nanopore structures *in silico* using the KMC etching algorithm developed recently by Rajan *et al*.[35] The principal knob that is varied during nanopore generation in the simulations is the etching time *t*. The generated nanopores are then checked for uniqueness using a previously developed cataloging algorithm based on chemical graph theory.[35] Subsequently, the permeances of H_2, CO_2, and CH_4 through each unique nanopore at temperatures ranging from 30 to 150 °C are calculated according to Chapters 2 and 3. These three gases are chosen because their separations are crucial in commodity-scale chemical processes, such as synthetic gas and natural gas processing.[7,139] I then evaluate the effect of the etching time *t* and the temperature on the gas permeances and the selectivities of the generated nanopore ensembles. Finally, I attempt to fit the theoretical predictions to available experimental datasets, and propose that the graphene nanopores should be allowed to effectively expand at a higher temperature in order to better fit the experimental data. A partial pore clogging hypothesis is also proposed to explain the expansion of the nanopores with temperature.

4.2 Generating Pore Ensembles

Consider a nanopore ensemble consisting of N nanopores (i = 1, 2, …, N), with their respective gas permeances per pore Π_i (*i.e.*, the pressure-normalized gas flow rate, unit: mol s^{-1} Pa^{-1}). The total gas

permeance $\Pi = \sum_{i=1}^{N} \Pi_i$. Using the following set of equations (Equations (4-1)–(4-4)) developed in Chapters 2 and 3, the gas permeance per pore Π_i through each nanopore i can be predicted as follows:

$$\Pi_{\mathrm{trans},i} = \frac{H_{\mathrm{pore}}(T)}{L_i}\sqrt{\frac{k_{\mathrm{B}}T}{2\pi m}}\exp\left(\frac{\Delta S_i^{\ddagger}}{k_{\mathrm{B}}}\right)\exp\left(-\frac{\Delta E_i^{\ddagger}}{k_{\mathrm{B}}T}\right) \tag{4-1}$$

$$\Pi_{\mathrm{direct},i} = \delta_i\sqrt{\frac{\pi}{2mk_{\mathrm{B}}T}}\frac{D_{\mathrm{p},i}^2}{4} \tag{4-2}$$

$$\Pi_{\mathrm{surface},i} = \gamma_i\sqrt{\frac{\pi k_{\mathrm{B}}T}{2m}}D_{\mathrm{p},i}H_{\mathrm{surf}} \tag{4-3}$$

$$\Pi_i = \left[\Pi_{\mathrm{trans},i}^{-1} + \left(\Pi_{\mathrm{direct},i} + \Pi_{\mathrm{surface},i}\right)^{-1}\right]^{-1} \tag{4-4}$$

Equation (4-1) predicts the gas transport rate $\Pi_{\mathrm{trans},i}$ (normalized by the pressure difference) of translocation from the pore mouth on one side to that on the other side (Chapter 2). In Equation (4-1), the energy barrier $\Delta E_i^{\ddagger}$ and the entropy barrier $-\Delta S_i^{\ddagger}$ through nanopore i are calculated by fitting the Helmholtz free energy barriers $\Delta A_i^{\ddagger} = \Delta E_i^{\ddagger} - T\Delta S_i^{\ddagger}$ to temperature T, and then finding the intercepts and the slopes, respectively. The graphene–gas interactions are modelled at an all-atomistic level using Lennard-Jones potentials. For simplicity, in the calculations, the nanopores are assumed to be non-terminated. Additional details about the calculation of the Helmholtz free energy profile are provided in the Section 4.6.2. Furthermore, in Equation (4-1), H_{pore} represents the average number of gas molecules adsorbed to the pore mouth per unit bulk pressure under adsorption equilibrium, and L_i is the full width at half maximum of the partition function of the gas–pore system, $Q_i(z)$, as a function of the gas molecule's vertical distance to the graphene basal plane, z. Note that $Q_i(z) = \exp[-A_i(z)/k_{\mathrm{B}}T]$, where $A_i(z)$ is the Helmholtz free energy profile associated with pore crossing for nanopore i (see Section 4.6.2 for additional details). Other parameters in Equation (4-1) include k_{B}, the Boltzmann constant, and m, the molecular weight of the gas molecule. It is worth noting that the entropy barrier $-\Delta S_i^{\ddagger}$ is, in fact, a key contributor to the gas separation and should not be ignored (see Appendix 4.7.1 for more details).

Equation (4-2) predicts the direct impingement rate of gas molecules approaching the nanopore from the bulk, where $D_{\mathrm{p},i}$ is the equivalent pore diameter and δ_i is a correction factor accounting for the success rate of the direct impingement attempts (Section 3.4, see also Section 4.6.2 for additional details

about $D_{p,i}$ and δ_i). Equation (4-3) predicts the surface diffusion rate of gas molecules approaching the nanopore along the graphene surface, where H_{surf} is the areal density of gas molecules adsorbed on the "bulk" graphene surface (far away from the nanopore) per unit bulk pressure, and γ_i is a correction factor accounting for the success rate of the surface diffusion pathway (Section 3.5, see also Section 4.6.2 for additional details about γ_i). The values of H_{pore} and H_{surf} can be calculated based on the Helmholtz free energy profile of gas molecules (Section 4.6.2). The gas permeance per pore Π_i is then derived according to Equation (4-4). In this chapter, $\Pi_{trans,i}$ is typically much smaller than $\Pi_{direct,i}$ + $\Pi_{surface,i}$, because the nanopores are sufficiently small and the energy and entropy barriers make the translocation step rate-determining ($\Pi_i \approx \Pi_{trans,i}$). Utilizing Equations (4-1)–(4-4), the permeance per pore Π_i through each nanopore in an ensemble is predicted for H_2, CO_2, and CH_4.

One important metric to characterize the temperature dependence of the total permeance of a nanopore ensemble Π is the average energy barrier $\overline{\Delta E^{\ddagger}}$. Note that $\overline{\Delta E^{\ddagger}}$ is equal to the average of the energy barriers of all the nanopores weighted by their respective gas permeances (see Appendix 4.7.2 for the derivation):

$$\overline{\Delta E^{\ddagger}(T)} = \frac{\sum_{i=1}^{N} \Pi_i(T) \Delta E_i^{\ddagger}}{\sum_{i=1}^{N} \Pi_i(T)} \tag{4-5}$$

Note that because the gas permeance through an individual nanopore Π_i is temperature dependent, the average energy barrier $\overline{\Delta E^{\ddagger}}$ is strictly temperature dependent as well. However, when the pore sizes have a realistic distribution, $\overline{\Delta E^{\ddagger}}$ is dominated by low-energy-barrier nanopores because they weight significantly more in the sums in Equation (4-5).

The formalism above for predicting the gas permeance applies for any pore size distributions. Next, I will discuss how a realistic nanopore ensemble is generated. Pore etching simulations *in silico* were carried out using a Kinetic Monte Carlo (KMC) algorithm (Figure 4-1a; additional details are provided in Section 4.6.1). Starting from a single point defect in pristine graphene, carbon atoms were removed sequentially, at rates which were estimated according to the energy barriers provided in ref. 35. In this manner, graphene nanopore structures that match well with TEM images are generated. Typically, because there are multiple choices regarding which carbon atom to etch away at each step, the Gillespie algorithm is utilized to randomly select one of them.[213] Each possible carbon etching event *j* has a rate

r_j, and the probability that event j is chosen is r_j/r_{tot}, where r_{tot} is the sum of all the r_j values. The expected value of the time interval E(Δt) of this etching step is $1/r_{tot}$, and the time interval Δt is randomly sampled from an exponential distribution with a probability density function given by:

$$P(\Delta t) = r_{tot} e^{-r_{tot}\Delta t} \tag{4-6}$$

As shown in Figure 4-1a, the current (c) time t_c was updated after each etching event ($t_c \rightarrow t_c + \Delta t$). The iteration terminated when the current time t_c exceeded the predetermined etching time t. For each etching time t, the KMC algorithm was run repeatedly to generate 500000 nanopores separated in 50 batches of size N = 10000 each.

Figure 4-1b shows the simulated pore size distributions for etching times ranging from 20 to 60, with a batch size of 10,000. The error range represents the estimated standard deviation of the probabilities from the 50 batches. As the etching time increases, the pore size distribution shifts to the right, indicating an increase in the average pore size. Note that the etching time used here is dimensionless, because the etching rate r_j is nondimensionalized by the typical atomic vibrational frequency of 10^{13} Hz. In other words, when the prefactor of the carbon etching reaction is 10^{13} s^{-1}, the etching time t has a unit of second (Section 4.6.1). In order to achieve a considerable selectivity, the etching time cannot be too high. Otherwise, the largest non-selective nanopore will dominate the overall gas flux and make the entire nanopore ensemble non-selective. As a reference, pore size = 30 corresponds to a pore diameter of ~ 1 nm for a circular nanopore. This criterion restricts relevant etching times to be below ~ 100. In this etching time range, the probability distribution decays exponentially as the pore size increases (Figure 4-1b), and the majority of the nanopores are smaller than size 5. Further, the probability of generating larger nanopores is prone to high uncertainty, where the error range increases significantly as the pore size increases.

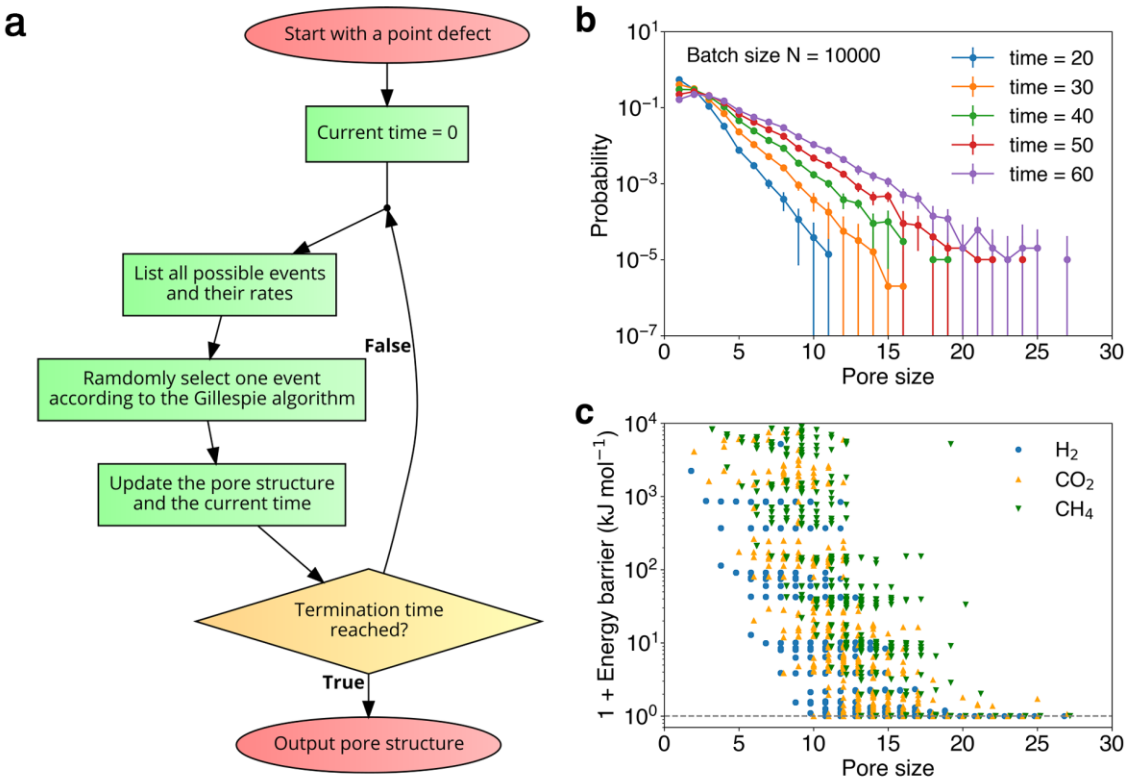

Figure 4-1. (a) Flowchart of the Kinetic Monte Carlo algorithm used to generate graphene nanopore structures with a predefined etching time. (b) Simulated size distributions of nanopores generated at various etching times. Some confidence intervals extend to negative values and are not fully shown on the log-*y* axis. (c) Scatter plot of theoretically predicted energy barrier values of H_2, CO_2, and CH_4 as a function of pore size. Each pore size corresponds to multiple isomers, and hence, to multiple possible energy barriers. Scatter points are slightly shifted horizontally to prevent overlap. The horizontal black dashed line corresponds to a zero energy barrier.

Although the larger nanopores are a minor species in the nanopore ensemble, they do not necessarily contribute a minority of the total gas permeance, because they present low energy barriers for gas permeation. Figure 4-1c shows that the simulated energy barriers of gases crossing the nanopores, $\Delta E^{\ddagger}$, decay rapidly by orders of magnitude as the pore size increases. Each pore size corresponds to multiple energy barrier values because of the existence of nanopore isomers (same size but different shapes). Some isomers with very high energy barriers have elongated shapes, and are rarely generated in my KMC algorithm. Note that on the *y* axis of Figure 4-1c one is added to the energy barrier values (in kJ mol^{-1}) in order to prevent zero-energy-barrier nanopores from disappearing on the log scale used. Those zero-energy-barrier nanopores emerge as the pore size reaches ~ 10, corresponding to a pore diameter of ~ 0.6 nm if the pore is approximately circular.

The low fraction of large nanopores in a nanopore ensemble results in a low fraction of low-energy-barrier nanopores. Figure 4-2a plots the histograms of the theoretically predicted energy barriers of H_2, CO_2, and CH_4 crossing 10,000 nanopores generated by an etching time of 30. The fractions of nanopores with relatively low energy barriers, *e.g.*, $\Delta E^{\ddagger} < 10$ kJ mol^{-1} ($\sim 4k_BT$ at room temperature) are 1.2%, 0.6%, and 0.015% for H_2, CO_2, and CH_4, respectively (Figure 4-2a). Modest change to this threshold does not affect the validity of the following findings. This ordering is consistent with the ranking of their kinetic diameters (H_2: 0.29 nm, CO_2: 0.33 nm, CH_4: 0.38nm), because a smaller gas molecule is less impeded from crossing the nanopores. Due to the stochasticity during nanopore generation, the fraction of the low-energy-barrier nanopores has a high relative error, especially when the etching time is short (Figure 4-2b, c, d). Figure 4-2b, c, d also show that the fraction of low-energy-barrier nanopores generally increases as the etching time increases, in accordance with the pore size distribution shown in Figure 4-1b.

For each nanopore ensemble generated with each etching time t, I predict the individual gas permeances Π_i through every nanopore and the total permeance Π using Equations (4-1)–(4-4). In order to evaluate the unevenness of the gas permeance distribution in a nanopore ensemble, I plot the Lorenz curves of the permeance distributions of H_2, CO_2, and CH_4 through different nanopore ensembles at two temperatures, 30 °C and 150 °C (Figure 4-3). The Lorenz curve was developed by Max O. Lorenz to represent income inequality.[214] It plots the percentiles of population on the x-axis according to income, and the cumulative income on the y-axis. Here, I borrow this concept and plot the percentiles of nanopores ordered from low to high gas permeance on the x-axis, and the proportion of their cumulative gas permeance on the y-axis. Figure 4-3a shows the Lorenz curves of the theoretically predicted H_2, CO_2, and CH_4 permeance distributions through the nanopore ensemble generated with etching time t = 20 at 30 °C and 150 °C. As indicated by the light blue (30 °C) and dark blue (150 °C) curves in Figure 4-3a, 0.3% of the nanopores contribute almost 100% of the total H_2 permeance. This percentage of permeable nanopores is 0.2% for CO_2 (orange and red curves), and is 0.01% for CH_4 (green and dark green curves) when the etching time is 20 (Figure 4-3a). As the etching time increases, the fraction of permeable nanopores increases, but remains lower than 15% even for an etching time of 80 (Figure 4-3b, c). This trend is also illustrated in Figure 4-3d, e, f, where the Lorenz curves shift to the upper-

left as the etching time increases. Generally, the permeance distribution of H_2 is the most even among those of the three gases considered due to its smallest kinetic diameter, while that of CH_4 is the most uneven due to its largest kinetic diameter.

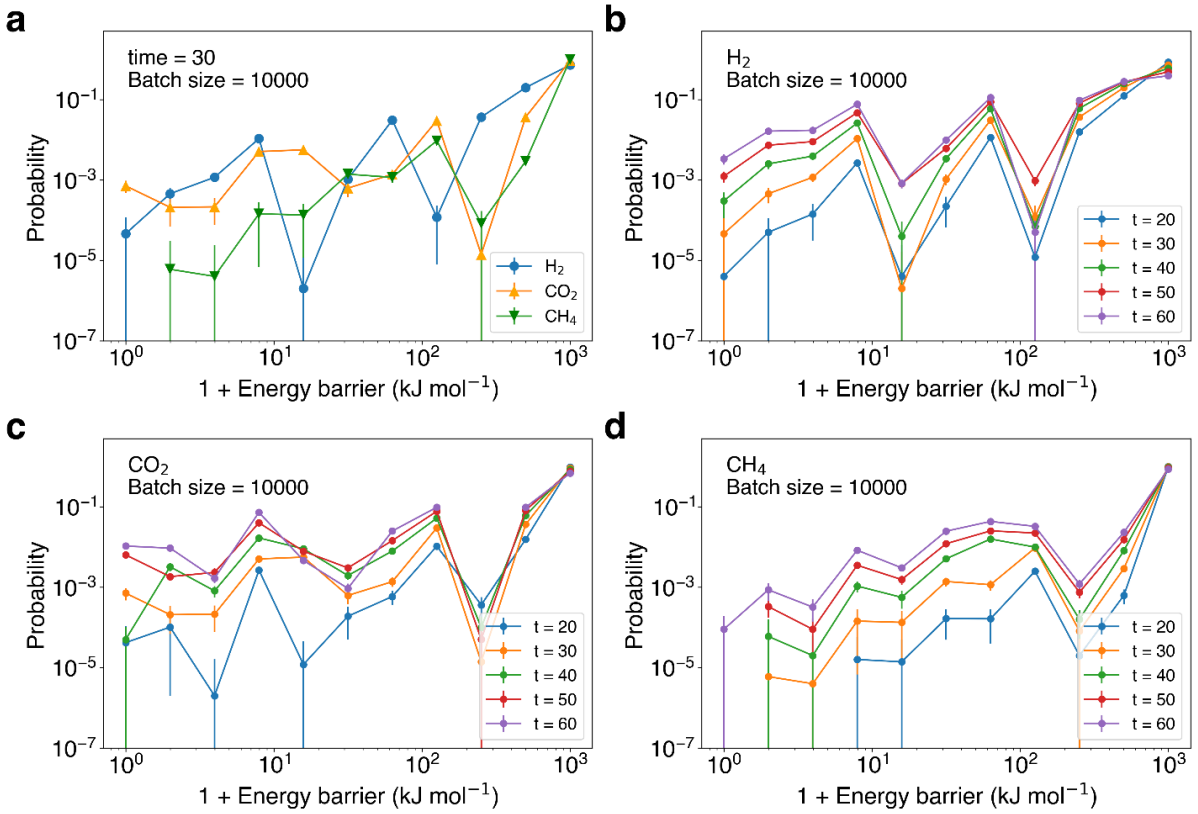

Figure 4-2. (a) Distribution of theoretically predicted energy barriers of pore crossing for H_2, CO_2, and CH_4 with etching time = 30. Distribution of energy barriers of pore crossing for (b) H_2, (c) CO_2, and (d) CH_4 with etching time from 20 to 60. Energy barriers greater than 10^3 kJ mol^{-1} are treated as 10^3 kJ mol^{-1}. Missing datapoints indicate zero nanopores in the corresponding bins.

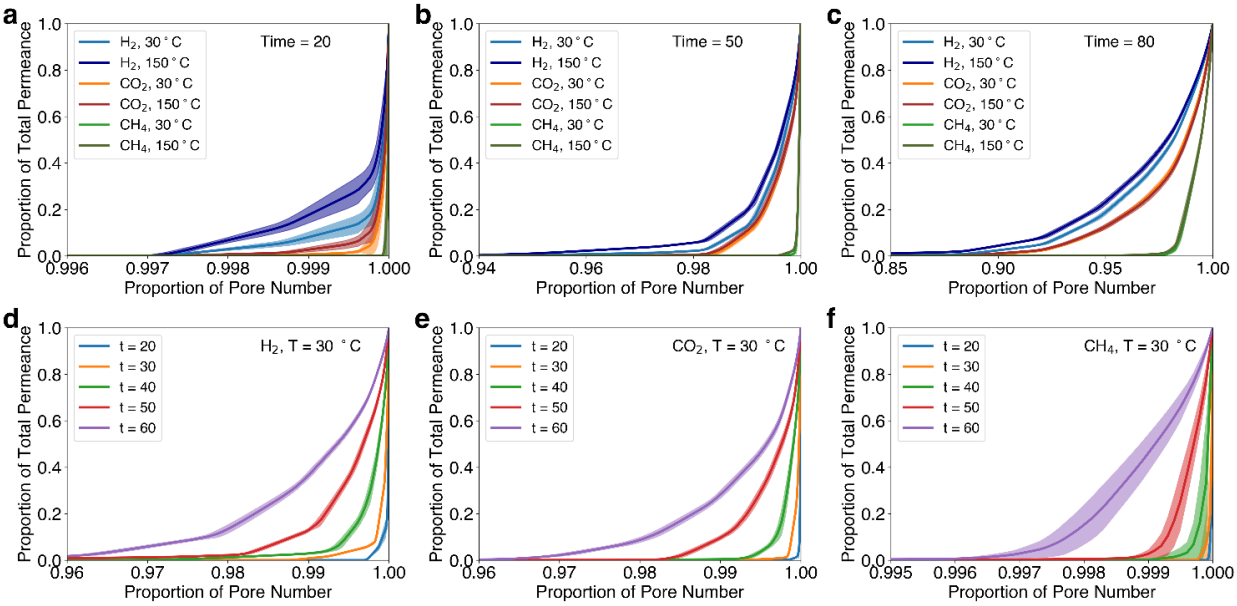

Figure 4-3. Lorenz curves of theoretically predicted H_2, CO_2, and CH_4 permeance distributions at 30 and 150 °C for nanopore ensembles generated with etching times of (a) 20, (b) 50, and (c) 80, respectively. Lorenz curves of theoretically predicted (d) H_2, (e) CO_2, and (f) CH_4 permeance distributions at 30 °C for nanopore ensembles generated with various etching times from 20 to 60.

4.3 Predicted Gas Permeance and Selectivity through Pore Ensemble

As demonstrated in Figure 4-1b and Figure 4-2, a longer etching time t leads to a higher fraction of large and low-energy-barrier nanopores. Therefore, the theoretically predicted gas permeance of a nanopore ensemble is positively correlated with the etching time (Figure 4-4a, b). At both 30 and 150 °C, H_2 exhibits the highest permeance per pore (averaged over the entire ensemble) for $20 < t < 80$, while the permeances per pore of CO_2 and CH_4 rank intermediate and lowest, respectively. The gas permeance exhibits much greater variance for a short etching time t, for which the probability of generating low-energy-barrier nanopores is low and has a large variance. On the other hand, as shown in Figure 4-4c, d, the theoretically predicted selectivities of the three gas separation pairs (CO_2/CH_4, H_2/CO_2, and H_2/CH_4) decrease as the etching time t increases. The selectivity decrease for $20 < t < 30$ is significant, decreasing from 10^3 to ~10. Subsequently, the selectivity gradually decays to 1 as t increases further. Similar to the gas permeance, the selectivity also exhibits a high relative error for short etching times, partially reducing the precision of the theoretical estimation.

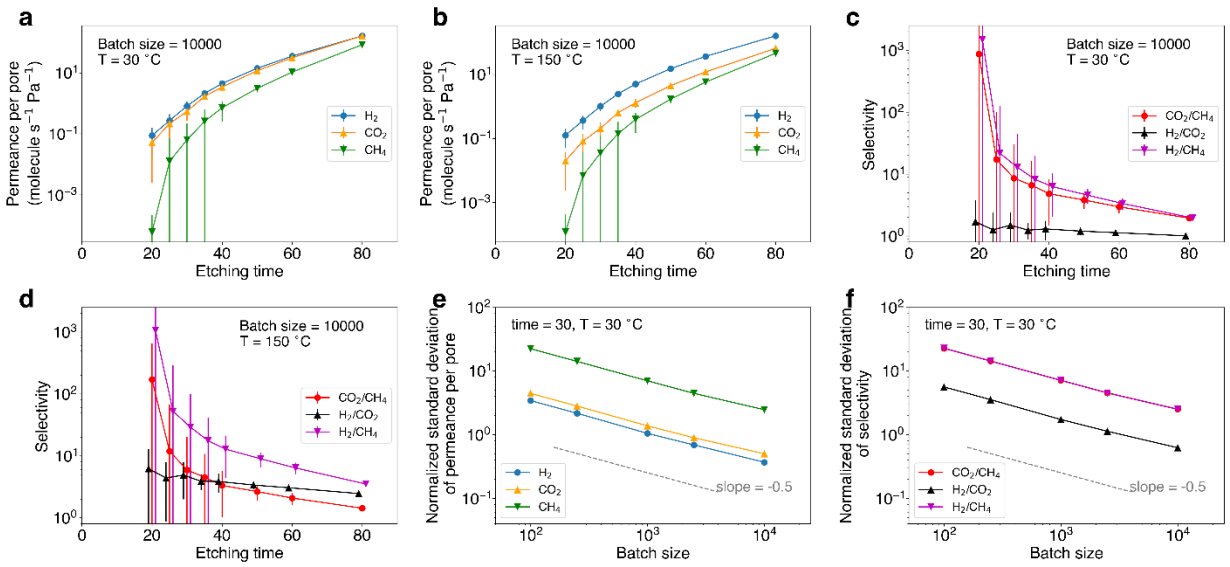

Figure 4-4. Theoretically predicted permeances per pore of H_2, CO_2, and CH_4 as functions of the etching time at (a) 30 °C and (b) 150 °C. Theoretically predicted selectivities of CO_2/CH_4, H_2/CO_2, and H_2/CH_4 as functions of the etching time at (c) 30 °C and (d) 150 °C. In (c) and (d), some datapoints are horizontally shifted to avoid overlap of their error bars. The normalized standard deviations (relative errors) of (e) the permeance per pore, and (f) the selectivity, both decrease as the batch size N increases.

The high errors observed in the gas permeance and selectivity bring into question the reproducibility of the results, obtained both theoretically and experimentally. Fortunately, according to the central limit theorem, the standard deviation of the sample average of N independent and identically distributed random variables should scale as $N^{-1/2}$. This -1/2 scaling is confirmed in Figure 4-4e, f, for the gas permeance per pore and for the selectivity, respectively. When the batch size N is as small as 100, the standard deviation of the sample average can be 10 times greater than the sample average (normalized standard deviation > 10). Because both gas permeances and selectivities are non-negative quantities, the normal distribution does not seem to be the optimal choice for representing the uncertainty. However, according to the central limit theorem, as N increases, the sample average will approach a normal distribution. Therefore, the normal distribution is chosen for consistency. If the $N^{-1/2}$ decay of the standard deviation persists as N increases further, it is anticipated that the normalized standard deviation (or the relative error) should decrease to 5% when N reaches ~ 4 million. Generating millions of nanopores *in silico* requires long real-world time for calculations, and $N = 10000$ is nearly the largest batch size that I can consider computationally. However, experimentally, if the graphene etching method is macroscopically scalable (*e.g.*, oxygen plasma), then, generating millions of

nanopores in one graphene membrane is indeed possible. For example, Zhao *et al.* exposed graphene to oxygen plasma to increase the areal nanopore density to 5.7×10^{11} cm^{-2}.[122] At this areal density, 4 million nanopores require a membrane area of ~ 700 μm^2, which has already been realized by reinforcing graphene with a highly porous supporting film.[120] Nevertheless, the inherent stochasticity associated with the pore size and shape distributions does exist, and can partially account for the high variance of the experimentally measured gas permeances and selectivities carried out so far.[120,122]

Compared to the etching time, the effect of temperature on gas permeances and selectivities is more complex. Assuming that the translocation step is rate-determining ($\Pi_i \approx \Pi_{trans,i}$, for small nanopores), according to Equation (4-1), the gas permeance is affected by temperature due to three terms: the adsorption term $H_{pore}(T)$, the Arrhenius term $\exp(-\Delta E^{\ddagger}/k_BT)$, and the kinetic term $\sqrt{k_BT/2\pi m}$. $H_{pore}(T)$ is negatively correlated with temperature because it involves the heat of gas adsorption onto the graphene nanopore $\Delta E_{ads} < 0$ based on the following expression, $H_{pore}(T) = A_{pore}\exp(-\Delta E_{ads}/k_BT)$, where A_{pore} is the prefactor. If the kinetic term is neglected because its $T^{1/2}$ dependence is weaker than the exponential dependence in the other two terms, the gas permeance is positively correlated with temperature when $\Delta E^{\ddagger} > -\Delta E_{ads}$, and is negatively correlated with temperature when $\Delta E^{\ddagger} < -\Delta E_{ds}$. On the one hand, the heat of adsorption ΔE_{ads} is estimated to be -3.4, -11.1, and -8.0 kJ mol^{-1} for H_2, CO_2, and CH_4, respectively, based on calculations using all-atomistic force fields (Section 4.6.2). On the other hand, when the etching time $t = 30$, the average energy barriers $\overline{\Delta E^{\ddagger}}$ for H_2, CO_2, and CH_4 are 2.8, 0.4, and 0.3 kJ mol^{-1} at 30 °C, respectively. This set of data is counterintuitive, because H_2 exhibits the highest average energy barrier although it is the smallest of the three gases considered. This is because the CO_2 and CH_4 permeances are dominated by nanopores with energy barriers close to zero, and all the other nanopores do not contribute to the sum in Equation (4-5) because their energy barriers are too high.

The analysis above helps explain Figure 4-5, where the correlations of the gas permeances and the selectivities with temperature are presented. For CO_2 and CH_4, $\Delta E^{\ddagger} \approx 0 < -\Delta E_{ads}$, and their permeances decrease as the temperature increases (Figure 4-5a). Because CO_2 is more adsorptive than CH_4, the permeance decrease of CO_2 is greater in magnitude. For H_2, $\Delta E^{\ddagger} \approx -\Delta E_{ads}$, and its permeance only

slightly increases as a function of temperature (recall the $T^{1/2}$ term in Equation (4-1)). Consequently, the H_2/CO_2 and H_2/CH_4 selectivities increase as the temperature increases while the CO_2/CH_4 selectivity decreases (Figure 4-5b).

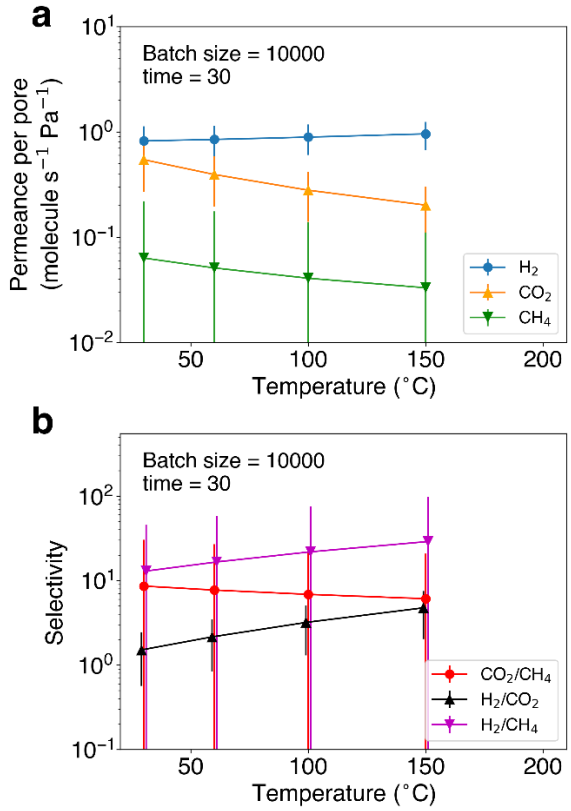

Figure 4-5. (a) Theoretically predicted temperature dependence of H_2, CO_2, and CH_4 permeances per pore. (b) Theoretically predicted temperature dependence of CO_2/CH_4, H_2/CO_2, and H_2/CH_4 selectivities. The etching time is 30 and the batch number is 10000. The nanopore structures are assumed to be invariant as the temperature changes.

Next, the data reported in Figure 4-4 are combined to predict the permeance-selectivity Robeson plot in Figure 4-6. In the Robeson plot, the selectivity of gas A vs. gas B is plotted on the *y*-axis (assuming that gas A is more permeable), and the permeance per pore of gas A through a single nanopore or a nanopore ensemble is plotted on the *x*-axis. The orange and red curves in Figure 4-6a represent the permeance-selectivity trade-off for H_2/CH_4 separation at 30 and 150 °C, respectively, where each datapoint corresponds to a nanopore ensemble generated with an etching time ranging from 20 to 80, in the direction from left to right on the *x* axis. Therefore, a short etching time corresponds to small pore sizes, a low gas permeance, and a high selectivity (top-left datapoints), while a long etching time corresponds to the opposite (bottom-right datapoints).

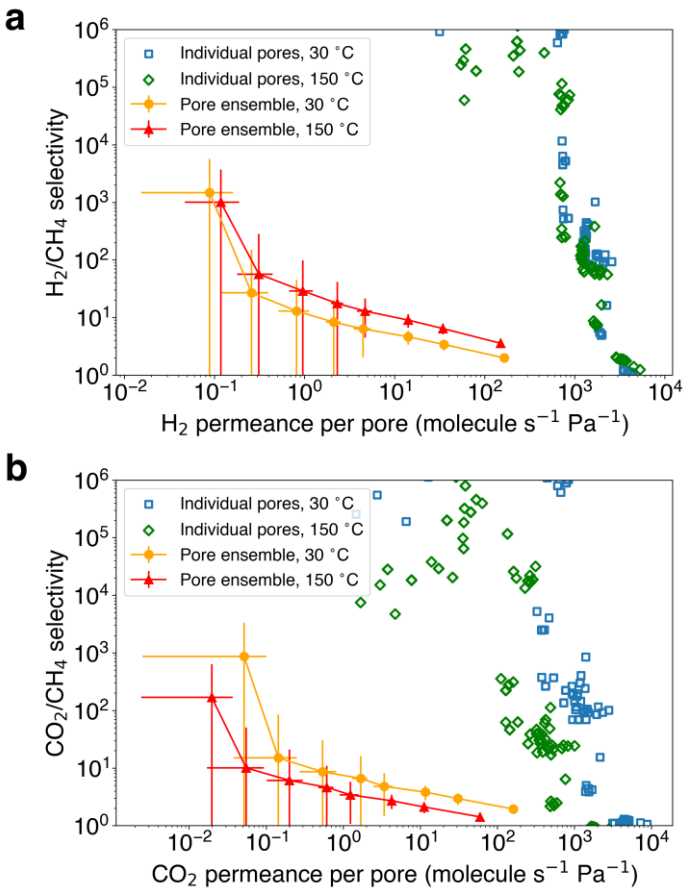

Figure 4-6. Theoretically predicted permeance-selectivity Robeson plot of (a) H_2/CH_4 separation and (b) CO_2/CH_4 separation at 30 and 150 °C. The orange and red curves represent the performance of nanopore ensembles, and the blue and green dots represent the performance of the individual nanopores.

In order to evaluate the importance of considering the pore size and shape distributions, I also plot the gas separation performances of the individual nanopores in the ensembles on the same Robeson plot (blue and green markers in Figure 4-6a for 30 and 150 °C, respectively). Note that all the datapoints of the individual nanopores lie above the ensemble-averaged curves (orange and red curves in Figure 4-6a). This gap between the individual nanopores and the nanopore ensembles highlights the need of taking the pore size and shape distributions into account. Most nanopores in an ensemble are basically not permeable (Figure 4-3), which reduces the average gas permeance. In Figure 4-6a, a nanopore ensemble that yields a H_2/CH_4 selectivity of 10^3 only permits a H_2 permeance per pore of 10^{-1} molecule s^{-1} Pa^{-1}, which is four orders of magnitude lower compared to that of individual nanopores yielding the same selectivity. This gap in permeance shrinks as the selectivity target decreases, because the permeance distribution in a nanopore ensemble becomes more even as the etching time increases (Figure 4-3). The

gap diminishes as the selectivity target approaches 1, when all the nanopores in an ensemble are too large to provide any selectivity. Features similar to those observed in Figure 4-6a are also observed in Figure 4-6b, where the CO_2/CH_4 separation is evaluated. In spite of being similar in terms of the gap between the nanopore ensembles and the individual nanopores, the CO_2/CH_4 and H_2/CH_4 separations are different in terms of their temperature dependence. Increasing temperature shifts the H_2/CH_4 selectivity-permeance curve upwards (orange to red, Figure 4-6a), but shifts the CO_2/CH_4 selectivity-permeance curve downwards (orange to red, Figure 4-6b). This is a manifestation of the different temperature dependences of the permeances of the three gases, as reported in Figure 4-5a.

It is important to note that my simulation results on the temperature dependence discussed above are based on the assumption that the nanopore structure remains unchanged as the temperature changes. However, temperature influences almost every aspect of an experimental measurement, and the actual experimental conditions may be more complex than those considered above by my theory. As shown in Figure 4-5a, the permeances of CO_2 and CH_4 are predicted to decrease as the temperature increases, which contradicts the experimental findings.[120,122,128] In the next section, I will propose a strategy to correct my theory in order to match the experimental findings.

4.4 Matching theory with experiments

In this section, I compare my theoretically predicted gas permeances through nanoporous graphene membranes to experimentally measured ones.[118,122] For convenience, the 95% confidence interval of the theoretically predicted H_2, CO_2, and CH_4 permeances per pore and selectivities between the gases are reported in Table 4-1 (30 °C), Table 4-2 (100 °C), and Table 4-3 (150 °C) as functions of the etching time. The experimental dataset used in this chapter was obtained by He *et al.*,[118] and is reported in Table 4-4. This dataset was chosen because it has relatively low error and high reproducibility. The dataset considered includes three types of nanoporous graphene samples, NG-1s, NG-2s, and NG-3s, fabricated by exposing pristine graphene grown by chemical vapor deposition (CVD) to 1 s, 2 s, and 3 s of oxygen plasma, respectively. Each membrane was tested to measure its H_2, CO_2, and CH_4 permeances at 30, 100, and 150 °C. Note that the nanopore edges are expected to be terminated by oxygen atoms or hydroxyl groups after oxygen plasma etching. However, the density and the positions of the oxygen-

containing termination groups cannot be easily predicted or modelled. Moreover, the additional rotational degrees of freedom contributed by the termination groups could significantly expand the phase space of nanopore–gas interactions, boosting the computational cost. In fact, if the nanopore–gas interactions remain mainly dispersive and not electrostatic, *i.e.,* if the oxygen-containing termination groups are sparse, which results in weak gas–nanopore electrostatic interactions, my calculations without edge termination can still effectively accommodate for the edge termination groups by considering them as part of the graphene lattice. This is likely the case for oxygen plasma-etched nanopores.[118] Therefore, for simplicity and efficiency, the nanopores are assumed to be unterminated.

Table 4-1. Predictions of selectivities (S) and permeances per pore (Π) of H_2, CO_2, and CH_4 at 30 °C through graphene nanopore ensembles generated using different etching times.

Etching time	Predicted selectivity			Predicted permeance per pore (molecule s^{-1} Pa^{-1})		
	$S(H_2/CH_4)$	$S(CO_2/CH_4)$	$S(H_2/CO_2)$	$\Pi(H_2)$	$\Pi(CO_2)$	$\Pi(CH_4)$
20	1479.0±1067.5	865.4±642.2	1.7±0.6	0.09±0.02	0.05±0.01	(6.0±4.1)E-5
21	132.8±212.1	85.4±137.1	1.6±0.5	0.12±0.03	0.07±0.02	0.0009±0.0014
22	25.5±49.0	14.3±27.6	1.8±0.6	0.15±0.03	0.09±0.02	0.0060±0.0114
26	22.3±24.6	14.2±15.7	1.6±0.3	0.33±0.05	0.21±0.03	0.015±0.016
27	16.3±15.2	11.1±10.4	1.5±0.3	0.46±0.06	0.31±0.05	0.028±0.026
28	14.9±11.0	10.1±7.5	1.5±0.3	0.56±0.06	0.38±0.05	0.037±0.027
30	13.0±8.1	8.6±5.4	1.5±0.2	0.82±0.08	0.54±0.07	0.063±0.039
31	11.8±7.1	8.5±5.1	1.4±0.2	0.97±0.09	0.70±0.08	0.082±0.048
32	10.0±13.6	7.3±10.0	1.4±0.5	0.98±0.20	0.71±0.20	0.098±0.132
35	8.3±5.9	6.6±4.7	1.3±0.3	2.12±0.32	1.69±0.29	0.256±0.178
40	6.3±3.1	4.8±2.4	1.3±0.2	4.49±0.50	3.41±0.48	0.708±0.334
45	5.6±0.8	4.4±0.6	1.3±0.1	8.00±0.31	6.22±0.29	1.42±0.19
50	4.6±1.1	3.8±0.9	1.2±0.1	14.20±0.98	11.66±0.97	3.06±0.71
52	4.1±0.4	3.3±0.3	1.2±0.1	17.59±0.50	14.31±0.51	4.29±0.37
55	3.7±0.3	3.0±0.2	1.2±0.1	24.07±0.61	19.57±0.63	6.46±0.48
60	3.4±0.5	3.0±0.4	1.2±0.1	35.53±1.69	30.88±1.81	10.46±1.39
70	2.5±0.1	2.3±0.1	1.1±0.0	84.84±1.29	79.03±1.46	34.23±1.17
80	2.0±0.1	1.9±0.1	1.0±0.0	165.19±4.32	160.98±5.08	83.01±4.25

Table 4-2. Predictions of selectivities (S) and permeances per pore (Π) of H_2, CO_2, and CH_4 at 100 °C through graphene nanopore ensembles generated using different etching times.

Etching time	Predicted selectivity			Predicted permeance per pore (molecule s^{-1} Pa^{-1})		
	$S(H_2/CH_4)$	$S(CO_2/CH_4)$	$S(H_2/CO_2)$	$\Pi(H_2)$	$\Pi(CO_2)$	$\Pi(CH_4)$
20	1127.5±787.4	291.9±211.6	3.9±1.3	0.10±0.02	0.03±0.01	(9,2±6.2)E-5
21	178.1±243.1	51.4±70.8	3.5±1.1	0.13±0.02	0.04±0.01	0.0008±0.0010
22	46.0±85.8	11.8±22.1	3.9±1.1	0.18±0.03	0.05±0.01	0.0038±0.0071
26	38.2±39.9	11.0±11.6	3.5±0.7	0.37±0.04	0.11±0.02	0.0098±0.0102
27	27.9±25.2	9.0±8.2	3.1±0.6	0.51±0.05	0.16±0.02	0.018±0.016

28	25.2±17.9	8.0±5.8	3.1±0.5	0.61±0.06	0.19±0.03	0.024±0.017
30	21.9±13.3	6.9±4.2	3.2±0.5	0.89±0.07	0.28±0.03	0.041±0.025
31	19.6±11.3	6.8±4.0	2.9±0.4	1.04±0.08	0.36±0.04	0.053±0.030
32	16.9±22.4	5.8±7.9	2.9±0.9	1.06±0.19	0.37±0.10	0.063±0.083
35	13.5±9.4	5.2±3.7	2.6±0.6	2.21±0.30	0.86±0.15	0.164±0.111
40	10.1±4.8	3.8±1.9	2.6±0.5	4.57±0.46	1.74±0.25	0.453±0.210
45	8.8±1.2	3.5±0.5	2.6±0.2	8.01±0.28	3.14±0.15	0.909±0.120
50	7.2±1.7	3.0±0.7	2.4±0.2	14.03±0.90	5.96±0.50	1.96±0.45
52	6.3±0.6	2.7±0.2	2.4±0.1	17.30±0.46	7.30±0.26	2.74±0.24
55	5.7±0.4	2.4±0.2	2.3±0.1	23.48±0.55	9.99±0.33	4.13±0.30
60	5.2±0.7	2.4±0.3	2.2±0.2	34.44±1.54	15.79±0.95	6.67±0.88
70	3.7±0.1	1.9±0.1	2.0±0.0	80.34±1.16	40.58±0.77	21.77±0.74
80	2.9±0.2	1.6±0.1	1.8±0.1	154.19±3.86	83.38±2.70	52.74±2.69

Table 4-3. Predictions of selectivities (S) and permeances per pore (Π) of H_2, CO_2, and CH_4 at 150 °C through graphene nanopore ensembles generated using different etching times.

Etching time	Predicted selectivity			Predicted permeance per pore (molecule s^{-1} Pa^{-1})		
	$S(H_2/CH_4)$	$S(CO_2/CH_4)$	$S(H_2/CO_2)$	$\Pi(H_2)$	$\Pi(CO_2)$	$\Pi(CH_4)$
20	1007.0±688.9	168.5±120.1	6.0±1.9	0.12±0.02	0.02±0.01	(1.1±0.8)E-4
21	205.6±251.4	38.6±47.7	5.3±1.6	0.15±0.02	0.03±0.01	(7.3±8.8)E-4
22	63.3±114.8	10.7±19.5	5.9±1.6	0.20±0.03	0.03±0.01	0.003±0.006
26	51.0±51.4	9.6±9.8	5.3±1.0	0.41±0.04	0.08±0.01	0.008±0.008
27	37.3±32.8	8.1±7.1	4.6±0.8	0.55±0.05	0.12±0.02	0.015±0.013
28	33.4±23.1	7.1±5.0	4.7±0.8	0.66±0.06	0.14±0.02	0.020±0.014
30	28.9±17.2	6.1±3.7	4.8±0.7	0.96±0.07	0.20±0.02	0.033±0.020
31	25.8±14.5	6.1±3.5	4.2±0.6	1.11±0.08	0.26±0.03	0.043±0.024
32	22.5±29.3	5.2±6.9	4.3±1.4	1.15±0.19	0.27±0.07	0.051±0.066
35	17.5±11.9	4.6±3.2	3.8±0.8	2.32±0.29	0.61±0.11	0.13±0.09
40	12.9±6.0	3.4±1.6	3.8±0.6	4.72±0.45	1.25±0.18	0.36±0.17
45	11.2±1.5	3.0±0.4	3.7±0.2	8.19±0.28	2.23±0.10	0.73±0.10
50	9.0±2.1	2.7±0.7	3.3±0.3	14.21±0.87	4.26±0.36	1.58±0.36
52	7.9±0.7	2.4±0.2	3.3±0.1	17.47±0.44	5.22±0.19	2.20±0.19
55	7.1±0.5	2.2±0.2	3.3±0.1	23.59±0.53	7.14±0.24	3.32±0.24
60	6.4±0.9	2.1±0.3	3.1±0.2	34.47±1.48	11.28±0.68	5.36±0.70
70	4.5±0.2	1.7±0.1	2.7±0.1	79.27±1.11	29.03±0.56	17.45±0.59
80	3.6±0.2	1.4±0.1	2.5±0.1	150.80±3.68	59.85±1.95	42.24±2.15

Table 4-4. Experimentally measured H_2/CH_4, CO_2/CH_4, and H_2/CO_2 selectivities (S) in ref. 118. Each membrane-temperature combination was matched to an etching time that best reproduces the experimental selectivities.

Condition		Measured selectivity			Best fit of etching time	Fitted selectivity		
Membrane	Temperature (°C)	H_2/CH_4	CO_2/CH_4	H_2/CO_2		H_2/CH_4	CO_2/CH_4	H_2/CO_2
NG-1s	30	15.9±3.8	8.7±0.7	1.8±0.3	28	14.9±11.0	10.1±7.5	1.5±0.3
NG-1s	100	14.1±7.3	5.9±2.3	2.3±0.3	35	13.5±9.4	5.2±3.7	2.6±0.6
NG-1s	150	10.1±3.0	3.7±0.7	2.7±0.3	45	11.2±1.5	3.0±0.4	3.7±0.2
NG-2s	30	9.2±1.9	6.7±2.9	1.5±0.4	35	8.3±5.9	6.6±4.7	1.3±0.3
NG-2s	100	8.2±1.6	3.5±1.1	2.4±0.3	45	8.8±1.2	3.5±0.5	2.6±0.2
NG-2s	150	7.6±1.7	2.6±0.6	3.0±0.1	52	7.9±0.7	2.4±0.2	3.3±0.1
NG-3s	30	5.0±1.1	3.1±0.8	1.6±0.3	50	4.6±1.1	3.8±0.9	1.2±0.1
NG-3s	100	5.6±1.9	2.2±0.5	2.5±0.3	60	5.2±0.7	2.4±0.3	2.2±0.2
NG-3s	150	4.9±0.9	1.7±0.1	2.8±0.3	70	4.5±0.2	1.7±0.1	2.7±0.1

As shown in Table 4-4, for each membrane considered, the experimentally measured H_2/CO_2 selectivity increases as the temperature increases, while the CO_2/CH_4 selectivity shows the opposite trend. These trends are correctly predicted by the theory (Figure 4-5b). However, my theoretical prediction in Figure 4-5b fails to match the experimentally observed decrease in the H_2/CH_4 selectivity

with increasing temperature (Table 4-4). As indicated earlier, Figure 4-5 was derived based on the assumption that the nanopore size remains unchanged as the temperature increases, an assumption that could be relaxed in order to reproduce realistic experimental conditions. Specifically, by relaxing this assumption, different etching times can be assigned to the same graphene membrane at different temperatures. For example, as listed in the first entry in Table 4-4, the H_2/CH_4, CO_2/CH_4, and H_2/CO_2 selectivities are 15.9±4.0, 8.7±0.7, and 1.8±0.3, respectively, for membrane NG-1s at 30 °C. As shown in Table 4-1, it is predicted that an etching time of 28 corresponds to selectivities of 14.9±11.0, 10.1±7.5, and 1.5±0.3, which yields the closest match to the experimentally measured values (equal weights are assigned to the three selectivities). Similarly, I find the etching times that best match the experimentally measured selectivities for each membrane at each temperature (rows 2–9 in Table 4-4). The uncertainty of the theoretically predicted H_2/CH_4 and CO_2/CH_4 selectivities for short etching times ($t < 40$) makes the fitting more challenging. However, Table 4-1, Table 4-2, and Table 4-3 show that the selectivity decrease as a function of temperature is smooth, thereby corroborating the reliability of my theoretical predictions. The fit does a reasonably good job in matching the experimental selectivities (Table 4-4). In addition, the fit successfully confirms the intuitive fact that, at the same temperature, a nanoporous graphene membrane exposed to a longer duration of oxygen plasma is always matched to a longer etching time t (*e.g.,* $50 > 35 > 28$ for NG-3s, NG-2s, and NG-1s at 30 °C).

This fit leads to the following important finding: for the same graphene membrane, the fitted etching time t is longer at a higher temperature of permeation measurement (not the temperature of graphene etching) than that at a lower temperature. Note that the fitted etching time is only a one-degree-of-freedom representation of the underlying pore size distribution, and therefore, the nanopores are effectively larger at a higher temperature of permeation measurement. This effective pore size expansion is also observed in other experimental dataset reported in ref. 122, ref. 128, and ref. 130 (see Appendix 4.7.3 for more details, where the effect of ozone treatment is also investigated). This phenomenon is inconsistent with the previous assumption in Figure 4-5 and Figure 4-6 that the nanopore structure does not depend on temperature. One could explain this phenomenon by arguing that the graphene nanopores expand due to the contraction of the graphene lattice. However, the thermal

expansion coefficient of graphene at room temperature is only -7×10^{-6} K^{-1},[215] suggesting that the thermally induced expansion of a graphene nanopore is minimal.

In order to resolve this apparent contradiction, I hypothesize that under the experimental conditions used, the graphene nanopores are partially clogged, likely by some airborne hydrocarbon contaminants. It is known that the adsorption of airborne hydrocarbons on graphitic surfaces renders them more hydrophobic.[216,217] Heat treatment at 150 °C has been confirmed to be effective in alleviating the clogging,[122] but is not able to fully remove the contaminants, because a single to few layers of the contaminant molecules are sufficient to clog the nanopores. The partial clogging hypothesis can also help rationalize the following three discrepancies between theory and experiment (see Section 6.4 for additional experimental evidence).

Firstly, the effective thermal expansion of nanopores can be interpreted as a result of the partial desorption of the contaminants from the nanopore. In other words, the clogging of the nanopores is alleviated at a higher temperature. A prerequisite for this explanation is that the original, unclogged graphene nanopores should be larger than those fitted by my theoretical prediction. Ref. 118 presents the pore diameter distributions of graphene membranes NG-1s and NG-3s obtained by high resolution transmission electron microscopy (HR-TEM). Membrane NG-1s contains a long tail of nanopores with diameters over 2 nm, and the tail of the pore diameter distribution of membrane NG-3s extends to over 3 nm. In contrast, the predicted pore diameter distribution does not extend over 1 nm, even for the longest etching time investigated t = 80 (Appendix 4.7.4). If the large nanopores generated in the experiments are completely free from clogging, they would exhibit a total CO_2 permeance 6600 times higher than that measured.[118] The long pore size tail observed in ref. 118 could also be partially attributed to nanopore merging during HR-TEM imaging, but my statement remains valid because the average pore diameter observed by HR-TEM is greater than my theoretically fitted value.

Secondly, the effective thermal expansion of the nanopores explains why the experimentally measured gas permeances almost always increase as the temperature increases. At a higher temperature, CO_2 and CH_4 adsorb less, reducing their gas permeances (Figure 4-5a). However, the permeance increase due to the effective thermal expansion of the nanopores *via* the desorption of contaminants is much more significant. In this case, the definition of the energy barrier (or the activation energy) derived

from the experimental data should be carefully revisited. If the effective pore size changes at different temperatures, it follows that the apparent "energy barrier" derived by fitting the Arrhenius equation to the gas permeance as a function of temperature actually contains contributions from both the intrinsic energy barrier for a given pore size $\Delta E^{\ddagger}$ and from the desorption of the contaminants. In fact, the latter is likely to be dominant because the average energy barrier of a temperature-invariant nanopore ensemble is close to zero, much lower than 10 to 30 kJ mol^{-1} measured in the experimental studies.[120,122,128] Without the nanopore clogging by the contaminants, He *et al*. predicts that 99.9% of the CO_2 permeance through NG-1s in ref. 118 was contributed by nanopores larger than 5.8 Å in diameter, whose activation energies for CO_2 are close to 0, directly contradicting the experimentally measured CO_2 apparent energy barrier of 13.8 kJ mol^{-1}. This hypothesis also explains why in those studies, the apparent "energy barriers" are very similar across various nanoporous graphene membranes fabricated by different methods, because they are strongly affected by the universal thermal behavior of the contaminants.

Finally, the partial clogging hypothesis helps explain why my theory underpredicts the gas permeances compared to the experimental measurements reported in ref. 118. As shown in Table 4-4, I attempt to find the etching time *t* that best matches the selectivities between theory and experiment, instead of the gas permeances. In fact, the selectivities and the gas permeances cannot be matched simultaneously. As shown in Table 4-5, when the etching time *t* is fitted to match the selectivity data, my theory underpredicts the gas permeances by 15–202 times. The predicted permeance (in gas permeation units, *i.e.*, GPU) equals the predicted permeance per pore (in molecule s^{-1} Pa^{-1}) times the experimentally measured areal defect density in the graphene membranes using Raman spectroscopy, with an appropriate unit conversion. This significant underprediction cannot be easily explained without the partial clogging hypothesis. Note that the clogging was not considered in my original theoretical model. When clogging is accounted for and reduces the open nanopore area, in order to maintain the same selectivity through the nanopore ensemble, the etching time *t* needs to be increased to compensate for the area loss. As shown in Figure 4-1b, the tail in the pore size distribution elongates as *t* increases. As a result, taking pore clogging into consideration leads to an increase in the fraction of low-energy-barrier nanopores in the nanopore ensemble. In other words, the etching time *t* is underestimated by

fitting my model to the selectivity data because of clogging, which leads to an underestimation of the number of permeable nanopores and an underestimation of the gas permeances. As reported in the last column in Table 4-5, the magnitude of the underestimation decreases as the nanopore size increases. This makes intuitive sense because larger nanopores are less affected by contaminants, which likely clog the nanopores from the nanopore edges.

Table 4-5. Experimentally measured H_2, CO_2, and CH_4 permeances reported in ref. 118, and theoretical predictions of the gas permeances using the best fit of etching time in Table 4-4.

Condition		Measured permeance (GPU)			Best fit of etching time	Predicted permeance (GPU)			Average factor of permeance underesti-mation
Mem-brane	Tempe-rature (°C)	H_2	CO_2	CH_4		H_2	CO_2	CH_4	
NG-1s	30	3130	1765	205	28	18.0±1.9	12.2±1.6	1.2±0.8	163
NG-1s	100	1.32E4	5782	1112	35	71.2±9.7	27.7±4.8	5.3±3.6	202
NG-1s	150	2.17E4	7931	2222	45	263.8±9.0	71.8±3.2	23.5±3.2	96
NG-2s	30	1.73E4	1.20E4	1963	35	189.1±28.5	150.8±25.9	22.8±15.9	86
NG-2s	100	4.47E4	1.91E4	5522	45	714.6±25.0	280.1±13.4	81.1±10.7	66
NG-2s	150	6.69E4	2.25E4	8928	52	1559±39	476.7±16.9	196.3±16.9	46
NG-3s	30	3.23E4	2.00E4	6830	50	1548±107	1271±106	333.6±77.4	19
NG-3s	100	8.06E4	3.40E4	1.59E4	60	3755±168	1722±104	727.3±96.0	21
NG-3s	150	1.29E5	4.73E4	2.76E4	70	8643±121	3165±61	1903±64	15

Other hypotheses that can explain the effective pore size expansion include: (1) the pore size distributions generated by my KMC algorithm do not match experimental ones, and (2) the effective pore size expansion is induced by the more mobile termination groups (*e.g.*, carbonyl groups) at a higher temperature. Regarding (1), the pore size distribution generated by my KMC algorithm can reproduce the apparent energy barriers observed experimentally (Table 4-12 in Appendix 4.7.5), suggesting that the difference between the experimental and theoretically derived pore size distributions is minor. Regarding (2), the graphene nanopores in ref. 128 and ref. 130 were formed during CVD in a reductive atmosphere, and therefore, were not likely terminated by large, oxygen-containing groups. Nevertheless, these nanopores still exhibit the effective pore size expansion as the temperature increases (Table 4-10 and Table 4-11 in Appendix 4.7.3), indicating that the termination groups alone cannot account for the effective pore size expansion.

4.5 Conclusions

In this chapter, I formulate a theoretical framework that predicts the pore size and shape distributions of nanopore ensembles generated by etching, as well as the gas permeances of H_2, CO_2, and CH_4 through these nanopore ensembles. I show that a small fraction of low-energy-barrier nanopores contribute the majority of the total gas permeances through a nanopore ensemble that sieves gases. I quantitatively predict the increase of the gas permeances and the decrease of the gas selectivities as the etching time of graphene increases. Assuming that the nanopore structure is independent of temperature given the small thermal expansion coefficient of graphene, my theory predicts that the CO_2 and CH_4 permeances decrease, and the H_2 permeance increases as the temperature increases. The CO_2 and CH_4 permeance predictions contradict the experimental results, where all the experimental gas permeances are increasing functions of temperature. In order to explain this contradiction, my theoretical model is fitted to the experimentally measured H_2/CH_4, CO_2/CH_4, and H_2/CO_2 selectivities, and it is found that the nanopores effectively expand at a higher temperature. I hypothesize that under typical experimental conditions, the graphene nanopores are partially clogged by hydrocarbon contaminants, and that the contaminants desorb as the temperature increases. An important implication of this hypothesis is that the apparent "energy barriers" directly derived from the experimentally measured gas permeances can be significantly affected by the thermal behavior of the contaminants. Therefore, a high apparent "energy barrier" does not necessarily prove the existence of angstrom-scale graphene nanopores. On the bright side, another implication of my hypothesis is that it may not be necessary to reduce the graphene nanopore size to the angstrom scale in order to attain a high selectivity, because clogging by contaminants effectively reduces the pore size. Experimental research can be conducted to verify the effect of hydrocarbon contaminants on gas permeances by, for example, deliberately decorating graphene membranes using strongly adsorptive hydrocarbons (see Chapter 6).

This chapter provides an important theoretical benchmark for future experimental gas permeation measurements through graphene membranes. The experimentally measured selectivities can be compared with Table 4-1 to Table 4-3 to find the best-fitted etching time, and the pore size distribution can be inferred from the etching time according to Figure 4-1b.

Beginning with next chapter, I will present experimental results of gas separation using single-layer graphene membranes.

4.6 Methods

4.6.1 Kinetic Monte Carlo Nanopore Generation

The major steps involved in the Kinetic Monte Carlo (KMC) simulation are presented in Figure 4-1a. Starting from a point defect in a pristine graphene lattice containing 12×12 unit cells, carbon atoms were etched away sequentially. The 12×12 graphene lattice is large enough to contain the nanopores considered in this chapter. The rate of a carbon atom being removed is related to its nearby edge configuration. The energy barrier E_a for removing a single carbon atom is 2.30 eV at a zigzag edge, 2.28 eV at an armchair edge, and 1.03 eV for a singly bonded atom.[35] The corresponding etching rate r is computed using an Arrhenius-type equation: $r = \nu \exp(-E_a/k_B T)$, where ν is a prefactor related to the etchant concentration. In this chapter, ν is chosen to be 10^{13} s^{-1}. The value of ν is arbitrary, because it does not affect the pore size and shape distributions generated using the KMC algorithm. In fact, the etching time t can be rescaled if ν is assumed to be different. The temperature was assumed to be 500 °C to match the experimental graphene etching condition in ref. 147. The nanopore ensembles predicted using the KMC algorithm are insensitive to temperature.[35] This is likely because the energy barriers for removing a carbon atom at a zigzag edge or at an armchair edge are similar, making the effect of temperature less important. When multiple choices exist about which carbon atom to etch, the Gillespie algorithm was implemented to randomly select one of them. The probability of a carbon atom being etched is proportional to its respective etching rate r.

Among the 500000 nanopores generated using the KMC algorithm, many of them are identical to one another. Two nanopores are considered to be the same if the adjacency matrices of their respective antimolecules, augmented to include bond orientations, are isomorphic.[35] The antimolecule of a nanopore is the collection of the carbon atoms removed during etching. For additional details and for the KMC simulation and nanopore counting code, interested readers are referred to ref. 35. One nanopore isomer was evaluated only once to calculate its permeance to avoid calculational redundancy.

As the pore size increases, the number of isomers significantly increases, leading to a long calculation time. To make the calculation more tractable, the number of nanopores generated was reduced to 100000 for etching time $t \geq 60$.

4.6.2 Permeance Prediction

The gas permeance per pore Π through a nanopore was calculated using Equations (4-1)–(4-4). In Equation (4-1), H_{pore} (average number of gas molecules adsorbed to the pore mouth per unit bulk pressure), L (the characteristic length of the adsorbed state at the pore mouth), $-\Delta S^{\ddagger}$ (the entropy barrier), and $\Delta E^{\ddagger}$ (the energy barrier) all depend on the force fields used to simulate graphene and the three gases considered (H_2, CO_2, CH_4). In my simulations, all-atom force fields were used to describe the atomic interactions, where all the molecules were assumed to be rigid in order to reduce computational cost. As shown in Chapter 2, enforcing rigidity on all the molecules leads to a slight underprediction of the gas permeance. Specifically, the entropy barrier $-\Delta S^{\ddagger}$ is overpredicted because the vibrational degrees of freedom are frozen, reducing the number of microstates at the transition state. Recall that non-bonded interactions include Lennard-Jones potentials and point-charge-based electrostatic potentials. I adopted the three-site model for H_2,[218] the transferable potential for phase equilibria (TraPPE) force field for CO_2,[154] and the all-atom-optimized potentials for liquid simulations (OPLS-AA model) for CH_4.[168] The carbon atoms in the graphene lattice were modeled as uncharged atoms using the Lennard-Jones parameters reported by Cheng and Steele.[171] The edge carbon atoms were not terminated by any functional groups. In reality, the edge termination depends on the etching method, and the nanopore could be terminated by hydrogen, oxygen, hydroxyl groups, or left unterminated. If the nanopore edge is highly polarized (*e.g.*, a large number of oxygen heteroatoms), my theory tends to underpredict the permeances of gases with a dipole moment (*e.g.*, H_2O) or a quadrupole moment (CO_2), which is the case for ozone-treated nanopores.[122] This underprediction is discussed in Appendix 4.7.3. The cutoff distance for the Lennard-Jones interactions was chosen to be 1.2 nm. Geometric-mean combining rules were implemented to describe the non-bonded interactions between different atoms.

The selected all-atom force fields are utilized to calculate the interaction energy $E(r, \phi, z, \vec{\theta})$ between the gas molecule and the single-layer graphene sheet with one nanopore generated by the KMC

algorithm, where (r, ϕ, z) and $\vec{\theta}$ are the position (cylindrical coordinate) and the orientation of the gas molecule relative to the graphene surface, respectively. In this chapter, the normal direction to the graphene basal plane is defined as the z direction. In order to calculate the Helmholtz free energy profile of pore crossing $A(z)$, I first calculated the canonical partition function profile $Q(z)$ as follows (see Section 2.4):

$$Q(z) = \frac{\int \mathrm{d}\vec{\theta} \iint_{\Omega} r\mathrm{d}r\mathrm{d}\phi \exp\left[-\frac{E(r,\phi,z,\vec{\theta})}{k_{\mathrm{B}}T}\right]}{\int \mathrm{d}\vec{\theta} \iint_{\Omega} r\mathrm{d}r\mathrm{d}\phi} \tag{4-7}$$

where Ω is the nanopore area around the nanopore center with a radius of 0.4 nm. This nanopore area is sufficiently large to include relevant nanopore–gas interactions because the diameters of the nanopores considered here rarely exceed 0.8 nm. I then calculated the Helmholtz free energy profile using the well-known statistical mechanical relation: $A(z) = -k_{\mathrm{B}}T\ln Q(z)$.[219] The Helmholtz free energy barrier is then calculated as: $\Delta A^{\ddagger}$ = max($A(z)$)-min($A(z)$). The entropy barrier ($-\Delta S^{\ddagger}$) and the energy barrier ($\Delta E^{\ddagger}$) are then calculated by linearly fitting $\Delta A^{\ddagger}(T) = \Delta E^{\ddagger} - T\Delta S^{\ddagger}$ to the temperature T.

The full width at half maximum L of the canonical partition function of the gas–pore system $Q(z)$ is derived as follows (see Section 2.4):

$$L = \frac{\int_0^{z_{\max}} Q(z)\,\mathrm{d}z}{\max\left(Q(z)\right)} \tag{4-8}$$

where $z_{\max}$ is the thickness of the adsorption layer. Note that I chose $z_{\max}$ = 0.5 nm, where the density of the gas molecules approaches the bulk value. The average number of gas molecules adsorbed at the pore mouth per unit bulk pressure H_{pore} was calculated as follows:

$$H_{\mathrm{pore}}(T) = \frac{\Omega \int_0^{z_{\max}} Q(z)\,\mathrm{d}z}{k_{\mathrm{B}}TQ(z \to \infty)} \tag{4-9}$$

In Equation (4-9), the number of gas molecules near the nanopore (the numerator) is calculated relative to the bulk gas density (the denominator). The heat of adsorption ΔE_{ads} was derived by fitting $H_{\mathrm{pore}}(T) = A_{\mathrm{pore}} \exp(-\Delta E_{\mathrm{ads}}/k_{\mathrm{B}}T)$ to the temperature.

In practice, the phase space $(r, \phi, z, \vec{\theta})$ should be discretized to approximate the integrals by sums. Specifically, the r space was divided into grids of 0.013 nm, the ϕ space was divided into grids of 18°, the z space was divided into grids of 0.033 nm, and the $\vec{\theta}$ space was discretized by randomly sampling ten three-dimensional directions per position (r, ϕ, z). The grid sizes in the r, ϕ, and z directions and the number of randomly sampled directions in $\vec{\theta}$ were selected to ensure convergence of the Helmholtz free energy barrier $\Delta A^{\ddagger}$. Additional details about the convergence are provided in Appendix 4.7.6.

Equations (4-2) and (4-3) involve additional parameters, including the two correction factors δ and γ, the areal density of gas molecules adsorbed on the graphene surface per unit bulk pressure H_{surf}, and the equivalent pore diameter D_{p}. According to Section 3.4, $\delta = \left(1 - \frac{D_{\text{m}}}{D_{\text{p}}}\right)^{\alpha}$, where D_{m} is the kinetic diameter of the gas, and α is a gas-dependent exponent (4.6 for H_2 and CO_2, and 3.7 for CH_4). Because the graphene nanopores are not perfectly circular, the equivalent pore diameter is approximated by $D_{\text{p}} = \sqrt{\frac{4n_{\text{C}}}{\pi \rho_{\text{C}}}}$, where n_C is the pore size (number of removed carbon atoms) and ρ_C is the areal density of the carbon atoms in graphene, 3.82×10^{19} m^{-2}. The surface adsorption term H_{surf} can be derived in a similar way as H_{pore}, except that the graphene sheet has no nanopore. Note that the correction factor $\gamma = \gamma(T, D_{\text{p}})$ in Equation (4-3) does not yet have an analytical expression due to the complex gas–gas collisions and gas–pore interactions. Empirically, I interpolated the γ values based on Section 3.5. Typically, γ is on the order of 0.05–0.10 regardless of gas type or temperature. Fortunately, Π_{trans} (calculated using Equation (4-1)) is typically much lower than $\Pi_{\text{direct}} + \Pi_{\text{surface}}$ (calculated using Equations (4-2) and (4-3)), and therefore, $\Pi \approx \Pi_{\text{trans}}$ (Equation (4-4)). Consequently, my final prediction of the gas permeance is insensitive to the parameters in Equations (4-2) and (4-3).

4.7 Appendices

4.7.1 Importance of the Entropy Barrier

Equation (4-1) includes the term $\exp\left(\Delta S_i^{\ddagger}/k_{\text{B}}\right)$ which involves the entropy barrier $-\Delta S_i^{\ddagger}$. Recall that an entropy barrier exists because when a gas molecule crosses the nanopore it is confined in its

translational and rotational degrees of freedom. As a result, the entropy of a gas molecule decreases as it moves from the bulk towards the nanopore. The entropy change $\Delta S_i^{\ddagger}$ from the bulk to the transition state is therefore negative. Here, the entropy barrier is defined as $-\Delta S_i^{\ddagger}$ because minus $T\Delta S^{\ddagger}$ is involved in the Helmholtz free energy.

Interestingly, the entropy barrier is typically ignored in the literature when calculating the gas permeance through graphene nanopores.[49,96,105] However, the entropy barriers of different gases through the same nanopore can vary by more than 10 J mol^{-1} K^{-1}, thereby contributing a factor of more than 3.3 to the total selectivity. Table 4-6 and Table 4-7 below show how neglecting the entropy barrier term affects the selectivity predictions at 30 and 150 °C, respectively. Most importantly, neglecting the contribution from the entropy barrier leads to a significantly reduced H_2/CO_2 selectivity, which can no longer match the experimental results reported in the main text (Table 4-3).

Table 4-6. Predicted H_2/CH_4, CO_2/CH_4, and H_2/CO_2 selectivities at 30 °C through graphene nanopore ensembles generated as a function of etching time, with and without considering the entropy barrier $-\Delta S_i^{\ddagger}$.

Etching time	Predicted selectivity with $-\Delta S_i^{\ddagger}$			Predicted selectivity without $-\Delta S_i^{\ddagger}$		
	$S(H_2/CH_4)$	$S(CO_2/CH_4)$	$S(H_2/CO_2)$	$S(H_2/CH_4)$	$S(CO_2/CH_4)$	$S(H_2/CO_2)$
20	1479.0±1067.5	865.4±642.2	1.7±0.6	120.2±77.2	251.9±161.8	0.48±0.06
21	132.8±212.1	85.4±137.1	1.6±0.5	43.4±39.6	73.8±67.5	0.59±0.07
22	25.5±49.0	14.3±27.6	1.8±0.6	51.0±46.2	94.7±85.8	0.54±0.06
26	22.3±24.6	14.2±15.7	1.6±0.3	27.9±15.3	57.1±31.3	0.49±0.04
27	16.3±15.2	11.1±10.4	1.5±0.3	27.6±13.2	64.8±31.0	0.43±0.03
28	14.9±11.0	10.1±7.5	1.5±0.3	22.2±9.3	51.2±21.5	0.43±0.03
30	13.0±8.1	8.6±5.4	1.5±0.2	22.3±8.0	43.5±15.7	0.51±0.03
31	11.8±7.1	8.5±5.1	1.4±0.2	17.1±5.1	34.7±10.4	0.49±0.03
32	10.0±13.6	7.3±10.0	1.4±0.5	20.7±14.2	40.8±28.0	0.51±0.06
35	8.3±5.9	6.6±4.7	1.3±0.3	12.9±5.7	26.1±11.4	0.49±0.05
40	6.3±3.1	4.8±2.4	1.3±0.2	8.8±2.5	19.7±5.5	0.45±0.03
45	5.6±0.8	4.4±0.6	1.3±0.1	6.3±0.5	11.2±1.0	0.57±0.02
50	4.6±1.1	3.8±0.9	1.2±0.1	5.3±0.8	9.1±1.3	0.58±0.03
52	4.1±0.4	3.3±0.3	1.2±0.1	4.9±0.3	9.0±0.5	0.54±0.01
55	3.7±0.3	3.0±0.2	1.2±0.1	4.3±0.2	7.5±0.4	0.58±0.01
60	3.4±0.5	3.0±0.4	1.2±0.1	3.8±0.3	7.4±0.7	0.52±0.02
70	2.5±0.1	2.3±0.1	1.1±0.0	2.6±0.1	4.4±0.1	0.59±0.01
80	2.0±0.1	1.9±0.1	1.0±0.0	1.9±0.1	3.5±0.1	0.56±0.01

Table 4-7. Predicted H_2/CH_4, CO_2/CH_4, and H_2/CO_2 selectivities at 150 °C through graphene nanopore ensembles generated as a function of etching time, with or without considering the entropy barrier $-\Delta S_i^{\ddagger}$.

Etching time	Predicted selectivity with $-\Delta S_i^{\ddagger}$			Predicted selectivity without $-\Delta S_i^{\ddagger}$		
	$S(H_2/CH_4)$	$S(CO_2/CH_4)$	$S(H_2/CO_2)$	$S(H_2/CH_4)$	$S(CO_2/CH_4)$	$S(H_2/CO_2)$
20	1007.0±688.9	168.5±120.1	6.0±1.9	122.2±71.6	121.7±71.4	1.00±0.09
21	205.6±251.4	38.6±47.7	5.3±1.6	67.2±40.8	57.9±35.3	1.16±0.10
22	63.3±114.8	10.7±19.5	5.9±1.6	77.8±45.1	72.3±41.9	1.08±0.08
26	51.0±51.4	9.6±9.8	5.3±1.0	49.9±19.7	49.5±19.5	1.01±0.06
27	37.3±32.8	8.1±7.1	4.6±0.8	44.2±14.4	46.9±15.2	0.94±0.05
28	33.4±23.1	7.1±5.0	4.7±0.8	39.6±12.3	43.4±13.5	0.91±0.04
30	28.9±17.2	6.1±3.7	4.8±0.7	37.5±9.7	35.4±9.2	1.06±0.05
31	25.8±14.5	6.1±3.5	4.2±0.6	29.0±6.4	29.0±6.4	1.00±0.04
32	22.5±29.3	5.2±6.9	4.3±1.4	33.8±16.3	31.2±15.1	1.08±0.10
35	17.5±11.9	4.6±3.2	3.8±0.8	21.5±7.1	21.6±7.1	1.00±0.07
40	12.9±6.0	3.4±1.6	3.8±0.6	14.0±3.0	15.1±3.2	0.92±0.05
45	11.2±1.5	3.0±0.4	3.7±0.2	10.2±0.7	9.3±0.6	1.11±0.03
50	9.0±2.1	2.7±0.7	3.3±0.3	8.2±0.9	7.4±0.9	1.11±0.05
52	7.9±0.7	2.4±0.2	3.3±0.1	7.8±0.4	7.3±0.3	1.06±0.02
55	7.1±0.5	2.2±0.2	3.3±0.1	6.8±0.3	6.1±0.2	1.11±0.02
60	6.4±0.9	2.1±0.3	3.1±0.2	6.0±0.4	6.1±0.4	0.99±0.03
70	4.5±0.2	1.7±0.1	2.7±0.1	4.0±0.1	3.6±0.1	1.09±0.01
80	3.6±0.2	1.4±0.1	2.5±0.1	3.0±0.1	2.9±0.1	1.01±0.02

The importance of the entropy barrier for CO_2 is explained as follows. Note that CO_2 is a linear molecule with a high aspect ratio. A CO_2 molecule could align itself perpendicularly to the graphene basal plane to reduce the energy barrier, although such a configuration would incur a higher entropy penalty to reach the middle of a nanopore. As a result, many nanopores exhibit very low energy barriers but very high entropy barriers for CO_2. Consequently, neglecting the entropy barriers leads to significant overprediction of the permeance of CO_2. However, this effect is not significant for H_2 or CH_4, and neglecting the entropy barriers only leads to a mild overprediction of their permeances.

4.7.2 Derivation of the Average Energy Barrier

The average energy barrier of a pore ensemble $\overline{\Delta E^{\ddagger}}$ presented in Equation (4-5) is derived as follows. Consider the total gas permeance $\Pi = \sum_i \Pi_i = \sum_i A_i \exp\left(-\Delta E_i^{\ddagger}/k_B T\right)$, where $\Delta E_i^{\ddagger}$ is the energy barrier of nanopore i in a pore ensemble and A_i is the prefactor corresponding to nanopore i (nearly temperature independent). According to the Arrhenius equation, the average energy barrier can be derived as follows:

$$\overline{\Delta E^{\ddagger}(T)} = \frac{\mathrm{d}\ln\Pi}{\mathrm{d}\left(-\frac{1}{k_{\mathrm{B}}T}\right)} = \frac{1}{\Pi}\frac{\mathrm{d}\Pi}{\mathrm{d}\left(-\frac{1}{k_{\mathrm{B}}T}\right)} = \frac{1}{\Pi}\frac{\mathrm{d}\left[\sum_i A_i \exp\left(-\frac{\Delta E_i^{\ddagger}}{k_{\mathrm{B}}T}\right)\right]}{\mathrm{d}\left(-\frac{1}{k_{\mathrm{B}}T}\right)}$$

$$= \frac{1}{\Pi}\sum_i A_i \frac{\mathrm{d}\exp\left(-\frac{\Delta E_i^{\ddagger}}{k_{\mathrm{B}}T}\right)}{\mathrm{d}\left(-\frac{1}{k_{\mathrm{B}}T}\right)} = \frac{1}{\Pi}\sum_i \Delta E_i^{\ddagger} A_i \exp\left(-\frac{\Delta E_i^{\ddagger}}{k_{\mathrm{B}}T}\right) \tag{4-10}$$

$$= \frac{\sum_i \Delta E_i^{\ddagger}\Pi_i(T)}{\sum_i \Pi_i(T)}$$

4.7.3 Matching the Theory to Other Experimental Datasets

The theoretical model developed in this chapter is also used to fit to three other experimental datasets by Zhao *et al.*,[122] Khan *et al.*,[128] and Rezaei *et al.*,[130] assuming that the pore clogging hypothesis is valid. Table 4-8 lists the H_2/CH_4, CO_2/CH_4, and H_2/CO_2 selectivities of graphene membranes M5, M6, and M11 in that dataset at 30, 100, and 150 °C. Note that membranes M5, M6, and M11 were exposed to 1 s of oxygen plasma before testing.[122] All the membranes in that study were fabricated according to the same procedure, but they behaved slightly differently due to randomness in the experiments. For each membrane, the best fit of etching time increases as the temperature increases, which is consistent with the findings reported in Section 4.4.

Table 4-8. Experimentally measured H_2/CH_4, CO_2/CH_4, and H_2/CO_2 selectivities of membranes M5, M6, and M11 reported by Zhao *et al.*[122]. Each membrane-temperature combination is matched to an etching time that reproduces the selectivities best.

Condition		Measured selectivity			Best fit of etching time	Fitted selectivity		
Mem-brane	Tempera-ture (°C)	H_2/CH_4	CO_2/CH_4	H_2/CO_2		H_2/CH_4	CO_2/CH_4	H_2/CO_2
M5	30	8.1	3.9	2.1	35	8.3±5.9	6.6±4.7	1.3±0.3
M5	100	8.4	3.1	2.7	45	8.8±1.2	3.5±0.5	2.6±0.2
M5	150	8.5	2.3	3.7	52	7.9±0.7	2.4±0.2	3.3±0.1
M6	30	7.5	3.5	2.1	40	6.3±3.1	4.8±2.4	1.3±0.2
M6	100	10.8	4.1	2.6	40	10.1±4.8	3.8±1.9	2.6±0.5
M6	150	9.7	3.3	2.9	50	9.0±2.1	2.7±0.7	3.3±0.3
M11	30	12.7	8.8	1.4	30	13.0±8.1	8.6±5.4	1.5±0.2
M11	100	11.6	4.8	2.4	35	13.5±9.4	5.2±3.7	2.6±0.6
M11	150	9.5	2.6	3.7	50	9.0±2.1	2.7±0.7	3.3±0.3

The effect of ozone treatment on the graphene membranes is also examined using my theoretical predictions. Membranes M2 and M4 were treated by different stages of ozone treatment sequentially, and their gas permeances were measured at each stage.[122] As shown in Table 4-9, for both membrane M2 and M4, the best fit of etching time t first decreases and then increases as the ozone treatment progresses. This implies that mild ozone treatment only functionalizes the nanopore edge without too much etching, effectively reducing the pore size. Further, extensive ozone treatment etches away carbon atoms and expands the nanopores in graphene. It is worth noting that my theory tends to underpredict the CO_2/CH_4 selectivity and overpredict the H_2/CO_2 selectivity. This is likely caused by the oxygen termination at the nanopore edge introduced by the ozone treatment. The quadrupole–dipole interaction between CO_2 and the oxygen termination atoms favors the adsorption of CO_2 at the pore mouth, and therefore increases the CO_2 permeance. Meanwhile, the preferential adsorption of CO_2 could hinder the passage of other gases. My theoretical model does not consider edge terminations, which results in an underprediction of the CO_2/CH_4 selectivity and an overprediction of the H_2/CO_2 selectivity.

Table 4-9. Experimentally measured H_2/CH_4, CO_2/CH_4, and H_2/CO_2 selectivities of membranes M2 and M4 reported in Zhao *et al.*[122] Each membrane-temperature combination was matched to an etching time that reproduces the selectivities best. Note that some datapoints are not available because they were not experimentally measured, or because they are not reliable due to large errors.

Condition		Measured selectivity			Best fit of etching time	Fitted selectivity		
Membrane	Temperature (°C)	H_2/CH_4	CO_2/CH_4	H_2/CO_2		H_2/CH_4	CO_2/CH_4	H_2/CO_2
M2, pristine	150	21.1	5.8	3.7	32	22.5±29.3	5.2±6.9	4.3±1.4
M2, 1 cycle O_3	150	30.3	7.9	3.8	28	33.4±23.1	7.1±5.0	4.7±0.8
M2, 1 cycle O_3	100	38.6	12.1	3.2	26	38.2±39.9	11.0±11.6	3.5±0.7
M2, 1 cycle O_3	30	53.6	28.6	1.9	21~22	-	-	1.8±0.6
M2, 2 cycles O_3	150	27.8	-	-	30	28.9±17.2	6.1±3.7	4.8±0.7
M2, 3 cycles O_3	150	11.8	-	-	45	11.2±1.5	3.0±0.4	3.7±0.2
M4, pristine	150	23.3	6.4	3.6	31	25.8±14.5	6.1±3.5	4.2±0.6
M4, low T O_3	150	38.8	8.2	4.7	27	37.3±32.8	8.1±7.1	4.6±0.8
M4, 1 cycle O_3	150	26.1	7.4	3.5	30	28.9±17.2	6.1±3.7	4.8±0.7
M4, 1 cycle O_3	100	26.9	10.0	2.7	27	27.9±25.2	9.0±8.2	3.1±0.6
M4, 1 cycle O_3	30	35.2	22.5	1.6	21~22	-	-	1.8±0.6
M4, 2 cycles O_3	150	7.6	-	-	52	7.9±0.7	2.4±0.2	3.3±0.1

Similar analyses are carried out for the results reported by Khan *et al.*[128] and Rezaei *et al.*[130] in Table 4-10 and Table 4-11, respectively. The nanopores in these two studies were intrinsic defects formed during chemical vapor deposition of graphene in a reductive atmosphere, and therefore, were

not likely terminated by dense oxygen-containing groups such as carbonyl groups. Nevertheless, these nanopores still exhibit the effective pore size expansion as the temperature increases.

Table 4-10. Experimentally measured H_2/CH_4 selectivities of membranes reported by Khan *et al.*[128]. Each membrane-temperature combination is matched to an etching time that reproduces the selectivity best.

Condition		Measured selectivity	Best fit of etching time	Fitted selectivity
Membrane	Temperature (°C)	$S(H_2/CH_4)$		$S(H_2/CH_4)$
1	30	5.5	45	5.6±0.8
1	100	6.7	52	6.3±0.6
1	150	8.4	52	7.9±0.7
2	30	6.0	40	6.3±3.1
2	100	4.1	70	3.7±0.1
2	150	5.1	70	4.5±0.2
3	30	6.9	40	6.3±3.1
3	100	7.4	50	7.2±1.7
3	150	6.8	55	7.1±0.5
4	30	5.3	45	5.6±0.8
4	100	5.5	55	5.7±0.4
4	150	6.1	60	6.4±0.9
5	30	4.7	50	4.6±1.1
5	100	5.0	60	5.2±0.7
5	150	4.9	70	4.5±0.2
6	30	4.2	52	4.1±0.4
6	100	5.5	55	5.7±0.4
6	150	6.3	60	6.4±0.9

Table 4-11. Experimentally measured H_2/CH_4 selectivities of membranes reported by Rezaei *et al.*[130]. Each membrane-temperature combination is matched to an etching time that reproduces the selectivity best.

Condition		Measured selectivity	Best fit of etching time	Fitted selectivity
Membrane	Temperature (°C)	$S(H_2/CH_4)$		$S(H_2/CH_4)$
σ-1	25	3.3	60	3.3±0.5
σ-1	150	2.9	100	2.6±0.2
σ-2	25	3.1	60	3.3±0.5
σ-2	150	3.6	80	3.6±0.2
σ-3	25	2.9	60	3.3±0.5
σ-3	150	3.4	80	3.6±0.2
α-1	25	3.8	52	3.9±0.4
α-1	150	5.1	70	4.5±0.2
α-2	25	5.0	45	5.4±0.8
α-2	150	6.3	60	6.4±0.9
σ-A_H-1	25	9.9	32	9.6±13.0
σ-A_H-1	150	11.9	45	11.2±1.5

σ-A_H-2	25	6.1	40	6.1±3.0
σ-A_H-2	150	9.1	50	9.0±2.1
σ-A_H-3	25	6.1	40	6.1±3.0
σ-A_H-3	150	7.4	55	7.1±0.5
α-A_H-1	25	6.0	40	6.1±3.0
α-A_H-1	150	9.2	50	9.0±2.1
α-A_H-2	25	10.4	32	9.6±13.0
α-A_H-2	150	13.0	40	12.9±6.0

4.7.4 Predicted Pore Diameter Distribution

As shown in Figure 4-7, the predicted pore diameter distribution terminates at 1 nm for all the etching times investigated in this chapter, which is smaller than the high-resolution transmission electron microscopy (HR-TEM) imaging results reported in ref. 118 (without clogging). Note that the predicted pore diameter distributions in Figure 4-7, represent the open areas of nanopores in a membrane, with the effect of pore clogging included. This inconsistency is indirect evidence for the clogging of the nanopores under the experimental conditions considered.

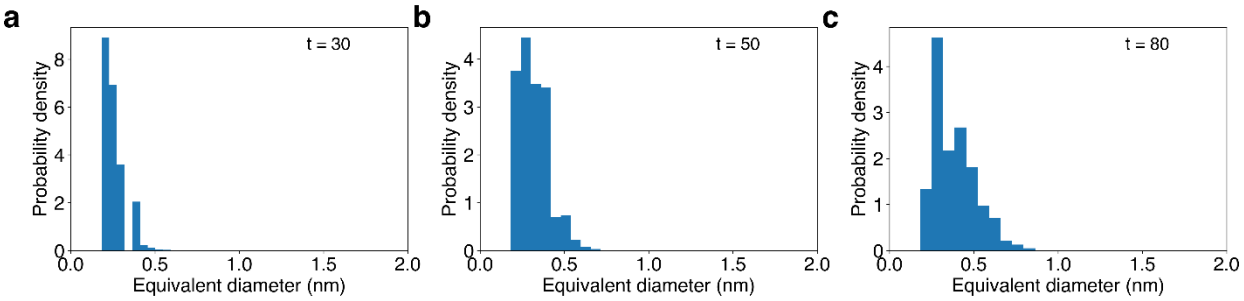

Figure 4-7. Distribution of the equivalent diameter of the nanopores generated by the Kinetic Monte Carlo algorithm with etching times of (a) 30, (b) 50, and (c) 80.

4.7.5 Comparison of Apparent Energy Barriers between Experiments and Theory

Table 4-12 compares the apparent energy barriers of H_2, CO_2, and CH_4 measured by He *et al.*[118] experimentally and the apparent energy barriers derived by the theoretical fitting to the same dataset (Table 4-5). The reasonably good match suggests that the theory advanced in this chapter can generate pore size distributions that closely match those in the experimental samples.

Table 4-12. Comparison between experimentally measured H_2, CO_2, and CH_4 apparent energy barriers reported by He *et al.*[118] and the theoretically derived apparent energy barriers, with the partial clogging hypothesis.

Condition		Apparent energy barrier (kJ mol^{-1})	
Membrane	Gas	Experiment	Theory
NG-1s	H_2	17.5±0.8	23.1
NG-1s	CO_2	13.8±1.3	15.1
NG-1s	CH_4	21.3±0.2	25.6
NG-2s	H_2	11.9±2.4	18.6
NG-2s	CO_2	5.7±1.9	9.8
NG-2s	CH_4	13.7±2.0	18.8
NG-3s	H_2	12.3±1.8	14.8
NG-3s	CO_2	7.4±1.2	7.6
NG-3s	CH_4	12.2±3.1	14.8

4.7.6 Convergence Test of the Phase Space Discretization

Figure 4-8 shows how the Helmholtz free energy barrier $\Delta A^{\ddagger}$ of CO_2 crossing a three-fold symmetric size 13 graphene nanopore depends on the number of grid points in the r, ϕ, z, and $\vec{\theta}$ directions. As shown in Figure 4-8a, $\Delta A^{\ddagger}$ converges when the number of grid points in the r direction exceeds ~20. Meanwhile, Figure 4-8b, c, d show that $\Delta A^{\ddagger}$ is not sensitive to the number of grid points in the ϕ or z directions, nor to the number of randomly sampled molecular rotational directions $\vec{\theta}$. Consequently, I choose 30, 20, and 15 grid points in the r, ϕ, and z directions, and 10 randomly sampled $\vec{\theta}$ directions in my calculations.

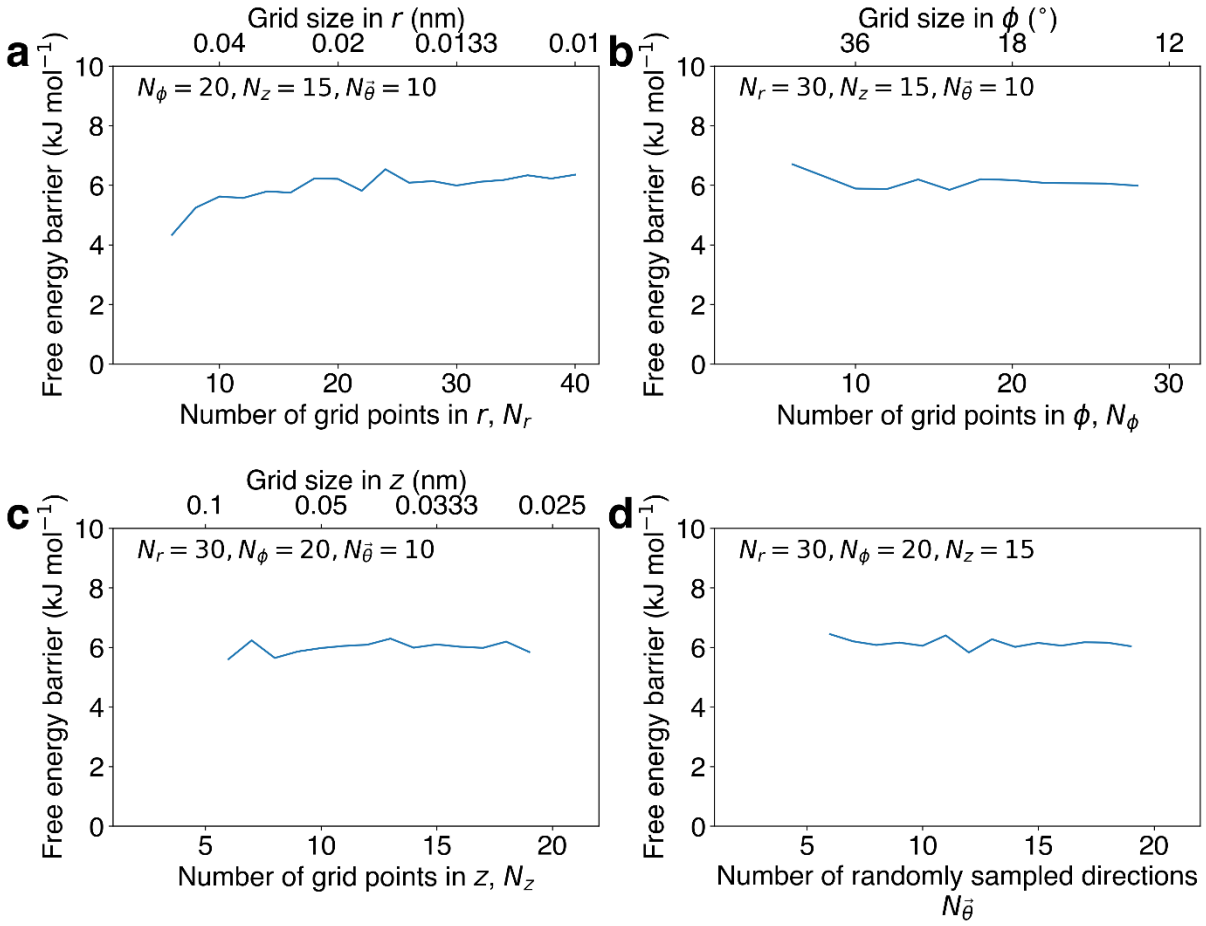

Figure 4-8. Convergence of the Helmholtz free energy with the increase in the number of grid points in (a) the r direction, (b) the ϕ direction, and (c) the z direction. (d) Convergence of the Helmholtz free energy with the increase in the number of randomly sampled directions $\vec{\theta}$ of molecular rotation.

5 Demonstration of Gas Mixture Separation through Suspended Nanoporous Single-Layer Graphene Membranes

5.1 Introduction

Graphene monolayers perforated with nanometer-scale pores have the potential to enable a new class of ultra-high flux, high selectivity membrane for gas mixture separations.[29,109,111,140,167,201,220–223] Recent studies have shown that graphene's outstanding chemical, mechanical, and thermal stability could enable these monolayer membranes to withstand the high pressure differentials and elevated temperatures necessary to separate gas mixtures, even with thicknesses of only a single atomic layer.[29,136,224–226] Due to its single atom thickness, gas permeation through single-layer graphene membranes could be orders of magnitude faster than permeation through conventional gas separation membranes.[140,201,221] As a result, graphene membrane modules sized to separate a given gas mixture flow rate could be substantially smaller in area and volume compared with conventional polymer-membrane or hollow fiber modules, offering a solution to the challenging problem of membrane scale-up.[1,227] Finally, many theoretical and computational studies have predicted that gas molecule translocation through graphene nanopores with diameters on the order of ~1 nm or less is likely to be an activated process, with energy barriers varying substantially based on the nanopore morphology and gas molecule size,[25,75,152] which provides an opportunity to design graphene membranes with properties tailored to achieve excellent separation performance.

Previous experimental efforts have investigated the transport of single, pure component gases through graphene membranes with nanometer-scale pores[109,110] or larger rips and tears.[126] Recently, Boutilier *et al*. measured the permeances of individual gases through polymer-coated three-layer porous graphene supported by polycarbonate track etched membranes, and the selectivities confirmed the Knudsen effusion mechanism.[113] Further, they observed molecular sieving of gas molecules through anodic-aluminum-oxide-supported single-layer graphene membranes perforated by ion bombardment

and oxygen plasma.[115] In these studies, gas selectivities were estimated from single gas permeation measurements, which may not accurately account for phenomena such as competitive adsorption and diffusion that could influence mixture separations through these membranes.[66,152] Meanwhile, the transport resistance from the support holes confounded the intrinsic performance of the graphene membranes. Celebi *et al*. provided the first demonstration of gas mixture separation through double layer graphene membranes supported by SiN_x with pores of 7.6 nm to 1 μm in diameter.[111] While these studies have provided highly valuable insights into the properties of graphene membranes, further direct measurements of gas mixture separations are critical for understanding graphene membrane separations. In particular, studying gas separation through single-layer graphene membranes with pores small enough to enable activated translocation is a central long-term goal. In this regard, measuring the temperature dependence of the gas permeance is an important new approach for understanding the mechanism of gas permeation through graphene nanopores and identifying activated transport processes.

In this chapter, for the first time, I directly measured gas mixture separation through single-layer graphene membranes. Using an on-line mass spectrometer, I quantified gas mixture separation through nanopores created spontaneously during chemical vapor deposition (CVD) synthesis of graphene. This chapter also report the first measurement of trans-membrane gas permeance at various temperatures from 22 to 208 °C, which provides important insights into the mechanisms of gas permeation that have not been elucidated previously. Two graphene membranes exhibited gas selectivities superior to the Knudsen selectivities. This superior selectivity is attributed to a steric selectivity mechanism due to the gas molecular size,[26] which supports that the pore sizes in these two membranes are on the nanometer scale. A third membrane exhibited relatively high gas permeances, as well as selectivities lower than the Knudsen effusion prediction, indicating a combination of gas effusion and collective viscous flow.[111] However, a fourth membrane exhibited lower gas permeances but higher selectivity, and increasing permeance as a function of temperature, which supports an activated transport mechanism. As temperature increased, the trans-membrane gas transport shifted from the activated regime to a non-activated regime. Finally, a fifth membrane exhibited extremely low gas permeance at or below the detection limit of my technique across the entire temperature range tested. Note that this chapter represents the first direct measurement of gas mixture selectivity beyond the Knudsen selectivity for

any graphene membrane. These results underscore the potential of graphene membranes as high flux, high selectivity membranes for gas mixture separation.

5.2 Membrane Fabrication and Characterization

Polycrystalline graphene were synthesized on Cu foils by controlled pressure chemical vapor deposition (CPCVD),[228] and transferred onto Ni supports with ~5 μm diameter holes to create suspended membranes for gas permeation measurements (for experimental methods, see Section 5.5). Out of eight graphene membranes initially fabricated in this way, five remained intact after transfer and allowed for characterization and extensive gas permeation testing that lasted several weeks. As shown in Figure 5-1, scanning electron microscopy (SEM) imaging of these five membranes (labeled hereafter A, A', B, C, and D) confirmed that each graphene membrane was suspended over the 5 to 10 um diameter straightline channel machined into the Ni supports without any large tears. Membranes A and A' were fabricated from the same CPCVD growth. The contrast in the suspended graphene domains likely arises from poly (methyl methacrylate) (PMMA) residue remaining from the transfer procedure, amorphous carbon, or other adsorbed residue on the membrane. These residues could potentially influence gas permeation through these areas by impeding direct gas impingement through graphene nanopores, or by affecting gas adsorption at the graphene surface. Areas of the membrane with no residue are expected to allow gas permeation directly through pores in the graphene. Any pores with sizes on the order of ~10 nm or less are below the resolution of the SEM under the imaging conditions. Figure 5-1D also shows ~1 μm diameter regions marked by red arrows with some straight sides that are uniformly brighter than the rest of the membrane. These regions are likely graphene double or multilayers.

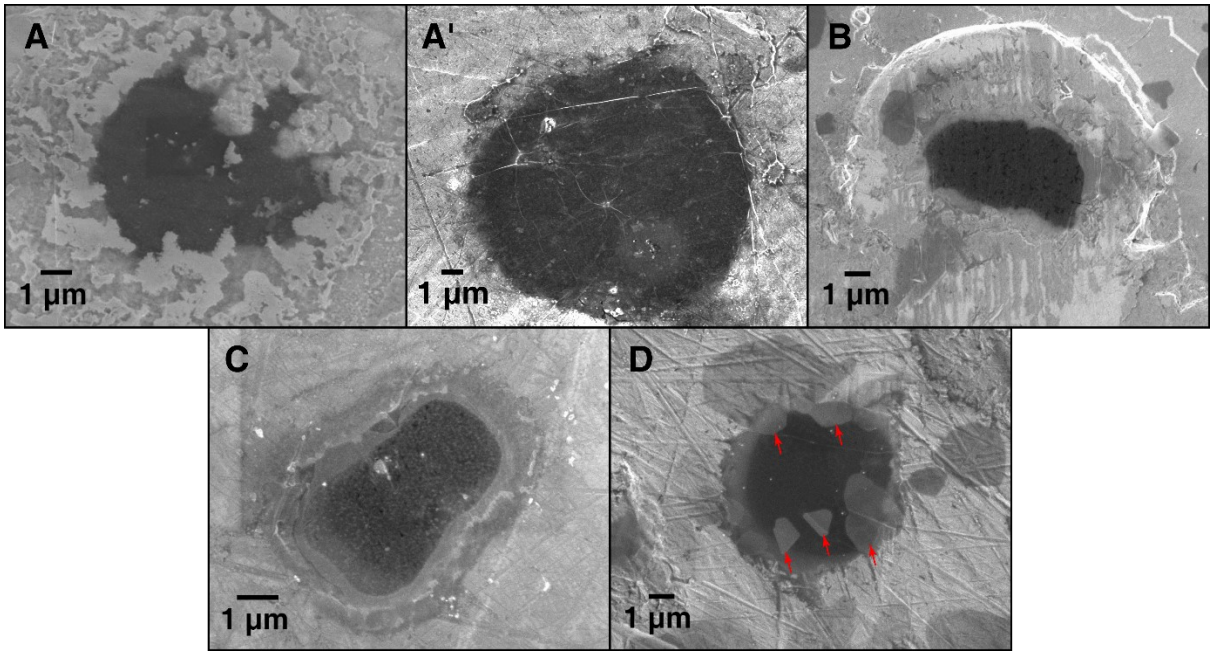

Figure 5-1. Scanning electron microscope (SEM) images of graphene membranes suspended on nickel foil supports with laser drilled holes. The holes were designed to be circular and 5 μm in diameter. The Ni foils were polished to increase the success rate of graphene transfer, which deformed the hole edges. These five membranes, A, A', B, C, and D, were used for gas mixture permeation measurements. The contrast likely arises from residue on the membranes after the transfer process, while the lighter regions in membrane D indicated by red arrows are likely graphene double or multilayers.

Raman spectroscopy was used to characterize the CPCVD-grown graphene transferred onto a Si wafer piece. A representative spectrum is shown in Figure 5-2A. In this case, a clear D peak is observed, indicating the presence of some defects in this region of the graphene sample.[229–231] The D peak arises from nanopores in the graphene, defects at grain boundaries, point defects, and/or carbonaceous impurities.[229–232] The measured D to G peak intensity ratio, I_D/I_G in this region is 0.16. The average distance between defects L_D can be correlated to I_D/I_G by the amorphization trajectory in the following form: $L_D^2\ (\mathrm{nm}^2) = (1.8 \pm 0.5) \times 10^{-9} \cdot \lambda_L^4 (I_D/I_G)^{-1}$, where λ_L is the excitation laser wavelength (in nanometers).[232,233] A 532 nm laser was used to obtain Raman spectra, and L_D is predicted to be (30 ± 4.5) nm. To investigate the defect density and layer number distribution, spectra were collected in a square array of 16 × 16 points spaced apart by a pitch of 20 μm across the graphene sample supported on Si wafer. The Raman laser spot diameter is 1.22 λ_L/NA, where NA is the numerical aperture of the microscope objective. Assuming NA = 0.5 for a 50x objective, the laser spot diameter was approximately 1 μm for the measurements. Thus, these laser spot areas do not overlap. Figure 5-2B

shows the distribution of I_D/I_G ratios. The majority of the regions on this graphene sample have I_D/I_G < 0.2, corresponding to a low defect density.[232,233] However, a significant fraction of the points display a larger D peak with I_D/I_G ranging up to 3. Additionally, it is well known that the 2D/G peak intensity ratio I_{2D}/I_G can be used identify single-layer graphene. These data are contained in Figure 5-2C. Approximately 2/3 of the graphene regions measured have I_{2D}/I_G > 2, corresponding to single-layer graphene, while some regions have lower I_{2D}/I_G ratios corresponding to double or multilayer graphene.[229–231] Overall, the relatively broad I_D/I_G and I_{2D}/I_G distributions indicate that there appears to be spatial heterogeneity in this as-produced graphene, but the majority of the active area of each membrane appears to be monolayer graphene.

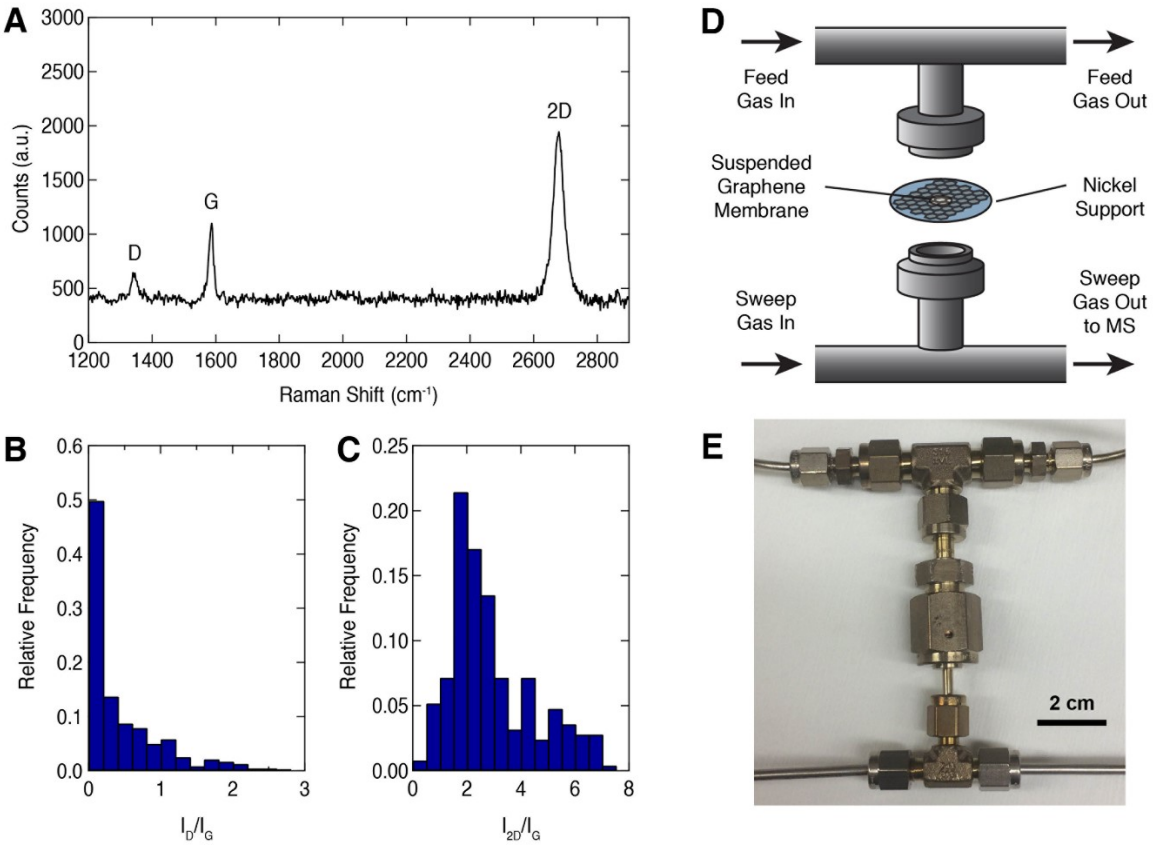

Figure 5-2. (A) Representative Raman spectrum of the graphene membrane transferred instead to Si. The 2D/G peak intensity ratio indicates that this region is single-layer graphene, while the presence of the D peak may arise from grain boundaries, impurities, or defects in the film. (B) Distribution of D/G peak intensity ratios, I_D/I_G, measured at an array of points on the graphene spaced apart by 20 μm. The majority of the points measured have I_D/I_G lower than 0.2, corresponding to low defect densities, while some points have higher D peak intensities, corresponding to a higher density of defects. (C) Distribution of 2D/G peak intensity ratios, I_{2D}/I_G, measured at the same array of points on the graphene. The majority of the points have I_{2D}/I_G > 2, corresponding to single-layer graphene, while some points have lower ratios corresponding to double or multilayer graphene. (D) Diagram and (E) photograph of

the module used to measure gas permeance through the suspended graphene membranes. The Ni foil support was compressed between the two metal beads of a Swagelok VCR fitting to create a metal/metal seal.

Each of the supported graphene membranes was sealed inside a module designed for gas permeation testing, as illustrated in Figure 5-2D, E. The feed side of the membrane was pressurized to 1.4 to 1.5 bar with an equimolar mixture of gases spanning a large range of sizes and molecular weights, including H_2, He, CH_4, CO_2, and SF_6. Gas molecules that translocated through the membrane were swept with Ar carrier gas at 1.1 bar into a calibrated mass spectrometer, which was used to measure the permeance of each gas in the feed mixture (see Section 5.5 for details). The flow rates of the mixture feed gas and the carrier gas were both 4 sccm. The membranes were tested at temperatures ranging from 22 to 208 °C. The results of these measurements revealed the gas transport behavior for the five membranes.

5.3 Gas Separation Performances

As shown in Figure 5-3A, membrane A exhibited gas permeance values substantially above the detection limit of the technique, which was determined through control measurements using Ni foils with no hole (see Section 5.5.7). Meanwhile, the permeances through membrane A were well below the values expected for the gas flow through an open channel in the Ni with no graphene membrane (~10^{-2} mol m^{-2} s^{-1} Pa^{-1}, Figure 5-9), indicating that these gases translocated through pores in the intact graphene membrane. The gas permeances measured for membrane A were on the order of 10^{-5} mol m^{-2} s^{-1} Pa^{-1}, while the permeances through typical polymer membranes range from 10^{-10} to 10^{-7} mol m^{-2} s^{-1} Pa^{-1}.[111] This difference of 2 to 5 orders of magnitude highlights a key advantage of graphene compared to conventional membrane materials.

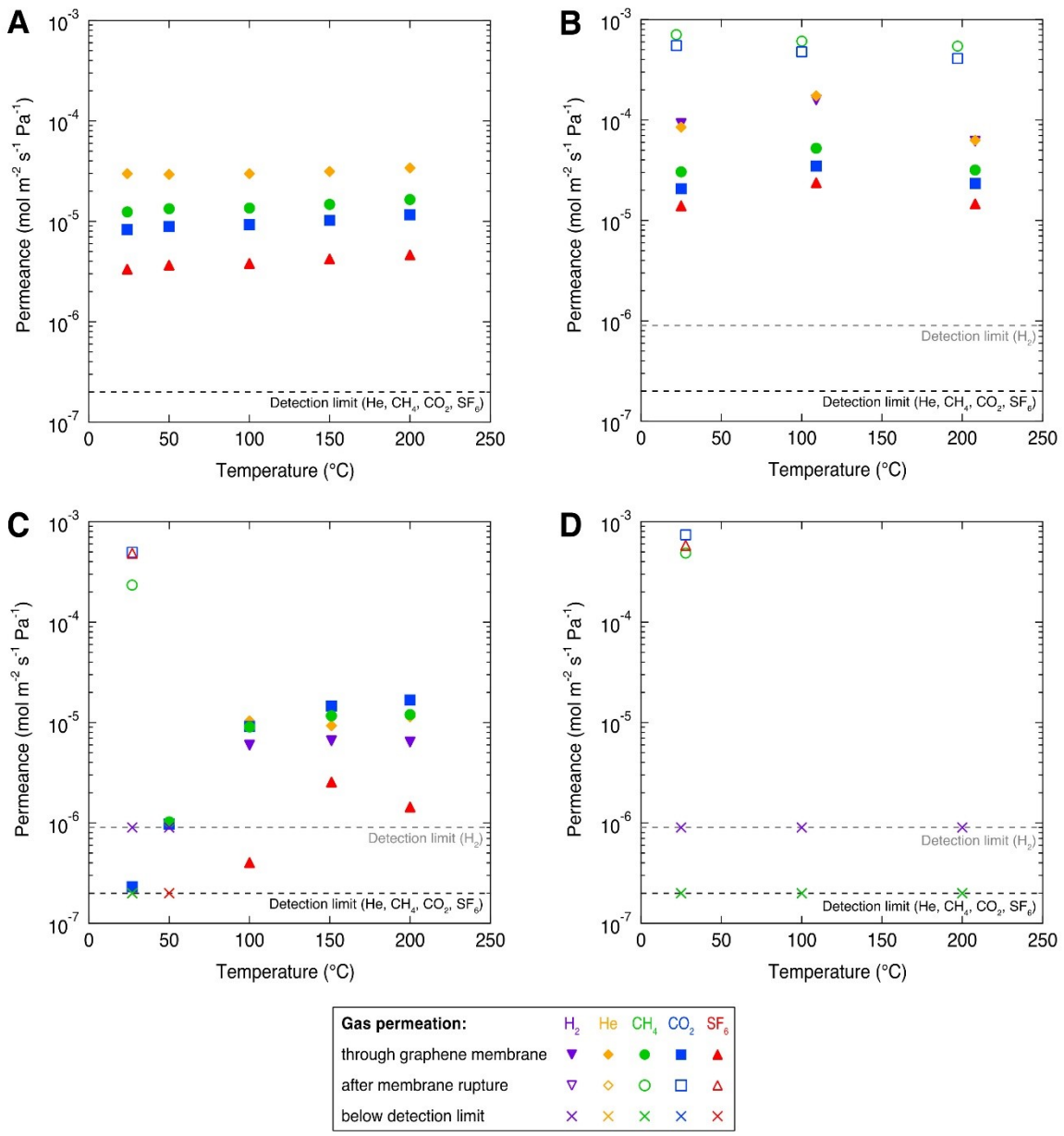

Figure 5-3. Gas permeation through graphene membranes A, B, C, and D measured as a function of temperature. The filled symbols represent permeance through the intact graphene membranes (before membrane rupture). The open symbols represent permeance measured after membrane rupture. The X symbols represent measurements that showed permeance at or below the detection limit of the technique.

For membrane A, at each temperature, He had the highest permeance, followed by CH_4, CO_2, and SF_6 with the lowest permeance, mirroring the trend in the molecular weights of these gases from low to high. The permeance through the membrane did not vary substantially as a function of temperature. This trend of permeance as a function of temperature through membrane A suggests that gas translocation was likely dominated by the gas effusion mechanism (Section 1.2), which is known to

have a weak temperature scaling of $T^{-1/2}$ (where T is the temperature). Slight deviations of the permeances from the $T^{-1/2}$ scaling existed, likely due to the effective thermal expansion of the graphene nanopores caused by the partial clogging effect of airborne hydrocarbons (Section 4.4 and Section 6.4). For pores with diameters of microns or larger, the gas flux is dominated by collective viscous flow described by the Sampson's model for transport through a circular aperture in an infinitely thin membrane.[38–40] In this regime, the flux of a pure gas is inversely proportional to its viscosity. In the case of a mixture gas feed, the gas mixture shares a mixture viscosity. Therefore, the selectivity approaches 1, indicating that no separation occurs.[111] In contrast, the gas effusion mechanism is expected to dominate transport when the pore diameter is smaller than the mean free path of the gas, which is on the order of 100 nm near room temperature and atmospheric pressure.[37] If there is no energy barrier for gas translocation, then the flow rate of each gas *via* this mechanism is given by the impingement rate, $\mathrm{d}n/\mathrm{d}t$:

$$\frac{\mathrm{d}n}{\mathrm{d}t} = A_{\mathrm{open}} \frac{\Delta p}{\sqrt{2\pi MRT}} \tag{5-1}$$

where A_{open} is the area open for impingement, Δp is the partial pressure drop across the membrane, M is the gas molar weight, and R is the gas constant (Section 1.2). Following Equation (5-1), the selectivity of the gas effusion mechanism, known as the Knudsen selectivity, is determined by the square root of the ratio of the molar mass of each gas species (Graham's Law of effusion).

The selectivity is defined as the ratio of the permeance values of a gas pair. Each gas pair among the mixture explored in this chapter has a selectivity value. The selectivities of graphene membrane A measured at 25 °C for He, CH_4, CO_2, and SF_6 in the gas mixture are shown in Table 5-1, which approximately match the prediction from the gas effusion mechanism with some deviations (see values in parentheses). Therefore, in membrane A, there existed spontaneously formed graphene pores large enough so that the trans-membrane transport of gas molecules through these pores was not hindered by an energy barrier. This requires a graphene pore size which is substantially greater than the gas molecular size (Section 3.7). However, the graphene pores in membrane A must also be smaller than the mean free path of the gas molecules, on the order of ~100 nm, to yield selectivities which are close to those predicted by the effusion mechanism. This suggests that the graphene nanopores responsible

for the gas mixture separation likely had diameters between 1 nm and 100 nm. These pores may have been formed as defects during the graphene growth process.[149,234] It is unlikely that the pores are small rips or tears in the graphene membrane created during the transfer procedure, because at least one other sample transferred in the same way had no such defects (Membrane D, Figure 5-3D) and the mechanical stresses involved in the transfer cannot create such small pores.

Table 5-1. Selectivities for membrane A measured at 25 °C. For comparison, the Knudsen selectivities are shown in parentheses.

Gas	Molar weight (g mol^{-1})	Selectivity with respect to			
		He	CH_4	CO_2	SF_6
He	4.00	-	2.40 (2.00)	3.62 (3.32)	9.30 (6.04)
CH_4	16.04	0.42 (0.50)	-	1.51 (1.66)	3.88 (3.02)
CO_2	44.01	0.28 (0.30)	0.66 (0.60)	-	2.57 (1.82)
SF_6	146.06	0.11 (0.17)	0.26 (0.33)	0.39 (0.55)	-

The absolute values of the gas permeance measured through membrane A can be used with Equation (5-1) to further refine the estimate of the pore diameters in this membrane. The permeance of gas *i* through a membrane is defined as the gas flux normalized by the partial pressure difference of gas *i*. Therefore, according to Equation (5-1), the permeance *K* from effusion can be expressed as follows:

$$K = \frac{1}{\Delta p} \cdot \frac{\mathrm{d}n/\mathrm{d}t}{A_{\mathrm{membrane}}} = \frac{A_{\mathrm{open}}}{A_{\mathrm{membrane}}} \cdot \frac{1}{\sqrt{2\pi MRT}} \tag{5-2}$$

where A_{membrane} is the area of the suspended graphene membrane. Note that A_{membrane} equals 28.2 μm^2 for membrane A (Figure 5-1A). The area open for impingement A_{open} in membrane A can be calculated according to Equation (5-2) based on the permeance data for each gas. The results are summarized in Table 5-2. Even assuming that the gas permeance in membrane A was contributed by one circular pore, the resulting pore diameter is below the upper bound set by the gas effusion mechanism (100 nm).

Table 5-2. Area open for impingement A_{open} in membrane A for four different gases at 25 °C, and the corresponding pore diameter if only one circular pore existed. The open area is negatively correlated with the gas kinetic diameter.[6,36] The theoretically fitted open areas are listed for comparison, exhibiting high consistency with the experimental results.

Gas	A_{open} (nm^2)	Pore diameter if only one circular pore existed (nm)	A_{open} relative to He	Kinetic diameter (Å)	Theoretically fitted A_{open} (nm^2)

He	7.08×10^3	94.9	1.00	2.6	7.10×10^3
CH_4	5.92×10^3	86.8	0.84	3.8	5.97×10^3
CO_2	6.49×10^3	90.9	0.92	3.3	6.42×10^3
SF_6	4.60×10^3	76.5	0.65	5.5	4.59×10^3

The possible pore size range in membrane A can be further narrowed down by considering the difference in open areas A_{open} for different gases. If A_{open} is identical for all the gases, according to Equation (5-1), the experimental selectivities should have matched the Knudsen selectivities. On the contrary, the area open for impingement was the largest for He, followed by CO_2 and CH_4, with SF_6 ranking last. As shown in Table 5-2, the open area for SF_6 was only 65% of that for He. This difference in open areas is consistent with the steric selectivity mechanism introduced by Wang *et al* in the steric transport regime.[26] Under this mechanism, gas transport shares common characteristics with the effusion mechanism, including pore sizes which are smaller than the gas mean free path and zero energy barrier for crossing. However, the steric selectivity mechanism takes the size of a gas molecule into consideration, while the original effusion mechanism treats a gas molecule as a mass point devoid of volume. Therefore, in the steric selectivity mechanism, it is possible for a gas molecule to hit the pore edge and bounce off, even if its center of mass impinges within the pore region. This implies that the "effective" open area A_{open} is smaller than the "actual" pore area A_{pore}. The permeation coefficient δ is defined as the ratio of A_{open} to A_{pore}, where $A_{\mathrm{open}} = \delta A_{\mathrm{pore}}$ and $0 < \delta < 1$. The larger the gas molecule, the greater the likelihood that it hits the pore edge and gets rejected, and hence, the smaller the permeation coefficient δ. Recall that the size of a gas molecule in the context of a collision is characterized by the kinetic diameter D_m.[36] As shown in Table 5-2, the open area A_{open} was found to be negatively correlated with the gas kinetic diameter, which is consistent with the characteristics of the steric selectivity mechanism.

To be more quantitative, assuming that the pore is a circle and that the gas molecule is a hard sphere, the permeation coefficient δ can be expressed as a function of the gas kinetic diameter D_m and the pore diameter D_p: $\delta = \delta(D_m, D_p)$. This equation contains three variables and one physical dimension (length). According to the Buckingham π theorem,[235] the original equation can be rewritten in terms of a set of two (= 3 – 1) dimensionless parameters. One obvious choice of the set is δ and

D_m/D_p. Defining the size factor $w = D_m/D_p$, it follows that $\delta = \delta(w)$. Sun *et al.* previously studied this function using a Monte Carlo hit-and-miss method.[46] An approximate function $\delta(w) \approx (1-w)^2$ was proposed by Wang *et al.*[26] and by Boutilier *et al.*[115] Here, I show that this function can be analytically expressed and numerically integrated, assuming a Maxwell-Boltzmann velocity distribution of an ideal gas (Appendix 5.6.1). Although the exact expression of $\delta(w)$ involves a complex double integration, the following approximate formula for δ can be derived as (Appendix 5.6.1):

$$\delta(w) \approx (1-w)^3 \tag{5-3}$$

Equation (5-3) has a maximum absolute error of only 2.2% for $0 \le w \le 1$ (Figure 5-12 in Appendix 5.6.1). The exact function $\delta = \delta(w)$ is a monotonically decreasing function (dashed curve in Figure 5-4a). When $w = 0$ (infinitely small gas molecule), $\delta = 1$, and the gas effusion limit is obtained. On the other end, when $w = 1$ (gas molecule and pore of the same size), $\delta = 0$, suggesting a 100% rejection probability.

Assuming a monodisperse pore size distribution, I fit the open areas for the four gases using the steric selectivity mechanism using two parameters: the pore number n and the pore diameter D_p. The total open area for impingement of gas i can be obtained by multiplying the open area of each pore by the pore number n:

$$A_{\text{open},i}^{\text{model}} = n \cdot \frac{\pi}{4} D_p^2 \cdot \delta\left(\frac{D_{m,i}}{D_p}\right) \tag{5-4}$$

Then the following residual sum of squares (RSS) is minimized by tuning the parameter set (D_p, n):

$$\text{RSS} = \sum_{i=He,CH_4,CO_2,SF_6} \left(A_{\text{open},i}^{\text{model}} - A_{\text{open},i}\right)^2 \tag{5-5}$$

The resulting optimized mean pore diameter D_p is 2.5 nm, and the optimized pore number n is 2074, giving an areal pore density of 7.3×10^{13} m^{-2} and an average inter-pore distance of ~120 nm. Note that this inter-pore distance is greater than the inter-defect distance estimated by the amorphization trajectory (~30 nm), implying that a large fraction of the defects are not pores, or are pores which are too small for a significant gas flow. The corresponding theoretical fitted open areas are listed in Table 5-2, showing high consistency with the experimental results. For D_p = 2.5 nm, the theoretical permeation

coefficients δ for He, CO_2, CH_4, and SF_6 and their experimental ratios are also plotted in Figure 5-4A ($A_{\mathrm{open},i}/A_{\mathrm{open},j} = \delta_i/\delta_j$ because A_{pore} was the same for all gases during one test). The consistency between the theoretical and the experimental values further validates the steric selectivity mechanism. On the other hand, if the gas molecular size is neglected, the open areas would be the same, and $\delta = 1$ for all the gases. This null hypothesis of simple effusion predicts $A_{\mathrm{open}} = A_{\mathrm{pore}} = 6.02 \times 10^3$ nm^2 for all the gases, and leads to a large RSS which is 440 times greater than that predicted by the steric selectivity mechanism.

The contour plot of lg(RSS) as a function of (D_p, n) is shown in Figure 5-4B. The order of magnitude of RSS is plotted according to the color bar on the right. A single local minimum resides at D_p = 2.5 nm and n = 2074, which is colored in dark blue. As shown by the narrow dark blue region (RSS < 10^5 nm^2), only a small fraction of the parameter space can match the experimental data with reasonable error. The narrow (D_p, n) window for a small RSS suggests that the pore size dominating the gas flux can be bracketed between 2.2 to 2.6 nm, and the corresponding pore number can be bracketed within 1800 to 2600 total pores over the 28.2 μm^2 area. The single local minimum of RSS implies that the graphene pores in membrane A are likely to be monodisperse in terms of pore size. In the case of polydisperse pore sizes, the current dataset with four independent data points limits the number of independent variables to four, and therefore, is insufficient to generate an intricate pore size distribution. Nevertheless, I attempted to fit the experimental open pore areas using two discrete pore sizes D_{p1} and D_{p2}, with pore numbers n_1 and n_2, respectively. In this case, the open area for gas i can be expressed as follows:

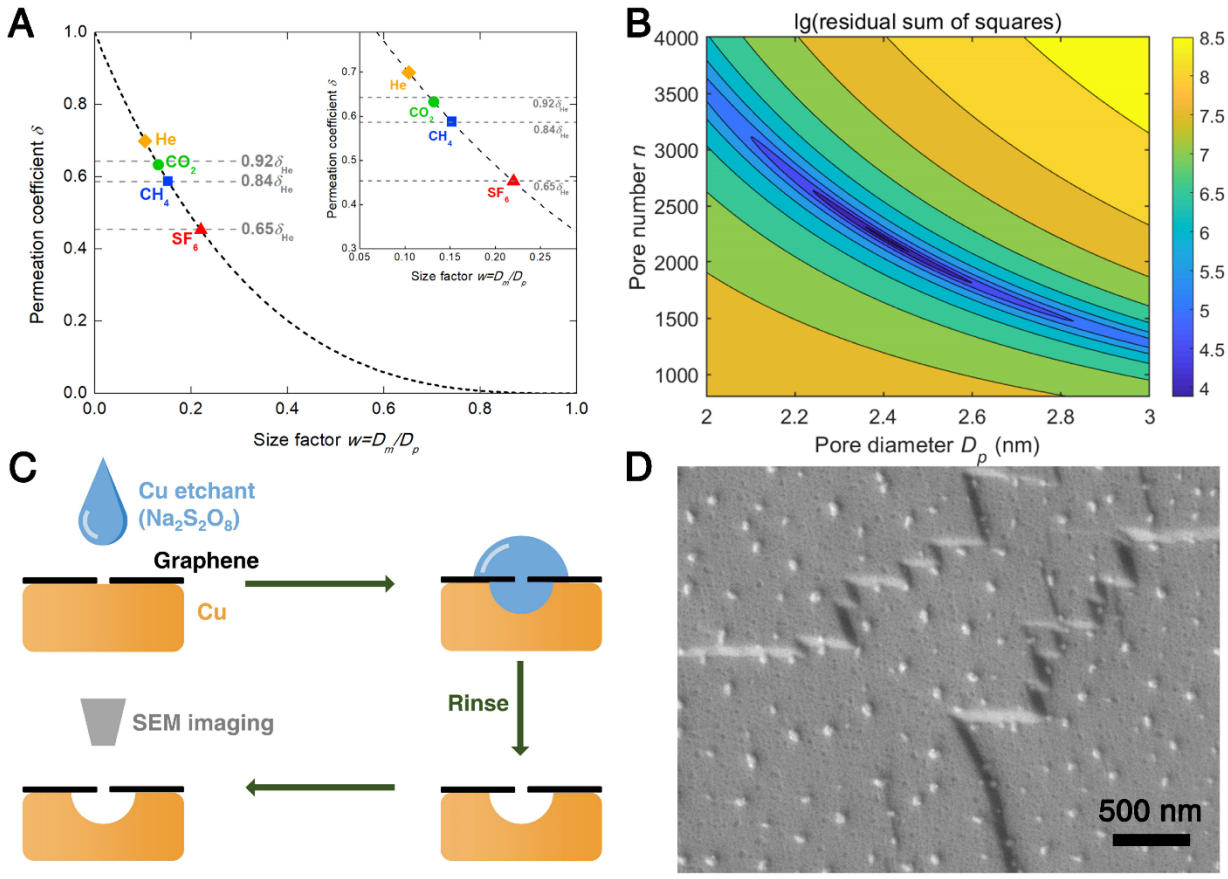

Figure 5-4. (A) Steric selectivity mechanism prediction of the permeation coefficient δ as a function of the size factor w (dashed curve). The model predictions for He, CO_2, CH_4, and SF_6 for a pore diameter of 2.5 nm are marked along the curve. The model predictions match the experimental values (horizontal lines in grey). A zoomed-in version is shown in the inset. (B) Contour plot of lg(residual sum of squares) as a function of the pore diameter D_p and the pore number n. The residual sum of squares is evaluated using Equation (5-3) for calculational efficiency. (C) Schematic illustration of the Cu etching process through a nanoporous graphene layer. (D) SEM image of the etch pits formed after $Na_2S_2O_8$ etch for 20 s. The areal pit density is 2.8×10^{13} m^{-2} and the pits are of similar sizes.

$$A_{\text{open},i}^{\text{model}} = n_1 \cdot \frac{\pi}{4} D_{\text{p1}}^2 \cdot \delta\left(\frac{D_{\text{m},i}}{D_{\text{p1}}}\right) + n_2 \cdot \frac{\pi}{4} D_{\text{p2}}^2 \cdot \delta\left(\frac{D_{\text{m},i}}{D_{\text{p2}}}\right) \tag{5-6}$$

The parameter set (D_{p1}, n_1, D_{p2}, n_2) that minimizes the RSS is equivalent to the fitting results of a monodisperse pore size distribution ($D_{\text{p1}} = D_{\text{p2}} = 2.5$ nm, $n_1 + n_2 = 2074$), suggesting that the sizes of the nanopores in membrane A are likely to be close to monodisperse.

A 2.5-nm pore cannot be easily imaged by SEM, but its size can be effective magnified by selective etching of Cu beneath the graphene pore, using a method developed by Kidambi *et al.*[236] A droplet of aqueous sodium persulfate ($Na_2S_2O_8$) solution was placed on as-synthesized single-layer graphene grown on Cu substrate (Figure 5-4C) for 20 s. Persulfate ions crossed the graphene pores and etch the

underneath Cu into pits, which were substantially larger the graphene pores and are observable by SEM imaging. Figure 5-4D shows the SEM image of etched Cu foil covered by porous graphene. Note that this graphene/Cu sample was fabricated in the same CPCVD batch as membrane A. As shown in Figure 5-4D, the pits are of ~50 nm in diameter, and the average inter-pit distance is ~120 nm, consistent with the steric selectivity mechanism prediction. To be more exact, the pit density is 2.8×10^{13} m^{-2}, which is on the same order of magnitude as the predicted pore density in membrane A (7.3×10^{13} m^{-2}). Assuming a uniform pore size distribution, the pore size and the pore density are inversely correlated because the overall gas permeance was measured experimentally. A close prediction of the areal pore density suggests a reasonable estimation of the pore size. This agreement between calculated and experimental pore densities provides strong support for the validity of the steric selectivity mechanism described above.

Assume that the influx of etchant ions and the efflux of Cu^{2+} ions are limited by the small graphene pore bottleneck D_p, and that the growth rate of the pit volume is proportional to the efflux of Cu^{2+} ions. Then the pit diameter D_{pit} should scale with $\left(D_p t\right)^{1/3}$.[48] As shown in Figure 5-4D, the sizes of the Cu pits are similar, indicating a monodisperse graphene pore size distribution. The directly observed areal pit density (a proxy for the graphene pore density) and the monodisperse pit size distribution strongly validate the prediction from the steric selectivity mechanism.

Note that certain factors are neglected in the steric selectivity mechanism, including a non-circular pore geometry, a non-spherical gas molecule geometry, out-of-plane graphene ripples, and non-hard sphere interactions between the gas molecules and the pore edge.[209,237] Adsorptive flux is not likely to dominate the gas flux through membrane A because if gas adsorption was the rate-limiting step, the gas permeance should have significantly decreased as the temperature increased because adsorption is typically exothermic (Section 3.5).

The analyses based on the steric selectivity mechanism show that the gas mixture selectivity can be enhanced above the Knudsen selectivity when the lighter gas is also smaller in kinetic diameter, and can access a larger effective open area for impingement, which is typically the case. One exception is CO_2 vs. CH_4, where CO_2 (M = 44 g mol^{-1}, D_m = 3.3 Å) is heavier but smaller than CH_4 (M = 16 g mol^{-}

[1], D_m = 3.8 Å). As a result, the experimental CH_4/CO_2 selectivity is less than the Knudsen selectivity (Table 5-2). This steric effect at pore entrance can only be observed when entering the pore has the greatest transport resistance along the permeation route. This is especially true for graphene, because it has negligible thickness and there is no transport resistance "within" the pore. In contrast, the gas transport resistance through a long straight pore in a thick membrane is necessarily dominated by the resistance from the inner pore wall. In this regard, the steric selectivity mechanism can be applied to other two-dimensional nanoporous membranes, such as transition metal dichalcogenides and hexagonal boron nitride.

Figure 5-5A shows the entire testing history of gas separation by membrane A with temperature cycling. The permeances of He, CH_4, CO_2, and SF_6, as well as the testing temperatures, are shown in Figure 5-5A in time order. Time was counted only when the system was under testing condition for gas permeation, and membrane A survived 25 days of continual testing without breaking, before I loaded another membrane. Notably, an irreversible permeance increase during the temperature cycling was observed. As shown in Figure 5-5B, the He permeance started at 4.8×10^{-6} mol m^{-2} s^{-1} Pa^{-1} at 24 °C, and increased to 7.7×10^{-6} mol m^{-2} s^{-1} Pa^{-1} when the permeation setup was heated to 50 °C. This increase was not reversible, as the He permeance remained nearly remained unchanged after cooling down back to room temperature. The He permeance again increased to 3.3×10^{-5} mol m^{-2} s^{-1} Pa^{-1} upon heating to 100 °C and did not revert at room temperature. Finally, the permeance of He slightly increased when heated to 200 °C and then stayed nearly invariant to temperature. A similar behavior was observed for the other three gases (the result of CH_4 is shown in Figure 5-5C). Note that the gas permeances had a daily fluctuation pattern, with a high permeance value followed by a low one. On average, a fluctuation of 8% was observed. This is because, typically, two tests were carried out per day, with an accumulation time of ~400 min and ~900 min, respectively (see Section 5.5.5 for description of the gas accumulation mode). Note that the permeance value from the longer accumulation time is smaller because of (i) reverse permeation of the permeated gas back to the feed gas, and/or (ii) a potential gas leak from the isolated permeate compartment. In Chapter 6, this variation was eliminated by increasing the total membrane area and measuring gas permeances in real time (no accumulation was needed).

The hypothesis for the observed irreversible permeance increase is the non-recoverable change of polymer residue desorption from the graphene nanopores upon heating. The graphene membrane was transferred from the initial Cu substrate to the Ni foil with a hole using PMMA as an intermediate supporting layer. As reported in the literature, PMMA residue is difficult to remove entirely from graphene.[206,238] Some PMMA residue could be observed by SEM imaging (Figure 5-1A). The testing history data suggest that, initially, the PMMA residue covered a majority of the graphene nanopores, thereby blocking the gas effusion or providing a mass transfer resistance in series to the covered pores. Upon heating, the residue may decompose, degrade, or otherwise relocate, thereby opening the underlying nanopores to allow gas effusion or to eliminate this resistance. Two other hypotheses include (1) the structure of the existing pores irreversibly changed, and (2) new graphene pores were created upon heating. Hypotheses (1) and (2) are less likely because of the previously observed thermal stability of graphene.[239] In addition, the relatively stable gas selectivity during temperature cycling indicates that the graphene pores are of similar sizes, with only the number density of uncovered pores increasing upon heating. As shown in Figure 5-5A, the gas permeances through membrane A remained stable after the gas permeation setup was heated to 100 °C (day 11). The permeance data shown in Figure 5-3A are extracted from the raw data (Figure 5-5A) after membrane stabilization was completed by heating. In order to eliminate the effect of PMMA blockage, all the other graphene membranes were heated up to 200 °C inside the module before permeation testing.

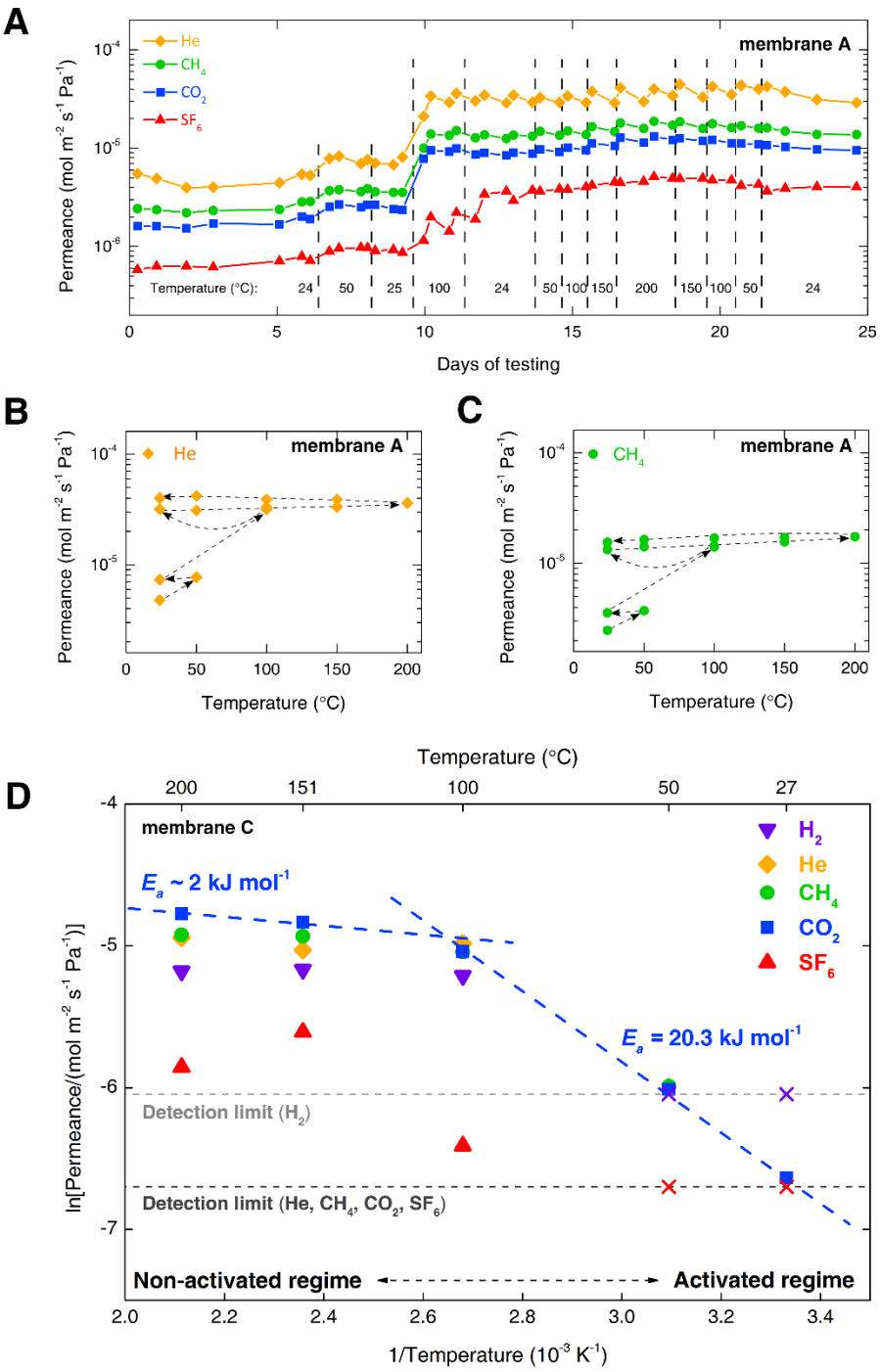

Figure 5-5. (A) Gas permeation temperature cycling history of graphene membrane A. Each symbol represents the permeance of each gas measured during one test. Time was accumulated onto days of testing only when the system was under testing condition for gas permeation. The temperatures of the tests are shown at the bottom. Permeance results of (B) helium and (C) methane through membrane A when carrying out temperature cycling. The sequence of the tests is marked by the arrows. (D) Arrhenius fitting results of gas permeances through membrane C. The natural logarithms of permeances are shown as functions of the inverse temperature.

In summary, the gas mixture separation results for membrane A show that selectivities beyond the Knudsen effusion limit can be achieved by graphene pores of several nanometers in size. The steric

selectivity mechanism is implemented to fit the pore size and the pore number, and the results suggest a monodisperse pore size distribution. A stabilization process driven by heating the system removed the PMMA residue blocking the pores, thereby irreversibly increasing the gas permeance.

Graphene membrane A' (Figure 5-1A') was fabricated from the same CPCVD batch as membrane A. the gas permeances through membrane A' were measured at room temperature, and the results are listed in Table 5-3. Note that the selectivities of membrane A' and A are similar, indicating similar pore sizes in these two membranes. This implies that the graphene nanopores were formed during the CPCVD growth of graphene but not during the subsequent transfer, because it is unlikely that two separate graphene transfers yielded highly consistent defect and tear structures. Meanwhile, the pore density in membrane A' is 53% of that in membrane A, which is closer to the pore density measured using the Cu-etching method (Figure 5-4D). This suggests that the areal pore density may not be uniform across the whole length of the CPCVD-grown graphene (see Section 6.2 for additional discussion).

Table 5-3. Gas permeances and selectivities of membranes A' and A measured at 25 °C. The permeances of both membranes are of the same order of magnitude, and their selectivities are similar and exceed the Knudsen selectivities.

Gas	Permeance of membrane A' (mol m^{-2} s^{-1} Pa^{-1})	Permeance of membrane A (mol m^{-2} s^{-1} Pa^{-1})	Selectivity relative to SF_6 of membrane A'	Selectivity relative to SF_6 of membrane A	Knudsen effusion Selectivity
He	17.0×10^{-6}	31.8×10^{-6}	9.44	9.30	6.04
CH_4	7.2×10^{-6}	13.3×10^{-6}	4.00	3.88	3.02
CO_2	4.7×10^{-6}	8.8×10^{-6}	2.61	2.57	1.82
SF_6	1.8×10^{-6}	3.4×10^{-6}	1.00	1.00	1.00

Graphene membrane B exhibited similar characteristics as membrane A in terms of gas permeances, including near Knudsen effusion selectivity and little temperature dependence (Figure 5-3B). The permeances of H_2, He, CH_4, CO_2, and SF_6 are ranked from high to low, in accordance with the order of their molar weights (from low to high). Therefore, the gas transport through membrane B is also dominated by the effusion mechanism. The gas permeance of membrane B was found to be approximately four times higher than that of membrane A, indicating a greater open area for gas

molecule impingement. However, as shown in Table 5-4, the selectivities between gases were generally inferior to the Knudsen effusion selectivity. This suggests that collective viscous flow contributed a considerable fraction to the total gas flux. This transition from the Knudsen effusion mechanism to the non-selective collective flux has been reported by Celebi *et al*.[111] In this transition regime, the equations describing the gas effusion mechanism (Equations (5-1) and (5-2)) are not precise. Nevertheless, an order-of-magnitude estimation of the pore area can be given as follows. According to Equation (5-2), the open area for impingement A_{open} on membrane B is 1.7×10^4 nm^2 (based on the CO_2 permeance at 208 °C). Estimations of A_{open} from other gases and temperatures are between 1×10^4 and 2×10^4 nm^2. If only one circular pore existed in membrane B, then, the pore diameter would be on the order of ~150 nm, which is on par with the gas mean free path at ambient pressure (~100 nm). This suggests that the gas flux through membrane B is dominated by one or several large holes or tears of ~100 nm in size.

Table 5-4. Selectivities for membrane B measured at 208 °C. Knudsen selectivities are shown in parentheses.

Gas	Molar mass (g mol^{-1})	Selectivity with respect to				
		H_2	He	CH_4	CO_2	SF_6
H_2	2.01	-	1.01 (1.41)	2.00 (2.82)	2.72 (4.68)	4.48 (8.52)
He	4.00	0.99 (0.71)	-	1.98 (2.00)	2.69 (3.32)	4.44 (6.04)
CH_4	16.04	0.50 (0.35)	0.50 (0.50)	-	1.36 (1.66)	2.24 (3.02)
CO_2	44.01	0.37 (0.21)	0.37 (0.30)	0.74 (0.60)	-	1.65 (1.82)
SF_6	146.06	0.22 (0.12)	0.23 (0.17)	0.45 (0.33)	0.61 (0.55)	-

The gas permeances through membrane B were found to be well below the no-graphene-membrane permeances (Figure 5-9B in Section 5.5.7), indicating the existence of an intact graphene membrane. Further, the permeances were found to be orders of magnitude higher than the detection limit (Figure 5-3B). After completing the gas permeation measurements with membrane B, the graphene membrane ruptured, potentially due to the mechanical stresses exerted on the membrane from pressurization, or due to thermal expansion and contraction of the support upon temperature cycling. The membrane rupture was detected by a significant permeance increase and by the loss of membrane selectivity. The permeances of an equimolar mixture of CH_4 and CO_2 through the ruptured membrane B are shown as the open points in Figure 5-3B. These permeance values (~10^{-3} mol m^{-2} s^{-1} Pa^{-1}) are 1–2 orders of

magnitude higher than those observed before rupture (10^{-5} – 10^{-4} mol m^{-2} s^{-1} Pa^{-1}), again confirming that the intact membrane acted as a barrier to gas permeation, including imparting the observed selectivity. Note that the permeances through the ruptured membrane (~10^{-3} mol m^{-2} s^{-1} Pa^{-1}) are still considerably lower than those through a totally open hole (~10^{-2} mol m^{-2} s^{-1} Pa^{-1}, Figure 5-9B in Section 5.5.7). This indicates that the ruptured graphene membrane B did not fully detach from the nickel support. The membrane rupture likely originated from previously existing pores, because the mechanical stress near a graphene pore is higher than that in the perfect lattice region.[225] The reduced mechanical stability of membrane B is consistent with the prediction that it has at least one large pore defect (> 100 nm).

Note that unlike membrane B, the H_2 permeance through membrane A is not shown in Figure 5-3A. This is because the permeance data of membrane A were collected using a different set of mass spectrometer tuning parameters, which resulted in a much lower H_2 sensitivity (Figure 5-13 in Appendix 5.6.2). Nevertheless, the discussions about membrane A remain valid.

Compared to graphene membranes A, A', and B, membrane C exhibited a more complicated gas permeation behavior (Figure 5-3C), which has not been observed previously for graphene membranes. At the lowest temperature tested, 27 °C, the permeances of H_2, He, CH_4, and SF_6 were found to be at or below the detection limit of the technique. These data points are indicated by X markers overlaying the detection limit lines. The permeance of CO_2 was found to be barely above the lower detection limit at 27 °C. As the temperature increased, the permeances of all the gases drastically increased to above the detection limit at 100 °C, and then remained relatively stable up to 200 °C. Overall, the gas permeances through membrane C were found to be lower than those through membranes A, A', and B. It is worth noting that the gas selectivity of membrane C does not match the gas effusion mechanism. Firstly, the permeances of H_2 and He are not substantially higher than those of CH_4 and CO_2. In fact, at the highest temperature of 200 °C, CO_2 exhibits the highest permeance, followed by CH_4, He, H_2, and SF_6. Secondly, SF_6 exhibits much lower permeances than those predicted by the Knudsen effusion mechanism. For example, the CO_2/SF_6 selectivity is 12 at 200 °C, and at least 20 at 100 °C, far exceeding the Knudsen effusion selectivity of 1.82. Note that the testing of membrane C commenced at 200 °C, and then the temperature was decreased until it reached 27 °C. Therefore, as discussed above, the potential effect of polymer residue can be ruled out.

The observed large deviation in the selectivity of membrane C relative to the Knudsen selectivity implies that the pore size in this membrane may be comparable to the size of the gas molecules considered in this chapter. In this scenario, a gas molecule needs to overcome an energy barrier to translocate through the pore. In this activated regime, the gas permeance and selectivity are controlled by the energy barrier, and are sensitive to the gas molecule size, the pore size, and the pore-gas interaction.[26] The observed dramatic increase of gas permeance from 27 to 100 °C supports the existence of an energy barrier. To deduce the energy barrier, the CO_2 permeance is fitted to temperature using the Arrhenius equation. Specifically, in the activated regime, the permeance k is proportional to $e^{-E_a/RT}$, where E_a is the apparent energy barrier. As shown in Figure 5-5D, the apparent energy barrier of CO_2 permeating through membrane C is 20.3 kJ mol^{-1} at low temperatures. At higher temperatures (100 °C and above), the apparent energy barrier is merely ~2 kJ mol^{-1}, indicating a weak temperature dependence. Therefore, gas transport through graphene nanopores in membrane C was found to shift from the activated regime to the non-activated regime as the temperature increased. An alternative hypothesis is that the pore sizes effectively expanded between 27 to 100 °C due to the desorption of surface contaminants (Section 4.4). Above 100 °C, most of the contaminants had desorbed and the effective pore expansion plateaued. The low permeance of SF_6 suggests that the apparent energy barrier of SF_6 is higher than that of other gases, which is reasonable because SF_6 has the largest size among the five gases in the feed mixture.

As mentioned above, the CH_4 and CO_2 permeances through membrane C were found to be higher than, or almost equal to, the H_2 and He permeances, even in the non-activated regime, which does not obey the effusion mechanism nor the steric effusion mechanism. This paradox can be resolved by considering the surface diffusion from the gas adsorption layer on graphene. Adsorptive gases such as CO_2 and CH_4 tend to accumulate on the graphene surface to form an adsorption layer with a local molecular density which is higher than that in the bulk gas phase. Gas molecules in the adsorption layer can then diffuse along the graphene surface and approach graphene pores (Section 3.5). This route proceeds in parallel to the direct gas impingement, and provides another source of gas molecule supply to the pore. The impingement rate from the bulk phase scales as the pore area (Equation (5-1)).

Assuming a circular pore with diameter D_p, the bulk impingement rate scales as D_p^2. However, the gas molecules in the adsorption layer diffuse to the pore entrance via a circular pore rim, and the surface diffusion rate should scale as D_p (Equation (3-10)). Therefore, surface diffusion has a more pronounced effect on gas permeance when the pore size is small. CO_2 and CH_4 are much more adsorptive than He and H_2, and therefore, have larger contributions from surface diffusion to their overall permeances. According to previous simulation studies, a more adsorptive, albeit larger gas such as N_2, can have a higher permeance than a smaller gas such as H_2 for certain pore configurations.[47,152] Note that SF_6 is more adsorptive than CO_2 and CH_4, and the fact that SF_6 has the lowest permeance suggests that the graphene pore size in membrane C is comparable to the SF_6 molecular size.

After completing the gas permeation testing, in order to verify that the gas permeance could be attributed to the graphene membrane, membrane C was intentionally ruptured by increasing the feed pressure to > 2 bar. The permeance values measured after rupturing membrane C, shown by the open symbols in Figure 5-3C, are several orders of magnitude higher than those observed before rupture, again confirming that the observed gas permeation behavior is due to gases permeating through the intact membrane.

The gas permeance through membrane D, shown in Figure 5-3D, was also found to be different from those of membranes A, A', B, and C. For membrane D, the permeances of all measured gases considered were found to be at or below the detection limit of the technique at temperatures between 25–200 °C, as indicated by the X markers at the detection limit lines. These data suggest that, apparently, membrane D has very few, or possibly, no pores which are large enough to allow permeation of H_2, He, CH_4, CO_2, or SF_6. After completing the initial gas permeation measurements, graphene membrane D was exposed to 6 mol% O_3 in O_2 for 30 s, while the membrane was maintained at 200 °C inside the module. Ozone is a strong oxidant that has the potential to create pores through reaction with the carbon atoms in the graphene membrane.[240,241] This treatment resulted in the abrupt rupture of the membrane, as reflected in the substantial gas permeances observed after the treatment, indicated by the open markers in Figure 5-3D. In the study by Agrawal *et al.*, a single-layer graphene membrane with no measurable gas permeance was exposed to ozone treatment, but catastrophic failure did not occur until

the membrane was exposed to 5 mol% O_3 for 180 s at 200 °C.[224] It is possible that the impurity polymer layer is first attacked by the O_3, delaying chemical attack of the underlying graphene. Comparison between the two ozone treatment processes suggests that the process is stochastic, and requires further effort for optimization. Specifically, shorter treatment times, pulsing O_3 input, and/or lower ozone concentrations will likely be required to create pores without destroying membranes of this type.

The five graphene membranes exhibited diverse gas separation performances, indicating different pore size distributions in these membranes. It is found that the spontaneous formation of the graphene pores during the CVD process is correlated to the O_2 leak into the CVD system (see Section 5.5.9). An O_2 leak of 6.2 μmol generated two graphene membranes that had gas separation performance which are similar to those of membranes A and A'. When the pipeline was sufficiently sealed and no major O_2 leak was allowed, the resulting graphene membrane showed no measurable permeance for all the gases considered (below the detection limit). The effect of the trace O_2 on the formation of graphene nanopores will be discussed in Section 6.2. This also explains why the five membranes exhibited diverse gas permeation properties: the graphene membranes could be grown at different O_2 leak conditions, which was stochastic and depended on the mass flow controller condition, the atmospheric pressure, and the leak tightness.

5.4 Conclusions

In conclusion, for the first time, I measured the permeances of individual gases in a gas mixture through spontaneously formed pores in five suspended single-layer graphene membranes. Further, for the first time, I measured the temperature dependence of the gas permeance, which is a useful technique to investigate transport mechanisms through the graphene membrane. Membrane A displayed selectivities which were higher than the Knudsen selectivities. I fitted the permeance data using the steric selectivity mechanism and obtained a monodisperse pore size distribution peaked at a diameter of 2.5 nm. Membrane A' displayed gas transport characteristics which are similar to those of membrane A. Membrane B exhibited selectivities which are inferior to those predicted by the gas effusion mechanism, suggesting a combination of effusion and viscous flow and pore sizes of ~100 nm. Membrane C displayed a much higher selectivity than that predicted by the effusion mechanism. The CO_2/SF_6

selectivity was found to be greater than 20 at 100 °C. Membrane C also displayed significantly increasing permeances as a function of temperature. Membrane D displayed extremely low permeances at or below the detection limit of my technique, indicating that few or no gas-permeable pores are present in membrane D. This type of graphene membrane is suitable for further pore creation investigations.

In the future, developing a strategy starting from impermeable membranes and then creating pores of well-defined structure, or tailoring the pore size distribution during the graphene CVD process will be critical to establish structure-permeance relationships. My results demonstrate that with continued research, graphene membranes have great potential for high flux, high selectivity gas mixture separation.

In the next chapter, I will further investigate the mechanism of graphene nanopore formation during CVD, including controlling the pore size accordingly. I will also significantly scale up the area of the graphene membrane.

5.5 Methods

5.5.1 Graphene Synthesis

To begin the graphene synthesis process, copper (Cu) foil substrates for graphene growth were first electropolished to reduce surface roughness.[242] The electrolyte solution was prepared by mixing 100 mL water, 50 mL ethanol, 10 mL isopropanol, 50 mL orthophosphoric acid, and 1 g urea, and then stirring for several minutes. The Cu foil growth substrate (25 μm thick, 2.5 cm wide, 6 cm long, 99.999% purity, Alfa Aesar) was used as the anode of an electrolytic cell for the electropolishing process. A second piece of Cu foil (25 μm thick, 2.5 cm wide, 30 cm long folded several times to a reduced length of 6 cm long, 99.8% purity, Alfa Aesar) was used as the cathode. The anode and cathode were positioned parallel to each other, approximately 3 cm apart, in a glass vessel.

A power supply was used to apply a voltage of +3.5 V between the anode and the cathode for 180 s. The resulting current stabilized at 0.5–0.6 A after several seconds. Immediately after the power supply was switched off, the Cu anode was rinsed under a flow of ethanol, and then sonicated in ethanol twice for 1 minute each to remove oxidized copper particles from the foil surface. The Cu foil was then rinsed

with water and isopropanol, dried under a flow of air, and cut to a size of 2 cm wide by 5 cm long for the graphene synthesis.

Graphene films were grown on the electropolished Cu foils using a controlled pressure chemical vapor deposition (CPCVD) procedure adapted from Yan and coworkers.[228] A schematic diagram of the reactor is shown in Figure 5-6. The electropolished Cu foil was placed on a 3 mm thick Cu frame, which provided mechanical support at the edges of the Cu foil during the growth process. The Cu foil and frame were inserted into a 25 mm outer diameter quartz tube and positioned in the center of a tube furnace (MTI OTF-1200X-S). The ends of the quartz tube were sealed with KF flanges (Kurt J. Lesker Co.), and the tube was purged with H_2 at a flow rate of 500 sccm using a MKS GE50A mass flow controller (MFC). A metering valve and gate valve downstream of the reactor were opened, and a vacuum pump was turned on to evacuate the quartz tube while maintaining the 500 sccm H_2 flow to purge air out of the system. The base pressure attained during this evacuation under H_2 flow was lower than 2 Torr. After several minutes of purging, the valves to the vacuum pump were closed, and the pressure inside the tube was raised. The H_2 flow rate was decreased to 70 sccm, and the metering valve downstream of the tube furnace was opened and adjusted to achieve a steady pressure of 800–900 torr, as measured using a MKS Baratron capacitance manometer. The furnace temperature was ramped up to 1077 °C over 120 minutes, and the Cu foil was annealed under the H_2 atmosphere for 12–18 hr. After the annealing step was complete, the metering valve downstream of the reactor was adjusted to reduce the pressure to 108 Torr, and an additional flow of 0.1 sccm CH_4 was allowed into the reactor using a MKS GE50A MFC. After 6–8 hours growth time, the CH_4 flow was stopped and the quartz tube was quickly pushed out of the furnace tube and cooled with a fan. The H_2 pressure in the reactor was raised again to 800 – 900 Torr while the furnace cooled. After the temperature was below 100 °C, approximately 1 hour later, the reactor was opened, the H_2 flow was stopped, and the graphene/Cu foil was removed from the quartz tube.

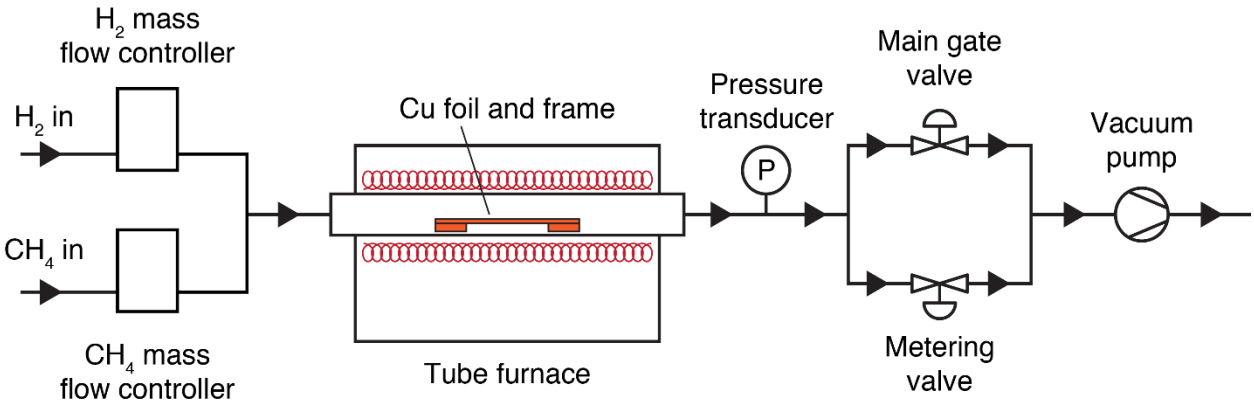

Figure 5-6. Diagram of the controlled pressure chemical vapor deposition (CPCVD) reactor used to synthesize the graphene films.

5.5.2 Support Preparation

Circular pieces of nickel foil (125 μm thick, 11.9 mm diameter, 99.9% purity, Alfa Aesar) were used as supports for the graphene membranes. A commercial laser drilling service (Potomac Photonics Inc.) was used to create a single cylindrical hole of 5 ± 2 μm diameter in the center of each nickel support. After the laser drilling, each support was polished for 60 s using a diamond lapping film with 1 μm average particle size, then polished for an additional 60 s using a diamond lapping film with 0.1 μm average particle size (3M). Subsequently, the supports were cleaned via sonication in water, acetone, and isopropanol for 3–5 minutes each and dried under a flow of air. The supports were further cleaned in air plasma for 3 min (Harrick Plasma PDC-32G). Silicon wafer pieces were used as supports for Raman spectroscopy characterization of the graphene. In this case, Si pieces were cleaned in solvents and air plasma, as described above, prior to the graphene transfer process.

5.5.3 Graphene Transfer

The graphene films were transferred to the supports using a wet transfer process.[243] This process involved several steps: coating the graphene on Cu foil with polymethyl methacrylate (PMMA), etching away the Cu, rinsing the PMMA/graphene composite film, scooping the PMMA/graphene composite film onto the support, annealing the PMMA, and finally dissolving the PMMA film with acetone.

After the CPCVD graphene synthesis, the graphene on Cu foil and the supporting Cu frame were attached to a Si wafer using adhesive polytetrafluoroethylene (PTFE) tape. Then, a PMMA solution

(MicroChem Corp. 950 PMMA A4, 4% in anisole) was spin coated onto the graphene on Cu foil at 2000 rpm for 2 minutes, followed by 500 rpm for 30 s. The coated film was dried in air for at least 30 min.

Next, the PMMA/graphene/Cu foil was cut out of the supporting Cu frame and sectioned into several square pieces of approximately 5 mm by 5 mm each. Each piece was suspended via surface tension on top of a reservoir of a copper etchant solution containing $Na_2S_2O_8$ (Transene Co.). After 10 minutes, each Cu foil piece was removed from the etchant and suspended via surface tension on top of a second reservoir of the same etchant solution to prevent contamination from the graphene etched away from the back side of the Cu foil. The samples were left in this etchant solution until all the Cu was dissolved and the composite film was transparent (typically after 60–90 min).

A clean Si wafer piece was then used to scoop the floating PMMA/graphene film off of the surface of the copper etchant. To rinse the graphene, the sample was placed onto the surface of a large reservoir of deionized (DI) water with a volume of approximately 2 L. The suspended PMMA/graphene film was again scooped with a Si wafer pieces, and then suspended on the surface of a fresh DI water bath. This rinsing procedure was carried out three times to remove as much residual copper etchant from the graphene as possible. Finally, the PMMA/graphene film was scooped onto the desired support, either a Ni foil piece with a single hole to create a membrane, or a clean Si wafer piece to create a sample for Raman characterization. The samples were dried completely in air. To reduce stresses in the PMMA film, the samples were annealed on a hot plate at 150 °C for 15 min, then at 200 °C for 10 min, and finally cooled back down to room temperature in air.

The PMMA was removed from the samples using acetone. For nickel foil supports, the back side of the support was masked with a small square of 2mm thick polydimethylsiloxane (PDMS) to prevent solvent from entering the laser drilled hole. The masked substrate was suspended horizontally over the surface of an acetone bath using a pair of self-closing tweezers, and positioned so that only the PMMA/graphene-coated front side of the film was submerged in acetone. The sample was held in this position for 8–10 min to fully dissolve the PMMA. PMMA/graphene samples on Si wafer pieces were fully submerged in a beaker of acetone for 20–30 minutes to dissolve the PMMA. The PMMA layer should be removed if the interference fringes could no longer be observed. After the samples were

removed from the acetone, they were completely dried in air, and the PDMS pieces were removed from the back of the Ni foil supports.

5.5.4 Graphene Characterization

Each graphene membrane was imaged using a JEOL JSM 6700 scanning electron microscope (SEM) operated at an accelerating voltage of 1.0–2.0 kV. The SEM images were used to confirm that the graphene membranes were intact, and to measure the precise area of the hole in each Ni foil support.

Raman spectra were collected using a Horiba LabRAM micro-Raman spectrometer with a 532 nm laser, 1800 grooves/mm grating, and 100x objective. The spectrometer was calibrated using cyclohexane's most intense peak at 801.8 cm^{-1}. To measure statistics on the peak intensity ratios, spectra were collected at a 16 x 16 square array of points with 20 μm pitch. Data acquisition was carried out using Horiba LabSpec version 6 software, and Matlab software was used for background subtraction and spectrum analysis.

5.5.5 Gas Permeation Measurements

Measurements of gas permeation through the graphene membranes were carried out in the custom gas permeation module shown in Figure 5-2D, E. Each graphene membrane on nickel foil support was sealed in a Swagelok VCR fitting, which separated the feed side and the permeate side of the module. On the feed side of the module, a feed gas mixture was flowed onto the membrane and out to vent (Figure 5-7). A metering valve downstream of the module was used to adjust the feed gas pressure to 1.4–1.5 bar absolute. The feed gas was typically an equimolar six-component mixture containing H_2, He, N_2, CH_4, CO_2, and SF_6. In some cases, as noted, an equimolar two-component mixture containing CH_4 and CO_2 was used. On the permeate side of the module, an Ar sweep gas was flowed at 4 sccm at a pressure of 1.1 bar. The permeate lines were heated to 200 °C to prevent gas adsorption. The temperature dependence of the membrane permeance was measured by placing the entire module inside a heating mantle (Series O Beaker Mantle, Glas-Col), insulating it with glass wool, and heating it using an external temperature controller. The temperature was measured with a small thermocouple affixed to the metal part of the permeation module at the location of the membrane using adhesive Kapton tape.

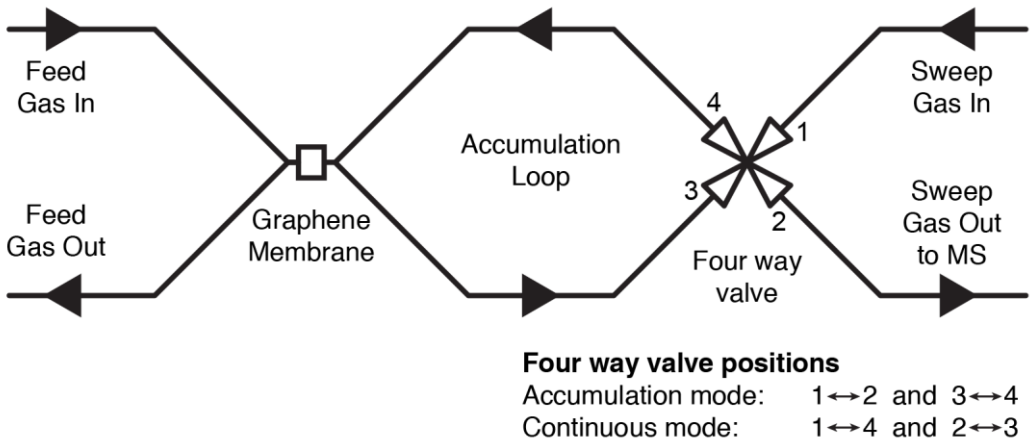

Figure 5-7. Diagram of the gas lines to and from the graphene module. The four-way valve position was switched to change between the accumulation and the steady-state measurement modes.

The permeate lines to and from the membrane module were connected to a four-way valve to enable the module to be operated in two modes. In the continuous mode, the sweep gas flowed across the membrane and carried the permeated gases into the mass spectrometer (MS, Agilent 5977A with Diablo 5000A real time gas analyzer). In the accumulation mode, the sweep gas bypassed the module, leaving the permeate compartment isolated and sealed so that permeating gases could accumulate in the closed loop. To end an accumulation measurement, the four-way valve was switched to place the module into the continuous mode, which caused the Ar sweep to carry all the permeated gas into the MS. Gas permeation measurements were always conducted in the accumulation mode, and depending on the permeance of the membrane, accumulation times of 30 min to 3 days were used to collect enough gas to be detected. The MS was pre-calibrated with respect to the gas composition, and provided a linear dependence of the MS signal intensity vs. the molar composition of the gas feed. The MS signals were recorded via computer software and used to calculate the permeance of each gas species. A sample of the raw data from the mass spectrometer is shown in Figure 5-8, and the procedure for calculating the gas permeance from these data is described in detail in Supporting Information Section 5.5.6.

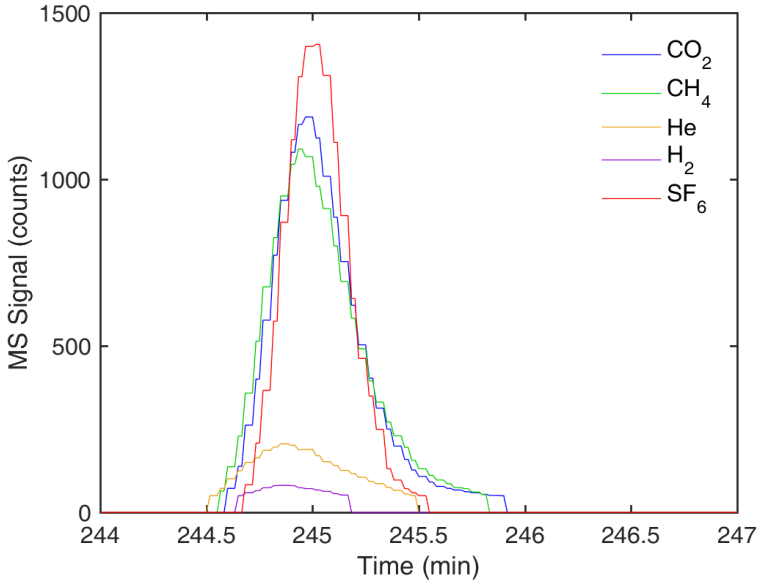

Figure 5-8. Example mass spectrometer raw data collected after completing an accumulation-mode gas permeation measurement. In this case, the four-way valve was switched from the accumulation mode to the continuous mode at 244 minutes. The gases were swept into the mass spectrometer, resulting in these peaks. The area of each peak was numerically integrated and used to calculate the permeance of each gas species.

5.5.6 Gas Permeance Calculation from Mass Spectrometer Raw Data

The gas permeances of the graphene membranes were calculated from the mass spectrometer data as follows. In an accumulation measurement (Figure 5-7, valve position: 1 ↔ 2 and 3 ↔ 4) started at time $t = 0$, the moles of permeating gas species i collected are given by the function $n_i(t)$. After accumulation at time $t = \tau$, the valve positions are switched to the continuous mode (Figure 5-7, valve position: 1 ↔ 4 and 2 ↔ 3), sweeping the accumulated gases to the MS.

The mole fraction of component i among other permeated components and the sweep gas can be expressed as follows:

$$x_i(t) = \frac{\left(\frac{dn_i}{dt}\right)}{\left[\left(\frac{dn}{dt}\right)_{sweep} + \Sigma_i\left(\frac{dn_i}{dt}\right)\right]} \tag{5-7}$$

where $\left(\frac{dn}{dt}\right)_{sweep}$ = sweep flow rate, n_i= moles of permeate component i, and x_i = mole fraction of component i among other permeated components and sweep gas.

Rewriting Equation (5-7), one obtains:

$$\left(\frac{\mathrm{d}n_i}{\mathrm{d}t}\right) = \left[\left(\frac{\mathrm{d}n}{\mathrm{d}t}\right)_{\text{sweep}} + \sum_i \left(\frac{\mathrm{d}n_i}{\mathrm{d}t}\right)\right] . x_i(t) \tag{5-8}$$

From the calibration of the MS, a linear relationship between the MS signal and the mole fraction was obtained such that:

$$x_i(t) = S_i . \mathrm{MS}_i \tag{5-9}$$

where MS_i = MS signal for component *i* and S_i = Calibration slope for component *i*.

The accumulation mode was designed such that the molar flows of the various components that accumulated on the permeate side would be much smaller than the sweep flow rate, that is,

$$\sum_i \left(\frac{\mathrm{d}n_i}{\mathrm{d}t}\right) \ll \left(\frac{\mathrm{d}n}{\mathrm{d}t}\right)_{\text{sweep}} \tag{5-10}$$

Therefore, combining with Equations (5-8) and (5-9) yields:

$$\left(\frac{\mathrm{d}n_i}{\mathrm{d}t}\right) = \left(\frac{\mathrm{d}n}{\mathrm{d}t}\right)_{\text{sweep}} \cdot S_i \cdot \mathrm{MS}_i \tag{5-11}$$

When the swept permeate is sent to the MS, the total moles of each component can be calculated by integrating the MS signal intensity as follows:

$$n_i(\tau) = \left(\frac{\mathrm{d}n}{\mathrm{d}t}\right)_{\text{sweep}} \cdot S_i \cdot \left[\int_{\tau}^{\tau+\delta\tau} \mathrm{MS}_i \, \mathrm{d}t\right] \tag{5-12}$$

In Equation (5-12), the integral of the MS signal for component *i* is calculated numerically using Matlab software beginning at the end of the accumulation, τ, and ending once all the gas has been swept into the MS at time $\tau + \delta\tau$, where $\delta\tau$ is typically 2–3 minutes.

The molar flow rate of component *i* through the membrane is related to the total number of moles of component *i* that permeated through the membrane as follows:

$$n_i(\tau) = J_i * \tau \tag{5-13}$$

where J_i = molar flow rate of component *i* through the membrane (mol s^{-1}).

The permeance can be calculated by dividing the molar flow rate by the membrane area measured by SEM, A_{membrane}, and the pressure differential across the membrane, ΔP_i. Accordingly, the final expression used to calculate the permeance is given by:

$$\text{Permeance}_i = \frac{\left(\frac{\mathrm{d}n}{\mathrm{d}t}\right)_{\text{sweep}} \cdot S_i \cdot \left[\int_{\tau}^{\tau+\delta\tau} \text{MS}_i \, \mathrm{d}t\right]}{\tau \cdot A_{\text{membrane}} \cdot \Delta p_i} \tag{5-14}$$

5.5.7 Error and Control Measurements

Although the feed gas mixture contained N_2, due to a small leak rate of air into the system, it was not possible to accurately determine the N_2 permeance through these membranes, so N_2 is omitted from the analysis. The MS sensitivity to H_2 and He was 10–30 times lower than the sensitivities for CH_4, CO_2, and SF_6, which in some cases resulted in additional measurement error in the calculated H_2 and He permeance values.

Control measurements were carried out to determine the gas permeance lower detection limit of the measurement technique. The samples used for these measurements were nickel foils identical to the nickel supports for the suspended graphene membranes, but with no laser drilled hole and no graphene. For each of the five tested nickel foils with no hole, accumulation mode gas permeation measurements were carried out under the same conditions used to test the suspended graphene membranes. The foils were tested at temperatures of 25 °C and/or 200 °C, accumulation times of 1–3 days, and an equimolar mixture of H_2, He, CH_4, N_2, CO_2, and SF_6 as the gas feed. As with the graphene membranes, the N_2 data were discarded due to a small leak rate of air into the system.

Three of the five tested control samples resulted in no detectable signal of H_2, He, CH_4, CO_2, or SF_6. In the remaining two samples, small signals of CH_4, CO_2, and/or H_2 were observed, but no signal of He or SF_6 was observed. These small CH_4, CO_2, and H_2 background signals may originate from a leak of the feed gas through the module to the permeate side of the Ni foil, a leak into the module from the air, and/or gas generation inside the module due to organic contaminants.

I calculated the "equivalent permeance" through a 5 μm diameter circular graphene membrane that would have given rise to the measured CH_4, CO_2, and H_2 background signals. These equivalent permeance values are displayed in Supporting Information Figure 5-9A. The H_2 lower detection limit was set at the highest H_2 equivalent permeance value observed in any control measurement, 9×10^{-7} mol m^{-2} s^{-1} Pa^{-1}. The lower detection limit for He, CH_4, CO_2, and SF_6 was set conservatively at the highest CO_2 equivalent permeance value observed in any control measurement, 2×10^{-7} mol m^{-2} s^{-1} Pa^{-1}. Figure

5-9B shows additional control measurements using a nickel support with an open hole and no graphene membrane. These measurements revealed that the permeance of each gas through the support is on the order of 10^{-2} mol m^{-2} s^{-1} Pa^{-1}, and therefore, transport through the support does not limit the permeance through the graphene membranes.

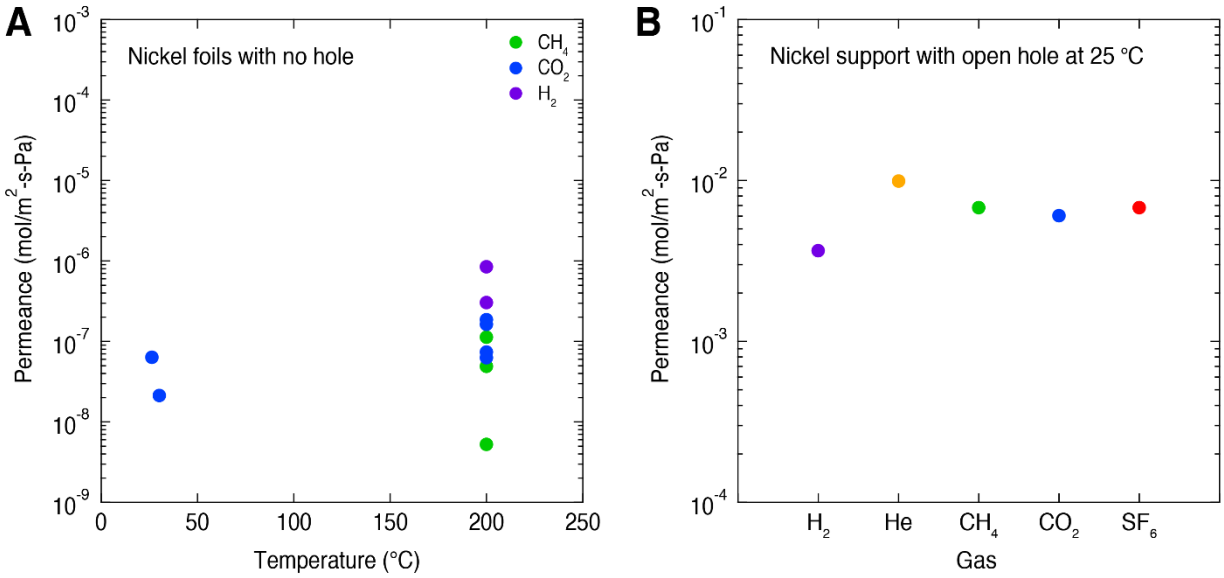

Figure 5-9. (A) Control measurements carried out on five Ni foils with no hole. The feed gas was the same equimolar six-component mixture of H_2, He, CH_4, N_2, CO_2, and SF_6 used for the membrane measurements, and the tests were carried out using an identical procedure. No He or SF_6 signals were detected in any tests, and the N_2 measurements were discarded. These data, which represent the "equivalent permeance" through a 5 μm diameter circular graphene membrane that would have given rise to the measured CH_4, CO_2, and H_2 signals, were used to calculate the gas permeance lower detection limits as described above. (B) Control measurement with a Ni foil with an open hole. The high permeance measured through the open support hole shows that the support did not limit the gas flux through any of the tested membranes.

5.5.8 Ozone Exposure

Graphene membrane ozone exposure was carried out with a membrane mounted inside the module described above. A pure O_2 feed was flowed at 50 sccm through a corona discharge ozone generator (Ozone Engineering LG-7) and onto the feed side of the membrane. The ozone generator power was set to 40%, which resulted in a 6 mol% O_3 concentration with the balance O_2 according to calibration measurements carried out by the manufacturer.

5.5.9 Oxygen Leak and Graphene Pore Formation

As shown in Figure 5-10A, upon introduction of the CH_4 feed, the O_2 concentration abruptly increased to 4000 ppm and then gradually decayed, suggesting an air leak near the CH_4 mass flow controller. The oxygen concentration was measured by a trace oxygen analyzer (MTI Corporation) placed right at the upstream of the CVD chamber. The total amount of the O_2 spike was 6.2 μmol. Figure 5-10B shows that the graphene membrane synthesized this way exhibited gas permeation results that are similar to those of membranes A and A' (Figure 5-3). In contrast, when the pipeline was sealed and the O_2 spike was eliminated, the resulting graphene membrane showed no measurable permeance for all the gases considered, similar to membrane D.

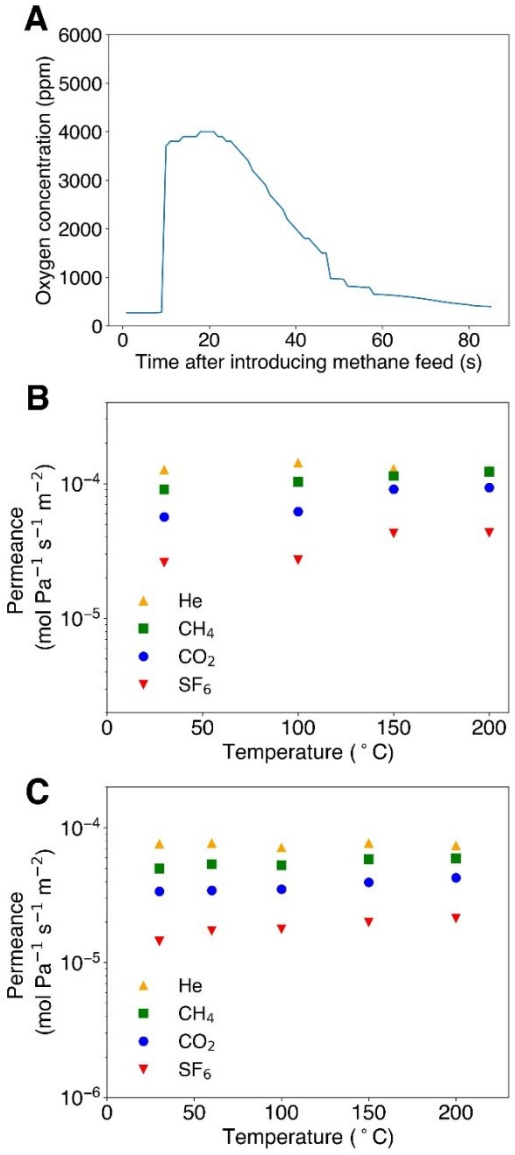

Figure 5-10. (A) Oxygen molar concentration in front of the CVD chamber after the CH_4 feed was introduced when the CVD system leaked. (B, C) Gas permeances through two graphene membranes fabricated with the O_2 leak.

5.6 Appendices

5.6.1 Evaluation of Permeation Coefficient $\delta = \delta(w)$

Definitions:

R_m, D_m – Kinetic radius and kinetic diameter of a gas molecule. $R_\mathrm{m} = 0.5D_\mathrm{m}$.

R_p, D_p – Pore radius and pore diameter. The atomic size of the rim atoms is taken into account. $R_\mathrm{p} = 0.5D_\mathrm{p}$.

θ – Angle of incidence.

$w = \mathrm{R_m}/R_\mathrm{p} = D_\mathrm{m}/D_\mathrm{p}$ – Size factor.

$\delta = A_\mathrm{open}/A_\mathrm{pore} = A_\mathrm{open}/\left(\pi R_\mathrm{p}^2\right)$ – Permeation coefficient.

As shown in Figure 5-11A, when approaching a circular pore with an angle of incidence $\theta \in [0, \pi/2]$, the gas molecule sees an ellipse instead of a circle. In the view of an incident gas molecule, the ellipse has a semi-major axis length of R_p and a semi-minor axis length of $R_\mathrm{p}\cos\theta$ (Figure 5-11B). Because the gas molecule has a radius of R_m, any point whose distance to the ellipse perimeter is less than R_m is inaccessible for permeation (assuming a hard-sphere interaction). The remaining area (filled in blue) is encompassed by an ellipse parallel curve (EPC). Define the remaining area as A_EPC, which should be transformed back to the perpendicular view by multiplying by $(\cos\theta)^{-1}$ to obtain the accessible open area on the graphene basal plane.

According to the Maxwell-Boltzmann distribution of an ideal gas, the direction of the gas velocity is uniformly distributed for any solid angle Ω. Notice that the incident gas molecules can only inject from above the graphene basal plane. Therefore, the differential form of the angular distribution of the solid angle Ω is as follows:

$$\mathrm{d}F_\Omega(\Omega) = \frac{1}{2\pi}\mathrm{d}\Omega \tag{5-15}$$

where F is the cumulative distribution function.

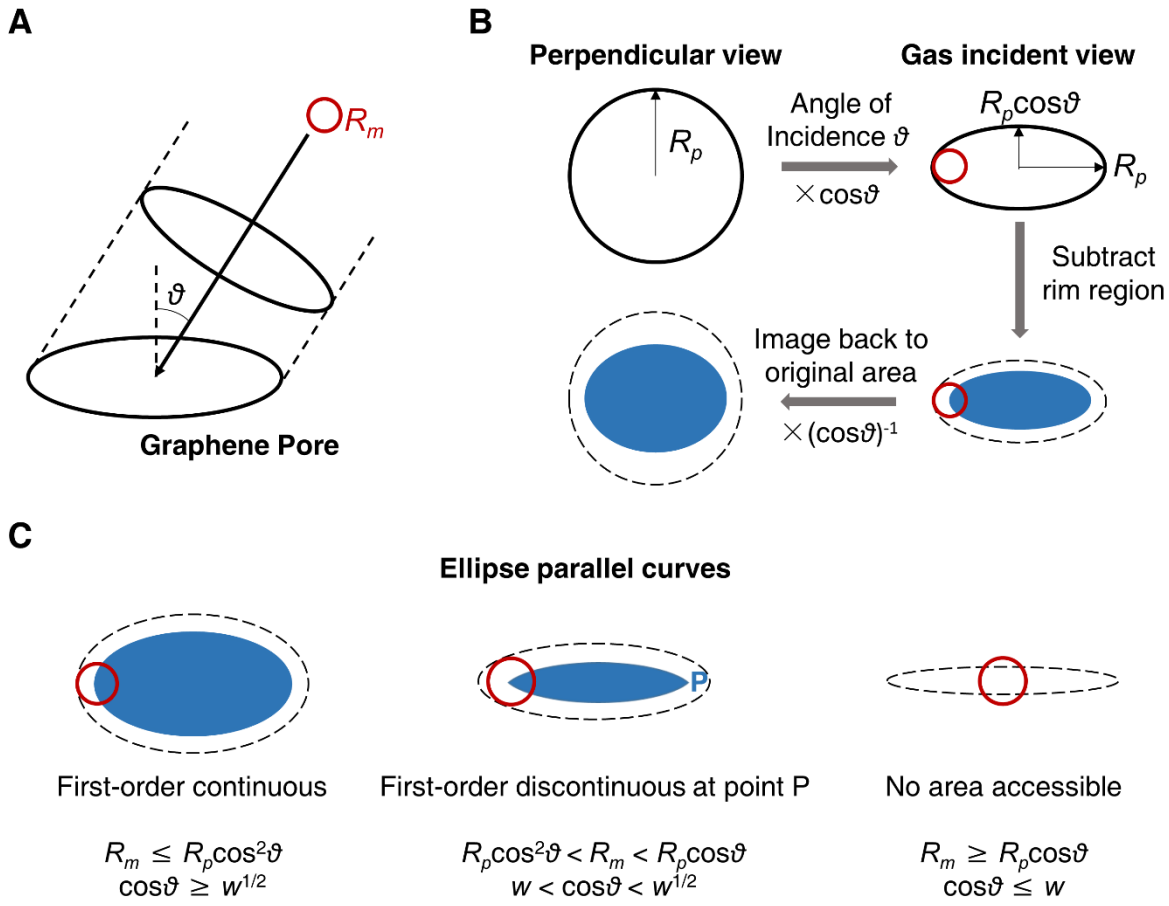

Figure 5-11. Scheme of the steric selectivity mechanism. (A) When approaching a circular pore with an injection angle θ, the gas molecule (red circle) sees an ellipse. (B) The size of the gas molecule reduces the accessible area for permeation (the remaining areas are filled in blue). In the view of gas injection, the accessible area is encompassed by an ellipse parallel curve. (C) Three cases of the ellipse parallel curve at different conditions.

In a spherical coordinate system, a direction is described by the polar angle θ (equivalent to the angle of incidence) and the azimuthal angle φ. Note that $\mathrm{d}\Omega = \sin\theta\,\mathrm{d}\theta\mathrm{d}\varphi$. Therefore, the distribution of the angle of incidence θ can be expressed as follows:

$$\mathrm{d}F_\theta(\theta) = \int_0^{2\pi} \frac{1}{2\pi}\sin\theta\,\mathrm{d}\theta\mathrm{d}\varphi = \sin\theta\,\mathrm{d}\theta \tag{5-16}$$

However, the rate of incidence also depends on the velocity normal to the graphene plane $v_\perp = v\cos\theta$. In other words, the gas molecules with low angles of incidence have an advantage in terms of their injection velocities.

As a result, the probability density function f of the angle of incidence θ onto a two-dimensional area is proportional to $\sin\theta\cos\theta$. After normalization, it follows:

$$f(\theta) = 2\sin\theta\cos\theta \tag{5-17}$$

Each angle of incidence θ corresponds to an ellipse of different shape, and therefore, the remaining area A_{EPC} is a function of θ. Integrating over the entire angle of incidence range, $\theta \in [0, \pi/2]$, one obtains the effective open area A_{open}:

$$A_{\mathrm{open}} = \int_0^{\frac{\pi}{2}} f(\theta) A_{\mathrm{EPC}}(\theta) \frac{1}{\cos\theta} \mathrm{d}\theta \tag{5-18}$$

The area surrounded by the EPC can be evaluated numerically, since there is no analytical solution. The parallel curve for inward offset R_{m} of an ellipse with semi-axis lengths R_{p} and $R_{\mathrm{p}}\cos\theta$ is given by the following parametric equations:

$$\begin{cases} x(t) = \left(R_{\mathrm{p}} - \dfrac{R_{\mathrm{p}}\cos\theta \cdot R_{\mathrm{m}}}{\sqrt{R_{\mathrm{p}}^2 \sin^2 t + R_{\mathrm{p}}^2 \cos^2\theta \cos^2 t}} \right) \cos t \\ y(t) = \left(R_{\mathrm{p}}\cos\theta - \dfrac{R_{\mathrm{p}} \cdot R_{\mathrm{m}}}{\sqrt{R_{\mathrm{p}}^2 \sin^2 t + R_{\mathrm{p}}^2 \cos^2\theta \cos^2 t}} \right) \sin t \end{cases} \tag{5-19}$$

Note that $w = R_{\mathrm{m}}/R_{\mathrm{p}}$, and Equation (5-19) can be simplified as follows:

$$\begin{cases} x(t) = R_{\mathrm{p}} \left(1 - \dfrac{w\cos\theta}{\sqrt{1 - \sin^2\theta\cos^2 t}} \right) \cos t \\ y(t) = R_{\mathrm{p}} \left(\cos\theta - \dfrac{w}{\sqrt{1 - \sin^2\theta\cos^2 t}} \right) \sin t \end{cases} \tag{5-20}$$

As shown in Figure 5-11C, the shape of EPC depends on the angle of incidence θ, and can be categorized into three situations. Firstly, when the gas molecule sphere (red circle) is tangential to the ellipse (black dashed line) at the vertex point, the EPC is a first-order continuous curve (left panel in Figure 5-11C). This tangency condition is satisfied when the gas kinetic radius R_{m} is less than or equal to the radius of curvature at the vertex point of the ellipse $R_{\mathrm{c}} = \left(R_{\mathrm{p}}\cos\theta\right)^2 / R_{\mathrm{p}} = R_{\mathrm{p}}\cos^2\theta$ (or equivalently, $\cos\theta \geq w^{1/2}$). In this case, one can integrate the EPC parameter t from π/2 to 0 to obtain a quarter of the A_{EPC}. Therefore, A_{EPC} can be expressed as follows:

$$A_{\mathrm{EPC}}(\theta) = 4\int_0^{R_{\mathrm{p}} - R_{\mathrm{m}}} y(x)\mathrm{d}x = 4\int_{\frac{\pi}{2}}^{0} y(t)x'(t)\mathrm{d}t \tag{5-21}$$

where $x'(t)$ is the first derivative of x with respect to the parameter t, and is expressed as follows:

$$x'(t) = R_{\mathrm{p}}\left[\frac{w\sin t\cos\theta}{(1-\sin^2\theta\cos^2 t)^{3/2}} - \sin t\right] \tag{5-22}$$

Secondly, when the gas kinetic radius R_{m} is greater than the radius of curvature at the vertex point $R_{\mathrm{c}} = R_{\mathrm{p}}\cos^2\theta$, and is less than the semi-minor axis length of the ellipse $R_{\mathrm{p}}\cos\theta$ (or equivalently, $w < \cos\theta < w^{\frac{1}{2}}$), the EPC is first-order discontinuous at endpoint P (middle panel in Figure 5-11C). At point P, $y(t) = 0$ but $t \neq 0$. This gives the threshold t value at point P expressed as $t_{\mathrm{P}} = \cos^{-1}\sqrt{\frac{1}{\sin^2\theta}\left(1-\frac{w}{\cos^2\theta}\right)}$. One can integrate the EPC parameter t from π/2 to t_{P} to obtain a quarter of the A_{EPC}. Therefore, A_{EPC} can be expressed as follows:

$$A_{\mathrm{EPC}}(\theta) = 4\int_{\frac{\pi}{2}}^{t_{\mathrm{P}}} y(t)x'(t)\mathrm{d}t \tag{5-23}$$

Lastly, when the gas kinetic radius R_{m} is greater than the semi-minor axis length of the ellipse $R_{\mathrm{p}}\cos\theta$ (or equivalently, $\cos\theta \leq w$), the gas molecule cannot permeate through the pore because the ellipse is too narrow.

Combining Equations (5-18)–(5-23), one can evaluate the open area A_{open} by numerical integration using Matlab according to following equation:

$$\begin{aligned} A_{\mathrm{open}} = 8\int_0^{\cos^{-1}\sqrt{w}} \mathrm{d}\theta\sin\theta\int_{\frac{\pi}{2}}^{0} y(t)x'(t)\mathrm{d}t \\ + 8\int_{\cos^{-1}\sqrt{w}}^{\cos^{-1}w} \mathrm{d}\theta\sin\theta\int_{\frac{\pi}{2}}^{t_{\mathrm{P}}} y(t)x'(t)\mathrm{d}t \end{aligned} \tag{5-24}$$

A factor of R_{p}^2 can be factored out from A_{open}, so that $\delta = A_{\mathrm{open}}/\left(\pi R_{\mathrm{p}}^2\right)$ is only a function of w.

One way to simplify Equation (5-24) is to approximate the area surrounded by the ellipse parallel curve (EPC) A_{EPC} as an ellipse as well. This smaller ellipse has a semi-major axis length of $R_{\mathrm{p}} - R_{\mathrm{m}}$, and a semi-minor axis length of $\left(R_{\mathrm{p}}\cos\theta - R_{\mathrm{m}}\right)$. The gas kinetic radius R_{m} should be greater than $R_{\mathrm{p}}\cos\theta$ to allow possible permeation (or equivalently, $\cos\theta \geq w$). Therefore, the open area A_{open} can be expressed as follows:

$$A_{\mathrm{open}} = \int_0^{\cos^{-1}w} \pi\left(R_{\mathrm{p}} - R_{\mathrm{m}}\right)\left(R_{\mathrm{p}}\cos\theta - R_{\mathrm{m}}\right)\tan\theta\,\mathrm{d}\theta \tag{5-25}$$

An expression to approximate the permeation coefficient δ (Equation (5-3)) can then be derived as follows:

$$\delta \approx \frac{A_{\text{open}}}{A_{\text{pore}}} = \frac{A_{\text{open}}}{\pi R_{\text{p}}^2} = \int_0^{\cos^{-1} w} 2(1-w)(\cos\theta - w)\sin\theta \, \mathrm{d}\theta = (1-w)^3 \qquad (5\text{-}26)$$

As shown in Figure 5-12, $(1-w)^3$ provides a good approximation compared to the exact function $\delta(w)$. However, the intuitive function $\delta(w) \approx (1-w)^2$ derived by neglecting the effect of the angle of incidence has a large error.

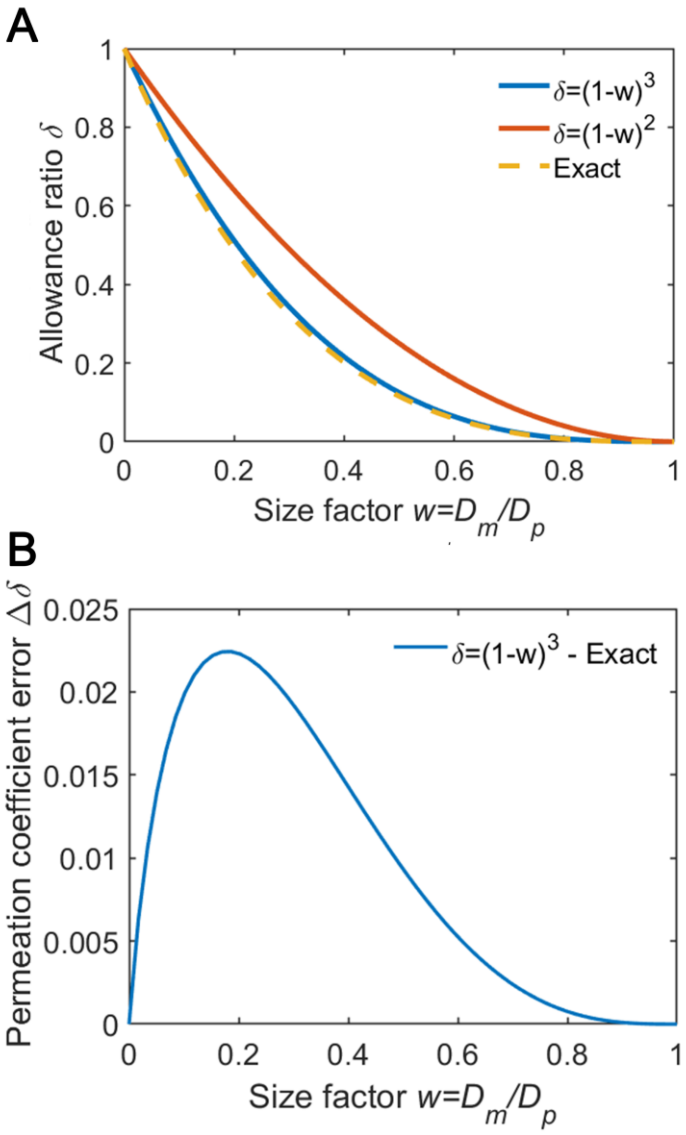

Figure 5-12. (A) Permeation coefficient δ as a function of the size factor w using the steric selectivity mechanism, its approximation $\delta(w) = (1\text{-}w)^3$ (Equation (5-3)) and the $\delta(w) = (1\text{-}w)^2$ approximation. (B) Absolute error between $\delta(w) = (1\text{-}w)^3$ and the exact steric selectivity mechanism. The maximum absolute error is 2.2%.

5.6.2 Internal Threshold of H_2 Signal

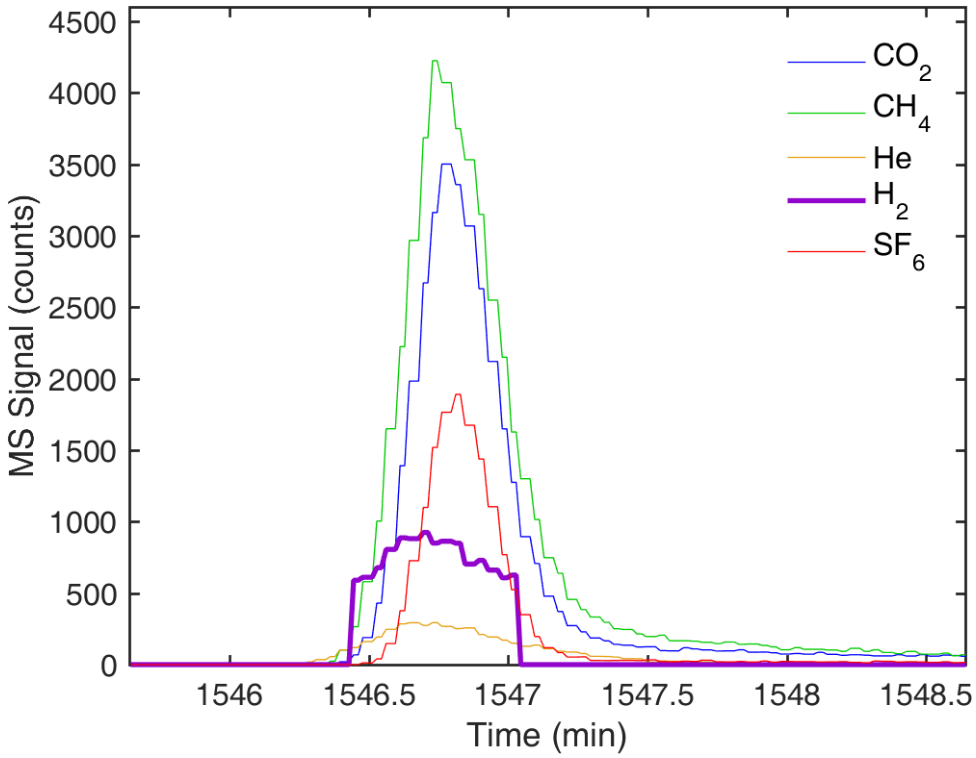

Figure 5-13. Mass spectrometer raw data collected after completing an accumulation-mode gas permeation measurement through membrane A. The mass spectrometer exhibited an internal threshold of H_2 signal of ~600 counts. This caused a large portion or even all of the H_2 signal to be truncated, and led to a large error.

6 Direct Chemical Vapor Deposition Synthesis of Porous Single-Layer Graphene Membranes with High Gas Permeances and Selectivities

6.1 Introduction

Membrane separation technology has attracted considerable interest due to its much lower energy consumption compared with thermal-based separation methods such as distillation.[1,244] To enhance the competitiveness of membrane separation processes, membranes exhibiting both high permeance and selectivity are in high demand. Compared with conventional membrane materials, porous single-layer graphene can yield orders of magnitude higher gas permeances because of its atomic thickness and low cross-membrane transport resistance.[26,245] A high gas permeance reduces the membrane area required in a separation module to attain a certain gas flow rate target. To realize the enormous potential of porous graphene for gas separation, the areal pore density in graphene should be considerably high. In Chapter 2, using molecular dynamics simulations and transition state theory, I predicted that the pore density needs to exceed 10^{14} m^{-2} for a graphene membrane to surpass the Robeson upper bound for polymers.[11] Further, to yield a high selectivity, the pore sizes in the graphene membrane should be precisely controlled such that they are commensurate with the gas molecular sizes. In fact, the pore sizes in porous graphene are typically widely distributed and fitted by a lognormal distribution, where a small fraction of larger pores determine the total gas permeance.[115,118,121,131] As a result, an even higher pore density is needed for porous graphene to achieve a high gas permeance with enough competitiveness.

Etching away atoms from pristine graphene has been the most widely applied strategy to increase the pore density in a graphene membrane. High-energy ion or electron bombardment was used to perforate graphene in some early studies.[111,113,115] Later, chemical oxidative etching was developed as a more scalable graphene perforation method.[109,110,116] For example, He *et al.* used O_2 plasma to perforate as-synthesized graphene from chemical vapor deposition (CVD) and measured a H_2/CH_4 selectivity >

15.[118] Zhao *et al*. exposed pristine graphene to O_2 plasma for a short pore nucleation burst, and then to mild O_3 etching for controllable pore expansion, in order to partially decouple the pore nucleation and growth and to obtain a narrow pore size distribution.[122] However, despite the efforts made to decouple the pore nucleation and growth, the correlation between them still exists for those etching-based methods. Because the nucleation and growth of the pores are both triggered by etching (*e.g.,* O_2 plasma), one needs to raise the energy intensity of the etching reaction to increase the pore density, which in turn generates larger, less selective pores. This trade-off between the pore density and the selectivity remains a major challenge for graphene membranes.

A promising way to tackle this challenge is to control the formation of intrinsic vacancies in graphene during its CVD synthesis. According to the theoretical study by Wang *et al*., the formation of the intrinsic vacancies during CVD is triggered by the random insertion of catalytic metal atoms into the front-most graphene edge during growth,[138] which is decoupled from oxidative etching. Therefore, the density of these intrinsic vacancies can be significantly increased without sacrificing their gas selectivity, as long as the density is not too high to induce defect coalescence. Several reported studies have investigated the gas separation performances of these intrinsic vacancies, including the one reported in Chapter 5.[126,120,128,130] However, the precise control over the density and the sizes of the intrinsic vacancies has not been realized, resulting in unsatisfactory permeances and selectivities.

In this chapter, for the first time, I systematically investigate the formation mechanism of the nanopores that are intrinsically formed during CVD, and systematically control the density of the intrinsic nanopores by tuning the CVD synthesis conditions. This can be done without significantly increasing the sizes of the nanopores themselves. This is important because it allows graphene membranes to present higher gas fluxes while maintaining high selectivities. Further, I demonstrate that the sizes of these intrinsic vacancies can be effectively modulated by manipulating the hydrocarbon adsorbates that partially block the vacancies. Using the strategies above, I reproducibly fabricated single-layer graphene membranes exhibiting high densities of intrinsic gas-sieving vacancies that exhibit record-high H_2/CH_4 separation performances to date: H_2/CH_4 selectivity > 2000 while H_2 permeance > 4000 GPU, or H_2/CH_4 selectivity > 100 while H_2 permeance > 10^4 GPU.

6.2 Formation of Intrinsic Graphene Pores

Porous single-layer graphene was synthesized by one-step CVD using Cu as the catalyst and CH_4 as the precursor (see Section 6.7.1 for details).[246] Figure 6-1a shows the positive correlation between the CH_4 partial pressure $P(CH_4)$ during graphene growth and the D to G peak intensity ratio (I_D/I_G) of graphene measured by Raman spectroscopy. Corresponding Raman spectra are presented in Figure 6-1b. According to the amorphization trajectory of graphene, I_D/I_G is a non-monotonic function of the areal defect density ρ — it reaches a maximum when the average defect distance L_D ($= \rho^{-1/2}$) is ~3 nm.[232,233] The high 2D peaks shown in Figure 6-1b indicate that the defects are sparse ($L_D > 3$ nm).[233] In this range, I_D/I_G is approximately proportional to the defect density ρ.[232] This positive correlation between $P(CH_4)$ and ρ can be explained by the mechanism proposed by Wang *et al*. as follows.[138] After a defect forms at the front-most graphene edge during growth, it can be healed before the front-most edge extends and moves past it. Otherwise, the defect gets "frozen" inside the lattice and cannot be healed.[247] As a result, when $P(CH_4)$ is high, the graphene growth is fast, leading to less time for the defects to be healed and subsequently, to a high defect density.[248–250]

Figure 6-1c demonstrates the effect of CVD temperature on the density of the intrinsic defects, where I_D/I_G is larger for graphene grown at 800 ℃ (blue) than for that grown at 900 ℃ (orange). According to *ab initio* calculations, the defect formation energy at the front-most graphene edge is 1.3 eV, while the energy barrier associated with defect healing is 1.86 eV.[138] Therefore, although a lower CVD temperature reduces the probability of defect formation, it reduces the probability of defect healing to a greater extent, resulting in a higher defect density. Similar temperature dependence was observed by Kidambi *et al.*[251] and Khan *et al.*,[128] but its mechanism has not been unveiled.

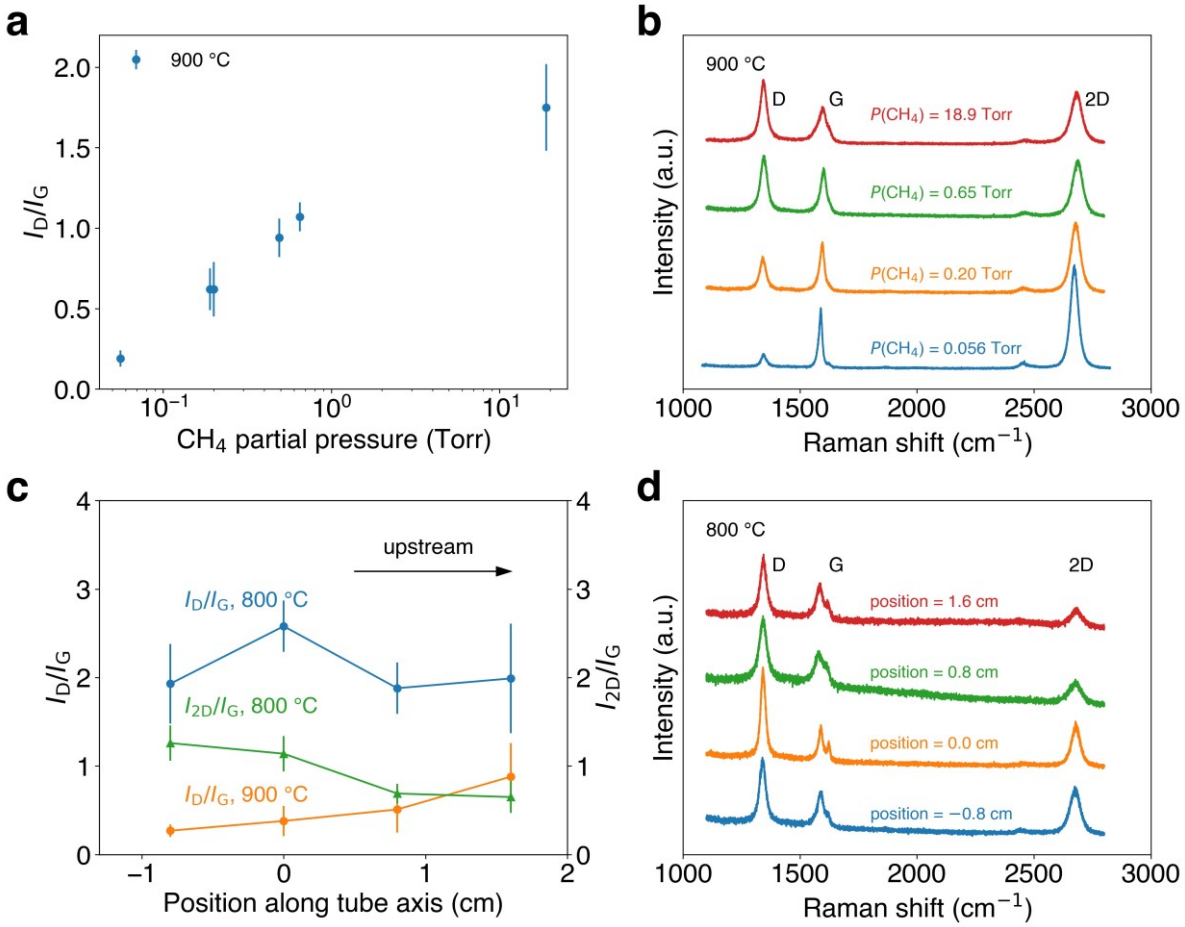

Figure 6-1. (a) D to G peak intensity ratio (I_D/I_G) of CVD graphene's Raman spectrum as a function of CH_4 partial pressure during CVD at 900 °C. (b) Raman spectra of CVD graphene samples grown with various CH_4 partial pressures at 900 °C. (c) I_D/I_G (left y axis) and 2D to G peak intensity ratio (I_{2D}/I_G, right y axis) of CVD graphene as functions of position in the CVD heating zone along the CVD tube axis. Position = 0 stands for the center of the heating zone. (d) Raman spectra of CVD graphene samples grown at 800 °C at different positions. The CH_4 partial pressure is 0.018 Torr for c) and d). The Raman excitation wavelength is 532 nm.

Figure 6-1c also presents the effect of a typically hidden CVD parameter — the position inside the heating zone. Ideally, the defect density should be nearly independent of the position. However, as will be discussed later, the density and sizes of the intrinsic graphene defects are spatially heterogeneous on the same Cu substrate, which can be exploited to improve the gas separation performance of the graphene membranes. Under the same growth condition, the defect density monotonically increases as the sample moves upstream. For example, I_D/I_G of CVD graphene grown at 900 °C (orange) increases as the position along CVD tube axis moves upstream from −0.8 to 1.6 cm relative to the heating zone center. The defect density of the graphene sample grown at 900 °C is low (Figure 6-5 in Appendix 6.8.1), and therefore, is positively correlated with I_D/I_G, according to the amorphization trajectory of

graphene when L_D > 3 nm. In contrast, I_D/I_G of CVD graphene grown at 800 °C (blue) first increases and then decreases while moving upstream. This is because L_D reaches the maximum point of the amorphization trajectory at ~3 nm. The monotonically decreasing I_{2D}/I_G moving upstream (green curve in Figure 6-1c, Figure 6-1d) indicates that the defect density increases.[232] This consistent spatial heterogeneity in defect density indicates the existence of a spatially variable parameter along the CVD tube axis. Possible parameters include H_2 concentration, CH_4 concentration, temperature, or other impurities. I rule out H_2 or CH_4 because their flow rates were at least three orders of magnitude higher than the rate of graphene deposition (Appendix 6.8.2). Therefore, it is unlikely that either H_2 or CH_4 had a considerable concentration gradient. Further, the variation in temperature can be ruled out as a possible reason. The temperature variation inside the CVD tube was < 1 K near the heating zone center. This variation is not only too small compared with the CVD temperature of > 1000 K, but is also symmetric with respect to the heating zone center (not monotonic).

Based on the discussion above, all the possibilities can be narrowed down to the gradient of an impurity component. I hypothesize that O_2 from an air leak was the reason. O_2 is known to significantly affect the CVD growth of graphene.[252,253] For a CVD system operated under vacuum, an air leak is difficult to be eliminated completely, and O_2 is the only major reactive component in air. In order to identify the source of the air leak (upstream or downstream), the air leak was artificially increased by using a pair of leakier O-rings to seal the connection between the CVD quartz tube and the metal flange. The increased air leak led to a decrease in defect density (Figure 6-6 in Appendix 6.8.1). This result i) confirmed the effect of O_2 on the graphene pore density, and ii) confirmed that the correlation between the O_2 concentration and the pore density is negative. Note that in this work, O_2 does not cause defect nucleation. Instead, O_2 inhibits defect nucleation by reducing the graphene growth rate, because O_2 can react with graphene edges or active carbon species on the catalytic substrate.[254] Because the pore density was found to monotonically increase from downstream to upstream, the O_2 concentration should monotonically decrease from downstream to upstream, which indicates a major air leak source from the downstream pipeline. Interestingly, it was found that normal CVD graphene growth could not occur when the gas ballast of the vacuum pump used to evacuate the CVD chamber was open. The gas ballast allowed air into the pump in order to remove condensed vapor (like water) in the pump oil. This

indicates that air entering the vacuum pump can find its way diffusing backwards to affect CVD-grown graphene. A trace oxygen analyzer was used to quantify the O_2 concentration in the reactor, and it was found that the majority of the O_2 leakage was in fact contributed by the vacuum pump (Appendix 6.8.2). This finding is important because the unnoticed difference in air leak conditions among laboratories might have caused the low reproducibility of graphene CVD synthesis.

An alternative hypothesis of the intrinsic defects is that they are solely formed at grain boundaries due to imperfect merging. This hypothesis can be ruled out because consistent $I_D/I_G > 0$ can be observed inside a single graphene crystal (Figure 6-7 in Appendix 6.8.1). Furthermore, the graphene defects are mainly vacancies instead of sp^3-like defects or boundary defects because the D to D' peak intensity ratio ($I_D/I_{D'}$) of the CVD graphene is 8.2±0.2 (Figure 6-8 in Appendix 6.8.1), consistent with the study by Eckmann *et al.* ($I_D/I_{D'}$ ~7 for vacancies, ~3.5 for boundary defects, and ~13 for sp^3-like defects).[255] Therefore, in this chapter, "pore", "defect", and "vacancy" are used interchangeably. Note that in the literature, Raman spectroscopy measurements have been shown to be reliable for predicting the pore density in graphene and to be consistent with high-resolution microscopy imaging.[118,121]

6.3 Gas Separation Performances

After synthesizing a continuous single-layer graphene film with intrinsic defects on Cu, I transferred the graphene onto a Ni disk with a 100×100 array of 4.2±0.3-μm-diameter holes (Figure 6-2a, b). In order to prevent graphene rupture due to its macroscopic fragility, a porous carbon scaffold was utilized as the mechanical support, which was synthesized by the carbonization of phase-separated poly(styrene)-poly(4-vinylpyridine) (PS-P4VP) + turanose for the graphene layer (see Section 6.7.2 for details).[120,256] The porous carbon scaffold ensures that the graphene membrane remains intact on the hole-array (Figure 6-2c). The enhanced graphene membrane remained intact after several weeks' testing. Furthermore, its gas permeances remained nearly the same after two month's storage in a petri dish. Furthermore, the carbon scaffold is highly permeable (Table 6-1 in Appendix 6.8.3), such that the gas permeance through the porous carbon/graphene composite membrane is dominated by the graphene layer (Figure 6-2d).[120,122] The thickness of the porous carbon scaffold is ~200 nm (Figure 6-14 in Appendix 6.8.6).

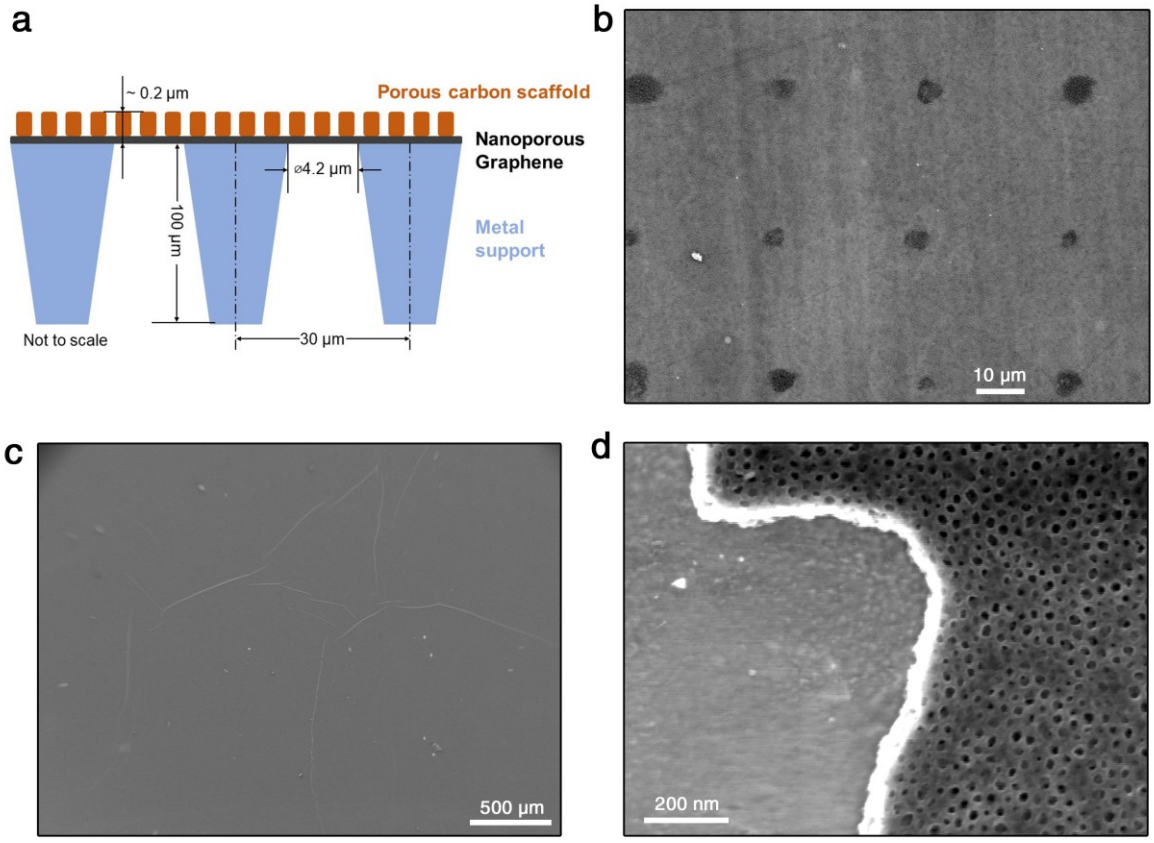

Figure 6-2. (a) Schematic of the final membrane (not to scale). (b, c) Scanning electron microscopy (SEM) images of a single-layer graphene membrane supported by a porous carbon scaffold on a 100×100 hole-array, using accelerating voltages of (b) 7 kV and (c) 2 kV, respectively. (b) shows a zoomed-in image and (c) shows that the membrane is intact. (d) SEM image of a top view of the edge of the porous carbon scaffold.

After graphene synthesis and membrane transfer, the graphene membranes suspended over the hole-array were tested for their H_2, He, CH_4, and SF_6 permeances using a mass spectrometer. Because the mass spectrometer is not sensitive to H_2, the H_2 permeance data of some membranes exhibit high uncertainty (Figure 6-17c in Appendix 6.8.6). As a solution, He was used as the representative for small gas molecules (kinetic diameter D_m = 0.26 nm),[6] because i) its signal was higher and more stable, ii) the H_2/He selectivity was ~ 1.4 for all the membranes investigated, close to the Knudsen selectivity for effusion-type gas transport (Table 6-1 in Appendix 6.8.3), and iii) He/CH_4 separation is essential for helium recovery from natural gas.[57,257] Because graphene adhered to the Ni support could not contribute any gas flow,[31] in this chapter, gas permeances were calculated based on the area of the laser-drilled

holes (see Figure 6-12 in Appendix 6.8.5 for permeances calculated based on the total area of the Ni support).

Figure 6-3a, b show the He/CH_4 and He/SF_6 separation performances of the graphene membranes. Datapoints of the same color represent the same membrane measured under different conditions, including temperature, surface decoration, and air exposure. The graphene membranes were classified into four color families, red, orange, green, and blue, corresponding to four different CVD parameter sets. Comparing the blue family (900 °C, $P(CH_4)$ = 0.19 Torr) to the green family (1000 °C, $P(CH_4)$ = 0.19 Torr), or the red family (800 °C, $P(CH_4)$ = 0.018 Torr) to the orange family (900 °C, $P(CH_4)$ = 0.018 Torr), it is observed that a lower CVD temperature yields higher He permeances because of the higher defect density (Figure 6-1c). Further, a lower CVD temperature does not lead to a significant decrease in selectivity. The effect of $P(CH_4)$ is different. Compared to the orange family ($P(CH_4)$ = 0.018 Torr, 900 °C), the blue family ($P(CH_4)$ = 0.19 Torr, 900 °C) exhibits higher He permeances but also lower selectivities. The observed selectivity decrease for high $P(CH_4)$ can be attributed to the coalescence of overly dense intrinsic defects into larger ones, thereby reducing the gas selectivity. In Figure 6-3a, several top-left datapoints with long dashed error bar upwards indicate the lower bound of He/CH_4 selectivities, because their CH_4 signals were below the detection limit (Appendix 6.8.6).

The position of graphene inside the CVD heating zone also plays a major role. Within each color family, datapoints of deeper color represent a membrane sample closer to the upstream (legend in Figure 6-3a, b; also see Figure 6-9 in Appendix 6.8.3 for individual subplots for each color family). For example, in the orange family in Figure 6-3a, b, the membrane position moves upstream from the light yellow to the orange, and then to the brown circles. Generally, the upstream membranes exhibit higher selectivities compared to the downstream ones while exhibiting similar He permeances, making moving a graphene sample upstream in the CVD heating zone a simple and reliable strategy to improve its membrane performance. This trend suggests that the upstream membranes have smaller pore sizes as well as higher pore densities (consistent with Figure 6-1c). This further strengthens the hypothesis that the spatial heterogeneity in pore density and pore size was caused by the gradient of O_2 concentration. Note that O_2 serves as an etchant that expands graphene pores.[224,254,258] The monotonic decrease of O_2 concentration from downstream to upstream was consistent with the pore size decrease in the same

direction. Note that O_2 has a dual effect on the intrinsic graphene pores. On the one hand, O_2 inhibits the nucleation of the intrinsic pores. On the other hand, O_2 expands the pores that survive the defect healing process. Therefore, a low O_2 concentration is beneficial for both gas permeance and selectivity. After a graphene pore is nucleated at the front-most edge, its growth could occur during one or more stages of the graphene CVD process, as hypothesized below. i) The pore could be expanded by O_2 at CVD temperature while it is still at the front-most edge during graphene growth. ii) The pore could be expanded by O_2 at CVD temperature when it is inside a graphene crystal after the front-most edge has moved along. iii) The pore could be expanded by O_2 during the cooling period after the graphene growth (when CH_4 feed has been stopped). Hypothesis iii) is not likely because the graphene membrane remains highly permeable even though a rapid cooling strategy has been applied, where the Cu substrate was shifted out from the heating zone and quickly cooled to room temperature by a fan, reducing the cooling period to a minimum. Hypothesis ii) can also be ruled out because the gas separation properties of the graphene membranes are very similar before and after reducing the graphene growth period from 3 to 1 h (membrane ID = 10 *vs.* 17 in Table 6-1 in Appendix 6.8.3). Therefore, the O_2-induced pore growth most likely occurs when the pore is still chemically active at the front-most graphene edge, while it is still decoupled from pore nucleation triggered by Cu insertion. Note that membrane ID = 17 was synthesized one month later than membrane ID = 10. This consistency indicates that my fabrication method of porous graphene was robust enough to withstand random external fluctuations.

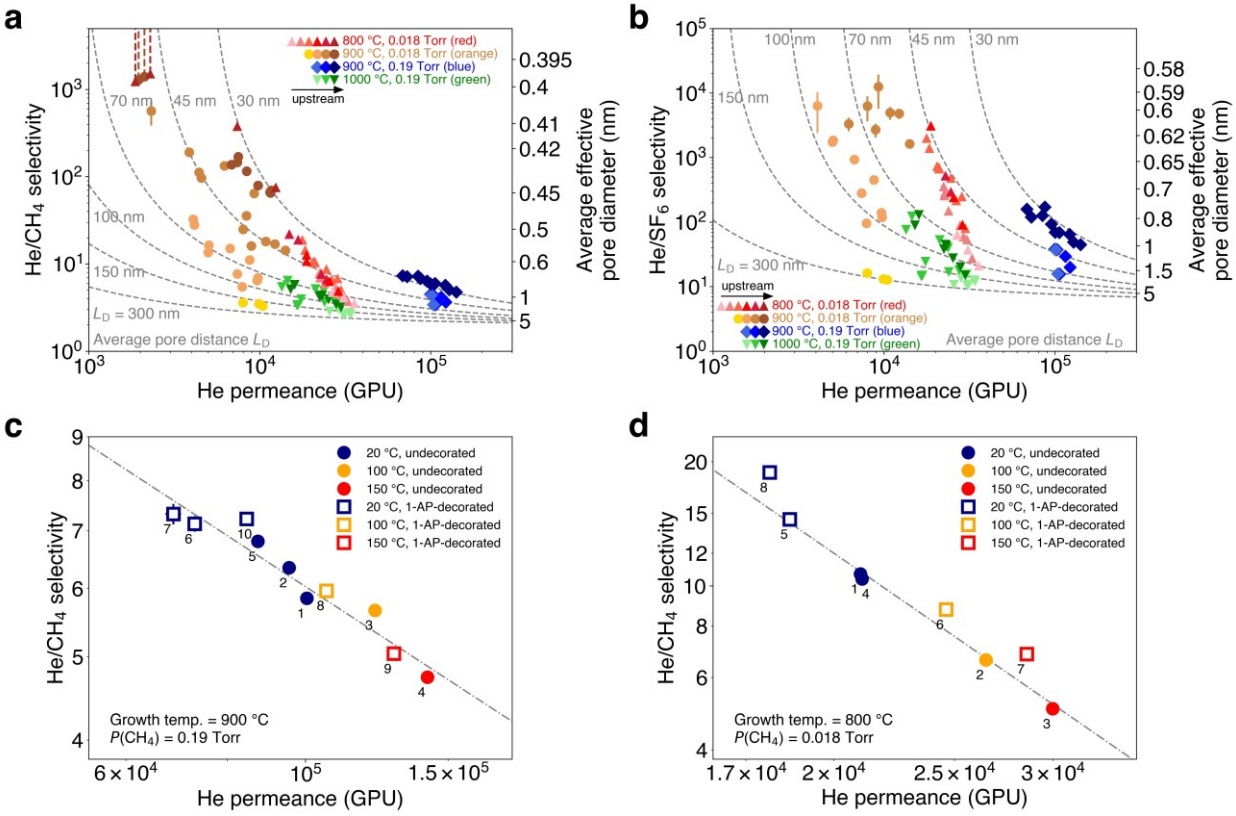

Figure 6-3. (a) He/CH_4 selectivities and He permeances of graphene membranes. Datapoints of the same color represent the same membrane under different conditions (temperature, surface decoration, *etc.*). Top-left datapoints with long dashed error bar upwards indicate the lower bound of He/CH_4 selectivities, because CH_4 signals were below the detection limit. Dashed grey curves indicate the theoretically predicted selectivity-permeance trade-off curves for various pore densities (iso-pore-density trade-off curves). Right *y* axis presents the theoretically predicted average effective pore diameter that corresponds to the left *y* axis. (b) He/SF_6 selectivities and He permeances of graphene membranes. Other details are the same as in (a). (c, d) He/CH_4 separation performance history of two graphene membranes, tested at different temperatures and surface decoration states. The numbers below the datapoints represent the testing sequence. 1-AP indicates 1-aminopyrene.

6.4 Iso-Pore-Density Trade-off Curves

After evaluating the effects of the CVD parameters (temperature, CH_4 partial pressure, and sample position), in this section, I examine how the gas separation property of the same graphene membrane depends on the condition of permeation measurement. The effects of measurement temperature (not CVD temperature) and surface decoration are illustrated in Figure 6-3c, d, where the selectivity-permeance trade-off of two individual graphene membranes are presented. Figure 6-3c corresponds to the deep blue datapoints in Figure 6-3a, and Figure 6-3d corresponds to the red datapoints. The numbers below the datapoints represent the testing sequence. Regarding Figure 6-3c, d, the following

observations can be made. First, a higher measurement temperature yields a lower selectivity and a higher gas permeance, and the change is reversible. This is a phenomenon observed for various types of membranes.[12,34,118,259] A plausible explanation is that the gas permeation is activated, and the energy barrier of pore crossing is positive,[31] which seems reasonable for high-selectivity membranes. For example, the apparent energy barriers (derived by direct fitting to the Arrhenius equation) of He and CH_4 through membrane ID = 6 (Table 6-1 in Appendix 6.8.3) are 9.4 and 26.5 kJ mol^{-1}, respectively. However, this temperature effect persists for membranes with low selectivity (He/CH_4 selectivity < 4, He/SF_6 selectivity < 20, see membrane ID = 7, 8 in Table 6-1 in Appendix 6.8.3). For example, the apparent energy barriers of He, CH_4 and SF_6 through membrane ID = 7 are 1.7, 2.4, and 1.6 kJ mol^{-1}, respectively. If the He transport is activated through this membrane, its pore diameters should be commensurate with the kinetic diameter D_m of He (0.26 nm). In this case, its energy barrier for CH_4 (D_m = 0.38 nm) and SF_6 (D_m = 0.55 nm) should be extremely high instead of being only ~2 kJ mol^{-1} (0.8 k_BT at room temperature), and its He/CH_4 and He/SF_6 selectivities should be much higher than those measured experimentally. To resolve this inconsistency, I hypothesize that under experimental conditions, graphene pores are partially blocked by airborne hydrocarbon contaminants adsorbed on graphene surfaces. As the temperature increases, the contaminants partially desorb, alleviating the pore blockage and effectively expanding the pore size. In Section 4.4, I fit the theory of gas permeation through graphene nanopores to the data reported in the literature,[118,122,128,130] and show that the graphene pores have to effectively expand as a function of temperature to obtain a reasonable fitting. Further, Zhao *et al*. showed that annealing the graphene membrane at high temperature alleviates the contamination and increases the gas permeance.[122] It has also been observed that the adsorption of airborne hydrocarbons on graphitic surfaces renders them more hydrophobic during water contact angle measurements.[216,217] This contamination hypothesis also explains the observed shift from datapoint 1 to 2 in Figure 6-3c resulting solely from exposing the membrane to air. The adsorption of lighter molecules such as water cannot account for the observed temperature dependence because they cannot remain adsorbed on the graphene surface at an elevated temperature > 100 °C.

The second observation from Figure 6-3c, d is that the non-covalent decoration of 1-aminopyrene (1-AP) on the graphene membranes leads to increased selectivity and reduced He permeance (hollowed

squares vs. solid circles). 1-AP can strongly bind to the graphene surface due to strong π-π stacking, thereby enhancing pore blockage and effectively reducing the pore sizes. The effect of 1-pyrenebutyric acid (1-PBA) is almost identical to that of 1-AP, suggesting that pyrene plays the major role (membrane ID = 1 vs. 2 in Table 6-1 in Appendix 6.8.3). Furthermore, the temperature dependences of the selectivity and the permeance in Figure 6-3c, d are very similar before and after the 1-AP decoration. This strongly suggests that the undecorated graphene surface has already been covered by some pore-blocking adsorbates, which play a similar role as those of 1-AP or 1-PBA, albeit weaker in terms of pore blockage.

Based on the analysis above, the selectivity-permeance trade-off curves observed in Figure 6-3c, d can be attributed to the effective pore size change, which is induced by the status change of the pore-blocking contaminants, or the "nanoscale fouling". Graphene membranes are susceptible to this nanoscale fouling effect because the gas transport resistance through graphene nanopores is dominated by the entrance/exit resistance at the surface. Assuming that the pore density of a graphene membrane remains constant during its testing history, hereafter, the selectivity-permeance trade-off curves are referred to as "iso-pore-density trade-off curves", where moving along the curves reflects the changes in the effective pore size. Manipulating the nanoscale fouling effect by temperature change or surface decoration could be utilized as a routine method for examining membranes made by two-dimensional materials.

These iso-pore-density trade-off curves can also be observed for other graphene membranes, as shown in Figure 6-3a, b. Generally, at a higher selectivity, there are sharper changes in selectivity with small changes in permeance, indicating that smaller pores are more sensitive to the nanoscale fouling. To explain this trend, I carry out theoretical investigation as follows. According to the gas permeation mechanism through perfectly clean porous graphene discussed in Chapter 3, direct impingement from bulk gas, surface diffusion, and cross-pore translocation all affect the gas permeance. However, the nanoscale fouling hypothesis motivates me to consider solely the direct impingement permeance, the contribution that is not affected by the condition of the graphene surface. Therefore, the permeance of gas *i* through a graphene membrane can be predicted as follows, assuming uniform pore sizes (Section 3.4):

$$K_i = \rho \cdot \frac{\pi D_\mathrm{p}^2}{4} \cdot \frac{1}{\sqrt{2\pi m_i k_\mathrm{B} T}} \cdot \left(1 - \frac{D_{\mathrm{m},i}}{D_\mathrm{p}}\right)^{\alpha_i} \tag{6-1}$$

where ρ is the areal pore density, D_p is the effective pore diameter (after partial blockage by nanoscale fouling), m_i is the molecular weight of gas i, $D_{\mathrm{m},i}$ is the kinetic diameter of gas i, k_B is the Boltzmann constant, and T is the measurement temperature in degrees Kelvin. The graphene pores are assumed to be circular because the most probable pore isomers generated in the graphene lattice are nearly circular.[35] The $\left(1 - D_{\mathrm{m},i}/D_\mathrm{p}\right)^{\alpha_i}$ term in Equation (6-1) describes the steric rejection effect due to the collision between gas i and the pore edges, and α_i is a gas i-dependent parameter which equals 3 if all gas-graphene interactions, other than collisions, can be neglected (Section 3.4). According to Equation (6-1), the slope of the iso-pore-density trade-off curve (Figure 6-3c, d) can be expressed as follows (see Appendix 6.8.3 for derivation):

$$-\mathrm{Slope} = \frac{\frac{\alpha_2 D_{\mathrm{m},2}}{\alpha_1 D_{\mathrm{m},1}} \frac{D_\mathrm{p} - D_{\mathrm{m},1}}{D_\mathrm{p} - D_{\mathrm{m},2}} - 1}{\frac{2}{\alpha_1} \frac{D_\mathrm{p} - D_{\mathrm{m},1}}{D_{\mathrm{m},1}} + 1} \tag{6-2}$$

where i = 1 and 2 denote the more and the less permeable gas species, respectively. As shown in Equation (6-2), the slope of the iso-pore-density trade-off curve significantly increases (in absolute value) in a nonlinear manner as D_p approaches the kinetic diameter of the larger gas $D_{\mathrm{m},2}$. This nonlinearity is also displayed by the right y axes in Figure 6-3a, b, where the predicted average effective pore diameter corresponding to the left y axes is plotted. As the average D_p approaches 0.38 nm or 0.55 nm (D_m of CH_4 and SF_6, respectively), the He/CH_4 or He/SF_6 selectivity significantly increases. In fact, the iso-pore-density trade-off curves predicted with α_i = 3 for every i fit the experimental results in Figure 6-3a, b reasonably well, confirming the applicability of Equation (6-1) (Figure 6-10 in Appendix 6.8.3).

To further improve the fitting, α_i values of He, CH_4, and SF_6 can be treated as unknowns. It is also assumed that the pore diameters in the graphene membranes follow lognormal distributions, which are widely observed in graphene nanopore ensembles.[118,131] Based on the assumptions above, I attempted to fit the theoretical model to the experimental gas permeance data (see Appendix 6.8.3 for details). The fitting predicts that the effective graphene pore diameter shrinks by (9±3)% from 150 to 100 °C and

shrinks by (23±6)% from 150 to 20 °C (see Table 6-2 in Appendix 6.8.3 for details). The fitting also predicts that α equals 2.0, 2.8, and 3.2 for He, CH_4, and SF_6, respectively. Theoretically predicted iso-pore-density trade-off curves using these α values are plotted as the dashed curves in Figure 6-3a, b, where each curve corresponds to a certain pore density ρ (or L_D). The predicted iso-pore-density trade-off curves successfully reproduce the selectivity-permeance trade-off observed in Figure 6-3a, b. Note that the pore density estimated according to the iso-pore-density trade-off curves is typically lower than that estimated by I_D/I_G. For example, for membrane ID = 6 (Table 6-1 in Appendix 6.8.3), $L_D \sim 45$ nm according to the iso-pore-density trade-off curve (light brown dots in Figure 6-3a), larger than $L_D = 17$ nm predicted by I_D/I_G. This is because i) the porous carbon scaffold blocks some membrane area, and ii) only a fraction of the pores contribute to gas permeation due to the pore size distribution.

I also attempted to analyze the effective pore size change of other datasets in the literature based on the iso-pore-density trade-off curves. However, due to different laboratory environments and different membrane fabrication processes, Equation (6-1) may not always be the best approximation. For example, the contribution of surface diffusion flow to the gas permeance needs to be considered for the graphene membranes in ref. 118, ref. 120, ref. 128, and ref. 130 (see Appendix 6.8.4).

6.5 Comparison with the Literature

Figure 6-4 presents a comparison of the H_2/CH_4 separation performances of my intrinsically defective single-layer graphene membranes and other state-of-the-art membranes in the selectivity-permeance Robeson plot (see Figure 6-13 in Appendix 6.8.5 for He/CH_4 Robeson plot). Some of the highest-performance graphene membranes in this chapter show H_2 permeance > 10^4 GPU (gas permeation unit, 1 GPU = 3.35×10^{-10} mol s^{-1} m^{-2} Pa^{-1}) and H_2/CH_4 selectivity > 100, exceeding the Robeson upper bound for 1-μm thick polymer membranes and the performances of some other materials.[11,244] Some highly selective graphene membranes exhibit very low CH_4 permeances at room temperature such that their CH_4 signals are lower than the detection limit of the mass spectrometer, leading to extremely high H_2/CH_4 selectivities of at least 2000 (Appendix 6.8.6). Meanwhile, they still exhibit decent H_2 permeances > 4000 GPU. If the iso-pore-density trade-off curves predicted in Figure 6-3 remains valid

for these highly selective membranes, they can be regarded as nearly CH_4-impermeable. In comparison, the highest H_2/CH_4 selectivity obtained from a single-layer graphene membrane in previous studies was 37.5 (with H_2 permeance ~7200 GPU), obtained by Huang *et al.*[124] In general, the highest-performance graphene membranes were synthesized under the following conditions: low CVD temperature (800 to 900 °C), $P(CH_4)$ = 0.018 Torr, and upstream position in the CVD heating zone. These conditions contribute to the high membrane performance because i) the low CVD temperature generates more pores, ii) the appropriate $P(CH_4)$ prevents pore coalescence, and iii) the upstream position increases the pore density and reduces the pore sizes. Figure 6-4 demonstrates the advantage of single-layer graphene membranes for gas separations due to their atomic thickness and negligible interior gas transport resistance. This advantage is realized by effectively increasing the pore density while preserving small pore sizes, which relies on the effective control over the intrinsic vacancy formation during graphene CVD.

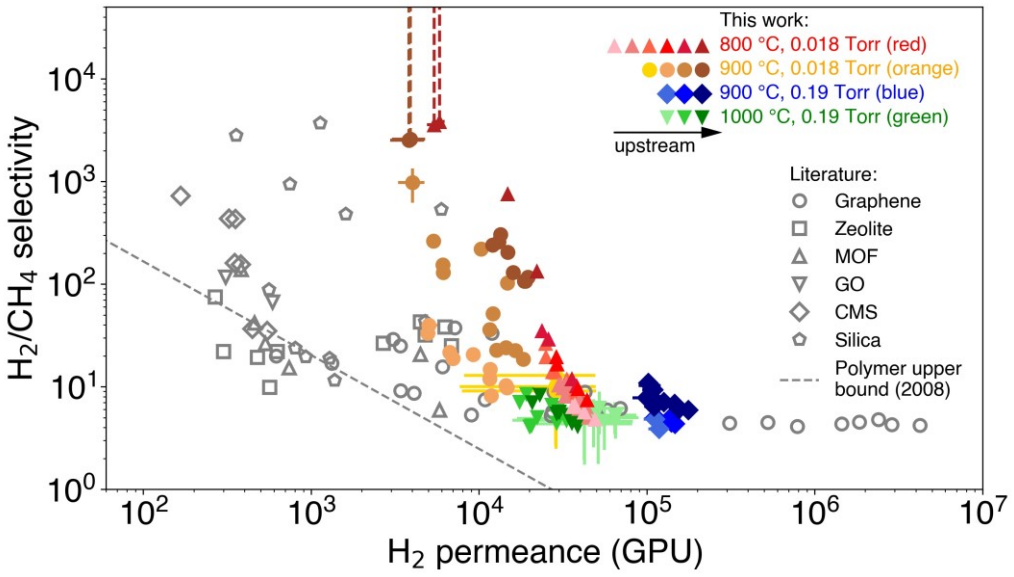

Figure 6-4. Selectivity-permeance Robeson plot of H_2/CH_4 separation. Results of this chapter are plotted as solid markers. Datapoints with long dashed error bar upwards indicate the lower bound of H_2/CH_4 selectivities, because CH_4 signals were below the detection limit. Performances of other state-of-the-art membranes in the literature are plotted as hollowed markers, including graphene,[116,120,122,124] zeolite,[260–265] metal-organic frameworks (MOF),[266–271] graphene oxide (GO),[167,272] carbon molecular sieves (CMS),[273–276] silica,[259,17,277–282] and Robeson upper bound for polymers assuming 1 μm thickness.[11]

6.6 Conclusions

In summary, in this chapter, I demonstrate a strategy to synthesize single-layer graphene with a high density of gas-sieving pores using one-step CVD. By generating intrinsic graphene pores during CVD, I decoupled pore nucleation and growth. This makes it possible to overcome the challenging trade-off between a high pore density and a high selectivity, which has been a key bottleneck for oxidative etching methods. I gain deep insight into the formation mechanism of the intrinsic graphene pores and substantially increased the pore density while maintaining precise pore sizes for gas separation. The resulting graphene membranes exhibit record-high gas separation performances to date, reaching H_2/CH_4 selectivity > 2000 while H_2 permeance > 4000 GPU, or H_2/CH_4 selectivity > 100 while H_2 permeance > 10^4 GPU. I also propose the nanoscale fouling effect, where the graphene pores are partially blocked by hydrocarbon contaminants. This effect highlights the critical role of the adsorbed molecules near the pore edge in gas permeation. Overall, the straightforward one-step CVD approach represents an important advance towards the application of nanoporous graphene as high-performance gas separation membranes. This chapter also sheds light on the controllable synthesis of highly porous two-dimensional materials for other applications such as energy storage and conversion, catalysis, and sensing. In the next chapter, I will summarize the main results reported in this thesis, as well as discuss future potential research directions.

6.7 Methods

6.7.1 Graphene Synthesis

Single-layer graphene was synthesized by CVD on a Cu foil (Sigma Aldrich, 99.98% purity, 25 μm thick, 2.4 cm×1.6 cm in length and width) using CH_4 (diluted in H_2) as the precursor. Prior to CVD, the Cu foil was electropolished in an acidic electrolyte to reduce its surface roughness. The electrolyte was prepared by mixing water (400 mL), ethanol (200 mL), isopropanol (40 mL), orthophosphoric acid (200 mL), and urea (4 g) followed by stirring. A voltage of 6.0 V was applied between the cathode (Cu foil

to be electropolished) and the anode (Cu foil) for 90 s, while the cathode and the anode were placed 2–3 cm apart. The electropolished Cu foil was rinsed with deionized water, ethanol, and isopropanol in sequence, dried under air flow, and placed inside the quartz tube (1'' outer diameter) on a quartz boat (see Figure 6-15 in Appendix 6.8.6 for a diagram of the CVD setup). A single-zone split tube furnace was used (MTI Corp., OTF-1200X-S). A pair of Quick Clamp Hi-Vacuum Flanges (MTI Corp.), along with a pair of high temperature silicone rubber O-rings (MTI Corp., QF-OR), were used to seal the connections between the quartz tube and the metal flanges. After sealing all immobile metal fittings using Torr Seal epoxy (K. J. Lesker), the minimum air leak rate was 5 mTorr L min^{-1}. Before CVD growth, the Cu foil was annealed at the growth temperature (800–1000 °C) in 0.5 atm H_2 for 16 h while the H_2 flow rate was 70 sccm. During a growth period of 3 h (except for membrane ID = 16–18, 1 h), a certain flow rate of CH_4 (ranging from 0.1 sccm to 3.0 sccm, depending on the desired CH_4 partial pressure) was fed, while the H_2 flow rate was 10 sccm. The chamber pressure during CVD growth was 1.5 Torr. The CVD chamber was evacuated by an oil-sealed rotary vacuum pump (Edwards RV12, ultimate pressure 1.5 mTorr, pumping speed 14.2 $m^3 h^{-1}$) with its gas ballast closed. The pump oil was Edwards Ultragrade 19. A molecular sieve foreline trap (MDC Precision, 4.5'' body, NW25) was connected to the vacuum pump to trap hydrocarbons and water. The CVD growth was terminated by stopping the CH_4 feed and shutting down the furnace. A trace oxygen analyzer (1–1000 ppm, EQ-W1000-LD, MTI Corp.) was sometimes connected to the quartz tube to measure the concentration of O_2. The trace oxygen analyzer must be detached from the reactor during the CVD growth of graphene because the organic electrolyte in the analyzer would interfere with the CVD process.

6.7.2 Graphene Membrane Fabrication

The as-synthesized graphene/Cu sample was spin-coated (500 rpm, 1 min) with a solution of PS-P4VP (0.1 g Polymer Source, M_n(PS) = 11800 g mol^{-1}, M_n(P4VP) = 12300 g mol^{-1}, M_w/M_n = 1.08) and turanose (0.2 g; Sigma Aldrich, ≥ 98% purity) in *N*,*N*-dimethylmethanamide (2 g). The solution was heated at 150 °C for 16 h before use. The spin-coated graphene/Cu was then pyrolyzed at 460 °C in an H_2/Ar atmosphere for 1.5 h, forming the porous carbon scaffold (PCS) adhering to graphene. Flat Cu surface is recommended during spin-coating. Otherwise, the thickness of the PCS would be uneven,

causing the PCS to fracture. The PCS/graphene/Cu was cut into ~0.8 cm×~0.8 cm pieces, and the Cu foil of each piece was etched away by an aqueous solution of $Na_2S_2O_8$ (Transene Co.) for 2 h. After being rinsed twice with deionized water, the PCS/graphene composite was transferred by scooping onto a 100-μm-thick Ni disk with an array of 100×100 laser-drilled 4.2±0.3-μm-diameter holes with a 30 μm pitch (Oxford Lasers). For some membranes, 50-μm-thick W disks with an array of 20×20 laser-drilled holes were used. The membrane was dried at room temperature overnight. The following human errors should be avoided during transfer: i) a bent metal support caused PCS/membrane to fracture, ii) surfactants caused the PCS/graphene composite to collapse, and iii) stacking multiple layers of PCS/graphene caused the membrane to crumple. The survival rate of the graphene membranes was 22/24 = 91.7% if no human error occurred. The two failed membranes simultaneously fractured because their PCS layers were too thin. Non-covalent decoration of the graphene surface was carried out by submerging a graphene membrane into a 2 mmol L^{-1} solution of 1-aminopyrene (97%, Sigma Aldrich) or 1-pyrenebutyric acid (97%, Sigma Aldrich) in ethanol. Subsequently, the graphene membrane was dried in the air for at least 30 min before gas permeation testing.

6.7.3 Gas Permeation Testing

The Ni disk carrying the graphene membrane was mounted into a homemade permeation module (Figure 6-16 in Appendix 6.8.6). A gas mixture containing H_2, He, CH_4, and SF_6 was fed towards the membrane. The pressure difference for gas permeation was 1.0 bar. Permeated gases were swept by an Ar flow into a mass spectrometer (Agilent 5977A with Diablo 5000A real time gas analyzer). The permeances of the gases and their confidence intervals were calculated based on the mass spectroscopy signals collected in a five-minute duration after steady state was reached (Appendix 6.8.6). The gas permeance from a pure feed was also measured, and was almost identical to that from a mixture feed (Figure 6-18 in Appendix 6.8.6).

6.7.4 Membrane Characterization

Graphene membranes were imaged using a Zeiss Sigma 300 VP SEM operated at an accelerating voltage of 0.5–10 kV. Raman spectra of graphene samples were collected using a Horiba LabRAM

micro-Raman spectrometer with a 532 nm excitation laser wavelength, 1800 grooves/mm grating, and 50x objective. For Raman spectroscopy measurements, graphene samples were transferred onto a Si wafer using polymethyl methacrylate (PMMA)-assisted transfer, where the PMMA layer was removed by acetone. Each I_D/I_G data point in Figure 6-1a, c was the average over a mapping of 25 individual Raman spot measurements. The pitch between neighboring spots was 30 μm in the *x* direction, and 25 μm in the *y* direction. The laser spot diameter was ~ 1 μm.

6.8 Appendices

6.8.1 Additional Raman Spectroscopy Data

Figure 6-5 presents the Raman spectra of CVD graphene grown at 900 ℃ at different positions along the CVD tube axis. The D to G intensity ratio (I_D/I_G) increases as the sample moves upstream. The high 2D peaks indicate that the defects are sparse in this graphene sample, suggesting a positive correlation between I_D/I_G and defect density according to the amorphous trajectory.[232,233]

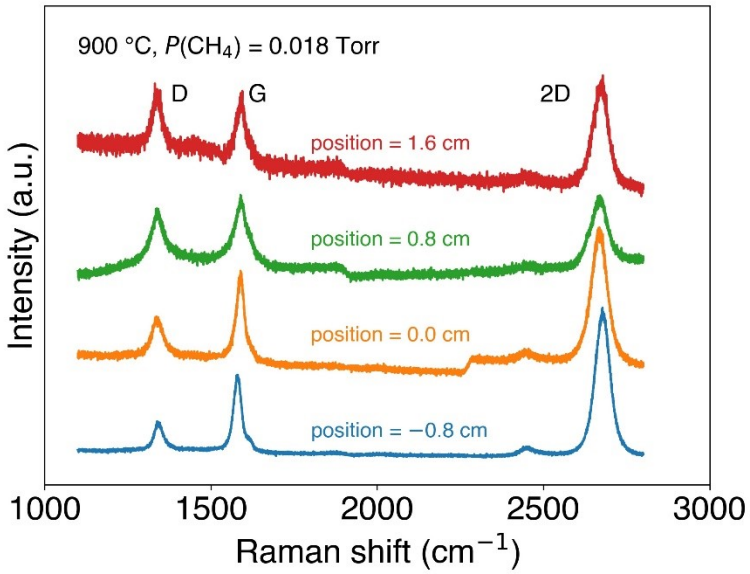

Figure 6-5. Raman spectra of CVD graphene samples grown at 900 ℃ at different positions. CH_4 partial pressure is 0.018 Torr.

Figure 6-6 presents the Raman spectra of two graphene samples synthesized using the same CVD parameters but different air leak conditions. The high air leak condition was realized by sealing the CVD quartz tube using a pair of failed O-rings due to repetitive usage. The air leak rate can be measured

by isolating the CVD pipeline in vacuum and monitoring the pressure increase. By substituting good O-rings with the leaky O-rings, the pressure increasing rate rises from 0.011 Torr L min^{-1} to 0.058 Torr L min^{-1}. As a result, the graphene defect density decreases from 0.62±0.13 to 0.25±0.12 as the O_2 concentration during CVD synthesis increases.

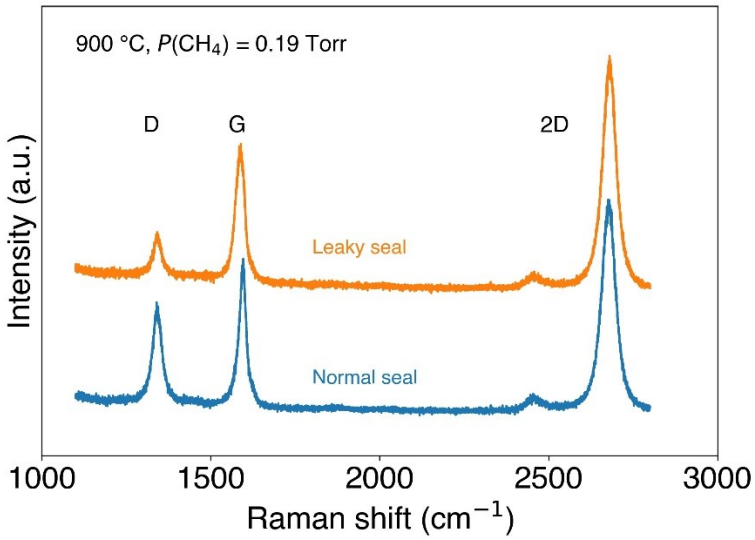

Figure 6-6. Raman spectra of CVD graphene grown under different air leak conditions. A pair of failed O-rings were used to increase the air leak.

Figure 6-7a shows an optical image of CVD-grown graphene single crystals of ~1 mm in lateral sizes. The CH_4 partial pressure and the growth time was reduced to prevent the single crystals from complete merging. Figure 6-7b presents the Raman spectrum of an area (laser spot ~1 μm in diameter) inside a single crystal. The average I_D/I_G is 0.24±0.04, indicating that the intrinsic defects form inside the graphene flakes.

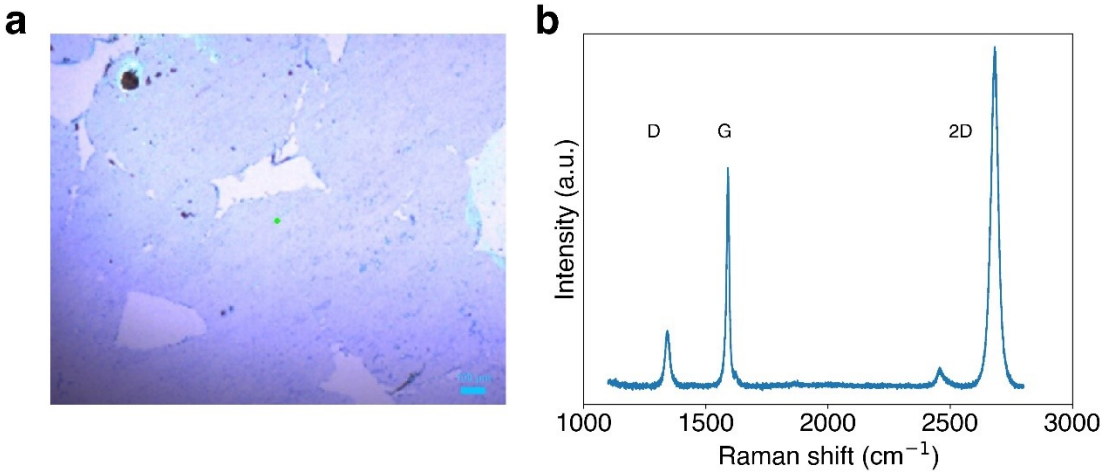

Figure 6-7. (a) Optical image of graphene single crystals on a Si wafer. (b) Raman spectrum of an area inside a graphene single crystal.

Figure 6-8a shows a zoomed-in Raman spectrum of a CVD graphene sample with a clearly observable D' peak. The D, G, and D' peaks are fitted with Lorentzian functions. The D to D' peak intensity ratio ($I_D/I_{D'}$) reflects the type of graphene defects: $I_D/I_{D'}$ ~ 13 for sp^3 defects, ~ 7 for vacancies, and ~ 3.5 for boundaries.[255] As shown in Figure 6-8b, $I_D/I_{D'}$ is 8.2±0.2 for the intrinsically defective graphene.

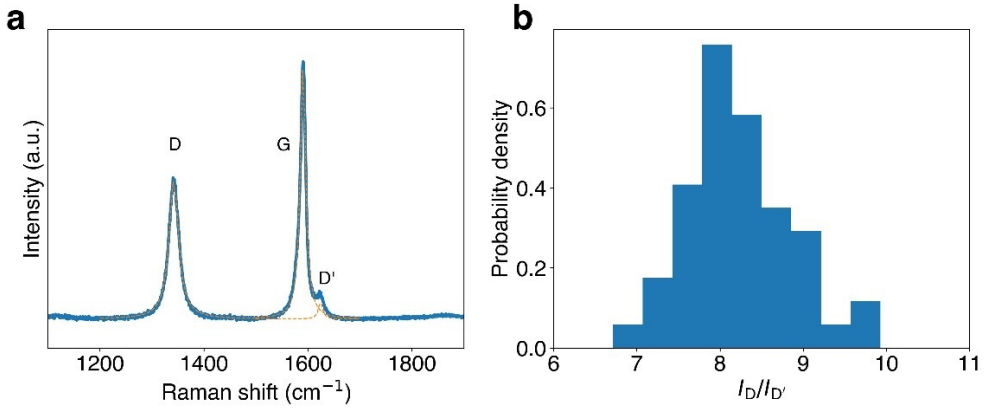

Figure 6-8. (a) Zoomed-in Raman spectrum of an intrinsically defective CVD graphene sample and the Lorentzian fitting of the D, G, and D' peaks (orange dashed curves). (b) Distribution of the D to D' peak intensity ratio ($I_D/I_{D'}$) of CVD graphene.

6.8.2 Discussion about Air Leak

In my experiments, it is found that a 10-min CVD growth could not yield a graphene sheet with full coverage under the experimental conditions. Note that the Cu substrate for graphene growth was 2.4

cm×1.6 cm in length and width. Therefore, the fastest CH_4 consumption rate on both sides of the Cu substrate is given by:

$$\frac{2 \times 0.024\ \text{m} \times 0.016\ \text{m} \times (\text{areal C density of graphene})}{10\ \text{min}} = 8.1 \times 10^{-11}\ \text{mol s}^{-1}$$

where the areal C density of graphene used is 3.82×10^{19} atom m^{-2}. In contrast, the flow rate of H_2 was 10 sccm = 7.45×10^{-6} mol s^{-1}, and the flow rate of CH_4 was at least 0.1 sccm = 7.45×10^{-8} mol s^{-1}. Both flow rates were at least three orders of magnitude higher than the rate of graphene deposition. Therefore, it is unlikely that either H_2 or CH_4 had a considerable concentration gradient.

Below, I present a mass balance analysis of O_2 in the CVD system. Consider an O_2 concentration $C(x)$ profile in the tubing (simplified as a one-dimensional coordinate x, where positive x points upstream). Assuming nearly constant pressure and constant density, according to the mass balance of O_2, it can be shown that:

$$D\frac{\mathrm{d}^2C}{\mathrm{d}x^2} + v\frac{\mathrm{d}C}{\mathrm{d}x} - r = 0 \tag{6-3}$$

where D is the binary gas diffusion coefficient, v is the convective flow velocity (towards the $-x$ direction), and r is the net rate of O_2 consumption. In the heating zone, according to Michael *et al.*, $r = kC(\mathrm{H_2})C(x)$, where k is the reaction rate constant of $2H_2 + O_2 \rightarrow 2H_2O$ and $C(H_2)$ is the concentration of H_2.[283] More specifically,

$$k = 1.228 \times 10^{-18} T^{2.4328} \exp\left(-\frac{26926\ K}{T}\right)\ \text{cm}^3\ \text{molecule}^{-1}\ \text{s}^{-1} \tag{6-4}$$

where T is the temperature in Kelvin.[283] At a CVD temperature of T = 800 °C = 1073 K, k = 220.6 cm^3 mol^{-1} s^{-1}. According to the ideal gas law, $C(H_2) = P(H_2)/RT$ = 1.5 Torr/(1073 K×R) = 2.24×10^{-8} mol cm^{-3}, where R is the gas constant, and $P(H_2)$ is approximately the CVD chamber pressure (1.5 Torr). Therefore, the O_2 consumption term $r = 4.95\times10^{-6}$ s^{-1} $C(x)$.

Considering the characteristic length scale L, the mass balance equation above can be non-dimensionalized as follows:

$$\frac{\mathrm{d}^2C}{\mathrm{d}\eta^2} + \mathrm{Pe}\frac{\mathrm{d}C}{\mathrm{d}\eta} - \mathrm{Da}C = 0 \tag{6-5}$$

where $\eta = x/L$, the Peclet number $\mathrm{Pe} = vL/D$, and the Damkohler number $\mathrm{Da} = 4.95 \times 10^{-6}\, L^2/D$. The diffusion coefficient D (in $\mathrm{cm^2\ s^{-1}}$) can be predicted as follows:[284]

$$D = \frac{A \cdot T^{1.5} \sqrt{\frac{1}{M_1} + \frac{1}{M_2}}}{P \sigma_{12}^2 \Omega} \tag{6-6}$$

where A is an empirical coefficient equal to 1.859×10^{-3} atm $\mathrm{Å^2\ cm^2\ g^{1/2}\ mol^{-1/2}\ K^{-3/2}\ s^{-1}}$, M_1 and M_2 are the molar weights of gas 1 and gas 2 (in $\mathrm{g\ mol^{-1}}$), respectively, P is the pressure (in atm), σ_{12} is the arithmetic average of the kinetic diameters of gas 1 and gas 2, and Ω is a collision integral whose value is close to 1. The kinetic diameters of O_2 and H_2 are 3.46 Å and 2.89 Å, respectively.[36]

Inside the heating zone, T = 1073 K and P = 1.5 Torr. It follows that D = 0.24 $\mathrm{m^2\ s^{-1}}$. The length of the heating zone is L = 0.2 m. Therefore, the Damkohler number Da in the heating zone is 8.3×10^{-7} << 1, indicating that the consumption of O_2 by H_2 is negligible.

Because Da << 1, the mass balance (Equation (6-5)) can be rewritten as follows:

$$\frac{\mathrm{d}^2 C}{\mathrm{d}\eta^2} + \mathrm{Pe}\frac{\mathrm{d}C}{\mathrm{d}\eta} = 0 \tag{6-7}$$

both inside and outside the heating zone. The solution to this differential equation is given by:

$$C(\eta) = C_1 \exp(-\mathrm{Pe} \cdot \eta) + C_2 \tag{6-8}$$

Note that the average flow velocity v can be derived by dividing the volumetric flow rate by the tube cross-sectional area, to obtain:

$$v = \frac{FRT}{P}\frac{1}{\frac{\pi}{4} d_{\mathrm{tube}}^2} \tag{6-9}$$

where F is the molar flow rate of the gas stream, and d_{tube} is the inner diameter of the tube. Therefore, the Peclet number Pe can be expressed as follows:

$$\mathrm{Pe} = \frac{vL}{D} = \frac{FRL}{\frac{\pi}{4} d_{\mathrm{tube}}^2} \cdot \frac{\sigma_{12}^2 \Omega}{A \cdot T^{0.5} \sqrt{\frac{1}{M_1} + \frac{1}{M_2}}} \tag{6-10}$$

In my experiment, $F = 7.45\times10^{-6}$ mol $\mathrm{s^{-1}}$ (converted from 10 sccm), d_{tube} = 2.05 cm in the heating zone, and d_{tube} = 2.5 cm outside the heating zone. The length of the heating zone is 0.2 m, and the length from the vacuum pump to the heating zone is ~ 1.5 m. Inserting these parameters into Equation (6-10), it is found that in the heating zone, Pe = 0.84, and that between the vacuum pump and the heating zone,

Pe = 4.2. These Peclet numbers are neither too low such that the O_2 concentration is nearly constant everywhere, nor too high such that O_2 cannot diffuse to the upstream.

A trace oxygen analyzer (1–1000 ppm, EQ-W1000-LD, MTI Corp.) was used to quantify the O_2 concentration in the reactor. When the H_2 flow rate was 70 sccm and the pressure was 108 Torr, the O_2 partial pressure was ~ 20 Pa (~ 0.15 Torr). A relative high pressure of 108 Torr was chosen because the trace oxygen analyzer could not withstand a high vacuum. Consider an average air leak rate in this chapter of 0.01 Torr L min^{-1}. Note that this air leak rate was measured by isolating the reactor from the vacuum pump and monitoring the real-time pressure increase using a pressure transducer. Therefore, the air leak rate was contributed by all the flanges and gaskets except for the vacuum pump. At room temperature, the flow rate of O_2 (21 mol % of air) from the air leak (vacuum pump excluded) is given by:

$$O_2 \text{ flow rate} = 21\% \times 0.01 \text{ Torr L min}^{-1} = 4.67 \times 10^{-6} \text{ Pa m}^3 \text{ s}^{-1} = 1.88 \times 10^{-9} \text{ mol s}^{-1}$$
$$= 0.0025 \text{ sccm}$$

Therefore, the O_2 partial pressure should have been $\frac{0.0025 \text{ sccm}}{70 \text{ sccm}} \times 108 \text{ Torr} = 0.0039 \text{ Torr} \ll 0.15 \text{ Torr}$ if the air leak from the vacuum pump were excluded. In other words, the vacuum pump contributes the majority of the O_2 leakage.

6.8.3 Gas Permeance Data and Fitting by Theory

All gas permeance data are presented in Table 6-1. For the same membrane, the entries are ordered by testing sequence. Non-covalent decoration by pyrene-based molecules is indicated in the "Membrane ID" column (1-pyrenebutyric acid = PBA, 1-aminopyrene = AP). DL stands for detection limit. Gas permeances measured without a graphene film are also presented, which are much higher than those measured with graphene. This indicates that gas transport through the entire membrane was dominated by the graphene film. The uncertainty of the membrane's position (±0.2 cm) stems from the fact that the lateral size of the graphene sample (~0.8 cm) was larger than the lateral size of the hole array (0.3

cm). Therefore, the permeable portion of the graphene sample may deviate from its center after the scooping transfer.

Table 6-1. Gas permeance data of the graphene membranes.

Mem-brane ID	CVD tempera-ture (°C)	$P(CH_4)$ (Torr)	Position upstream (cm)	Measurement temperature (°C)	Permeance (10^3 GPU)			
					H_2	He	CH_4	SF_6
Without graphene				20	1185	871	367	113
1	900	0.19	0.0±0.2	20	140.4±8.4	106.5±0.9	31.37±0.17	6.85±0.06
1/PBA				20	112.6±11.4	100.1±0.9	22.44±0.14	2.62±0.04
1/PBA				100	138.9±9.7	115.3±1.0	27.82±0.18	3.93±0.09
1/PBA				150	146.9±15.1	122.9±1.2	33.70±0.20	6.18±0.06
1/PBA				20	113.4±16.7	102.9±0.9	23.28±0.15	2.76±0.04
2	900	0.19	0.0±0.2	20	118.3±16.3	104.0±0.9	30.58±0.15	6.61±0.06
2/AP				20	111.9±16.3	101.1±1.2	23.08±0.18	2.72±0.06
3	900	0.19	0.8±0.2	20	110.4±13.9	100.4±0.9	17.18±0.12	1.45±0.02
3				20	111.4±13.1	95.5±0.9	15.06±0.11	1.03±0.02
3				100	146.2±12.9	121.9±1.0	21.54±0.15	1.89±0.03
3				150	177.1±8.5	141.5±1.0	29.91±0.18	3.17±0.07
3				20	100.0±17.9	87.4±0.8	12.84±0.11	0.51±0.02
3/AP				20	105.0±15.7	73.0±1.3	10.24±0.11	0.61±0.02
3/AP				20	102.3±12.8	68.7±1.5	9.39±0.14	0.44±0.02
3/AP				100	126.3±12.0	106.1±0.6	17.80±0.09	1.55±0.02
3/AP				150	155.2±10.5	128.5±0.7	25.51±0.11	2.64±0.03
3/AP				20	109.3±15.3	84.6±1.2	11.72±0.11	0.67±0.02
4	900	0.019	−0.8±0.2	20	26.9±18.6	8.9±0.3	2.34±0.04	0.54±0.02
4				20	28.7±20.5	8.0±0.4	2.22±0.05	0.49±0.02
4				100	28.6±21.0	9.9±0.4	2.85±0.05	0.76±0.02
4				150	28.8±20.9	10.4±0.4	3.17±0.06	0.82±0.02
4				20	25.3±18.1	7.4±0.3	2.31±0.04	0.54±0.02
5	900	0.019	0.0±0.2	20	11.83±0.21	7.90±0.07	1.445±0.013	0.0823±0.0025
5				20	11.59±0.25	7.41±0.10	0.967±0.013	0.0265±0.0036
5				100	14.67±0.13	9.66±0.05	1.496±0.008	0.0692±0.0013
5				150	14.45±0.12	9.74±0.05	1.406±0.008	0.0820±0.0015
5				20	6.99±0.44	5.00±0.05	0.370±0.007	0.0029±0.0004
5				20	6.67±0.39	5.05±0.05	0.307±0.007	0.0027±0.0005
5/PBA				20	4.94±0.58	4.15±0.05	0.149±0.003	< DL
5/PBA				100	9.22±0.14	6.70±0.05	0.447±0.005	0.0072±0.0007
5/PBA				150	11.65±0.12	8.75±0.06	0.788±0.006	0.0194±0.0008
5/PBA				20	5.02±0.63	4.08±0.05	0.126±0.003	0.0006±0.0004
6	900	0.019	0.8±0.2	20	12.69±0.23	8.94±0.12	0.557±0.011	0.0033±0.0008
6				20	11.55±0.14	8.00±0.06	0.322±0.009	0.0013±0.0005
6				100	14.48±0.14	10.87±0.06	0.603±0.006	0.0022±0.0005
6				150	18.33±0.16	14.12±0.08	0.988±0.008	0.0087±0.0006
6				20	6.09±0.48	4.43±0.04	0.040±0.002	< DL
6				20	5.35±0.47	3.88±0.05	0.020±0.002	< DL
6				100	12.08±0.13	8.35±0.06	0.234±0.007	< DL
6				150	16.46±0.14	12.28±0.07	0.728±0.006	0.0026±0.0005
6				20	6.13±0.51	4.56±0.04	0.047±0.002	< DL
6/AP				20	4.01±0.71	2.32±0.05	0.004±0.001	< DL
6/AP				100	10.28±0.11	6.23±0.05	0.047±0.002	< DL
6/AP				150	14.76±0.13	9.27±0.05	0.144±0.003	< DL
6/AP				20	2.52±1.10	1.22±0.03	< DL	< DL
7	1000	0.18	−0.8±0.2	20	42±29	22.2±0.7	7.73±0.23	1.90±0.05
7				20	43±27	25.7±0.7	9.03±0.17	2.41±0.05

7				100	51±30	30.8±0.6	11.73±0.13	2.96±0.05
7				150	56±26	31.3±0.7	12.09±0.12	2.90±0.05
7				20	42±25	28.3±0.6	8.63±0.17	2.09±0.04
7/PBA				20	48±24	28.9±0.7	9.54±0.16	1.94±0.04
7/PBA				100	64±22	33.5±0.9	12.22±0.13	2.66±0.04
7/PBA				150	65±24	34.1±0.9	13.01±0.13	2.84±0.04
7/PBA				20	52±23	30.7±0.6	8.43±0.17	1.95±0.04
8	1000	0.18	0.0±0.4	20	20.51±0.16	16.55±0.08	4.966±0.014	1.146±0.007
8				20	20.09±0.24	16.79±0.13	4.964±0.025	1.131±0.009
8				100	29.06±0.20	23.96±0.09	6.602±0.018	1.427±0.007
8				150	33.24±0.22	27.48±0.10	7.187±0.021	1.535±0.006
8				20	22.20±0.16	17.49±0.08	4.451±0.016	0.719±0.005
8/AP				22	17.43±0.14	13.49±0.08	2.478±0.010	0.178±0.003
8/AP				100	27.08±0.17	21.18±0.09	4.131±0.012	0.404±0.004
8/AP				150	29.82±0.18	23.71±0.08	4.831±0.015	0.599±0.005
8/AP				20	19.20±0.15	14.60±0.07	2.281±0.011	0.120±0.002
9	1000	0.18	0.8±0.2	20	29.03±0.15	23.23±0.09	5.382±0.014	0.549±0.004
9				100	35.78±0.23	28.03±0.10	8.178±0.019	1.402±0.006
9				150	38.78±0.21	29.94±0.10	9.485±0.022	1.998±0.008
9				20	29.89±0.12	22.93±0.06	5.285±0.011	0.514±0.003
9/AP				22	20.75±0.15	15.21±0.09	2.977±0.011	0.171±0.004
9/AP				100	30.07±0.20	22.46±0.08	5.358±0.016	0.592±0.005
9/AP				150	33.91±0.21	25.33±0.10	6.451±0.017	0.922±0.006
9/AP				20	22.99±0.15	16.05±0.07	2.796±0.012	0.125±0.002
10	800	0.018	1.2±0.2	22	27.42±0.16	20.45±0.09	1.947±0.008	0.0278±0.0008
10				22	27.82±0.17	21.01±0.08	1.966±0.010	0.0301±0.0008
10				100	34.99±0.19	26.49±0.10	4.004±0.013	0.1227±0.0018
10				150	39.90±0.20	29.97±0.10	5.953±0.015	0.3729±0.0033
10				20	28.38±0.18	21.07±0.08	2.028±0.010	0.0312±0.0008
10/AP				22	25.06±0.16	18.44±0.08	1.272±0.008	0.0131±0.0005
10/AP				100	33.31±0.18	24.61±0.08	2.810±0.011	0.0511±0.0011
10/AP				150	38.69±0.22	28.58±0.09	4.180±0.012	0.1148±0.0015
10/AP				25	24.95±0.16	17.76±0.08	0.943±0.006	0.0088±0.0005
11	800	0.018	0.4±0.2	23	30.49±0.43	22.74±0.19	2.895±0.026	0.0802±0.0034
11				20	29.82±0.18	22.34±0.08	2.851±0.011	0.0625±0.0013
11				100	39.36±0.20	29.19±0.10	6.370±0.015	0.4899±0.0040
11				150	44.80±0.20	32.85±0.10	8.831±0.019	1.1951±0.0053
11				20	32.57±0.18	23.87±0.08	4.003±0.011	0.1590±0.0032
11/AP				20	31.56±0.18	22.55±0.08	3.234±0.013	0.0874±0.0015
11/AP				100	39.69±0.20	27.96±0.10	5.332±0.015	0.3118±0.0024
11/AP				150	43.51±0.19	30.65±0.10	6.793±0.016	0.5700±0.0047
11/AP				20	33.11±0.17	23.15±0.09	3.052±0.011	0.0763±0.0013
12	800	0.015	−0.8±0.2	20	36.13±0.19	26.71±0.09	5.633±0.015	0.4235±0.0036
12				100	42.31±0.19	31.03±0.10	7.443±0.017	0.8279±0.0046
12				150	49.05±0.23	35.86±0.11	10.16±0.02	1.6900±0.0073
12				20	37.20±0.20	26.85±0.09	5.557±0.016	0.4239±0.0037
13	800	0.015	0.8±0.2	20	29.52±0.25	21.19±0.12	3.729±0.016	0.1451±0.0034
14	900	0.018	1.2±0.2	20	12.02±0.10	6.85±0.05	0.050±0.002	0.0006±0.0004
14				100	15.95±0.11	9.79±0.07	0.123±0.002	< DL
14				100	14.84±0.12	8.38±0.05	0.072±0.002	< DL
14				150	18.58±0.13	11.50±0.05	0.174±0.003	< DL
14				20	3.91±0.88	2.12±0.06	< DL	< DL
14				24	3.83±0.87	1.96±0.06	< DL	< DL
14				100	13.08±0.10	7.39±0.05	0.051±0.002	0.0009±0.0004
14				150	18.94±0.13	11.57±0.06	0.178±0.003	0.0019±0.0004
14				20	3.38±1.07	1.47±0.04	< DL	< DL
14				20	3.28±0.98	1.55±0.04	< DL	< DL
14				100	13.42±0.11	7.49±0.05	0.044±0.001	< DL

14				150	19.51±0.15	11.68±0.06	0.167±0.003	< DL
14				20	3.51±0.95	1.51±0.04	< DL	< DL
14				150	16.17±0.13	9.51±0.05	0.112±0.002	< DL
15	800	0.020	0.8±0.2	20	29.75±0.37	19.54±0.12	2.078±0.017	0.0123±0.0009
16	800	0.016	2.0±0.2	20	25.90±0.14	16.83±0.06	0.884±0.005	< DL
16				100	35.80±0.15	22.92±0.07	2.989±0.010	0.0437±0.0010
16				150	38.12±0.15	24.68±0.07	3.718±0.011	0.0835±0.0012
16				20	23.72±0.14	14.89±0.05	0.676±0.005	< DL
17	800	0.016	1.2±0.2	20	28.94±0.14	18.79±0.07	1.474±0.007	< DL
17				100	38.90±0.15	25.58±0.07	4.045±0.011	0.1058±0.0014
17				150	44.14±0.15	28.88±0.08	5.914±0.013	0.3170±0.0023
17				20	29.18±0.14	18.79±0.06	1.743±0.007	< DL
18	800	0.016	2.0±0.2	22	5.81±0.44	2.29±0.06	< DL	< DL
18				100	14.82±0.11	7.39±0.05	0.020±0.001	< DL
18				150	22.14±0.13	12.44±0.06	0.165±0.002	< DL
18				20	5.41±0.53	1.88±0.04	< DL	< DL

Figure 6-9 is a cleaner presentation of the selectivity-permeance data shown in Figure 6-3. The performances of graphene membranes synthesized with different parameter sets are separated in different subplots. Some membranes are missing on the right column because their He/SF_6 selectivities are too high to be reliably estimated.

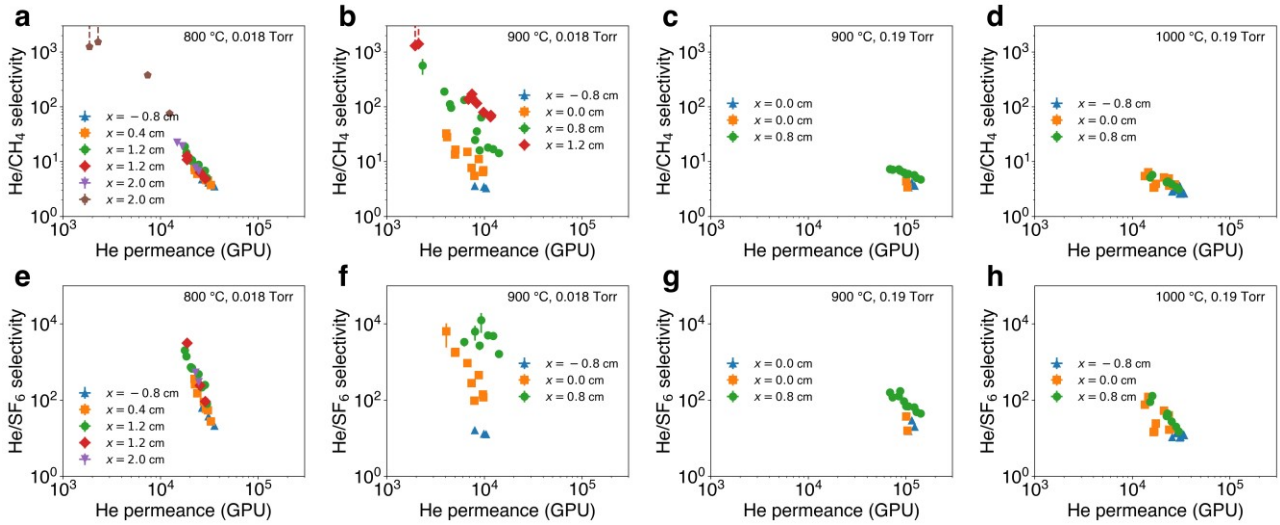

Figure 6-9. (a-d) He/CH_4 selectivities and He permeances of graphene membranes synthesized with four different CVD parameter sets, corresponding to Figure 6-3. (e-h) He/SF_6 selectivities and He permeances of graphene membranes synthesized with the four different CVD parameter sets. Note that *x* refers to the position of graphene relative to the heating zone center in the upstream direction.

The theoretical fitting of the gas permeation theory to the experimentally measured gas permeances was carried out as follows. As discussed Section 6.4, considering only the direct impingement permeance, the permeance per pore Π (pressure-difference-normalized gas permeation rate) of gas *i* (*i*

= He, CH_4, SF_6) through a circular graphene pore of effective diameter D_p at temperature T can be predicted as follows:

$$\Pi(D_p, i, T) = \frac{\pi D_p^2}{4} \cdot \frac{1}{\sqrt{2\pi m_i k_B T}} \cdot \left(1 - \frac{D_{m,i}}{D_p}\right)^{\alpha_i} \tag{6-11}$$

where m_i is the molecular weight of gas i, $D_{m,i}$ is the kinetic diameter of gas i, and k_B is the Boltzmann constant. The $\left(1 - D_{m,i}/D_p\right)^{\alpha_i}$ term describes the steric rejection effect due to the collision between gas i and the pore edges, and α_i is a gas i-dependent exponent. H_2 is not included because of the sometimes large uncertainty of the H_2 permeances. It is further assumed that the effective pore diameters in graphene membrane j follow a lognormal distribution. Note that the effective pore size is also a function of the measurement temperature due to the nanoscale fouling effect. Therefore, the pore size distribution function $f(D_p)$ should be parameterized by the membrane ID j and the measurement temperature T. Specifically,

$$f(D_p; j, T) = \frac{1}{D_p \sigma_{j,T} \sqrt{2\pi}} \exp\left[-\frac{\left(\ln D_p - \ln \mu_{j,T}\right)^2}{2\sigma_{j,T}^2}\right] \tag{6-12}$$

where $\mu_{j,T}$ and $\sigma_{j,T}$ are the two parameters for the lognormal distribution function, which are dependent on j and T. Subsequently, the total permeance of gas i through membrane j at temperature T can be predicted by combining Equations (6-11) and (6-12) as follows:

$$\widehat{K}_{i,j,T} = \rho_j \int_0^{+\infty} f(D_p; j, T)\, \Pi(D_p, i, T)\, \mathrm{d}D_p \tag{6-13}$$

where ρ_j is the areal pore density of membrane j. Finally, the predicted permeances $\widehat{K}_{i,j,T}$ are fitted to their corresponding experimentally measured permeances $K_{i,j,T}$ by minimizing the least squared relative error:

$$\left\{\alpha_i^*, \mu_{j,T}^*, \sigma_{j,T}^*, \rho_j^*\right\} = \underset{\{\alpha_i, \mu_{j,T}, \sigma_{j,T}, \rho_j\}}{\operatorname{argmin}} \sum_{i,j,T} \left(\frac{\widehat{K}_{i,j,T}}{K_{i,j,T}} - 1\right)^2 \tag{6-14}$$

This fitting provides an estimate for the pore size distribution and the pore density of each membrane, as well as the gas i-dependent α_i values. The least squared absolute error is not used because the He permeances are generally several orders or magnitude higher than the SF_6 permeances. As a result, the fitting would bias towards the He permeances if the absolute error was the minimization objective.

Before further simplifying the fitting problem, first consider if Equation (6-11) is a good approximation. In fact, even if I simply assume that $\alpha_i = 3$ for every gas i and that the pore size distribution in a graphene membrane is a delta function (uniform pore sizes), I can generate iso-pore-density trade-off curves that match the experimental results reasonably well (Figure 6-10a).

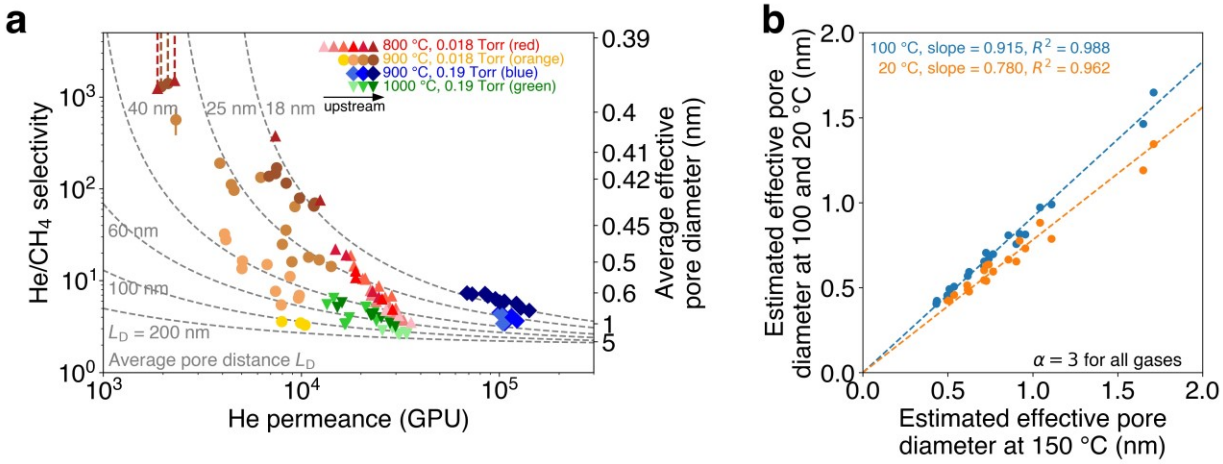

Figure 6-10. (a) He/CH_4 selectivities and He permeances of graphene membranes. Datapoints of the same color represent the same membrane under different experimental conditions (temperature, surface decoration, etc.). Dashed grey curves indicate the theoretically predicted selectivity-permeance trade-off trade-off curves. Right y axis presents the theoretically predicted average effective pore diameter that corresponds to the left y axis. The theoretical predictions were made assuming that $\alpha_i = 3$ for every gas i and that the pore size distributions are delta functions (uniform pore sizes). (b) Correlation between the effective pore diameter at 150 °C and that at 100 °C and 20 °C, sampled from all graphene membranes. The effective pore diameters are estimated assuming that $\alpha_i = 3$ for every gas i and that the pore size distributions are delta functions.

In order to minimize the risk of overfitting and reduce the amount of calculation, the number of unknown parameters can be further decreased as follows. Currently, each membrane j corresponds to seven unknowns: ρ_j (temperature independent), three $\mu_{j,T}$ values at T = 20, 100, and 150 °C, and three $\sigma_{j,T}$ values at T = 20, 100, and 150 °C. Denote J as the total number of membranes, which leads to a total of $7J$ unknows. Together with the three α_i's for the three gases (i = He, CH_4, SF_6), $7J$+3 unknowns need to be fit using $9J$ gas permeance datapoints (three gases and three temperatures for each membrane). Such large number of unknowns is not desirable.

The following physical intuition is used to reduce the number of unknowns. Note that the temperature effect on the effective pore sizes should be universal for every graphene membrane. Two

hypotheses can be proposed regarding how a graphene pore effectively shrinks in response to a decreasing temperature. The first hypothesis is that all the pores shrink by the same absolute amount:

$$D_{\mathrm{p}}(T) = D_{\mathrm{p}}(T_0) - g(T) \tag{6-15a}$$

The second hypothesis is that all the pores shrink by the same relative proportion:

$$D_{\mathrm{p}}(T) = D_{\mathrm{p}}(T_0)g(T) \tag{6-15a}$$

where $0 < g(T) < 1$. In order to determine which hypothesis is more plausible, one may fall into a circular logic. To find $g(T)$, one needs to know the pore size distributions at different temperatures $D_{\mathrm{p}}(T)$. To find the pore size distributions, one needs to solve the optimization problem in Equation (6-14). However, Equation (6-14) includes the expression of $g(T)$. To break the loop, I again assume that α_i = 3 for every gas i considered and that the pore size distributions in all the graphene membranes are delta functions. In this manner, I can estimate the effective pore diameters in all the membranes at 20, 100, and 150 °C. The correlations between the effective pore diameters at 150 °C and those at 100 °C and 20 °C are plotted in Figure 6-10b, where proportional correlations can be observed. The proportionality in Figure 6-10b supports the second hypothesis (Equation (6-15a)). As a result, the effect of temperature can be separated out from Equation (6-12), which is simplified as follows:

$$f\left(D_{\mathrm{p}}; j, T\right) = \frac{1}{D_{\mathrm{p}}\sigma_j\sqrt{2\pi}} \exp\left[-\frac{\left(\ln D_{\mathrm{p}} - \ln \mu_j g(T)\right)^2}{2\sigma_j^2}\right] \tag{6-16}$$

where μ_j and σ_j represent the pore size distribution of membrane j at T_0 = 150 °C, and g(20 °C) and g(100 °C) will be used to describe the universal temperature-induced pore size change. Note that scaling the lognormal pore size distribution function along the x axis only scales μ_j accordingly, and σ_j remains the same.

After this simplification, the number of unknowns is reduced to $3J$+5 (ρ_j, μ_j, and σ_j for each membrane, three α_i's, g(20 °C), and g(100 °C)). The fitting problem can be further simplified by noting that the non-covalent decoration of the graphene membranes by pyrene-based molecules is similar to a temperature decrease in terms of its effect on the effective pore size. Therefore, ρ_j and σ_j are assumed to remain constant after the non-covalent decoration. For accuracy, gas permeances with high error and

those below the detection limit are excluded. Furthermore, only membranes that were tested at multiple temperatures are included to enhance the fitting reliability.

The fitting results are summarized in Table 6-2. Note that the mean pore diameter of a lognormal distribution is not μ, but $\mu\exp(\sigma^2/2)$. Due to the large number of unknown parameters, the optimization of the objective function in Equation (6-14) is extremely difficult. Pattern search by Matlab was carried out to avoid shallow local minima. The objective function is not sensitive to parameters fitted with wider confidence intervals. The following fitted parameters yield a relative prediction error of 14% on average. Further optimization is possible, but the objective function landscape is flat near the optimization point and significant improvement in the fitting is not expected.

Table 6-2. Fitted parameters and their 90% confidence intervals.

α(He)	2.0±1.7	g(20 °C)	0.77±0.06
α(CH_4)	2.8±2.0	g(100 °C)	0.91±0.03
α(SF_6)	3.2±2.6		
Membrane ID	ρ (10^3 μm^{-2})	μ (nm)	σ
1/PBA	0.68±1.74	1.00±1.43	0.33±0.70
3	2.67±4.67	0.64±0.46	0.35±0.21
3/AP	2.67±4.67	0.60±0.44	0.35±0.21
4	0.22±2.95	0.21±2.19	1.00±2.22
5	0.27±0.39	0.65±0.35	0.18±0.09
5/PBA	0.27±0.39	0.56±0.29	0.18±0.09
6	1.28±1.89	0.47±0.19	0.14±0.08
6/AP	1.28±1.89	0.40±0.15	0.14±0.08
8/AP	0.21±0.38	0.90±0.70	0.18±0.28
9	0.15±0.29	1.25±1.10	0.0±15
9/AP	0.15±0.29	1.07±0.92	0.0±15
10	0.72±1.01	0.70±0.38	0.16±0.08
10/AP	0.72±1.01	0.64±0.33	0.16±0.08
11	0.29±0.49	0.99±0.74	0.0±2.8
11/AP	0.29±0.49	0.93±0.68	0.0±2.8
12	0.22±0.43	1.07±1.01	0.17±0.55
14	3.75±8.50	0.35±0.17	0.19±0.14
16	0.79±1.17	0.63±0.33	0.14±0.12
17	0.47±0.62	0.79±0.42	0.01±0.92
18	1.33±1.76	0.43±0.13	0.06±0.11

The slope of the iso-pore-density trade-off curve of selectivity-permeance trade-off in Figure 6-3 in can be derived analytically, based on Equation (6-1). Consider two gases, gas 1 and gas 2, where gas

1 is the more permeable species. The selectivity between the two gases S_{12} can be expressed as a function of pore diameter D_p as follows:

$$S_{12} = \frac{K_1}{K_2} = \left(1 - \frac{D_{m,1}}{D_p}\right)^{\alpha_1} \left(1 - \frac{D_{m,2}}{D_p}\right)^{-\alpha_2} \sqrt{\frac{m_2}{m_1}} \tag{6-17}$$

Therefore, the slope β of the iso-pore-density trade-off curve in a log-log scale is:

$$= \frac{\mathrm{d}\ln S_{12}}{\mathrm{d}\ln K_1} = \left(\frac{\mathrm{d}\ln S_{12}}{\mathrm{dD_p}}\right)\left(\frac{\mathrm{d}\ln K_1}{\mathrm{dD_p}}\right)^{-1}$$

$$= \frac{\alpha_1 \left(1 - \frac{D_{m,1}}{D_p}\right)^{-1} \frac{D_{m,1}}{D_p^2} - \alpha_2 \left(1 - \frac{D_{m,2}}{D_p}\right)^{-1} \frac{D_{m,2}}{D_p^2}}{\alpha_1 \left(1 - \frac{D_{m,1}}{D_p}\right)^{-1} \frac{D_{m,1}}{D_p^2} + \frac{2}{D_p}} \tag{6-18}$$

$$= -\frac{\alpha_2 \frac{D_{m,2}}{D_p - D_{m,2}} - \alpha_1 \frac{D_{m,1}}{D_p - D_{m,1}}}{2 + \alpha_1 \frac{D_{m,1}}{D_p - D_{m,1}}} = -\frac{\frac{\alpha_2 D_{m,2}}{\alpha_1 D_{m,1}} \frac{D_p - D_{m,1}}{D_p - D_{m,2}} - 1}{\frac{2}{\alpha_1} \frac{D_p - D_{m,1}}{D_{m,1}} + 1}$$

6.8.4 Iso-Pore-Density Trade-off Curves of Graphene Membranes Reported in the Literature

For other graphene membranes reported in the literature, Equation (6-1) may not be a good approximation because of potentially different laboratory environments and membrane fabrication processes. Certain graphene membranes in the literature exhibit increasing H_2/CH_4 selectivities with temperature,[120,122,128] which contradicts Equation (6-1). Equation (6-1) predicts that the H_2/CH_4 selectivity decreases as a function of temperature because of the effective pore size expansion. To resolve this contradiction, it can be assumed that the surface diffusion pathway dominates the gas permeation through those graphene membranes, which is expressed as follows:[7]

$$K_i \propto \exp\left(-\frac{\Delta H_{ads,i}}{k_B T}\right) \tag{6-19}$$

where the permeance of gas i is related to its heat of adsorption on graphene $\Delta H_{ads,i} < 0$. Because the iso-pore-density trade-off curve is also temperature dependent, the gas permeances measured at different temperatures need to be corrected back to the same temperature (30 °C) using Equation (6-19) for a meaningful comparison. The heats of adsorption of H_2 and CH_4 on graphene are −4 kJ mol^{-1} and

−13 kJ mol^{-1}, respectively, according to ref. 120. Figure 6-11 presents the iso-pore-density trade-off curves of the graphene membranes reported by Huang *et al.*,[120] Zhao *et al.*,[122] Khan *et al.*,[128] and He *et al.*[118] after the temperature correction. Generally, the slope of the curve is steeper when the H_2/CH_4 is higher, consistent with my observation in the main text.

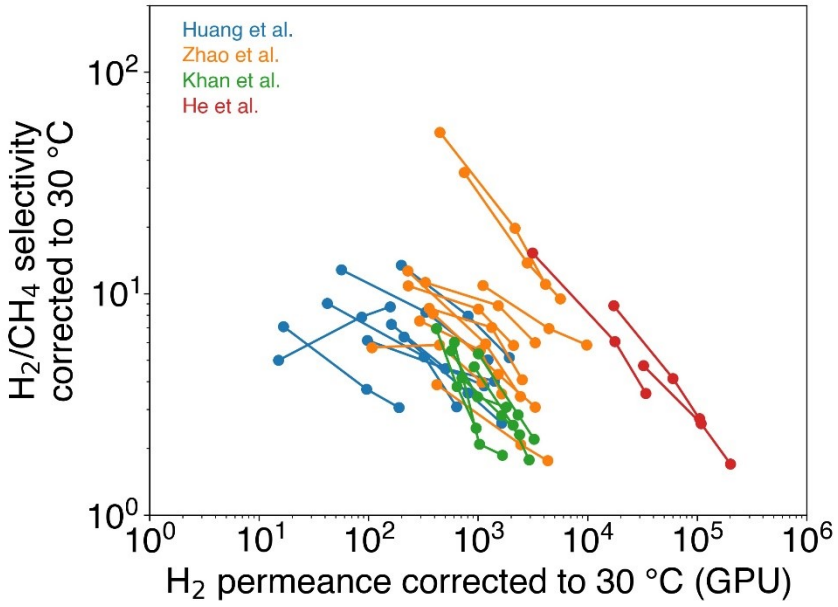

Figure 6-11. Iso-pore-density trade-off curves of graphene membranes reported by Huang *et al.*,[120] Zhao *et al.*,[122] Khan *et al.*,[128] and He *et al.*[118] Gas permeances are corrected to 30 °C according to Equation (6-19). Each curve represents an individual membrane.

To rationalize Equation (6-19), note that the H_2 permeances reported in the studies referenced above typically increase by 1000% from room temperature to 150 °C, much higher than ~ 150% value reported in this chapter. This suggests that the graphene membranes in this chapter are heavily contaminated, such that a higher temperature cannot significantly alleviate the pore blocking, as only one to few layers of contaminant molecules are enough to partially block the nanometer-sized pores. In contrast, the less contaminated graphene membranes in the literature are more sensitive to the thermal desorption of the contaminants. Further, the surface diffusion pathway of gas permeation is more likely to be dominant when the graphene surface is less contaminated (Section 3.7).

6.8.5 Comparison with Other Membranes Reported in the Literature

Table 6-3. H_2/CH_4 separation performances of other membranes reported in the literature.

Material	H_2 permeance (10^3 GPU)	H_2/CH_4 selectivity	Reference
Graphene			
Single-layer graphene perforated by oxidative etching	6.05	15.6	[122]
	3.07	29.0	
	3.40	25.1	
	10.83	7.5	
Single-layer graphene treated by O_3	1.33	17	[120]
	0.62	20	
Double-layer graphene perforated by ion irradiation and O_2 etching	3.4	9.2	[116]
	4.1	8.7	
	9.0	5.3	
	28.0	8.9	
	42.8	8.9	
	26.8	5.2	
	27.4	5.8	
	69.5	6.1	
	57.9	6.0	
	40.2	6.3	
	310	4.4	
	523	4.5	
	788	4.1	
	1446	4.4	
	1844	4.5	
	2399	4.8	
	2878	4.3	
	4227	4.2	
	11633	4.6	
Zeolite			
AlPO-18	0.30	22	[285]
FAU	0.57	9.9	[261]
SSZ-13	0.63	22	[264]
DDR	0.27	75	[14]
LTA	0.48	19.3	[263]
CHA	2.69	26.5	[262]
	4.48	42.9	
	4.78	32.0	
	6.27	38.1	
	6.87	25.0	
Metal-organic framework (MOF)			
ZIF-8/GO	0.38	139	[270]
ZIF-90	0.74	15.3	[269]
$Cu_3(BTC)_2$	5.83	5.9	[271]
ZIF-67	0.46	41.9	[268]
JCU-150	0.53	26.3	[267]
NH_2-MIL-53(Al)	4.47	20.7	[266]
Graphene oxide (GO)			
GO/AAO	0.309	117	[222]
GO-thiourea	0.589	66.7	[272]

Carbon molecular sieve (CMS)		
0.167	726	[275]
0.548	35	[274]
0.35	160	[273]
0.324	435	[276]
0.354	432	
0.381	156	
0.446	36.6	
Silica		
5.97	533	[17]
4.78	43	[281]
0.56	88	[282]
1.38	11.5	[280]
1.29	18.8	
0.93	19.5	
0.81	23.7	
1.61	480	[279]
0.36	2800	[259]
0.75	940	[278]
1.13	3700	[277]

Figure 6-12 reports the selectivity-permeance Robeson plot corresponding to the H_2/CH_4 separation. Different from Figure 6-4, the gas permeances here were calculated based on the full area of the 100×100 hole array, including the pitch of 30 μm, giving a total area of 9 mm^2. This would decrease the previously calculated gas permeances by 65 times.

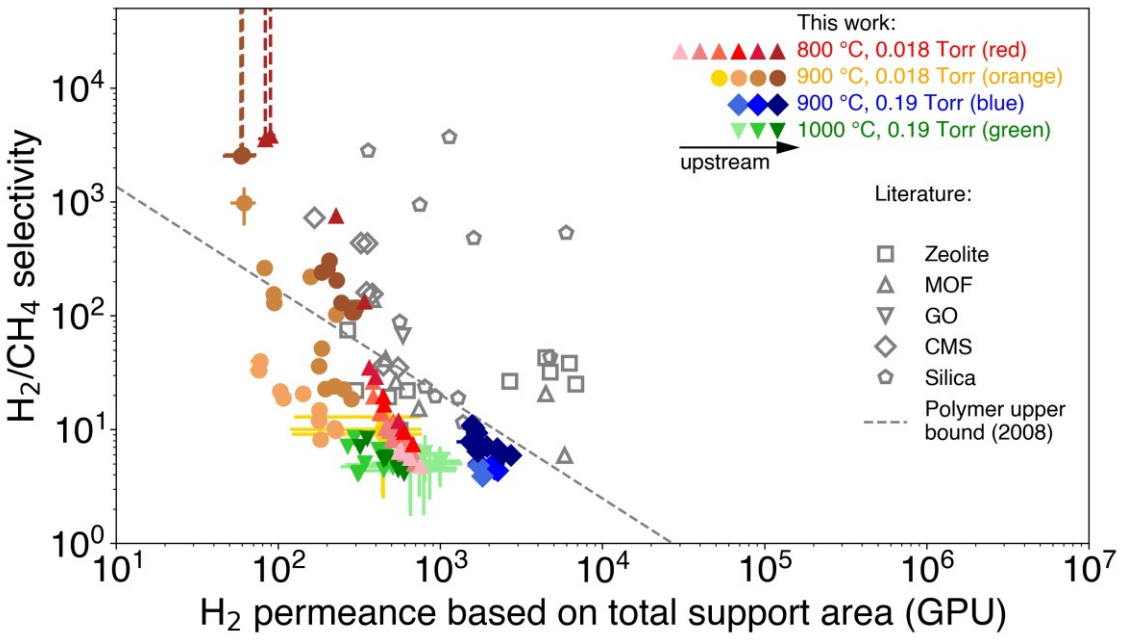

Figure 6-12. Selectivity-permeance Robeson plot corresponding to the H_2/CH_4 separation. Permeances are calculated based on the full area of the 100×100 hole array, including the pitch of 30 μm. Results of

this study are plotted as solid markers. Datapoints with long dashed error bar upwards indicate the lower bound of H_2/CH_4 selectivities, because CH_4 signals were below the detection limit. Performances of other state-of-the-art membranes in the literature are plotted as hollowed markers, including zeolites,[260–265] metal-organic frameworks (MOF),[266–271] graphene oxide (GO),[167,272] carbon molecular sieves (CMS),[273–276] silica,[259,17,277–282] and Robeson upper bound for polymers assuming 1 μm thickness.[11]

Similar to Figure 6-4, the He/CH_4 separation performances of the graphene membranes are compared with other membranes in the literature as well as with the Robeson polymer upper bound in Figure 6-13 (references provided in Table 6-4).

Table 6-4. He/CH_4 separation performances of other membranes reported in the literature.

Material	He permeance (10^3 GPU)	He/CH_4 selectivity	Reference
Ni doped silica	3.47	600	[286]
Silica	2.93	147	[287]
Silica	0.090	5000	[288]
Isoreticular Metal-Organic framework	2.99	1.6	[289]
IRMOF-3 and -6	2.39	1.3	[289]
$[Cu_2(bza)_4(pyz)]_n$	0.008	7.3	[290]
Cu-BTC	4.18	2.1	[291]

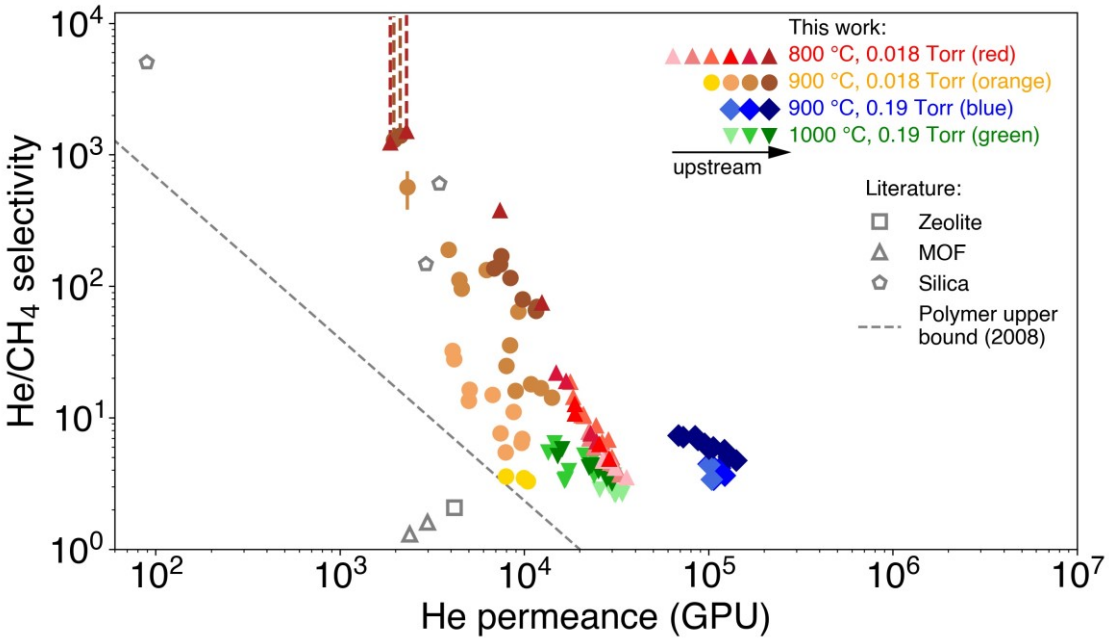

Figure 6-13. Selectivity-permeance Robeson plot of He/CH_4 separation. Results in this chapter are plotted as solid circles. Performances of other state-of-the-art membranes reported in the literature are plotted in hollowed markers, with their references provided in Table 6-4. The Robeson upper bound for polymers is plotted assuming 1 μm membrane thickness.

6.8.6 Experimental Details

Figure 6-14 shows that the thickness of the porous carbon scaffold is ~ 200 nm.

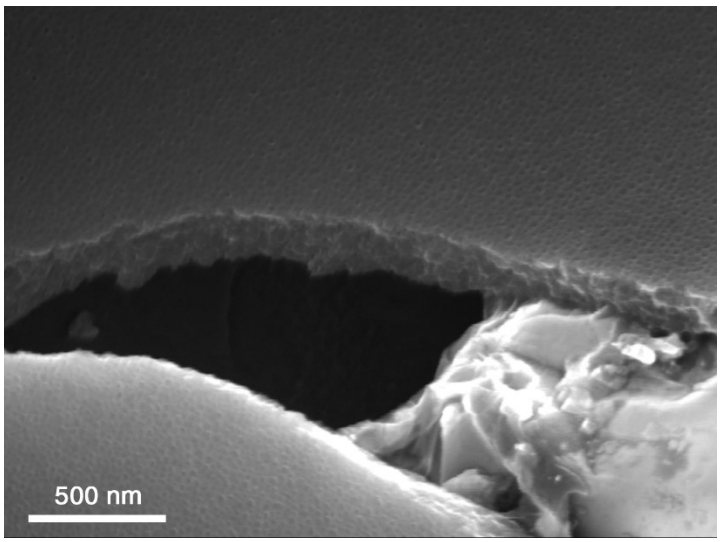

Figure 6-14. SEM image of the cross section of the porous carbon scaffold.

Figure 6-15 shows a schematic diagram of the chemical vapor deposition setup. Figure 6-16 shows the schematic diagram and photograph of the gas permeation module.

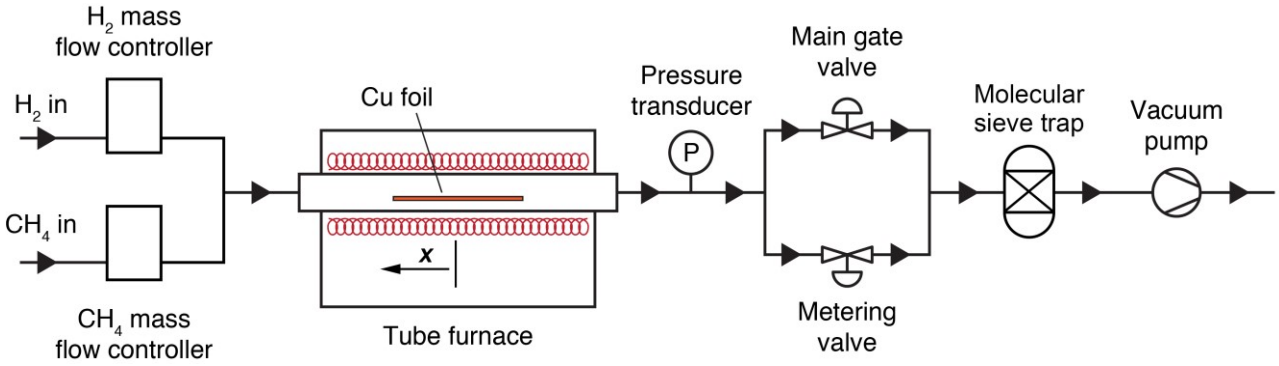

Figure 6-15. Diagram of the chemical vapor deposition setup for graphene synthesis. The *x* axis indicates the relative upstream position to the heating zone center.

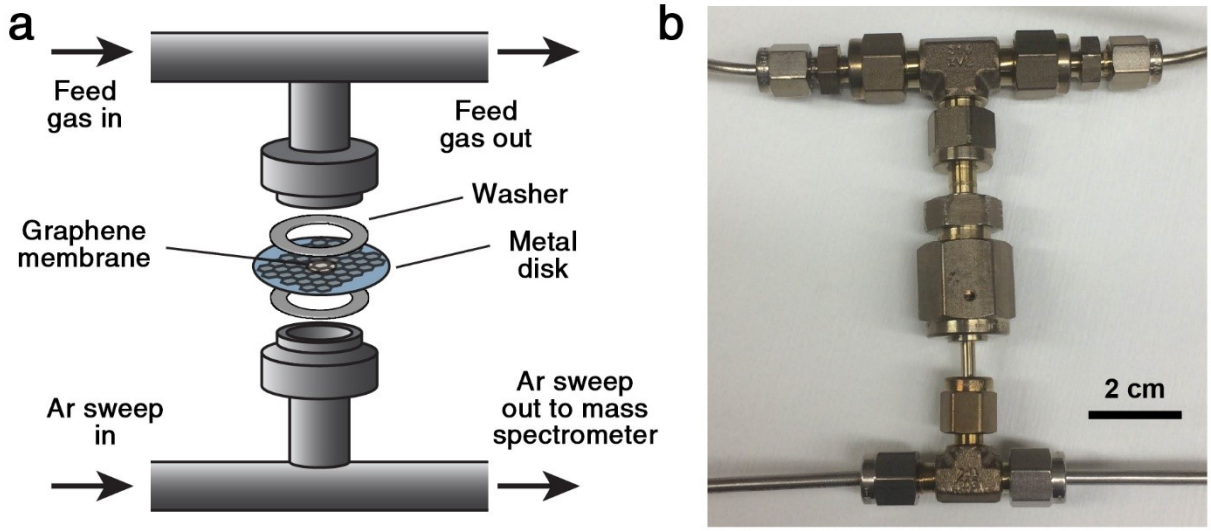

Figure 6-16. (a) Diagram and (b) photograph of the gas permeation module. Two stainless steel washers were inserted between the metal disk and the Swagelok VCR fitting to prevent the deformation of the metal disk.

Figure 6-17a, b presents the calibration curves used in this chapter to transform the mass spectrometer signals to the molar fractions of the gases (data collected by Dr. Guangwei He). The calibration curves report the correlation between the mole fraction of gas component *i* in a gas stream x_i and its corresponding fraction in the total mass spectrometer signal y_i. Each gas *i* has its own linear calibration curve, $y_i = C_i x_i$. When performing gas permeation testing through a graphene membrane, the real time mass spectrometer signal of gas *i*, $S_i(t)$, is transformed into its molar fraction $x_i(t)$ in the gas stream entering the mass spectrometer as follows:

$$x_i(t) = \frac{y_i(t)}{C_i} = \frac{1}{C_i}\frac{S_i(t)}{\sum_i S_i(t)} \tag{6-20}$$

The permeated gas through the graphene membrane was carried by 4 sccm Ar into the mass spectrometer. Because the flow rate of the permeated gas is < 2% of the Ar flow rate ($\sum_i x_i(t) < 0.02$), it can be approximated that the total flow rate of Ar and the permeated gas is ~ 4 sccm, and that the flow rate of gas *i* is $4x_i(t)$ sccm. The flow rate is further divided by the pressure driving force and the membrane area to obtain the gas permeance.

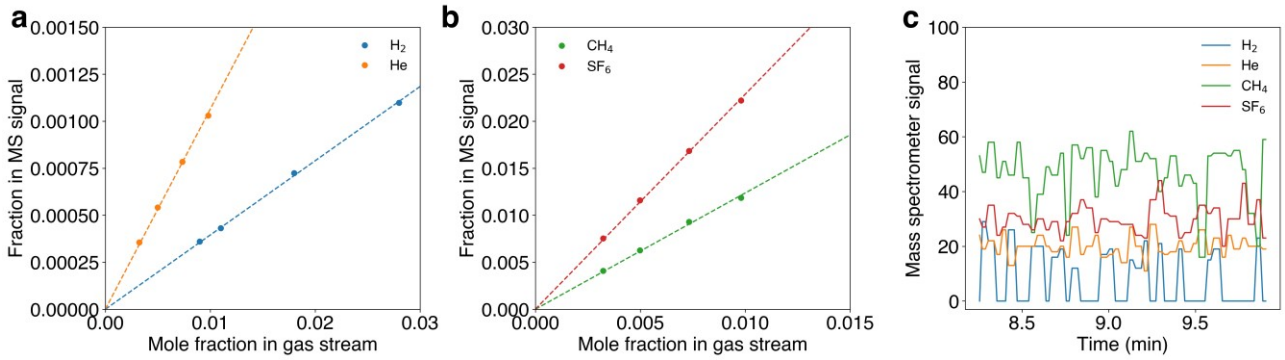

Figure 6-17. (a) Calibration curves of the mass spectrometer (MS) for H_2 and He. (b) Calibration curves of the MS for CH_4 and SF_6. (c) Real time MS signal of H_2, He, CH_4, and SF_6 from a graphene membrane (membrane ID = 7). The H_2 signal has a cutoff of ~10.

Note that the threshold signal for H_2 detection is high (Figure 6-17c). Any H_2 signal below ~10 will be cut off and show zero as the output signal. As a result, my estimations of H_2 permeances sometimes have very high uncertainty. In contrast, the signals of He, CH_4, and SF_6 have no such cutoff, and the lowest observable time-average signal is 1, corresponding to gas permeances of 75 GPU, 10 GPU, and 3 GPU for He, CH_4, and SF_6, respectively. These permeance values are the detection limits of my experimental setup. The detection limit can be further reduced by feeding pure gas instead of mixture gas. After switching the feed gas from a gas mixture containing 1/6 CH_4 (molar basis) to a pure CH_4 stream, the detection limit of CH_4 permeance is further reduced to 1.7 GPU. These detection limits allow me to calculate the selectivity lower bound of some highly selective membranes. For example, the membrane with ID = 18 exhibits H_2 permeance of 5.81×10^3 GPU, but no observable CH_4 permeance (< 1.7 GPU) at 20 °C. Therefore, the H_2/CH_4 selectivity is at least 3.48×10^3.

Figure 6-18 shows the real time mass spectrometer signal from membrane ID = 16. The feed gas was switched from a gas mixture containing 1/6 CH_4 (molar basis) to a pure CH_4 flow. Upon the switch, the CH_4 signal increased by six-fold, while the signals of other gases decreased to zero. Therefore, the permeance of a gas in a pure stream and that in a mixture are almost the same, indicating that competitive gas transport is negligible.

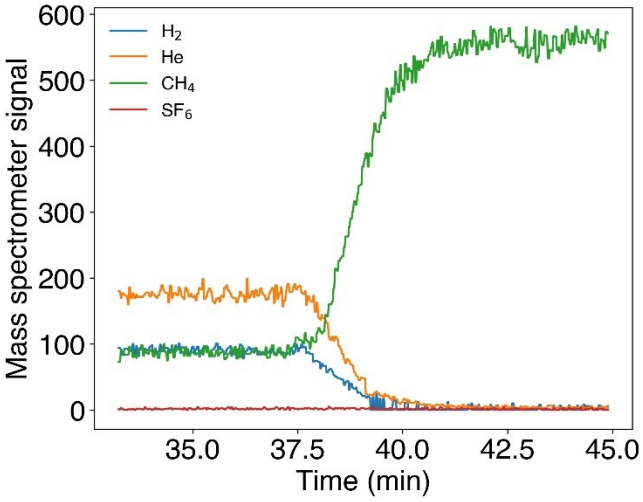

Figure 6-18. Real time mass spectrometer signal from membrane ID = 16. At 37 min, the feed gas was switched from a gas mixture (molar fraction of CH_4 = 1/6) to a pure CH_4 flow. The CH_4 signal increased by six-fold as a result.

7 Conclusions and Outlook

7.1 Thesis Summary

This thesis focuses on studying the implementation of nanoporous single-layer graphene membranes for gas separation, both theoretically and experimentally. Theoretically, this thesis (Chapters 2–4) aims at predicting gas permeances through a nanoporous single-layer membrane. This aim has been accomplished step-by-step, beginning with a simple case (an individual nanopore) and ending with a more complicated and realistic case (a pore ensemble having a pore size distribution). Experimentally, this thesis (Chapters 5 and 6) aims at fabricating nanoporous, single-layer graphene membranes, including improving their gas permeances and gas separation performances. To obtain high gas separation performances, the pore formation mechanism in graphene, as well as various strategies to control the pore density and the pore size, have been investigated. Furthermore, matching the theoretical predictions with the experimental results is an important goal of this thesis (Chapters 4–6), which leads to fundamental insights into the gas permeation mechanisms through graphene nanopores. Below, I summarize the various chapters comprising this thesis.

In Chapter 1, I introduced the basic concepts of membrane separation, gas permeance, and selectivity. I highlighted the enormous potential of nanoporous single-layer graphene membranes for high-performance gas separation due to their atomic thickness. I reviewed the research progress made in gas-selective nanoporous single-layer graphene membranes, including discussing several some remaining theoretical and experimental challenges.

In Chapter 2, I investigated the mechanism of activated gas permeation through sub-nanometer graphene pores. Using molecular dynamics simulations, I showed that the gas permeation through sub-nanometer graphene pores could be decoupled into two processes: (i) the adsorption to the pore mouth and (ii) the translocation through the pore. Transition state theory was used to predict the translocation rate and showed good agreement with the molecular dynamics simulations. Based on the transition state theory, I developed efficient algorithms to predict the gas permeance per pore through many graphene nanopores. By comparing the performance predicted for nanoporous graphene with those reported for

other membrane materials, I confirmed the high promise of graphene membranes for gas separation, if the areal pore density is sufficiently high.

In Chapter 3, I extended the theoretical framework developed in Chapter 2 from the activated regime to other non-activated regimes in order to accommodate larger pore sizes. Specifically, I derived analytical equations that model the gas transport rates associated with the direct impingement and the surface diffusion pathways, and further validated and refined these equations using molecular dynamics simulations. In addition, I integrated the refined equations using the translocation rate (studied in Chapter 2) to predict the overall gas permeation rate per pore. I showed that the gas permeation through a graphene pore begins from the activated regime, followed by a surface-pathway-dominated regime, and finally by a direct-pathway-dominated regime, as the pore diameter increases.

In Chapter 4, my theoretical prediction of gas permeation was further extended from a single graphene nanopore to a nanopore ensemble having a realistic pore size distribution. I generated nanopore ensembles *in silico* by etching carbon atoms away from pristine graphene using a Kinetic Monte Carlo algorithm. The total permeances of H_2, CO_2, and CH_4 through the nanopore ensembles were predicted using the equations developed in Chapters 2 and 3. I showed that a small fraction of large pores could contribute the majority of the total gas permeance through a nanopore ensemble, thereby highlighting the importance of considering the pore size distribution. I fitted the theoretical predictions to experimental results reported in the literature, and found that graphene nanopores effectively expand at a higher temperature under the experimental conditions used. I hypothesized that the graphene nanopores were partially clogged by airborne hydrocarbon contaminants, and that the contaminants would desorb at higher temperatures.

In Chapter 5, I reported the gas separation performances of five nanoporous single-layer graphene membranes that I fabricated using chemical vapor deposition. The graphene membranes were intrinsically porous after the chemical vapor deposition synthesis. For the first time, I measured gas mixture separation through suspended nanoporous single-layer graphene membranes. Further, for the first time, I measured the temperature dependence of the gas permeances. Membrane A and A' exhibited gas selectivities higher than the Knudsen selectivities. I fitted the permeance data using the steric selectivity mechanism and obtained a monodisperse pore size distribution that peaked at a diameter of

2.5 nm. Membrane B exhibited selectivities lower than the Knudsen selectivities, suggesting a combination of effusion and collective gas flow. Membrane C displayed a much higher selectivity than the Knudsen selectivities, and Membrane D displayed extremely low permeances at, or below, the detection limit.

In Chapter 6, I investigated the formation mechanism of intrinsic graphene pores during graphene synthesis. The intrinsic pores were formed due to the random insertion of catalytic Cu atoms into the growth front of graphene. This mechanism allowed me to decouple pore nucleation and pore growth and to overcome the challenging trade-off between a high pore density and a high selectivity. I systematically controlled the pore density and the pore sizes in the graphene membranes and obtained record-high H_2/CH_4 separation performances to date: H_2/CH_4 selectivity > 2000 while the H_2 permeance > 4000 GPU, or H_2/CH_4 selectivity > 100 while the H_2 permeance > 10^4 GPU. Furthermore, I identified the importance of nanoscale fouling on gas separation, where the graphene pores are partially blocked by airborne hydrocarbon contaminants.

7.2 Outlook

Along with the progress reported in this thesis, much progress has been made to advance gas separation using nanoporous single-layer graphene membranes. On the theory and simulation sides, the mechanism of gas permeation through nanometer-scale pores in graphene membranes has been investigated in depth. Novel design ideas of graphene pores that enhance gas separation have been proposed based on simulations, including edge functionalization,[292] asymmetrical pores,[87,90] and continuously tunable pore size by strain or by the overlapping of two pores.[62,84,104] Pore nucleation and pore expansion processes have also been gaining increasing attention. On the experimental side, gas perforation methods have significantly matured. Graphene membranes with areal pore densities exceeding 10^{16} m^{-2} (average pore distance < 10 nm) have been fabricated. Further, the gas permeances and selectivities have been greatly improved. Because of the advances made in the production of functional supporting layers, the areas of graphene membranes have been scaled up to centimeter scale.[125] The combination of experimental measurements and theoretical predictions have shed light on the mechanism of gas transport through confined spaces at a microscopic scale.

In spite of the great progress made as discussed above, additional theoretical and experimental advances are required for graphene membranes to become practically competitive. Below, I discuss four promising and important topics that, if resolved, will facilitate the use of graphene membranes (or other atomically thin 2D materials) for gas separation.

(i) The wide and right-skewed pore size distribution (PSD) resulting from oxidative etching has become a major hurdle that constrains the gas selectivity of graphene membranes. Improved methods are needed to narrow down the PSD in order to better separate some difficult yet important gas pair like O_2/N_2. Theoretical investigations of the pore nucleation and pore expansion processes associated with different perforation methods would allow the research community to formulate more advanced strategies to generate narrower and more controllable PSDs.

(ii) Hydrocarbon adsorbates on the graphene surface (usually airborne hydrocarbon contaminants) were shown to significantly affect gas transport through graphene nanopores. However, more investigations are needed to understand the composition of the adsorbates, the number of layers of the adsorbates and their spatial distribution with respect to the nanopore, and the mechanism of partial pore blocking at the molecular level. Methods of removing the adsorbates are of high research interest, but from an application perspective, it would be difficult to eliminate airborne hydrocarbons from the feed gas stream and the separation module. Therefore, understanding the behavior of the hydrocarbon adsorbates is important to exploit this phenomenon to our advantage.

(iii) For practical applications, the areas of single-layer graphene membranes need to be further scaled up, while maintaining, or even improving, their quality and uniformity. This requires additional development of the functional supporting layers and the membrane fabrication process. For large-scale applications, membrane packing and module design adapted for graphene membranes are critical. Because of the potentially high gas permeance through graphene membranes, creating compact membrane systems for laboratory or medical use (*e.g.*, to separate O_2 from other gases) may be a more realistic goal.

(iv) It will be exciting to couple the selective gas permeation through nanoporous graphene (or other 2D materials) with other applications, including catalytic membrane reactors,[293] sensing,[294] or

electrochemical systems involving gases.[295] The confined spaces created by the atomically thin nanopores may allow selective interfacial chemical reactions with controlled stereochemistry.

In summary, the development of gas selective single-layer graphene membranes in recent years has been inspiring. We have witnessed graphene membranes growing out of infancy and becoming promising next-generation gas separation membranes. However, in spite of their tremendous potential, practically, graphene membranes still face significant challenges associated with gas separation performance and robustness, which future theoretical, simulation, and experimental research need to address.

References

1. Sholl, D. S. & Lively, R. P. Seven chemical separations to change the world. *Nature* **532**, 435–437 (2016).
2. Angelini, P. *et al.* Materials for Spearation Technologies: Energy and Emission Reduction Opportunites. *DOE EERE Off. Wash. DC* 103 (2005).
3. Humphrey, J. L. *Separation process technology*. (McGraw-Hill (Canada), 1997).
4. Lively, R. P. & Sholl, D. S. From water to organics in membrane separations. *Nat. Mater.* **16**, 276–279 (2017).
5. Baker, R. W. Future Directions of Membrane Gas Separation Technology. *Ind. Eng. Chem. Res.* **41**, 1393–1411 (2002).
6. Baker, R. W. *Membrane technology and applications*. (John Wiley & Sons Ltd, 2004).
7. Baker, R. W. & Lokhandwala, K. Natural Gas Processing with Membranes: An Overview. *Ind. Eng. Chem. Res.* **47**, 2109–2121 (2008).
8. Freemantle, M. Membranes for gas separation. *Chem Eng News* **83**, 3 (2005).
9. Koros, W. J. & Zhang, C. Materials for next-generation molecularly selective synthetic membranes. *Nat. Mater.* **16**, 289–297 (2017).
10. Robeson, L. M. Correlation of separation factor versus permeability for polymeric membranes. *J. Membr. Sci.* **62**, 165–185 (1991).
11. Robeson, L. M. The upper bound revisited. *J. Membr. Sci.* **320**, 390–400 (2008).
12. Freeman, B. D. Basis of Permeability/Selectivity Tradeoff Relations in Polymeric Gas Separation Membranes. *Macromolecules* **32**, 375–380 (1999).
13. Van den Bergh, J., Zhu, W., Gascon, J., Moulijn, J. & Kapteijn, F. Separation and permeation characteristics of a DD3R zeolite membrane. *J. Membr. Sci.* **316**, 35–45 (2008).
14. Himeno, S. *et al.* Synthesis and Permeation Properties of a DDR-Type Zeolite Membrane for Separation of CO2/CH4 Gaseous Mixtures. *Ind. Eng. Chem. Res.* **46**, 6989–6997 (2007).
15. Xie, Z., Li, T., L. Rosi, N. & A. Carreon, M. Alumina-supported cobalt–adeninate MOF membranes for CO 2 /CH 4 separation. *J. Mater. Chem. A* **2**, 1239–1241 (2014).
16. Bohrman, J. A. & Carreon, M. A. Synthesis and CO 2/CH 4 separation performance of Bio-MOF-1 membranes. *Chem. Commun.* **48**, 5130–5132 (2012).
17. Vos, R. M. de & Verweij, H. High-Selectivity, High-Flux Silica Membranes for Gas Separation. *Science* **279**, 1710–1711 (1998).
18. Jones, C. W. & Koros, W. J. Carbon molecular sieve gas separation membranes-I. Preparation and characterization based on polyimide precursors. *Carbon* **32**, 1419–1425 (1994).
19. Richter, H. *et al.* High-Flux Carbon Molecular Sieve Membranes for Gas Separation. *Angew. Chem. Int. Ed.* **56**, 7760–7763 (2017).
20. Ma, X. *et al.* Carbon molecular sieve gas separation membranes based on an intrinsically microporous polyimide precursor. *Carbon* **62**, 88–96 (2013).
21. Husain, S. & Koros, W. J. Mixed matrix hollow fiber membranes made with modified HSSZ-13 zeolite in polyetherimide polymer matrix for gas separation. *J. Membr. Sci.* **288**, 195–207 (2007).
22. Chung, T.-S., Jiang, L. Y., Li, Y. & Kulprathipanja, S. Mixed matrix membranes (MMMs) comprising organic polymers with dispersed inorganic fillers for gas separation. *Prog. Polym. Sci.* **32**, 483–507 (2007).
23. Huang, L., Zhang, M., Li, C. & Shi, G. Graphene-Based Membranes for Molecular Separation. *J. Phys. Chem. Lett.* **6**, 2806–2815 (2015).
24. Yoo, B. M., Shin, J. E., Lee, H. D. & Park, H. B. Graphene and graphene oxide membranes for gas separation applications. *Curr. Opin. Chem. Eng.* **16**, 39–47 (2017).
25. Jiang, D., Cooper, V. R. & Dai, S. Porous Graphene as the Ultimate Membrane for Gas Separation. *Nano Lett.* **9**, 4019–4024 (2009).
26. Wang, L. *et al.* Fundamental transport mechanisms, fabrication and potential applications of nanoporous atomically thin membranes. *Nat. Nanotechnol.* **12**, 509–522 (2017).

27. Moghadam, F. & Park, H. B. Two-dimensional materials: an emerging platform for gas separation membranes. *Curr. Opin. Chem. Eng.* **20**, 28–38 (2018).
28. Frank, I., Tanenbaum, D. M., Van der Zande, A. & McEuen, P. L. Mechanical properties of suspended graphene sheets. *J. Vac. Sci. Technol. B* **25**, 2558–2561 (2007).
29. Geim, A. K. Graphene: Status and Prospects. *Science* **324**, 1530–1534 (2009).
30. Feng, J. *et al.* Single-layer MoS 2 nanopores as nanopower generators. *Nature* **536**, 197–200 (2016).
31. Bunch, J. S. *et al.* Impermeable Atomic Membranes from Graphene Sheets. *Nano Lett.* **8**, 2458–2462 (2008).
32. Berry, V. Impermeability of graphene and its applications. *Carbon* **62**, 1–10 (2013).
33. Sun, P. Z. *et al.* Limits on gas impermeability of graphene. *Nature* **579**, 229–232 (2020).
34. Wijmans, J. & Baker, R. The solution-diffusion model: a review. *J. Membr. Sci.* **107**, 1–21 (1995).
35. Rajan, A. G. *et al.* Addressing the isomer cataloguing problem for nanopores in two-dimensional materials. *Nat. Mater.* **18**, 129–135 (2019).
36. Ismail, A. F., Khulbe, K. & Matsuura, T. *Gas Separation Membranes: Polymeric and Inorganic*. (Springer International Publishing, 2015). doi:10.1007/978-3-319-01095-3.
37. Jennings, S. The mean free path in air. *J. Aerosol Sci.* **19**, 159–166 (1988).
38. Sampson, R. A. On Stokes's Current Function. *Philos. Trans. R. Soc. Lond. A* **182**, 449–518 (1891).
39. Tio, K.-K. & Sadhal, S. S. Boundary conditions for stokes flows near a porous membrane. *Appl. Sci. Res.* **52**, 1–20 (1994).
40. Jensen, K. H., Valente, A. X. & Stone, H. A. Flow rate through microfilters: influence of the pore size distribution, hydrodynamic interactions, wall slip, and inertia. *Phys. Fluids 1994-Present* **26**, 052004 (2014).
41. Atkins, P. & De Paula, J. *Atkins' physical chemistry (8th ed)*. (Oxford University Press, 2006).
42. Laidler, K. J. & Meiser, J. H. *Physical Chemistry*. (Benjamin/Cummings Pub. Co, 1982).
43. Schrier, J. Fluorinated and Nanoporous Graphene Materials As Sorbents for Gas Separations. *ACS Appl. Mater. Interfaces* **3**, 4451–4458 (2011).
44. Trinh, T. T., Vlugt, T. J. H., Hägg, M. B., Bedeaux, D. & Kjelstrup, S. H. Simulating CO2 adsorption and diffusion on a graphite surface. in *12th Joint European Thermodynamics Conference* (Cartolibreria Snoopy, 2013).
45. Jin, Y., Lee, D., Lee, S., Moon, W. & Jeon, S. Gravimetric Analysis of CO2 Adsorption on Activated Carbon at Various Pressures and Temperatures Using Piezoelectric Microcantilevers. *Anal. Chem.* **83**, 7194–7197 (2011).
46. Sun, C. *et al.* Mechanisms of Molecular Permeation through Nanoporous Graphene Membranes. *Langmuir* **30**, 675–682 (2014).
47. Du, H. *et al.* Separation of Hydrogen and Nitrogen Gases with Porous Graphene Membrane. *J. Phys. Chem. C* **115**, 23261–23266 (2011).
48. Sun, C. & Bai, B. Fast mass transport across two-dimensional graphene nanopores: Nonlinear pressure-dependent gas permeation flux. *Chem. Eng. Sci.* **165**, 186–191 (2017).
49. Blankenburg, S. *et al.* Porous Graphene as an Atmospheric Nanofilter. *Small* **6**, 2266–2271 (2010).
50. Qin, X., Meng, Q., Feng, Y. & Gao, Y. Graphene with line defect as a membrane for gas separation: Design via a first-principles modeling. *Surf. Sci.* **607**, 153–158 (2013).
51. Ambrosetti, A. & Silvestrelli, P. L. Gas Separation in Nanoporous Graphene from First Principle Calculations. *J. Phys. Chem. C* **118**, 19172–19179 (2014).
52. Hu, W., Wu, X., Li, Z. & Yang, J. Porous silicene as a hydrogen purification membrane. *Phys. Chem. Chem. Phys.* **15**, 5753–5757 (2013).
53. Jiao, Y. *et al.* Graphdiyne: a versatile nanomaterial for electronics and hydrogen purification. *Chem. Commun.* **47**, 11843–11845 (2011).
54. Lalitha, M., Lakshmipathi, S. & Bhatia, S. K. Defect-Mediated Reduction in Barrier for Helium Tunneling through Functionalized Graphene Nanopores. *J. Phys. Chem. C* **119**, 20940–20948 (2015).
55. Li, Y., Zhou, Z., Shen, P. & Chen, Z. Two-dimensional polyphenylene: experimentally available porous graphene as a hydrogen purification membrane. *Chem. Commun.* **46**, 3672 (2010).

56. Lu, R. *et al.* Prominently Improved Hydrogen Purification and Dispersive Metal Binding for Hydrogen Storage by Substitutional Doping in Porous Graphene. *J. Phys. Chem. C* **116**, 21291–21296 (2012).
57. Schrier, J. Helium Separation Using Porous Graphene Membranes. *J. Phys. Chem. Lett.* **1**, 2284–2287 (2010).
58. Zhang, H. *et al.* Tunable Hydrogen Separation in sp–sp2 Hybridized Carbon Membranes: A First-Principles Prediction. *J. Phys. Chem. C* **116**, 16634–16638 (2012).
59. Zhang, Y. *et al.* Hydrogen separation by porous phosphorene: A periodical DFT study. *Int. J. Hydrog. Energy* (2016) doi:10.1016/j.ijhydene.2016.10.108.
60. Bian, A., Dai, Y. & Yang, J. Porous Germanene as A Highly Efficient Gas Separation Membrane. *Nanoscale* (2017) doi:10.1039/C7NR05805E.
61. Yin, K. *et al.* Generating Sub-nanometer Pores in Single-Layer MoS_2 by Heavy-Ion Bombardment for Gas Separation: A Theoretical Perspective. *ACS Appl. Mater. Interfaces* **10**, 28909–28917 (2018).
62. Gao, E., Zhang, C., Zhou, K. & Wei, N. Computational Study on Strain-Engineered Graphene Nanopores for Selective Gas Separation. *ACS Appl. Nano Mater.* **3**, 11474–11480 (2020).
63. Li, Y., Zhang, L. & Wu, C. Uncertainty in the separation properties of functionalized porous graphenes. *Appl. Surf. Sci.* 146524 (2020) doi:10.1016/j.apsusc.2020.146524.
64. Wei, S. *et al.* Mechanistic insights into porous graphene membranes for helium separation and hydrogen purification. *Appl. Surf. Sci.* **441**, 631–638 (2018).
65. Solvik, K., Weaver, J. A., Brockway, A. M. & Schrier, J. Entropy-Driven Molecular Separations in 2D-Nanoporous Materials, with Application to High-Performance Paraffin/Olefin Membrane Separations. *J. Phys. Chem. C* **117**, 17050–17057 (2013).
66. Liu, H., Dai, S. & Jiang, D. Insights into CO2/N2 separation through nanoporous graphene from molecular dynamics. *Nanoscale* **5**, 9984 (2013).
67. Sun, C. & Bai, B. Molecular sieving through a graphene nanopore: non-equilibrium molecular dynamics simulation. *Sci. Bull.* **62**, 554–562 (2017).
68. Liu, H., Chen, Z., Dai, S. & Jiang, D. Selectivity trend of gas separation through nanoporous graphene. *J. Solid State Chem.* **224**, 2–6 (2015).
69. Au, H. (Harold S.). Molecular dynamics simulation of nanoporous graphene for selective gas separation. (Massachusetts Institute of Technology, 2012).
70. Cranford, S. W. & Buehler, M. J. Selective hydrogen purification through graphdiyne under ambient temperature and pressure. *Nanoscale* **4**, 4587–4593 (2012).
71. Lei, G., Liu, C., Xie, H. & Song, F. Separation of the hydrogen sulfide and methane mixture by the porous graphene membrane: Effect of the charges. *Chem. Phys. Lett.* **599**, 127–132 (2014).
72. Liu, H., Dai, S. & Jiang, D. Permeance of H2 through porous graphene from molecular dynamics. *Solid State Commun.* **175–176**, 101–105 (2013).
73. Schrier, J. Carbon Dioxide Separation with a Two-Dimensional Polymer Membrane. *ACS Appl. Mater. Interfaces* **4**, 3745–3752 (2012).
74. Shan, M. *et al.* Influence of chemical functionalization on the CO2/N2 separation performance of porous graphene membranes. *Nanoscale* **4**, 5477–5482 (2012).
75. Sun, C., Wen, B. & Bai, B. Application of nanoporous graphene membranes in natural gas processing: Molecular simulations of CH4/CO2, CH4/H2S and CH4/N2 separation. *Chem. Eng. Sci.* **138**, 616–621 (2015).
76. Wen, B., Sun, C. & Bai, B. Inhibition effect of a non-permeating component on gas permeability of nanoporous graphene membranes. *Phys. Chem. Chem. Phys.* **17**, 23619–23626 (2015).
77. Wu, T. *et al.* Fluorine-Modified Porous Graphene as Membrane for CO2/N2 Separation: Molecular Dynamic and First-Principles Simulations. *J. Phys. Chem. C* **118**, 7369–7376 (2014).
78. Azamat, J., Khataee, A. & Sadikoglu, F. Separation of carbon dioxide and nitrogen gases through modified boron nitride nanosheets as a membrane: insights from molecular dynamics simulations. *RSC Adv.* **6**, 94911–94920 (2016).
79. Wang, Y., Yang, Q., Li, J., Yang, J. & Zhong, C. Exploration of nanoporous graphene membranes for the separation of N2 from CO2: a multi-scale computational study. *Phys Chem Chem Phys* **18**, 8352–8358 (2016).

80. Esfandiarpoor, S., Fazli, M. & Ganji, M. D. Reactive molecular dynamic simulations on the gas separation performance of porous graphene membrane. *Sci. Rep.* **7**, 16561 (2017).
81. Khakpay, A., Rahmani, F., Nouranian, S. & Scovazzo, P. Molecular Insights on the CH4/CO2 Separation in Nanoporous Graphene and Graphene Oxide Separation Platforms: Adsorbents versus Membranes. *J. Phys. Chem. C* **121**, 12308–12320 (2017).
82. Sun, C. & Bai, B. Improved CO2/CH4 Separation Performance in Negatively Charged Nanoporous Graphene Membranes. *J. Phys. Chem. C* (2018) doi:10.1021/acs.jpcc.8b00181.
83. Tronci, G. *et al.* Theoretical Study of Nanoporous Graphene Membranes for Natural Gas Purification. *Appl. Sci.* **8**, 1547 (2018).
84. Wang, S., Dai, S. & Jiang, D. Continuously Tunable Pore Size for Gas Separation via a Bilayer Nanoporous Graphene Membrane. *ACS Appl. Nano Mater.* **2**, 379–384 (2019).
85. Wang, S., Tian, Z., Dai, S. & Jiang, D. Effect of pore density on gas permeation through nanoporous graphene membranes. *Nanoscale* **10**, 14660–14666 (2018).
86. Wang, S., Dai, S. & Jiang, D. Entropic selectivity in air separation via a bilayer nanoporous graphene membrane. *Phys. Chem. Chem. Phys.* (2019) doi:10.1039/C9CP02670C.
87. Liu, M., Song, D., Wang, X., Sun, C. & Jing, D. Asymmetric Two-Layer Porous Membrane for Gas Separation. *J. Phys. Chem. Lett.* 6359–6363 (2020) doi:10.1021/acs.jpclett.0c01797.
88. Xu, Y., Zhu, H., Wang, M., Xu, J. & Yang, C. Separation of 1-Butene and 2-Butene Isomers via Nanoporous Graphene: A Molecular Simulation Study. *Ind. Eng. Chem. Res.* (2020) doi:10.1021/acs.iecr.0c00362.
89. Sun, C., Luo, K., Zhou, R. & Bai, B. Theoretical description of molecular permeation via surface diffusion through graphene nanopores. *Phys. Chem. Chem. Phys.* (2021) doi:10.1039/D0CP05629D.
90. Sun, C., Zhou, R., Bai, B., Lin, Y. & Li, B. Multilayer Graphene Sheet with Conical Nanopores as a Membrane for High-Permeance Molecular Separation. *J. Phys. Chem. C* **125**, 3047–3054 (2021).
91. Hauser, A. W. & Schwerdtfeger, P. Methane-selective nanoporous graphene membranes for gas purification. *Phys. Chem. Chem. Phys.* **14**, 13292–13298 (2012).
92. Huang, C., Wu, H., Deng, K., Tang, W. & Kan, E. Improved permeability and selectivity in porous graphene for hydrogen purification. *Phys. Chem. Chem. Phys.* **16**, 25755–25759 (2014).
93. Brockway, A. M. & Schrier, J. Noble Gas Separation using PG-ESX (X = 1, 2, 3) Nanoporous Two-Dimensional Polymers. *J. Phys. Chem. C* **117**, 393–402 (2013).
94. Hauser, A. W., Schrier, J. & Schwerdtfeger, P. Helium Tunneling through Nitrogen-Functionalized Graphene Pores: Pressure- and Temperature-Driven Approaches to Isotope Separation. *J. Phys. Chem. C* **116**, 10819–10827 (2012).
95. Tao, Y. *et al.* Tunable Hydrogen Separation in Porous Graphene Membrane: First-Principle and Molecular Dynamic Simulation. *ACS Appl. Mater. Interfaces* **6**, 8048–8058 (2014).
96. Zhang, Y. *et al.* Hexagonal Boron Nitride with Designed Nanopores as a High-Efficiency Membrane for Separating Gaseous Hydrogen from Methane. *J. Phys. Chem. C* **119**, 19826–19831 (2015).
97. Qu, Y., Li, F. & Zhao, M. Theoretical Design of Highly Efficient CO2/N2 Separation Membranes Based on Electric Quadrupole Distinction. *J. Phys. Chem. C* **121**, 17925–17931 (2017).
98. Zhang, Y. *et al.* Nanoporous MoS_2 monolayer as a promising membrane for purifying hydrogen and enriching methane. *J. Phys. Condens. Matter* (2017) doi:10.1088/1361-648X/aa7d5e.
99. Zhao, L. *et al.* Promising monolayer membranes for CO2/N2/CH4 separation: Graphdiynes modified respectively with hydrogen, fluorine, and oxygen atoms. *Appl. Surf. Sci.* **405**, 455–464 (2017).
100. Rao, Y.-C., Chu, Z.-Q., Gu, X. & Duan, X.-M. Theoretical design of a strain-controlled nanoporous CN membrane for helium separation. *Comput. Mater. Sci.* **161**, 53–57 (2019).
101. Zhu, L. *et al.* C2N: an excellent two-dimensional monolayer membrane for He separation. *J. Mater. Chem. A* **3**, 21351–21356 (2015).
102. Vallejos-Burgos, F., Coudert, F.-X. & Kaneko, K. Air separation with graphene mediated by nanowindow-rim concerted motion. *Nat. Commun.* **9**, 1812 (2018).
103. Wang, Y. *et al.* The mechanisms study of the porous graphene for the purification of the mixed gases: A multi-scale computational method. *Comput. Mater. Sci.* **143**, 277–285 (2018).

104. Wang, M. *et al.* Strain-controlled carbon nitride: a continuously tunable membrane for gas separation. *Appl. Surf. Sci.* 144675 (2019) doi:10.1016/j.apsusc.2019.144675.
105. Jalil Mahdizadeh, S. & K. Goharshadi, E. Multicomponent gas separation and purification using advanced 2D carbonaceous nanomaterials. *RSC Adv.* **10**, 24255–24264 (2020).
106. Lin, S. *et al.* Hidden porous boron nitride as a high-efficiency membrane for hydrogen purification. *Phys. Chem. Chem. Phys.* (2020) doi:10.1039/D0CP03785K.
107. Wang, Y., Yang, Q., Zhong, C. & Li, J. Theoretical investigation of gas separation in functionalized nanoporous graphene membranes. *Appl. Surf. Sci.* **407**, 532–539 (2017).
108. Tian, Z., Dai, S. & Jiang, D. Expanded Porphyrins as Two-Dimensional Porous Membranes for CO2 Separation. *ACS Appl. Mater. Interfaces* **7**, 13073–13079 (2015).
109. Koenig, S. P., Wang, L., Pellegrino, J. & Bunch, J. S. Selective molecular sieving through porous graphene. *Nat. Nanotechnol.* **7**, 728–732 (2012).
110. Wang, L. *et al.* Molecular valves for controlling gas phase transport made from discrete ångström-sized pores in graphene. *Nat. Nanotechnol.* **10**, 785–790 (2015).
111. Celebi, K. *et al.* Ultimate Permeation Across Atomically Thin Porous Graphene. *Science* **344**, 289–292 (2014).
112. Rosłoń, I. E. *et al.* High-frequency gas effusion through nanopores in suspended graphene. *Nat. Commun.* **11**, 6025 (2020).
113. Boutilier, M. S. H., Hadjiconstantinou, N. G. & Karnik, R. Knudsen effusion through polymer-coated three-layer porous graphene membranes. *Nanotechnology* **28**, 184003 (2017).
114. Liu, J. *et al.* Selective Gas Permeation in Defect-Engineered Bilayer Graphene. *Nano Lett.* **21**, 2183–2190 (2021).
115. Boutilier, M. S. H. *et al.* Molecular Sieving Across Centimeter-Scale Single-Layer Nanoporous Graphene Membranes. *ACS Nano* **11**, 5726–5736 (2017).
116. Schlichting, K.-P. & Poulikakos, D. Selective Etching of Graphene Membrane Nanopores: From Molecular Sieving to Extreme Permeance. *ACS Appl. Mater. Interfaces* **12**, 36468–36477 (2020).
117. Thiruraman, J. P. *et al.* Gas flow through atomic-scale apertures. *Sci. Adv.* **6**, eabc7927 (2020).
118. He, G. *et al.* Synergistic CO2-Sieving from Polymer with Intrinsic Microporosity Masking Nanoporous Single-Layer Graphene. *Adv. Funct. Mater.* **30**, 2003979 (2020).
119. Guo, W., Mahurin, S. M., Unocic, R. R., Luo, H. & Dai, S. Broadening the Gas Separation Utility of Monolayer Nanoporous Graphene Membranes by an Ionic Liquid Gating. *Nano Lett.* **20**, 7995–8000 (2020).
120. Huang, S. *et al.* Single-layer graphene membranes by crack-free transfer for gas mixture separation. *Nat. Commun.* **9**, 2632 (2018).
121. He, G. *et al.* High-permeance polymer-functionalized single-layer graphene membranes that surpass the postcombustion carbon capture target. *Energy Environ. Sci.* **12**, 3305–3312 (2019).
122. Zhao, J. *et al.* Etching gas-sieving nanopores in single-layer graphene with an angstrom precision for high-performance gas mixture separation. *Sci. Adv.* **5**, eaav1851 (2019).
123. Hou, D. *et al.* Decimeter-Scale Atomically Thin Graphene Membranes for Gas–Liquid Separation. *ACS Appl. Mater. Interfaces* **13**, 10328–10335 (2021).
124. Huang, S. *et al.* Millisecond lattice gasification for high-density CO2- and O2-sieving nanopores in single-layer graphene. *Sci. Adv.* **7**, eabf0116 (2021).
125. Lee, W.-C. *et al.* Centimeter-scale gas-sieving nanoporous single-layer graphene membrane. *J. Membr. Sci.* **618**, 118745 (2021).
126. Boutilier, M. S. H. *et al.* Implications of Permeation through Intrinsic Defects in Graphene on the Design of Defect-Tolerant Membranes for Gas Separation. *ACS Nano* **8**, 841–849 (2014).
127. Choi, K., Droudian, A., Wyss, R. M., Schlichting, K.-P. & Park, H. G. Multifunctional wafer-scale graphene membranes for fast ultrafiltration and high permeation gas separation. *Sci. Adv.* **4**, eaau0476 (2018).
128. Khan, M. H. *et al.* Hydrogen sieving from intrinsic defects of benzene-derived single-layer graphene. *Carbon* **153**, 458–466 (2019).
129. Nikkho, S., Mirzaei, M., Karimi Sabet, J., Moosavian, M. A. & Hedayat, S. M. Enhanced quality of transfer-free graphene membrane for He/CH4 separation. *Sep. Purif. Technol.* **232**, 115972 (2020).

130. Rezaei, M., Li, S., Huang, S. & Agrawal, K. V. Hydrogen-sieving single-layer graphene membranes obtained by crystallographic and morphological optimization of catalytic copper foil. *J. Membr. Sci.* **612**, 118406 (2020).
131. O'Hern, S. C. *et al.* Selective Ionic Transport through Tunable Subnanometer Pores in Single-Layer Graphene Membranes. *Nano Lett.* **14**, 1234–1241 (2014).
132. O'Hern, S. C. *et al.* Nanofiltration across Defect-Sealed Nanoporous Monolayer Graphene. *Nano Lett.* **15**, 3254–3260 (2015).
133. Surwade, S. P. *et al.* Water desalination using nanoporous single-layer graphene. *Nat. Nanotechnol.* **10**, 459–464 (2015).
134. Hong, J.-Y. *et al.* A Rational Strategy for Graphene Transfer on Substrates with Rough Features. *Adv. Mater.* **28**, 2382–2392 (2016).
135. Kim, H. H., Lee, S. K., Lee, S. G., Lee, E. & Cho, K. Wetting-Assisted Crack- and Wrinkle-Free Transfer of Wafer-Scale Graphene onto Arbitrary Substrates over a Wide Range of Surface Energies. *Adv. Funct. Mater.* **26**, 2070–2077 (2016).
136. Wang, L., Williams, C. M., Boutilier, M. S. H., Kidambi, P. R. & Karnik, R. Single-Layer Graphene Membranes Withstand Ultrahigh Applied Pressure. *Nano Lett.* **17**, 3081–3088 (2017).
137. Dutta, S., Vahdat, M. T., Rezaei, M. & Agrawal, K. V. Crystallization of gas-selective nanoporous graphene by competitive etching and growth: a modeling study. *Sci. Rep.* **9**, 5202 (2019).
138. Wang, L., Zhang, X., Chan, H. L. W., Yan, F. & Ding, F. Formation and Healing of Vacancies in Graphene Chemical Vapor Deposition (CVD) Growth. *J. Am. Chem. Soc.* **135**, 4476–4482 (2013).
139. Bernardo, P., Drioli, E. & Golemme, G. Membrane Gas Separation: A Review/State of the Art. *Ind. Eng. Chem. Res.* **48**, 4638–4663 (2009).
140. Liu, G., Jin, W. & Xu, N. Graphene-based membranes. *Chem. Soc. Rev.* **44**, 5016–5030 (2015).
141. Park, H. B. *et al.* Polymers with Cavities Tuned for Fast Selective Transport of Small Molecules and Ions. *Science* **318**, 254–258 (2007).
142. Carreon, M. A., Li, S., Falconer, J. L. & Noble, R. D. Alumina-supported SAPO-34 membranes for CO2/CH4 separation. *J. Am. Chem. Soc.* **130**, 5412–5413 (2008).
143. Venna, S. R. & Carreon, M. A. Highly Permeable Zeolite Imidazolate Framework-8 Membranes for CO2/CH4 Separation. *J. Am. Chem. Soc.* **132**, 76–78 (2010).
144. Saufi, S. M. & Ismail, A. F. Fabrication of carbon membranes for gas separation—a review. *Carbon* **42**, 241–259 (2004).
145. Sun, P., Wang, K. & Zhu, H. Recent Developments in Graphene-Based Membranes: Structure, Mass-Transport Mechanism and Potential Applications. *Adv. Mater.* **28**, 2287–2310 (2016).
146. Booth, T. J. *et al.* Macroscopic graphene membranes and their extraordinary stiffness. *Nano Lett.* **8**, 2442–2446 (2008).
147. Robertson, A. W. *et al.* Atomic Structure of Graphene Subnanometer Pores. *ACS Nano* **9**, 11599–11607 (2015).
148. Drahushuk, L. W., Wang, L., Koenig, S. P., Bunch, J. S. & Strano, M. S. Analysis of Time-Varying, Stochastic Gas Transport through Graphene Membranes. *ACS Nano* **10**, 786–795 (2016).
149. O'Hern, S. C. *et al.* Selective Molecular Transport through Intrinsic Defects in a Single Layer of CVD Graphene. *ACS Nano* **6**, 10130–10138 (2012).
150. Chandler, D. Statistical mechanics of isomerization dynamics in liquids and the transition state approximation. *J. Chem. Phys.* **68**, 2959–2970 (1978).
151. Auerbach, S. M. Theory and simulation of jump dynamics, diffusion and phase equilibrium in nanopores. *Int. Rev. Phys. Chem.* **19**, 155–198 (2000).
152. Drahushuk, L. W. & Strano, M. S. Mechanisms of Gas Permeation through Single Layer Graphene Membranes. *Langmuir* **28**, 16671–16678 (2012).
153. Tian, Z., Mahurin, S. M., Dai, S. & Jiang, D. Ion-Gated Gas Separation through Porous Graphene. *Nano Lett.* **17**, 1802–1807 (2017).
154. Potoff, J. J. & Siepmann, J. I. Vapor–liquid equilibria of mixtures containing alkanes, carbon dioxide, and nitrogen. *AIChE J.* **47**, 1676–1682 (2001).
155. Harris, J. G. & Yung, K. H. Carbon Dioxide's Liquid-Vapor Coexistence Curve And Critical Properties as Predicted by a Simple Molecular Model. *J. Phys. Chem.* **99**, 12021–12024 (1995).

156. Bell, I. H., Wronski, J., Quoilin, S. & Lemort, V. Pure and Pseudo-pure Fluid Thermophysical Property Evaluation and the Open-Source Thermophysical Property Library CoolProp. *Ind. Eng. Chem. Res.* **53**, 2498–2508 (2014).
157. Span, R. & Wagner, W. A new equation of state for carbon dioxide covering the fluid region from the triple-point temperature to 1100 K at pressures up to 800 MPa. *J. Phys. Chem. Ref. Data* **25**, 1509–1596 (1996).
158. Setzmann, U. & Wagner, W. A new equation of state and tables of thermodynamic properties for methane covering the range from the melting line to 625 K at pressures up to 100 MPa. *J. Phys. Chem. Ref. Data* **20**, 1061–1155 (1991).
159. Schmidt, R. & Wagner, W. A new form of the equation of state for pure substances and its application to oxygen. *Fluid Phase Equilibria* **19**, 175–200 (1985).
160. Stewart, R. B., Jacobsen, R. T. & Wagner, W. Thermodynamic properties of oxygen from the triple point to 300 K with pressures to 80 MPa. *J. Phys. Chem. Ref. Data* **20**, 917–1021 (1991).
161. Brunauer, S., Emmett, P. H. & Teller, E. Adsorption of Gases in Multimolecular Layers. *J. Am. Chem. Soc.* **60**, 309–319 (1938).
162. Auerbach, S. M., Henson, N. J., Cheetham, A. K. & Metiu, H. I. Transport Theory for Cationic Zeolites: Diffusion of Benzene in Na-Y. *J. Phys. Chem.* **99**, 10600–10608 (1995).
163. Himeno, S., Komatsu, T. & Fujita, S. High-Pressure Adsorption Equilibria of Methane and Carbon Dioxide on Several Activated Carbons. *J. Chem. Eng. Data* **50**, 369–376 (2005).
164. Frenkel, D. & Smit, B. Chapter 16 - Rare Events. in *Understanding Molecular Simulation (Second Edition)* (eds. Frenkel, D. & Smit, B.) 431–464 (Academic Press, 2002).
165. Kumar, S., Rosenberg, J. M., Bouzida, D., Swendsen, R. H. & Kollman, P. A. The weighted histogram analysis method for free-energy calculations on biomolecules. I. The method. *J. Comput. Chem.* **13**, 1011–1021 (1992).
166. Cabrales-Navarro, F. A., Gómez-Ballesteros, J. L. & Balbuena, P. B. Molecular dynamics simulations of metal-organic frameworks as membranes for gas mixtures separation. *J. Membr. Sci.* **428**, 241–250 (2013).
167. Li, H. *et al.* Ultrathin, Molecular-Sieving Graphene Oxide Membranes for Selective Hydrogen Separation. *Science* **342**, 95–98 (2013).
168. Jorgensen, W. L., Maxwell, D. S. & Tirado-Rives, J. Development and Testing of the OPLS All-Atom Force Field on Conformational Energetics and Properties of Organic Liquids. *J. Am. Chem. Soc.* **118**, 11225–11236 (1996).
169. MacKerell, A. D. *et al.* All-Atom Empirical Potential for Molecular Modeling and Dynamics Studies of Proteins. *J. Phys. Chem. B* **102**, 3586–3616 (1998).
170. Patra, N., Wang, B. & Král, P. Nanodroplet Activated and Guided Folding of Graphene Nanostructures. *Nano Lett.* **9**, 3766–3771 (2009).
171. Cheng, A. & Steele, W. A. Computer simulation of ammonia on graphite. I. Low temperature structure of monolayer and bilayer films. *J. Chem. Phys.* **92**, 3858–3866 (1990).
172. Perng, B.-C., Sasaki, S., Ladanyi, B. M., Everitt, K. F. & Skinner, J. L. A new intermolecular potential for liquid oxygen. *Chem. Phys. Lett.* **348**, 491–496 (2001).
173. Cornell, W. D. *et al.* A second generation force field for the simulation of proteins, nucleic acids, and organic molecules. *J. Am. Chem. Soc.* **117**, 5179–5197 (1995).
174. Plimpton, S. Fast Parallel Algorithms for Short-Range Molecular Dynamics. *J. Comput. Phys.* **117**, 1–19 (1995).
175. Hoover, W. G. Canonical dynamics: equilibrium phase-space distributions. *Phys. Rev. A* **31**, 1695 (1985).
176. Voter, A. F. Parallel replica method for dynamics of infrequent events. *Phys. Rev. B* **57**, R13985 (1998).
177. Ross, S. M. *Introduction to probability and statistics for engineers and scientists*. (Academic Press, 2014).
178. Grossfield, A. *WHAM: the weighted histogram analysis method, version 2.09*. (2015).
179. Bouanich, J.-P. Site-site Lennard-Jones potential parameters for N2, O2, H2, CO and CO2. *J. Quant. Spectrosc. Radiat. Transf.* **47**, 243–250 (1992).
180. Li, S., Falconer, J. L. & Noble, R. D. SAPO-34 membranes for CO2/CH4 separations: Effect of Si/Al ratio. *Microporous Mesoporous Mater.* **110**, 310–317 (2008).

181. Vu, D. Q., Koros, W. J. & Miller, S. J. High Pressure CO2/CH4 Separation Using Carbon Molecular Sieve Hollow Fiber Membranes. *Ind. Eng. Chem. Res.* **41**, 367–380 (2002).
182. Favvas, E. P., Kapantaidakis, G. C., Nolan, J. W., Mitropoulos, A. Ch. & Kanellopoulos, N. K. Preparation, characterization and gas permeation properties of carbon hollow fiber membranes based on Matrimid® 5218 precursor. *J. Mater. Process. Technol.* **186**, 102–110 (2007).
183. Okui, T., Saito, Y., Okubo, T. & Sadakata, M. Gas permeation of porous organic/inorganic hybrid membranes. *J. Sol-Gel Sci. Technol.* **5**, 127–134 (1995).
184. Sea, B.-K., Kusakabe, K. & Morooka, S. Pore size control and gas permeation kinetics of silica membranes by pyrolysis of phenyl-substituted ethoxysilanes with cross-flow through a porous support wall. *J. Membr. Sci.* **130**, 41–52 (1997).
185. Tsai, C.-Y., Tam, S.-Y., Lu, Y. & Brinker, C. J. Dual-layer asymmetric microporous silica membranes. *J. Membr. Sci.* **169**, 255–268 (2000).
186. Oyama, S. T., Gu, Y., Allison, J. D., Gunter, G. C. & Scholten, S. A. Hybrid organic-inorganic gas separation membranes. (2011).
187. Sridhar, S., Suryamurali, R., Smitha, B. & Aminabhavi, T. M. Development of crosslinked poly(ether-block-amide) membrane for CO2/CH4 separation. *Colloids Surf. Physicochem. Eng. Asp.* **297**, 267–274 (2007).
188. Guo, C., Zhou, L. & Lv, J. Effects of expandable graphite and modified ammonium polyphosphate on the flame-retardant and mechanical properties of wood flour-polypropylene composites. *Polym. Polym. Compos.* **21**, 449 (2013).
189. Visser, T., Masetto, N. & Wessling, M. Materials dependence of mixed gas plasticization behavior in asymmetric membranes. *J. Membr. Sci.* **306**, 16–28 (2007).
190. Iqbal, M., Man, Z., Mukhtar, H. & Dutta, B. K. Solvent effect on morphology and CO2/CH4 separation performance of asymmetric polycarbonate membranes. *J. Membr. Sci.* **318**, 167–175 (2008).
191. Sridhar, S., Aminabhavi, T. M., Mayor, S. J. & Ramakrishna, M. Permeation of Carbon Dioxide and Methane Gases through Novel Silver-Incorporated Thin Film Composite Pebax Membranes. *Ind. Eng. Chem. Res.* **46**, 8144–8151 (2007).
192. Ismail, A. F., Kusworo, T. D. & Mustafa, A. Enhanced gas permeation performance of polyethersulfone mixed matrix hollow fiber membranes using novel Dynasylan Ameo silane agent. *J. Membr. Sci.* **319**, 306–312 (2008).
193. Hanioka, S. *et al.* CO2 separation facilitated by task-specific ionic liquids using a supported liquid membrane. *J. Membr. Sci.* **314**, 1–4 (2008).
194. Cserjési, P., Nemestóthy, N. & Bélafi-Bakó, K. Gas separation properties of supported liquid membranes prepared with unconventional ionic liquids. *J. Membr. Sci.* **349**, 6–11 (2010).
195. Scovazzo, P., Havard, D., McShea, M., Mixon, S. & Morgan, D. Long-term, continuous mixed-gas dry fed CO2/CH4 and CO2/N2 separation performance and selectivities for room temperature ionic liquid membranes. *J. Membr. Sci.* **327**, 41–48 (2009).
196. Liu, Y., Zeng, G., Pan, Y. & Lai, Z. Synthesis of highly c-oriented ZIF-69 membranes by secondary growth and their gas permeation properties. *J. Membr. Sci.* **379**, 46–51 (2011).
197. Zou, X. *et al.* Co3(HCOO)6 Microporous Metal–Organic Framework Membrane for Separation of CO2/CH4 Mixtures. *Chem. – Eur. J.* **17**, 12076–12083 (2011).
198. Bux, H., Chmelik, C., van Baten, J. M., Krishna, R. & Caro, J. Novel MOF-Membrane for Molecular Sieving Predicted by IR-Diffusion Studies and Molecular Modeling. *Adv. Mater.* **22**, 4741–4743 (2010).
199. Huang, A., Liu, Q., Wang, N. & Caro, J. Organosilica functionalized zeolitic imidazolate framework ZIF-90 membrane for CO2/CH4 separation. *Microporous Mesoporous Mater.* **192**, 18–22 (2014).
200. Liu, G., Jin, W. & Xu, N. Two-Dimensional-Material Membranes: A New Family of High-Performance Separation Membranes. *Angew. Chem. Int. Ed.* **55**, 13384–13397 (2016).
201. Yoon, H. W., Cho, Y. H. & Park, H. B. Graphene-based membranes: status and prospects. *Philos. Trans. R. Soc. Math. Phys. Eng. Sci.* **374**, 20150024 (2016).
202. Kazemi, A. S., Hosseini, S. M. & Abdi, Y. Large total area membrane of suspended single layer graphene for water desalination. *Desalination* **451**, 160–171 (2019).

203. Kidambi, P. R. *et al.* Selective Nanoscale Mass Transport across Atomically Thin Single Crystalline Graphene Membranes. *Adv. Mater.* 1605896 (2017) doi:10.1002/adma.201605896.
204. Rollings, R. C., Kuan, A. T. & Golovchenko, J. A. Ion selectivity of graphene nanopores. *Nat. Commun.* **7**, 11408 (2016).
205. Sun, C. & Bai, B. Gas diffusion on graphene surfaces. *Phys. Chem. Chem. Phys.* **19**, 3894–3902 (2017).
206. Lin, Y.-C. *et al.* Graphene Annealing: How Clean Can It Be? *Nano Lett.* **12**, 414–419 (2012).
207. Zhang, Y., Sunarso, J., Liu, S. & Wang, R. Current status and development of membranes for CO2/CH4 separation: A review. *Int. J. Greenh. Gas Control* **12**, 84–107 (2013).
208. Rowland, R. S. & Taylor, R. Intermolecular Nonbonded Contact Distances in Organic Crystal Structures: Comparison with Distances Expected from van der Waals Radii. *J. Phys. Chem.* **100**, 7384–7391 (1996).
209. Meyer, J. C. *et al.* The structure of suspended graphene sheets. *Nature* **446**, 60–63 (2007).
210. Wang, W. L. *et al.* Direct Imaging of Atomic-Scale Ripples in Few-Layer Graphene. *Nano Lett.* **12**, 2278–2282 (2012).
211. Hockney, R. W., Eastwood, J. W. & Eastwood, J. W. *Computer Simulation Using Particles*. (Taylor & Francis Group, 1988). doi:10.1201/9781439822050.
212. Johnson, N. L., Kemp, A. W. & Kotz, S. *Univariate discrete distributions*. (John Wiley & Sons, 2005).
213. Gillespie, D. T. A general method for numerically simulating the stochastic time evolution of coupled chemical reactions. *J. Comput. Phys.* **22**, 403–434 (1976).
214. Gastwirth, J. L. The Estimation of the Lorenz Curve and Gini Index. *Rev. Econ. Stat.* **54**, 306 (1972).
215. Bao, W. *et al.* Controlled ripple texturing of suspended graphene and ultrathin graphite membranes. *Nat. Nanotechnol.* **4**, 562–566 (2009).
216. Li, Z. *et al.* Effect of airborne contaminants on the wettability of supported graphene and graphite. *Nat. Mater.* **12**, 925–931 (2013).
217. Kozbial, A., Zhou, F., Li, Z., Liu, H. & Li, L. Are Graphitic Surfaces Hydrophobic? *Acc. Chem. Res.* **49**, 2765–2773 (2016).
218. Tanaka, H., Kanoh, H., Yudasaka, M., Iijima, S. & Kaneko, K. Quantum Effects on Hydrogen Isotope Adsorption on Single-Wall Carbon Nanohorns. *J. Am. Chem. Soc.* **127**, 7511–7516 (2005).
219. Callen, H. B. *Thermodynamics and an Introduction to Thermostatistics, 2nd ed.* (John Wiley & Sons, 1987).
220. Novoselov, K. S. *et al.* Electric field effect in atomically thin carbon films. *Science* **306**, 666–669 (2004).
221. Yuan, W., Chen, J. & Shi, G. Nanoporous graphene materials. *Mater. Today* **17**, 77–85 (2014).
222. Kim, H. W. *et al.* Selective Gas Transport Through Few-Layered Graphene and Graphene Oxide Membranes. *Science* **342**, 91–95 (2013).
223. Joshi, R. K. *et al.* Precise and ultrafast molecular sieving through graphene oxide membranes. *Science* **343**, 752–754 (2014).
224. Agrawal, K. V. *et al.* Fabrication, Pressure Testing, and Nanopore Formation of Single-Layer Graphene Membranes. *J. Phys. Chem. C* **121**, 14312–14321 (2017).
225. Liu, Y. & Chen, X. Mechanical properties of nanoporous graphene membrane. *J. Appl. Phys.* **115**, 034303 (2014).
226. Cohen-Tanugi, D. & Grossman, J. C. Mechanical Strength of Nanoporous Graphene as a Desalination Membrane. *Nano Lett.* **14**, 6171–6178 (2014).
227. Tsapatsis, M. Toward High-Throughput Zeolite Membranes. *Science* **334**, 767–768 (2011).
228. Yan, Z. *et al.* Toward the Synthesis of Wafer-Scale Single-Crystal Graphene on Copper Foils. *ACS Nano* **6**, 9110–9117 (2012).
229. Ferrari, A. C. Raman spectroscopy of graphene and graphite: Disorder, electron–phonon coupling, doping and nonadiabatic effects. *Solid State Commun.* **143**, 47–57 (2007).
230. Ferrari, A. C. & Basko, D. M. Raman spectroscopy as a versatile tool for studying the properties of graphene. *Nat. Nanotechnol.* **8**, nnano.2013.46 (2013).
231. Malard, L. M., Pimenta, M. A., Dresselhaus, G. & Dresselhaus, M. S. Raman spectroscopy in graphene. *Phys. Rep.* **473**, 51–87 (2009).

232. Cançado, L. G. *et al.* Quantifying Defects in Graphene via Raman Spectroscopy at Different Excitation Energies. *Nano Lett.* **11**, 3190–3196 (2011).
233. Lucchese, M. M. *et al.* Quantifying ion-induced defects and Raman relaxation length in graphene. *Carbon* **48**, 1592–1597 (2010).
234. Losurdo, M., Giangregorio, M. M., Capezzuto, P. & Bruno, G. Graphene CVD growth on copper and nickel: role of hydrogen in kinetics and structure. *Phys. Chem. Chem. Phys.* **13**, 20836–20843 (2011).
235. Brand, L. The Pi theorem of dimensional analysis. *Arch. Ration. Mech. Anal.* **1**, 35–45 (1957).
236. Kidambi, P. R. *et al.* Assessment and control of the impermeability of graphene for atomically thin membranes and barriers. *Nanoscale* **9**, 8496–8507 (2017).
237. Fasolino, A., Los, J. H. & Katsnelson, M. I. Intrinsic ripples in graphene. *Nat. Mater.* **6**, 858–861 (2007).
238. Pirkle, A. *et al.* The effect of chemical residues on the physical and electrical properties of chemical vapor deposited graphene transferred to SiO2. *Appl. Phys. Lett.* **99**, 122108 (2011).
239. Nan, H. Y. *et al.* The thermal stability of graphene in air investigated by Raman spectroscopy. *J. Raman Spectrosc.* **44**, 1018–1021 (2013).
240. Cheng, Y. C., Kaloni, T. P., Zhu, Z. Y. & Schwingenschlögl, U. Oxidation of graphene in ozone under ultraviolet light. *Appl. Phys. Lett.* **101**, 073110 (2012).
241. Dinh, S. T. *et al.* Oxidize Graphene by UV-Ozone Treatment in Vacuum Chamber. *J. Nanosci. Nanotechnol.* **16**, 7968–7972 (2016).
242. Awad, A. M., Ghany, N. A. A. & Dahy, T. M. Removal of tarnishing and roughness of copper surface by electropolishing treatment. *Appl. Surf. Sci.* **256**, 4370–4375 (2010).
243. Lin, Y.-C. *et al.* Clean Transfer of Graphene for Isolation and Suspension. *ACS Nano* **5**, 2362–2368 (2011).
244. Park, H. B., Kamcev, J., Robeson, L. M., Elimelech, M. & Freeman, B. D. Maximizing the right stuff: The trade-off between membrane permeability and selectivity. *Science* **356**, eaab0530 (2017).
245. Zhou, F., Fathizadeh, M. & Yu, M. Single- to Few-Layered, Graphene-Based Separation Membranes. *Annu. Rev. Chem. Biomol. Eng.* **9**, null (2018).
246. Li, X. *et al.* Large-Area Synthesis of High-Quality and Uniform Graphene Films on Copper Foils. *Science* **324**, 1312–1314 (2009).
247. Yuan, Q., Xu, Z., Yakobson, B. I. & Ding, F. Efficient Defect Healing in Catalytic Carbon Nanotube Growth. *Phys. Rev. Lett.* **108**, (2012).
248. Chin, H.-T., Lee, J.-J., Hofmann, M. & Hsieh, Y.-P. Impact of growth rate on graphene lattice-defect formation within a single crystalline domain. *Sci. Rep.* **8**, 1–6 (2018).
249. Bekdüz, B. *et al.* Relation between growth rate and structure of graphene grown in a 4″ showerhead chemical vapor deposition reactor. *Nanotechnology* **28**, 185601 (2017).
250. Hwang, J.-Y., Kuo, C.-C., Chen, L.-C. & Chen, K.-H. Correlating defect density with carrier mobility in large-scaled graphene films: Raman spectral signatures for the estimation of defect density. *Nanotechnology* **21**, 465705 (2010).
251. Kidambi, P. R. *et al.* Facile Fabrication of Large-Area Atomically Thin Membranes by Direct Synthesis of Graphene with Nanoscale Porosity. *Adv. Mater.* **30**, 1804977 (2018).
252. Hao, Y. *et al.* The Role of Surface Oxygen in the Growth of Large Single-Crystal Graphene on Copper. *Science* **342**, 720–723 (2013).
253. Xu, X. *et al.* Ultrafast growth of single-crystal graphene assisted by a continuous oxygen supply. *Nat. Nanotechnol.* **11**, 930–935 (2016).
254. Choubak, S., Biron, M., Levesque, P. L., Martel, R. & Desjardins, P. No Graphene Etching in Purified Hydrogen. *J. Phys. Chem. Lett.* **4**, 1100–1103 (2013).
255. Eckmann, A. *et al.* Probing the Nature of Defects in Graphene by Raman Spectroscopy. *Nano Lett.* **12**, 3925–3930 (2012).
256. Rodriguez, A. T., Li, X., Wang, J., Steen, W. A. & Fan, H. Facile Synthesis of Nanostructured Carbon through Self-Assembly between Block Copolymers and Carbohydrates. *Adv. Funct. Mater.* **17**, 2710–2716 (2007).
257. Scholes, C. A. & Ghosh, U. K. Review of Membranes for Helium Separation and Purification. *Membranes* **7**, 9 (2017).

258. Thomsen, J. D., Kling, J., Mackenzie, D. M. A., Bøggild, P. & Booth, T. J. Oxidation of Suspended Graphene: Etch Dynamics and Stability Beyond 1000 °C. *ACS Nano* **13**, 2281–2288 (2019).
259. Lee, D., Zhang, L., Oyama, S. T., Niu, S. & Saraf, R. F. Synthesis, characterization, and gas permeation properties of a hydrogen permeable silica membrane supported on porous alumina. *J. Membr. Sci.* **231**, 117–126 (2004).
260. Wang, B., Hu, N., Wang, H., Zheng, Y. & Zhou, R. Improved AlPO-18 membranes for light gas separations. *J. Mater. Chem. A* 9 (2015).
261. Zhou, C., Yuan, C., Zhu, Y., Caro, J. & Huang, A. Facile synthesis of zeolite FAU molecular sieve membranes on bio-adhesive polydopamine modified Al2O3 tubes. *J. Membr. Sci.* **494**, 174–181 (2015).
262. Kida, K., Maeta, Y. & Yogo, K. Pure silica CHA-type zeolite membranes for dry and humidified CO2/CH4 mixtures separation. *Sep. Purif. Technol.* **197**, 116–121 (2018).
263. Huang, A., Wang, N. & Caro, J. Synthesis of multi-layer zeolite LTA membranes with enhanced gas separation performance by using 3-aminopropyltriethoxysilane as interlayer. *Microporous Mesoporous Mater.* **164**, 294–301 (2012).
264. Kosinov, N. *et al.* Influence of support morphology on the detemplation and permeation of ZSM-5 and SSZ-13 zeolite membranes. *Microporous Mesoporous Mater.* **197**, 268–277 (2014).
265. Kosinov, N., Auffret, C., Borghuis, G. J., Sripathi, V. G. P. & Hensen, E. J. M. Influence of the Si/Al ratio on the separation properties of SSZ-13 zeolite membranes. *J. Membr. Sci.* **484**, 140–145 (2015).
266. Zhang, F. *et al.* Hydrogen Selective NH2-MIL-53(Al) MOF Membranes with High Permeability. *Adv. Funct. Mater.* **22**, 3583–3590 (2012).
267. Kang, Z. *et al.* Highly selective sieving of small gas molecules by using an ultra-microporous metal–organic framework membrane. *Energy Environ. Sci.* **7**, 4053–4060 (2014).
268. Nian, P. *et al.* ZnO Nanorod-Induced Heteroepitaxial Growth of SOD Type Co-Based Zeolitic Imidazolate Framework Membranes for H2 Separation. *ACS Appl. Mater. Interfaces* **10**, 4151–4160 (2018).
269. Huang, A., Dou, W. & Caro, J. Steam-Stable Zeolitic Imidazolate Framework ZIF-90 Membrane with Hydrogen Selectivity through Covalent Functionalization. *J. Am. Chem. Soc.* **132**, 15562–15564 (2010).
270. Huang, A., Liu, Q., Wang, N., Zhu, Y. & Caro, J. Bicontinuous Zeolitic Imidazolate Framework ZIF-8@GO Membrane with Enhanced Hydrogen Selectivity. *J. Am. Chem. Soc.* **136**, 14686–14689 (2014).
271. Guo, H., Zhu, G., Hewitt, I. J. & Qiu, S. "Twin Copper Source" Growth of Metal−Organic Framework Membrane: Cu3(BTC)2 with High Permeability and Selectivity for Recycling H2. *J. Am. Chem. Soc.* **131**, 1646–1647 (2009).
272. Yang, J. *et al.* Self-Assembly of Thiourea-Crosslinked Graphene Oxide Framework Membranes toward Separation of Small Molecules. *Adv. Mater.* **30**, 1705775 (2018).
273. Itta, A. K., Tseng, H.-H. & Wey, M.-Y. Fabrication and characterization of PPO/PVP blend carbon molecular sieve membranes for H2/N2 and H2/CH4 separation. *J. Membr. Sci.* **372**, 387–395 (2011).
274. Lee, H.-C. *et al.* Use of Steam Activation as a Post-treatment Technique in the Preparation of Carbon Molecular Sieve Membranes. *Ind. Eng. Chem. Res.* **52**, 1122–1132 (2013).
275. Tseng, H.-H. *et al.* Enhanced H2/CH4 and H2/CO2 separation by carbon molecular sieve membrane coated on titania modified alumina support: Effects of TiO2 intermediate layer preparation variables on interfacial adhesion. *J. Membr. Sci.* **510**, 391–404 (2016).
276. Llosa Tanco, M. A., Medrano, J. A., Cechetto, V., Gallucci, F. & Pacheco Tanaka, D. A. Hydrogen permeation studies of composite supported alumina-carbon molecular sieves membranes: Separation of diluted hydrogen from mixtures with methane. *Int. J. Hydrog. Energy* (2020) doi:10.1016/j.ijhydene.2020.05.088.
277. Ahn, S.-J., Takagaki, A., Sugawara, T., Kikuchi, R. & Oyama, S. T. Permeation properties of silica-zirconia composite membranes supported on porous alumina substrates. *J. Membr. Sci.* **526**, 409–416 (2017).

278. Gu, Y., Hacarlioglu, P. & Oyama, S. T. Hydrothermally stable silica–alumina composite membranes for hydrogen separation. *J. Membr. Sci.* **310**, 28–37 (2008).
279. Ahn, S.-J., Yun, G.-N., Takagaki, A., Kikuchi, R. & Oyama, S. T. Synthesis and characterization of hydrogen selective silica membranes prepared by chemical vapor deposition of vinyltriethoxysilane. *J. Membr. Sci.* **550**, 1–8 (2018).
280. Qureshi, H. F., Nijmeijer, A. & Winnubst, L. Influence of sol–gel process parameters on the micro-structure and performance of hybrid silica membranes. *J. Membr. Sci.* **446**, 19–25 (2013).
281. de Lange, R. S. A., Hekkink, J. H. A., Keizer, K. & Burggraaf, A. J. Permeation and separation studies on microporous sol-gel modified ceramic membranes. *Microporous Mater.* **4**, 169–186 (1995).
282. Castricum, H. L., Qureshi, H. F., Nijmeijer, A. & Winnubst, L. Hybrid silica membranes with enhanced hydrogen and CO2 separation properties. *J. Membr. Sci.* **488**, 121–128 (2015).
283. Michael, J. V., Sutherland, J. W., Harding, L. B. & Wagner, A. F. Initiation in H2/O2: Rate constants for H2+O2→H+HO2 at high temperature. *Proc. Combust. Inst.* **28**, 1471–1478 (2000).
284. Cussler, E. L. & Cussler, E. L. *Diffusion: Mass Transfer in Fluid Systems*. (Cambridge University Press, 2009).
285. Wang, B., Hu, N., Wang, H., Zheng, Y. & Zhou, R. Improved AlPO-18 membranes for light gas separation. *J. Mater. Chem. A* **3**, 12205–12212 (2015).
286. Kanezashi, M., Fujita, T. & Asaeda, M. Nickel-Doped Silica Membranes for Separation of Helium from Organic Gas Mixtures. *Sep. Sci. Technol.* **40**, 225–238 (2005).
287. Asaeda, M. & Yamasaki, S. Separation of inorganic/organic gas mixtures by porous silica membranes. *Sep. Purif. Technol.* **25**, 151–159 (2001).
288. Araki, S., Mohri, N., Yoshimitsu, Y. & Miyake, Y. Synthesis, characterization and gas permeation properties of a silica membrane prepared by high-pressure chemical vapor deposition. *J. Membr. Sci.* **290**, 138–145 (2007).
289. Yoo, Y., Varela-Guerrero, V. & Jeong, H.-K. Isoreticular Metal−Organic Frameworks and Their Membranes with Enhanced Crack Resistance and Moisture Stability by Surfactant-Assisted Drying. *Langmuir* **27**, 2652–2657 (2011).
290. Takamizawa, S., Takasaki, Y. & Miyake, R. Single-Crystal Membrane for Anisotropic and Efficient Gas Permeation. *J. Am. Chem. Soc.* **132**, 2862–2863 (2010).
291. Cao, F. *et al.* Helium Recovery by a Cu-BTC Metal–Organic-Framework Membrane. *Ind. Eng. Chem. Res.* **51**, 11274–11278 (2012).
292. Li, Y., Linghu, Y. & Wu, C. Separation properties of porous MoS2 membranes decorated with small molecules. *ACS Appl. Mater. Interfaces* (2020) doi:10.1021/acsami.0c02192.
293. Sanchez Marcano, J. G. & Tsotsis, T. T. *Catalytic Membranes and Membrane Reactors*. (Wiley-VCH Verlag GmbH & Co. KGaA, 2002). doi:10.1002/3527601988.
294. Sun, B. *et al.* Gas-Permeable, Multifunctional On-Skin Electronics Based on Laser-Induced Porous Graphene and Sugar-Templated Elastomer Sponges. *Adv. Mater.* **30**, 1804327 (2018).
295. Kwak, W.-J. *et al.* Lithium–Oxygen Batteries and Related Systems: Potential, Status, and Future. *Chem. Rev.* **120**, 6626–6683 (2020).